Internal Report
DESY F41
HASYLAB 80/11
October 1980

ELECTRONIC EXCITATIONS IN CONDENSED RARE GASES

by

Nikolaus Schwentner

Ernst-Eckhard Koch

and

Joshua Jortner

ELECTRONIC EXCITATIONS IN CONDENSED RARE GASES

Nikolaus Schwentner
Institut für Experimentalphysik, Universität Kiel, 2300 Kiel, BRD

Ernst-Eckhard Koch
Hamburger Synchrotronstrahlungslabor HASYLAB
Deutsches Elektronen-Synchrotron DESY, 2000 Hamburg 52, BRD

and

Joshua Jortner
Department of Chemistry, Tel Aviv University, Tel Aviv, Israel

to be published in RARE GAS SOLIDS, Vol. III,
ed. by M.L. KLEIN and J.A. VENABLES, Academic Press.

ABSTRACT

This review is concerned with the electronic structure and the excited-state nonradiative relaxation phenomena in condensed rare gases. We shall consider pure rare gas solids, solid rare gas alloys, solid two-component mixtures, such as metal rare gas solids, pure rare gas liquids and liquid alloys. We start from the experimental point of view considering the techniques utilized to probe the optical constants, transient absorption, the energy and time resolved luminescence as well as photoelectron yield and energy distribution. We then proceed to survey the electronic structure of valence and conduction bands and excitonic states in pure solid rare gases, emphasizing recent new experimental and theoretical results for bulk excitations and for surface excitons. This is followed by a review of electronic excitations, rare gas alloys and liquid rare gases. Next, we extend the scope of disordered materials to consider metal rare gas solid mixtures and gain information concerning electronic structure, transport properties and metal-nonmetal transitions. The information about the electronic structure provides the basic input data required for the elucidation of excited state dynamics in condensed rare gases. We discuss the experimental information obtained from luminescence and photoemission studies and the available theoretical framework pertaining to the microscopic relaxation processes in solid and liquid rare gases. We have considered a variety of dynamic processes including exciton trapping, vibrational relaxation, electronic relaxation, electronic energy migration via exciton states, electronic energy transfer between localized states, autoionization and electron-hole recombination. Finally, electron transport properties and electron-hole pair creation processes for electrons with kinetic energies of some eV's up to the MeV region are treated and discussed in terms of the electronic structure and the dynamical processes involved. This review will survey the present "state of art" in the understanding of the electronic structure of condensed rare gases with an emphasis on the effects of structural and compositional disorder on the electronic properties and will be concerned with the microscopic aspects of excited-state energy conversion, storage and disposal in these materials.

While we have tried to give reference to the major developments up to the end of 1979, we have not attempted to be complete in citing each original paper.

1. Introduction

Our current understanding of the electronic structure of pure rare gas solids (RGS) is rather complete. An extensive review of the experimental work which led to the elucidation of the dielectric and optical properties of RGS with an emphasis on the spectra in the vacuum ultraviolet (VUV) and soft X-ray region has been provided by SONNTAG (1977) in Chapter 17 of Volume II, while a review of the theoretical calculations of electronic states in pure RGS has been presented by RÖSSLER (1976) in Chapter 8 of Volume I of this book.

During the last decade these experimental and theoretical efforts have been considerably extended to investigate the mutual interdependence of the geometric, i.e. structural and the electronic properties. Furthermore, rigourous attempts have been made in order to understand the excited state relaxation phenomena in condensed rare gases. Pure RGS, solid alloys, condensed rare gases including solid two-component mixtures, pure liquids and liquid alloys provide useful information concerning the effects of the state of aggregation and disorder on the electronic structure and, in particular, to establish the influence of structural and compositional changes on the electronic properties. Structural, positional-type disorder is exhibited in liquids, in glasses and in structurally deformed solids. Compositional disorder prevails in binary mixtures. The effects of disorder on the electronic structure are characterized by some universal features (ECONOMOU et al., 1974, KRAMER 1976) which are drastically different from the electronic states of ideally ordered solids (MOTT and DAVIS, 1972). It turns out that rare gas solids, liquids and alloys can be considered as prototype materials to explore electronic structure on a much deeper level than originally anticipated. For an investigation of the static electronic properties and the influence of structural changes on the electronic states, the closed shell electron configuration and the weak dispersion forces in the ground state are of major importance. Comparative studies on rare gas alloys in gaseous, liquid and solid phase provide a wealth of information concerning electronic states of disordered insulators. In addition, metal-rare gas solid mixtures yield insight into the challenging problems of transport properties and the metal-nonmetal transition in disordered materials (MOTT1974).

One major theme of this chapter addresses these problems with an emphasis on the effects of the state of aggregation and compositional disorder on the electronic properties. The diverse information concerning the static features of electronic structure provides the basic input information for the understanding of dynamic processes in ordered and disordered condensed rare gases. In fact, the static information and the dynamic processes are complementary and cannot be disentangled, as the understanding of the electronic structure provides a prerequisite for the elucidation of dynamic relaxation phenomena.

The second major theme of the present chapter is concerned with the diverse and interesting problems of excited state dynamics in condensed rare gases considering the microscopic aspects of energy conversion, storage and disposal in these materials. The fate of electronically excited states in ordered and disordered condensed rare gases involves a variety of nonradiative channels, such as exciton selftrapping, electronic relaxation, vibrational relaxation, energy transfer via exciton states, electronic energy transfer between localized states and autoionization, just to mention a few examples. There has been remarkable progress in the experimental investigation of these various pathways of nonradiative energy dissipation in condensed rare gases. This experimental information established general trends and rules which can be used as testing ground for theoretical ideas.

Apart from the basic intrinsic interest in the electronic structure and in the general concepts and mechanisms governing radiationless transitions and dynamic processes, rare gas solids, liquids and alloys have attracted interest in other areas of science and technology. There has been important progress in matrix isolation spectroscopy (see e.g. PIMENTEL 1958, McCARTHY and ROBINSON 1959, MEYER 1971) and cryochemistry in rare gas matrices (RGM) (MOSKOWITZ and OZIN 1976). As a scientific and technological application we mention the progress in high power VUV excimer lasers based on excited rare gas molecules and rare gas halogen compounds (see e.g. RHODES 1979). To provide another example of technical relevance we recall that doped rare gas liquids play an important role in the recent development of new high energy particle detectors (see e.g. WEBER 1979). For all these developments a detailed understanding of the electronic structure and dynamic processes is required.

What are the relevant excited states and what are the important decay mechanisms in RGS? To answer this question we have sketched in Fig. 1 the energy regions for the basic excitations in molecular solids and the onset of decay channels. Phonon, vibrational and librational excitations mark the lower limit at around 0.01 eV. Investigation of the spectral range is for example one of the major domains of matrix isolation spectroscopy. For pure RGS due to their simple structure these excitations are not relevant. The elementary excitations at higher energies involve valence electronic excitations which in RGS result in Frenkel type excitations (for the $n = 1$ states) and localized impurity states, Wannier excitons and Wannier impurity states (for the $n \geq 2$ states), interband transitions and impurity ionization states. The dynamic processes involve electronic energy transfer between the exciton states in the energy range 5 - 20 eV, exciton diffusion, electronic relaxation of exciton states, exciton trapping with excimer formation, electron-hole recombination in the energy range above the band gap energy E_G, autoionization processes of core excited states and charge transfer processes involving ionic rare gas atoms in the energy range up to several thousand eVs. In order to provide an estiamte for the orders of magnitude of the energies involved we have collected in Table 1 the electron binding energies for all rare gases.

To be more specific we have sketched in Figs. 2, 3 and 4 the valence states involved and the decay processes in some detail. The optical absorption spectra of pure and lightly doped solid and liquidrare gases can be analyzed in terms of stable exciton or impurity states. A schematic scheme of the energy levels involved appears in Fig. 2 where we have depicted the case of a Xe impurity in an Ar matrix. The relative simplicity of these exciton and impurity states makes it possible to gain detailed information about the energy levels which is of prime importance for a subsequent discussion of the dynamical processes. The sources of experimental information concerning the energy levels are:

(a) Identification of Wannier exciton series in pure materials and of excitonic atomic or molecular impurity states in doped insulators by absorption spectroscopy. The Wannier series converge to the bottom of the conduction band. The lowest exciton ($n = 1$) is of the intermediate type (between Wannier and Frenkel), but can be described by a $n = 1$ Wannier state subjected to a large central cell correction.

(b) From the convergence limit of the Wannier series studied by absorption spectroscopy one can obtain the band gap, E_G, in the pure substance or the impurity ionization potential, E_G^i, of the impurity in the medium.

(c) The energetics of the Wannier states, monitored by absorption spectroscopy result in basic information regarding the characteristics of the conduction band. In particular, from the effective Rydberg constant of the Wannier series one can deduce the effective mass of the electron near the minimum of the conduction band.

(d) The threshold for photoconductivity in the pure solid or liquid results in a direct measurement of E_G.

(e) The threshold for external photoemission from the pure material E_{Th}, or from the doped insulator E_{Th}^i, results in the external ionization potentials. From the combination of optical spectra and photoemission yields in pure or in doped insulators one can determine the energy V_o of the bottom of the conduction band relative to the vacuum level.

For a cursory discussion of the dynamical processes in the excited states it is important to notice that the properties of a rare gas atom change dramatically upon electronic excitation and ionization (Fig. 3). In the ground state we have the typical weakly bonding Van der Waals potential curve (Fig. 3) with a shallow minimum and a strongly repulsive part for smaller distances. The equilibrium distancr r_o of rare gas molecules practically coincides with the nearest neighbor distance r_K in the crystal. The small depth D_o of the molecular potential curve corresponds to the weak bonding energy D_K of the atoms in the crystal (see Table 2). In the excited state a chemically active radical is formed. Thus, e.g. strongly bound rare gas molecular ions R_2^* with binding energies D_+ ranging from 1 to 2 eV can be formed. These are characterized by a considerably decreased equilibrium distance r_t compared to the ground state. Excited stable neutral states R_2^* (excimer states) also exist (MULLIKEN 1970). The additional electron on a large orbit around the R_2^* center only weakly disturbs the R^*-R bond. The excited R_2^* molecules can decay radiatively into two atoms in the ground state (Fig. 4). Since both atoms are on the strongly repulsive part of the potential curve, they fly rapidly apart.

An excited rare gas atom in the crystal will exert strong attractive forces upon the neighboring atoms. The experiments show that also in the solid molecular centers of the R_2^* type are strongly favored. In this case the nearest neighbor distance is reduced by about 30% from 4Å to about 3Å. These large structural changes upon excitation are favored by the weak bonding forces in the ground state resulting in only weak forces opposing the rearrangement and by the strong bonding in the excited state. The electronic excitation energy will be converted by a number of competing processes such as nonradiative electronic relaxation, autoionization, recapture of free electrons, formation of luminescence centers, energy transfer processes to guest atoms and boundaries and radiative decay. Some of these decay processes are schematically portrayed in Fig. 4 and will be discussed in detail in Section 6 of this review.

From the examination of Fig. 1 and Table 1 it is immediately apparent that the utilization of VUV and soft X-ray radiation is essential for a detailed study of the electronic structure and dynamics in condensed rare gases. Aside from the broad band excitation by electron or particle excitation the use of synchrotron radiation for selective excitation brought about a major experimental breakthrough in these studies. The combination of basic spectroscopic techniques, such as energy and time resolved luminescence and photoelectron spectroscopy, was of prime importance for the investigation of decay processes.

2. Experimental Aspects

Experimental techniques developed for the investigation of pure RGS have also been adopted in many cases to rare gas alloys and liquids. In general, the techniques described by SONNTAG (1977) can also be applied to these systems, but the different, more complicated nature of the samples requires several modifications in the preparation. Now a point has been reached where more attention has to be paid to the characterisation of the samples. Improvements concerning these problems are just emerging: for instance, data obtained on thin polycrystalline films are compared to those obtained on crystals, surface states and surface quenching processes are investigated, the influence of phase transitions is studied on luminescence spectra, and more experience has been gained concerning annealing effects and sample temperature. Parallel to these developments we have observed recently a tremendous improvement of the basic spectroscopic techniques, such as high resolution VUV-spectroscopy, energy and time resolved luminescence spectroscopy and the application of photoelectron spectroscopy to insulators, and in particular to RGS and RGM's.

In this section we illustrate with a few typical examples sample preparation techniques (for more references, see e.g. MEYER, 1971) and the many spectroscopic techniques (for more references see e.g. SAMSON (1967), CARDONA and LEY (1978, 1979) and LUMB (1979)).

2.1 Sample Preparation and Structure

A general review of crystal growth and crystal defects has been given by VENABLES and SMITH (1977) in Chapter 10 Vol. II of this book. The wealth of details and references is considered as a background which will not be cited here again. Also we will not repeat the discussion of problems of crystal structure related to optical investigations as discussed in Chapter 17 Vol. II of this book by SONNTAG (1977).

Liquid rare gases are prepared in cells. An example for a high pressure absorption cell is shown in Fig. 5. On a larger scale, liquid rare gases are used in ionization chambers for high energy physics. The proportional increase of the amount of charge with particle energy yields a high energy resolution

which has been applied in liquid rare gas particle detectors. The high electron mobility assures a fast response. As an example for such a device, a shower counter filled with Argon for high energy particle detection at the e+ e- storage ring PETRA in Hamburg is shown in Fig. 6. For these applications the purity of the gases is crucial. Smallest admixtures of O_2 even below the ppm level capture electrons quite effectively.

Commonly, for spectroscopic investigations, RGS's are condensed as thin films onto a cooled substrate. Rare gas alloys are usually prepared by mixing the constituents in the gas phase with appropriate partial pressures and depositing them in situ on a cryostat in the form of a thin film. In this kind of preparation, care has to be taken to work at extreme low base pressures in the gas handling system and UHV experimental vessel (in the range of 10^{-10} Torr or better). Only UHV bakeable stainless steel systems satisfy these conditions (see e.g. HARMSEN et al., 1974; SAILE, 1978). The concentration in the sample may differ from the gas phase composition due to demixing during the transfer from the storage vessel to the substrate (see for example MANN and BEHRENS, 1978) and due to different sticking coefficients for both components on the cold substrate.

The thickness of the film, typical some tenth of a nm up to some hundred μm, can be determined by monitoring the sequence of interference fringes observed for the light reflected from the sample during evaporation (BALDINI, 1965). Either laser light or, in order to get higher contrast and higher accuracy for film thicknesses in the Å region-VUV light - but still in the transparent region of the sample -, is used (HARMSEN, 1975). We mention that rare gas metal mixtures have to be prepared in a different way. Rare gas and metal vapour are deposited simultaneously from a gas nozzle and from a metal furnace on a substrate, which has to be cold enough to avoid clustering of the metal atoms. The concentration is derived by measuring both deposition rates independently. Clustering is a main difficulty for the preparation of these mixtures (see e.g. Vol. 82 of Ber. Bunsenges. Phys. Chem. 1978). COUFAL et al. (1978) demonstrated for Ar^{40}: K^{41} mixtures a new possibility by converting in an Ar^{40} sample some atoms to K^{41} by β-activation.

Vapor deposition of thin films is used because of its simplicity and because some spectroscopic techniques require thin films as samples: in absorption measurements a sufficiently high transmission of light is needed, in photoelectron emission experiments charging has to be avoided and in the study of

surface states the bulk background has to be reduced. Further, thin films are required for the investigation of those transport properties where small penetration depth are involved, such as the electron mean free path and the range of energy transfer of excitons to substrate and surface layers. In these experiments the thickness dependence of the signal gives additional information. Finally, for experiments which are sensitive to trapping sites, thin films are in some cases favorable. The structure of films and its dependence on the preparation conditions has been investigated and the epitaxial growth of single-crystalline films has been demonstrated (see e.g. Chapter 10 Vol. II of this book). Usually thin films have a polycrystalline structure. For pure polycrystalline RG-films an admixture of hcp structure has been observed in addition to the expected fcc structure (SONNENBLICK et al., 1977).

We note that in spectroscopic investigations on thin films a definite correlation with the structure of the samples is generally missing. In a few cases the influence of preparation conditions and of annealing has been discussed. SCHULZE and KOLB (1974) have studied changes of the density ϱ and refractive index n of solid films of rare gases on a metal mirror substrate as a function of the condensation conditions such as temperature, growth rate and layer thickness. For condensation temperatures above a value characteristic for each RGS these authors obtained results for ϱ and n in agreement with those given in the literature. Below this temperature an approximately linear decrease of ϱ and n with temperature was found.

For doped samples, structure investigations are available showing for example that Ar/Kr and Kr/Xe can be prepared as homogenious polycrystalline films with fcc structure up to large concentrations (CURZON and MASCAL 1969, KOVALENKO et al. 1972 and Capt. 10 Vol. II of this book). The concentration dependence of the lattice parameter in substitutional solid solutions of RGS is in good agreement with the mean potential model (PRIGOGINE, 1957). In most of the optical investigations the actual structure of the samples is not reported. This lack of information is even more severe for doped than for pure samples because here local distortions due to the guest atoms are a further point of concern. The size of the dopand determines if one or more matrix atoms in the lattice are replaced. Further it determines also the degree of rearrangement in the surrounding matrix atoms. In addition, clustering and accumulation of crystal defects at the site of a dopand may be important for the explanation of spectroscopic results. Some aspects like changes in selection

rules and splittings are dominant in spectra of metal atoms and can help to classify at least the local symmetry. Also rate constants and pathways of relaxation processes will be influenced by local phonons (LUCHNER and MICKLITZ, 1978).

The growth of large RGS single crystals by modified BRIDGEMAN methods is well known (HINGSAMMER and LÜSCHNER, 1968). The dominating stable structure of RGS crystals is the fcc lattice. For different growth conditions the coexistence of fcc and hcp phase and the stabilisation of the hcp phase by stress and impurities (O_2, N_2, CO) has been analysed (Chapt. 10 of Vol. II of this book and KOWALENKO et al. 1975). In Fig. 7 a device to grow free standing RGS polycrystals for luminescence experiments (SCHUBERTH and CREUZBURG, 1975) is shown.

A clear relation between crystal structure and spectroscopic data is evident in x-ray induced VUV luminescence (SCHUBERTH et al. 1976). A strong increase in luminescence efficiency of Ne crystals at 10.5 K is caused by a partical phase transition from fcc to hcp in polycrystalline samples. This phase transition has been indentified by Ramann scattering experiments. The optical phonons in the hcp phase will enhance the formation of the relaxed emission centers after x-ray excitation by dissipating more energy per phonon for small wave vectors than the acoustical phonons in the fcc phase (SCHUBERTH and CREUZBURG, 1975). A similar explanation for intensity changes in Ar, Kr and Xe polycrystals has been given by HEUMÜLLER (1978) and has been supported by the observation of correlated changes in birefringance.

2.2 Spectroscopic Techniques

In this section we first deal with the various sources for excitation. Here we can distinguish between broad band or energy selective excitation and pulsed or continuous excitation. High energy particles which are frequently used as excitation sources, deposit their energy via a broad spectrum of energy loss processes. The following sources have been used to study luminescence emission: (i) α-particles (e.g. JORTNER et al. (1965), BRODMANN et al. (1976)), (ii) electrons (e.g. BASOV et al.(1970), COLETTI and BONNOT (1978), HUBER et al. (1974), PACKARD et al. (1970), FUGOL et al. (1974), STOCKTON et al. (1970), SURKO et al. (1970), KETO et al. (1974)) and (iii) x-rays (e.g. SCHUBERTH et al. (1975), NANBA et al. (1974)). An example of a set-up for excitation of luminescence in liquid He by fast electrons is shown in

Fig. 8 (FITZSIMMONS, 1973). For time resolved luminescence spectroscopy electron beams can be pulsed in a convenient way (HAHN et al. (1977), KINK et al. (1977), COLETTI and HANUS (1977)). Also pulsed electric field discharge in RGS crystals has been used (SCHÖRNER, 1977). The statistical time structure of electrons and α-particles of ^{207}Bi, ^{210}Po, ^{90}Sr, ^{90}Y sources have been exploited for static and time dependent luminescence emission spectroscopy (KUBOTA et al. (1977), CARVALHO and KLEIN (1978)). In this way also electron-hole pair production rates have been analyzed in liquid rare gases (TAKAHASKI et al. (1975)).

The high intensities which are rather easily obtained are the major advantage of broad band excitation with high energy particles or x-rays compared to selective excitation with light. Therefore high resolution luminescence studies and the search for weak emission lines has been the domain of broad band excitation.

Also transient absorption spectroscopy (SUEMOTO and KANZAKI (1979), KETO et al. (1974)) requires the high currents which can be delivered from pulsed electron beams. In these experiments a sufficient high density of excited states is prepared by a high energetic ($\approx$ 500 keV) and short ($\approx 5 \times 10^{-9}$s) electron pulse. The absorption spectrum for transitions from e-beam excited states to higher lying excited states is measured using a light flash which is correlated in time to the excitation pulse (Fig. 9).

In general, energy selective excitation is more desirable compared to broad band excitation, because the initially excited state can be specified. Energy selective excitation needs light sources in the VUV. The source should be strong and also tunable to allow a free choise of the primary excited state.

Absorption, photoelectron yield (Chapter 17 Vol. II in this book) and luminescence studies have used monochromatized light from conventional discharge and flash lamps (DANILYCHEV et al., 1970, NAGASAVA and NANBA, 1974). The experiments are hampered by the weak intensity in the continuum, the superimposed lines and by problems with suitable window materials. Synchrotron radiation (see e.g. KUNZ, 1979) brought a major break through with tremendous improvements in absorption, reflection and photoelectron yield spectroscopy. It made possible a new generation of photoelectron energy distribution experiments and luminescence emission experiments from selected primary states. The following advantages of synchrotron radiation have been exploited for the investigation

of RGS: (i) the intense continuum from the visible to the x-ray region, (ii) the time structure providing short light pulses of the order of 100 ps with high repetition rates of 1 Mhz up to 500 Mhz and (iii) the low pressure in the source (10^{-9} Torr) which facilitates the operation of the experiment under UHV conditions.

The intensity of the monochromatized ($\Delta\lambda$ = 1Å) VUV light impinging onto the sample is shown in Fig. 10 (HAHN et al., 1978). The time distribution of the light at the storage ring DORIS is given in the lower panel Fig. 10. The repetition rate of the pulses depends on the mode of operation of the storage ring. Due to the detectors and electronics, the measured pulse width in actual set-ups is broadened to$\approx$0.4 ns. With dedicated storage rings and more sophisticated timing techniques a time resolution of some ps has been obtained and time resolutions in the subpicosecond regime are possible (SCHWENTNER et al., 1979, RHEN, 1980).

Several experimental set-ups at synchrotron radiation sources have been realized to exploit these properties and to provide as detailed information as possible by specifying the primary excited states and by analyzing secondary processes. For this purpose optical spectroscopy has been combined with photoelectron and/or luminescence spectroscopy.

Absorption and reflection experiments under extreme UHV condition have reached a level of sophistication which allows lineshape analysis of exciton bands with high resolution (SAILE, 1976, and SAILE et al., 1976). In addition, surface and bulk exciton states in thin films of variable thicknesses have been investigated with a setup for simultaneous reflection and transmission measurements which is attached to a high resolution ($\Delta\lambda$ = 0.03 Å) 3 m normal incidence monochromator at the storage ring DORIS (SAILE et al., 1976). Because of the high and stable light flux of this instrument it is possible e.g. to separate the weak absorption of surface states from the bulk absorption background. Recently a two-photon absorption experiment combining laser and synchrotron light flashes has been reported (SAILE et al., 1980).

Luminescence spectroscopy in RGS, exploiting synchrotron radiation, has been performed at the synchrotron DESY (BRODMANN et al., 1974), at the storage ring DORIS (BRODMANN et al., 1976, HAHN et al., 1978), at the storage ring

SPEAR (MONAHAN et al., 1976, 1978) and at the synchrotron NINA (HASNAIN et al., 1977). Photoelectron yield from RGS has been studied at the synchrotron DESY (SCHWENTNER et al., 1973) and at the synchrotron NINA (HASNAIN et al., 1977). Photoelectron energy distribution measurements from RGS and matrices have been carried out at DESY by SCHWENTNER (1974) and SCHWENTNER et al. (1974). In Fig. 11 the set up using a combination of retarding field and electrostatic lenses as an electron energy analyzer in connection with a 1.0 m vertical Wadsworth monochromator is shown. Simultaneously, the absolute sample reflectivity and the absolute photoelectric yield can be recorded with this instrument.

The experimental arrangement for simultaneous measurements of the reflection, transmission, luminescence excitation and photoemission yield spectra at the Synchrotron Radiation Facility at Daresbury Laboratory is shown in Fig. 12 (HASNAIN et al., 1977).

Photoluminescence experiments in which the primary excitation energy can be selected and where the emission spectra are dispersed by a second monochromator have been carried out at the storage ring DORIS (Fig. 3) (HAHN et al., 1978). Further this set-up allows the analysis of decay curves of the emission bands in a single photon counting mode (Fig. 13). For long lifitimes and for alignment purposes a plused electron gun (not shown in Fig. 13) has been integrated.

3. Electronic Structure of Valence and Conduction Bands and Excitonic States

Much information on the band structure of RGS has been inferred from optical data and photoemission experiments. The interest in the band structure is largely motivated by two aspects. First, RGS are prototype materials for the large class of Van der Waals crystals. In this respect comparison of experimental data with state-of-the-art ab initio band structure calculations plays a major role. Secondly, an accurate description of the band structure as well as the excitonic states within the band gap of pure RGS is basic for the discussion of impurity states, the more complex electronic structure of metal rare gas mixtures and the dynamical processes. Pertinent information about the dielectric and optical properties of pure RGS as obtained by optical absorption-, reflection- and energy loss spectroscopy as well as by photoemission has been collected and discussed by SONNTAG (1977). The theoretical concepts including band structure calculations and the theory of excitons in RGS has been summarized by RÖSSLER (1976). The main emphasis in our discussion will be on some new experimental and theoretical developments concerning the band structure (section 3.1) and the excitonic states (section 3.2). Within section 3.2 we shall also discuss the recent observations of surface excitons and our current understanding of this phenomenon. Finally, we shall focus our discussion on results for dilute and concentrated rare gas alloys (section 3.3).

3.1 Band Structure of Pure Rare Gas Solids

Over the past few years there has been a steady increase of our knowledge concerning the band structure (e.g. determination of band gaps, spin orbit splittings) mainly based on the analysis of optical spectra. Since the optical spectra are dominated by excitonic excitations little information was available about the dispersion of the bands, their widths and the absolute position of the energy levels. Thus a detailed comparison with the many available partly conflicting band structure calculations was more an indirect procedure.

Photoelectron spectroscopy (see e.g. SPICER 1969, SHIRLEY 1972, EASTMAN 1974, CARDONA and LEY 1978) has become the most powerful technique to probe for the density and dispersion of the valence bands and core levels. In measurements of the photoelectron energy distribution curves (EDC's) the sample is illuminated with monochromatic, or as monoenergetic as possible, light and those excited electrons which are emitted into vacuum are analyzed according to their energy and/or angle. In photoemission yield experiments all electrons are collected by an appropriate grid and the photocurrent is measured as a function of the energy of the exciting light.

For the following discussion, in particular the comparison of band structure calculations with experimentally determined EDC's the widely used phenomenological three step model (BERGLUND and SPICER 1964) is used. Within this model the three main steps are (i) absorption of photons and excitation above the band gap, (ii) transport of electrons from the point of excitation including possible scattering events within the sample and (iii) escape of electrons into vacuum and detection.

Rare gas solids have the advantage that the escape depth of photoelectrons is rather large for a wide range of energies below the electron exciton scattering onset (see section 7). Consequently, the EDC's are governed largely by the energy distribution at the site of excitation. The absorbed photons excite electrons from occupied states of the valence bands into empty conduction band states. Assuming vertical transitions with $\Delta k = 0$ the energy distribution N(E, hν) is given by

$$N(E, h\nu) = \text{const} \sum_{V,C} \int_{BZ} d^3\underline{k} \; |M_{VC}|^2 \; \delta(E_C(\underline{k})-E_V(\underline{k})-h\nu) \; \delta\,(E_C(\underline{k})-E) \qquad (3.1)$$

Here M_{VC} is the matrix element of the transition probability, E_V the energy of the valence band states, E_C the energy of the final states and E the energy of the excited electrons. The first δ -function guarantees energy conservation taking into account the momentum conservation.

The second δ -function reflects the choice of the energy of the electrons considered. The summation is over all valence and conduction band states and the volume of integration is the Brillouin Zone (BZ).

For a comparison with experiment the matrix elements are assumed to be constant leading to the simplified expression

$$N(E, h\nu) = \text{const} \sum_{V,C} \int_{BZ} d^3\underline{k} \; \delta\,(E_C(\underline{k}) - E_V(\underline{k}) - h\nu)\; \delta\,(E_C(\underline{k})-E) \qquad (3.2)$$

This equation neglecting the influence of electron scattering is frequently used for a discussion of the EDC's.

Due to the experimental difficulties encountered in photoemission experiments, when applied to insulators, and due to the general difficulty of working at very low temperatures only a few photoemission experiments have been performed on RGS. In most of these experiments synchrotron radiation has been used as a source of excitation. There have been a couple of photoemission yield experiments reported for pure RGS (O'BRION and TEEGARDEN 1966, SCHWENTNER et al. 1973, OPHIR et al. 1974, KOCH et al. 1974a , KOCH et al. 1974b, OPHIR et al. 1975, STEINBERGER et al. 1974, PUDEWILL et al. 1976). Photoelectron energy distribution studies were carried out at Deutsches Elektronen-Synchrotron DESY since 1974. In a series of papers SCHWENTNER and his colleagues (SCHWENTNER 1974, SCHWENTNER et al. 1974, SCHWENTNER et al. 1975, SCHWENTNER and KOCH 1976, SCHWENTNER 1976, NÜRNBERGER 1977, KOCH et al. 1978) have measured EDC's for Ne, Ar, Kr and Xe for a number of photon energies. The experimental set up used in these experiments has been discussed in section 2. (see Fig. 11). On the basis of these experiments detailed comparisons with predictions of band structure calculations for the various parameters have become possible.

In brief, it turned out that although the general features of the valence bands are predicted correctly by the calculations, almost all available band structure calculations failed to predict quantitatively features other than the spin orbit splitting (ΔE_{SO}). In order to illustrate this situation a comparison of some representative EDC's taken from SCHWENTNER's work (1974) with calculated valence bands are shown in Fig. 14. Theoretical results for the Ne 2p derived valence bands are taken from the work of RÖSSLER (1970) using the KKR-method, KUNZ and MICKISH(1973) and DAGENS and PERROT (1972). For the 3p-derived valence bands of solid Ar results from LIPARI and FOWLER (1970), LIPARI (1972), KNOX and BASSANI (1961) and MATTHEIS(1964) are displayed. In the heavier RGS the width of the valence bands (W_{VB}) increases considerably. For Kr calculated valence bands according to RÖSSLER (1970), KUNZ and MICKISH (1973), FOWLER (1963) and LIPARI (1970) are shown together with the experimentally determined EDC. Finally, for the Xe 5p derived bands comparison is made with the calculated valence bands according to RÖSSLER (1970) and REILLY (1967). In the uppermost panel for Xe a quantitative estimate based on the experimentally observed valence features (SCHWENTNER 1974) is included. Some of the relevant parameters characterizing the band structure have been compiled in Table 3. Results for slightly doped RGS which we shall discuss below are also given.

Inspection of Fig. 14 shows that the general features of the valence bands common for all rare gas solids are (i) a spin orbit splitting of the np 3/2 and np 1/2 states in the center of the Brillouin Zone, (ii) a $\underline{k}$ dependent dispersion to lower energies in going from Γ to the border of the Brillouin Zone, and (iii) a splitting of the np 3/2 bands, which are degenerate at Γ, into two subbands. A graphical summary of the parameters deduced from experimental data, as displayed in Fig. 14, appears in Fig. 15, plotted versus the energy gaps E_G. It is interesting to note that there is a nice correlation and linear dependence of all parameters on this scale. A more extensive and quantitative comparison with the predictions for the total width and the structure of the valence bands has been given by SCHWENTNER (1974), SCHWENTNER et a. (1975) and KUNZ et al. (1975). These comparisons have been significant in that they support the idea that the valence states of the RGS are band like with

a k-dependence of the bands stronger than predicted by most calculations (see also the discussion in section 3.3).

At the end of this section it is appropriate to discuss some limits of the band model. On first sight the fact that most of the band structure calculations are only moderately successful in a quantitative description is surprising, in particular in view of the success of band structure calculations in interpreting EDC's from metals and semiconductors (see e.g. GROBMAN 1975, CARDONA and LEY 1978). We note that the above comparison involves experimental excited state eigenvalues versus calculated ground state single-particle energies; such comparisons always involve questions concerning relaxation effects which accompany electronic excitations. Thus an atomic like approach with narrow np - bands subjected to the local symmetry of the valence hole might be more appropriate. Although this question has not yet been answered in a decisive way we draw attention to several observations and considerations which are relevant for the discussion.

(i) NÜRNBERGER et al. 1977 have studied the gradual band formation for Xe-Ar alloys for concentrations ranging from 0 to 100 % by photoemission spectroscopy. These authors have been able to describe their results by concentration dependent tigh-binding band structure. Rather high concentrations of Xe or Ar have been necessary in order to reach the fully developed Xe or Ar bands respectively. We shall discuss these experiments which support a band structure model in more detail in section 3.3.

(ii) Evidence for a gradual transition from an atomic to a solid state situation emerges from recent photoemission experiments on Xe-, Kr- and Ar-clusters in the gaseous phase by DEHMER and DEHMER 1978 a,b. In these experiments a He I line source together with a hemispherical photoelectron analyzer gave a resolution of 20 meV. Dimers and heavier clusters were produced by a supersonic molecular beam source. The results for a

nozzle stagnation pressure of 6.76 atm. appear in Fig. 16 together with the EDC's of atomic Xe (TURNER et al. 1970) and Xe in Ne matrix respectively (SCHWENTNER et al. 1975). Although the exact mass distribution of the clusters is unknown the supersonic beam experiments showed qualitatively how the photoelectron spectrum changes as the average cluster size is increased. In addition to the atomic $^2P_{1/2}$ and $^2P_{3/2}$ bands observed at low pressures and in the matrix spectra several peaks due to the dimers (marked by D in Fig.16) are clearly visible and very broad emission features are observed even at lower ionization potentials. These broader features have been assigned to heavier clusters; they increase with pressure relative to the dimer peaks. More detailed studies of this kind promise to provide a wealth of information on the energy level structure of cluster species.

(iii) Further we mention recent photoemission experiments of Xe overlayers on metal surfaces giving evidence for ligand field splitting and strong dispersion effects. Surface crystal field effects have been obtained by WACLAWSKI and HERBST (1975) in photoemission experiments for Xe physisorbed on a W(100) surface. The EDC for $h\nu = 21.2$ eV revealed two 5p levels. The spin orbit splitting of the two levels and their intensity ratio was close to the gas phase. A significant broadening of the 5p 3/2 peak with respect to the 5p 1/2 was observed. It has been interpreted as an unresolved doublet resulting from a splitting of the Xe 5p 3/2 states in the tungsten-surface crystal field (HERBST 1977, MATTHEW and DEVEY 1976) as well as ANTONIEWICZ (1977) have pointed out, however, that this model requires an unreasonable large positive charge on the metal surface atoms.

(iv) Angular resolved photoemission spectroscopy is capable to provide more insight into the nature of the splitting and the dispersion of bands (see e.g. SMITH 1978). Such experiments still need to be done for bulk RGS. Angular resolved photoemission from physisorbed Xe on Pd (100) surface by SCHEFFLER et al. (1978) showed an additional broadening of the $5p_{3/2}$ peak with increasing coverage. SCHEFFLER et al. (1978) concluded

that the splitting can only be due to the ligand field of the two dimensional Xe-lattice. Furthermore, they were able to observe the strong dispersion of both the $5p_{1/2}$ and the split $5p_{3/2}$ level. In view of the density of states discussed above (Fig. 14) we expect that this dispersion can also be observed for bulk rare gas single crystals in angle resolved experiments.

3.2 Excitons in Pure Rare Gas Solids

The optical spectra of pure and slightly doped RGS, in particular the rich exciton structure at the onset of interband transitions (see Figs. 17-20), have attracted much interest from both theoreticians and experimentalists. Since the dielectric screening in these large band gap insulators is weak one can expect to study the limits of the single particle model. The dominance of exciton states in the optical spectra already signals the importance of electron-hole correlation effects. Concerning the experimental development we may distinguish several stages: (i) The first systematic experiments in the VUV by SCHNEPP and DRESSLER (1960) and the following detailed investigations by BALDINI (1962), BALDINI and KNOX (1963) and BALDINI (1965) and others have led to a fairly detailed description of the excitons in Xe, Kr and Ar. (ii) With the possibilities offered by synchrotron radiation the restrictions concerning the light source became weaker and more detailed results including Ne became available for the valence band excitations (see e.G. HAENSEL et al. 1969c, HAENSEL et al. 1970c,1970d, BOURSEY et al. 1970, SCHARBER and WEBBER 1971, STEINBERGER and ASAF 1973, PUDEWILL et al. 1976a, 1976 b). Of particular importance during this stage of development was also the elucidation of core level excitons (see Fig. 21) for all four RGS (HAENSEL et al. 1969a, 1969b, 1970a, 1970b, 1971, 1973). The spectra available up to early 1977 have been critically reviewed and summarized by SONNTAG (1977). (iii) Presently we observe a third stage in the experimental development associated with the use of high resolution spectroscopy in the VUV by exploiting the possibilities of a storage ring as an extremely stable and intense radiation source (SAILE 1976, SAILE et al. 1976b, SAILE et al. 1977a and SAILE and KOCH 1978a, 1980). One of the main surprises of these experiments was the unambiguous identification of surface excitons in RGS which triggered a number of theoretical speculations about the nature of these states.

Concomitant with these developments remarkable theoretical progress has been made in order to provide an adequate description of exciton states in RGS.

3.2.1 Some Remarks on Recent Calculations

The theory of excitons dates back to the thirties when in the fundamental papers by FRENKEL (1931a, 1931b, 1936), PEIERLS (1932) and WANNIER (1937) the basic concepts have been formulated. Today excitons play a major role in the description of excited electronic states of almost every type of solids and excellent treatments of the general theory of excitons are available (see e.g. DAVYDOV 1962; KNOX 1963; RICE and JORTNER ; PHILPOTT and CHO).

For RGS the excitation energies E_n of the exciton bands have been mainly described in terms of a hydrogenic Wannier-Mott exciton model based on the effective mass approximation and expressed in the well known form

$$E_n = E_G - \frac{B}{n^2} \tag{3.3}$$

with the E_G gap energy, B binding energy of the first exciton and n principle quantum number. B is given by

$$B = \frac{\mu}{\varepsilon_0^2} \cdot \frac{e^4}{2\hbar^2} \tag{3.4}$$

where ε_0 is the static dielectric constant and μ the reduced effective mass of the exciton

$$\frac{1}{\mu} = \frac{1}{m_e} + \frac{1}{m_h} \tag{3.5}$$

with m_e and m_h as effective mass of the electron and hole respectively. This simple model has been applied successfully for describing the $n \geq 2$ states in pure RGS and for the description of excitations from deep impurity levels in RGS. Equation (3.3) is also frequently used to

obtain the energy gap E_G and the binding energy B of the first exciton and hence the effective mass μ.

For the first exciton one observes a defect Δ, defined as the difference between the experimental and the effective mass approximation (EMA) values:

$$\Delta = E^{n=1}_{expt} - E^{n=1}_{EMA} \tag{3.6}$$

This defect Δ reaches values of up to 1 eV. Considerable effort has been exerted to solve the problem for these so called intermediate excitons, where neither the Wannier model, nor the Frenkel picture (appropriate for tightly bound excitons) have given satisfactory results.

The basic reason for the failure of the Wannier model is the spatial localization of the electron and hole for the n=1 state. This is evident from Table 4 where we compare the radii ($r_{Bohr} = 0.529$ Å) calculated from

$$r_n = n^2 \cdot \frac{\varepsilon_0}{\mu} \cdot r_{Bohr} \tag{3.7}$$

with the nearest neighbour distances r_K in RGS's. Since in all cases $r_K > r_{n=1}$ the description using a screening of the Coulomb forces between electron and hole by a static dielectric constant becomes problematic. Different theoretical approaches have been persued in order to shed some light on this problem:

(i) Based on a band structure model and assuming a localization of the electron and hole in the same unit cell ANDREONI et al. (1975, 1976) applied an integral equation method to calculate the energy positions, oscillator strengths and the longitudinal (LO) - transverse (TO) splittings of the first excitons in solid Ar (ANDREONI et al. 1975) and Ne (ANDREONI et al. 1976). The main drawback of this theory is its limitation to states with electron and hole confined to the same unit cell. An extension to states with $n > 1$ seems to be complicated within an ab initio calculation.

(ii) Starting from the corresponding atomic transitions $2p^6 \rightarrow 2p^5ns$, ns' in Ne BOURSEY et al. (1977) calculated the n=1 excitons in solid Ne on the basis of the potential curves of the molecular excited states. This theory works very well for the n=1 states but is inadequate for the higher transitions.

(iii) RESCA et al.(1978b)described the energy positions of the n=1 excitons for all four rare gas solids within the framework of an integral equation approach (ANDREONI et al. 1975, 1976). In this theory the excitation energy is fixed between the atomic value and the EMA result by a parameter ρ/ρ_{cc} with an effective exciton radius ρ and central cell radius ρ_{cc}. Exploiting the close connection between rare gas atoms and solids, RESCA et al. (1978a, 1978c) extended the concept of a quantum defect to the excitonic series. As in atomic theory the space is divided into a sphere around the nucleus and the space outside. By parametrizing the potential inside the atom with the help of the known atomic excitation energies and introducing for the solid the screening of the Coulomb interaction outside the atom RESCA et al. (1978a, 1978c); RESTA (1978) obtained agreement with the experimental values for the whole excitonic series for all rare gas solids. In this concept the unknown effective masses of the excitons serve as parameters. This description provides the transition from a Frenkel to a Wannier-Mott picture. On the other hand this approach is semiempirical in that it uses the well known atomic energies and treats the effective masses as parameters. It yields energy levels but no oscillator strengths or longitudinal-transverse splittings.

With the recent observation of surface exciton states in Ar, Kr and Xe and new structures in some of the bulk exciton bands a new challenge has been put forward to further investigate these states theoretically. Several models have been developed to interpret surface excitons in rare gas solids:

(i) The energy shifts and splittings in environments with different symmetry have been treated by WOLFF (1977) starting from the corresponding atomic excitations. The calculated splittings for localized excitations at the surface of Ar and Kr compare favourably with the experimental results (SAILE and WOLFF 1977b).

(ii) In the same spirit CHANDRASEKHARAN and BOURSEY (1978) extended their picture described above to excitations in the (100)- and (111)-surface planes and obtained good agreement for the excitation energies of surface excitons in all rare gas solids.

(iii) UEBA and ICHIMURA (1976) established conditions for the energies of surface excitons relative to the bulk states by a localized perturbation method. In this approach the excitation energies as well as the Davydov splitting are determined by two quantities - the environment shift term and the exciton transfer term. In an application to Ar, Kr and Xe UEBA (1977) related the observed splittings of the surface excitons to the spin orbit splitting of the valence bands.

3.2.2 Volume and Surface Excitons - Recent Experimental Results

As far as the accurate determination of optical constants are concerned only a few papers such as the communication by HASNAIN et al. (1978) on Kr have appeared which are not covered by the review of SONNTAG (1977). In this section we want to summarize the recent new experimental results for volume and surface excitons obtained by SAILE et al. (1976, 1978a,b) and their connection to the recent theoretical developments as summarized in the previous section.

Transmission and reflection spectra of solid neon in the valence-exciton range ($16 \leq h\nu \leq 22$ eV) have been carefully reinvestigated by SAILE and KOCH (1978). An overview of the absorption spectrum for thin films of solid Ne appears in Fig. 18. The results of a coverage experiment are shown for the range of the n=1 excitons in the insert. Using highly monochromatized ($\Delta E \approx 4$ meV) synchrotron radiation with a resolution about 30 times better than the half width of the sharpest spectral features, these experiments

revealed a number of new features. Consequently information from the exciton line shapes could be extracted and more precise energy values than previously possible could also be obtained. The results of this study may be summarized as follows (see also Tables 5 and 6):

(a) for mono- or submonolayers of Ne evidence for an adsorbate induced resonance was found. The excitation energy of 16,91 eV of this resonance, which disappears for thicker samples, is close to the value for the $2p^6 \rightarrow 2p^5 3s$, j = 1/2 state in the gas phase at 16.85 eV.

(b) As for Ar, Kr and Xe surface excitons were observed. The behaviour of the surface exciton state at 17.15 eV was found to be different from that of the resonance mentioned above in that it can be observed for a full sequence of film thicknesses. Evidence that this exciton state is confined to the Ne-surface is based on the following observations: (i) The surface exciton is only observed under ultrahigh-vacuum conditions. (ii) Upon coating with a different rare gas film the surface exciton disappears (see the insert in Fig. 18) and (iii) from the thickness dependence of the surface exciton peak, where the contribution of the surface exciton remains almost constant whereas the bulk peaks increase with increasing film thickness, it was estimated that the absorption due to the surface exciton is confined to about one layer at the vacuum-sample boundary.

For the surface states a full width at half maximum (FWHM) of about 80 meV to 300 meV was found depending on sample preparation and background substraction for deconvolution. These halfwidths exceed considerably those for surface states in other RGS where 20 to 30 meV have been observed (SAILE et al. 1976b). Different reasons can be responsible for such broadening: either the surface exciton is broadened by the same mechanism which causes a broadening of the bulk n=1 excitons in solid Ne (see below) or this surface peak consists of several overlapping excitations. This latter explanation was found to be valid. It has been shown both experimentally (SAILE et al. 1976b) and theoretically (SAILE and WOLFF 1977b; CHANDRASEKHARAN and BOURSEY 1978) that three transitions to surface states correspond to the

two n=1 bulk excitons in RGS. Due to the small spin-orbit interaction in Ne we expect from an extrapolation of the splittings of surface excitons in Ar and Kr to the case of Ne three states below the n=1 (3/2) bulk exciton confined to an energy interval of less than 200 meV. In the molecular type calculation by CHANDRASEKHARAN and BOURSEY (1978) surface excitons are introduced by the different surface symmetry C_{4v} or C_{3v} compared to the bulk O_h symmetry. These ab initio calculations yield three states at about 17.30 eV with a splitting of about 150 meV between the first and third peak. Taking into account a natural halfwidth of 80 meV for the surface excitons (1/3 of the bulk widths as for the lighter rare gas solids) this result is consistent with the experimental observation of one rather broad structure at 17.1 eV.

(c) Extensive information has been obtained for the bulk exciton states in Ne. For the first time the spin orbit splitting of the j=3/2 and j=1/2 states was resolved and thus the main features of the spectrum can be grouped into two series split by spin orbit interaction which converge to the band gap. The precise values obtained, as well as derived quantities appear in Table 5. The value of 90 meV for the spin orbit splitting of the valence band maxima at the Γ-point in the Brillouin zone is close to the gas phase result. Further, using the quantum defect formalism where in e.q.(3.3) a quantum defect δ is introduced by replacing n^2 by $(n+\delta)^2$ (RESCA et al. 1978a,b,c) a new value for the band gap of 21.58 eV for solid Ne has been determined.

In Table 5 the experimental results are compared with recent theoretical predictions. Generally there is good agreement between theory and experiment. Since the higher numbers of the series are rather well described in a hydrogenic like picture the good agreement for $n \geq 2$ is not surprising once the proper value for E_G has been obtained. This holds also for a quantum defect theory as long as the quantum defect is small. The tightly bound lowest n=1 levels are more difficult to describe and pose more serious problems.

A complete theoretical analysis of the exciton states of solid neon has been presented by ANDREONI et al. (1976) (Table 5). For the n=1 exciton the main approximation was to assume that the electron and the hole are confined to the same unit cell (one site approximation). This seems justified in view of the small Bohr radii of the n=1 excitons (Table 4). While these theoretical results for the n=1 binding energies are in fair agreement with experiment, the calculated intensity ratio I (n=1, 3/2) / I (n=1, 1/2) = 1:50 is considerably smaller than the experimental one (between 1:5 and 1:10). Using the experimental data for an estimate of the exchange interaction one arrives at smaller values for this quantity than predicted (SAILE and KOCH 1979). For the states $n \geq 2$ ANDREONI et al. (1976) give also values for the excitation energies and intensity ratios on the basis of the atomic data and the effective mass approximation with a given B and corrections for electron-hole exchange and spin-orbit splitting. As for the n=1 excitons one observes experimentally also in this case quite different intensity ratios. Obviously the exchange interaction is considerably overestimated in this theory, an observation which is also supported by the analysis of the solid Ar data (SAILE 1976).

(d) Finally for the n=1 excitons of solid Ne the excitation of longitudinal modes has been observed by SAILE and KOCH (1978) in both transmission and reflection experiments (shoulder denoted by L (1/2) in Fig. 18). This assignment is supported by the results of electron energy loss experiments (see SONNTAG 1977) and by the observation of the broad "quasi"-stop band between 17.5 eV and 18.0 eV in the reflectance from thick Ne-films (PUDEWILL et al. 1976a) which yields $h\nu_{TO} \approx 17.5$ eV and $h\nu_{LO} \approx 17.8$ eV. The numerical value of 0.25 eV which was deduced for the LO-TO splitting by SAILE and KOCH (1978) for solid Ne is in very good agreement with the values calculated by ANDREONI et al. (1976) of 0.232 eV and by CHANDRASEKHARAN and BOURSEY (1978) who calculated 0.252 eV.

Now we turn to the discussion of volume and surface excitons in the heavier RGS. The excitonic range of the absorption spectra (see Fig. 17) with onsets above 8 eV (Xe), 10 eV (Kr) and 11.5 eV (Ar) are characterized by sharp intense exciton bands which, when studied with sufficient resolution (SAILE 1976 and SAILE et al. 1976, 1977, 1978a,b), reveal considerable structure and a wealth of new information. For thin films of Ar, Kr and Xe, spectra covering the first exciton states are displayed in Fig. 19. Energy positions for all structures including the results for Ne discussed above are compiled in Table 6. Derived parameters such as the band gaps, spin orbit splittings and binding energies have been included in Table 3. The additional sharp peaks and shoulders 200 - 500 meV below the bulk exciton peaks with halfwidths of the order of 30 meV have been interpreted as surface excitons by experiments with overlayers and by their thickness dependence in transmission (SAILE 1976, SAILE et al. 1976a,b, SAILE et al. 1977a). In the upper part of Fig. 19 the results for thin films of Ar are presented. For the clean sample the absorption spectrum shows at energies roughly 100 - 600 meV below the n=1 volume excitons three additional features and $\sim$ 500 meV below the n=2 exciton two additional peaks which disappear upon coverage of the Ar film with a Kr-overlayer.

For Kr the results shown in the middle part of Fig. 19 are analogous: With an Ar overlayer the additional maxima below the n=1 and n=1' bulk excitons disappear. Removal of the overlayer by gently heating the sample makes the surface excitons reappear again. The difference spectrum of the absorption for a clean sample minus the absorption of the same Kr-film with an Ar overlayer (also shown in Fig. 19) demonstrates that roughly the same amount by oscillator strength associated with the surface excitons is gained by the volume excitons upon coverage. It is also interesting to point out that the transmission in the surface excitons remains constant with thickness as has been shown by careful studies of the thickness dependence of the optical absorption of Ar and Kr (SAILE 1976).

Finally in the lower part of Fig. 19 the results for solid Xe in the excitonic part are displayed. For this sample with a film thickness of $\gtrsim$38 Å the n=3 volume exciton is missing since its diameter $d_{n=3}$ = 57 Å exceeds already the sample thickness. The position of this exciton found for thicker samples is, however, marked in the figure. The most important point is the double structure of the n=1 exciton which is displayed for a film with d= 27 Å in the insert on an expanded scale. On the low energy tale of the known n=1 volume excitons a sharp (FWHM 20 - 50 meV) maximum is found at 8.2 eV which again has been identified as a surface exciton.

SAILE et al. (1977) have performed a line shape analysis for the n=1 bulk and surface exciton for solid Xe. Their studies have shown that reasonable fits can only be obtained with Lorentzians. For the Xe spectrum displayed in Fig. 19 (lower part) they found halfwidths of 20 meV for the surface exciton and 80 meV for the bulk part. The result of this fit is shown in the insert. According to TOYOZAWA's model (1974) (see section 6) this result indicates that we are dealing with the case of weak exciton - phonon scattering. The derived scattering times are in the order of several 10^{-14} sec. It is interesting to contrast this result for Xe with the estimate of 200 meV for the halfwidths in solid Ne (SAILE and KOCH 1978). The latter value is indicative for the strong scattering case and localized exciton states. The localized nature of the n=1 excitons in solid Ne is also in accord with the current view of exciton dynamics as obtained from luminescence experiments.

We have already mentioned at several points the occurance of longitudinal excitons in RGS. Bulk excitons in cubic crystals are split by the long range dipole-dipole interaction into longitudinal (LO)(with $\underline{E}$ parallel to $\underline{k}$, where $\underline{E}$ is electric field vector and $\underline{k}$ the momentum of the exciton) and transvers (TO) ($\underline{E}$ perpendicular to $\underline{k}$) excitons. Observation of longitudinal bulk excitons is usually restricted to electron energy loss spectroscopy where they show up as maxima in $\mathrm{Im}\frac{1}{\epsilon}$ (see e.g. RAETHER 1965, 1974, 1980). In optical ($\underline{k}_0$0) normal incidence transmission

experiments the longitudinal excitons normally do not couple to the incident transverse electromagnetic field. However, in reflection geometry and for rough surfaces (e.g. FILINSKI 1972 and HALKANSKI 1972) optical excitation of longitudinal modes becomes possible. The summary of LO-TO splittings in Table 7 has been obtained from the widths of the quasimetallic reflection bands in reflectance spectra from thick films and from the analysis of optical transmission data from thin rare gas films. From these two sources a consistent set of LO-TO splitting emerges. In the case of Ne the TO-LO splitting has been theoretically calculated (Table 7). The result is in favourable agreement with the experiment. In principe one could obtain the splitting also from the difference in the peak positions in ϵ_2-spectra (optical data) compared to peak positions in electron energy loss spectra. Inspection of table IV, V, VI and VII in SONNTAGS review (1977), where the available experimental data have been compiled, shows that the scatter in the experimental data is still too large for that purpose.

This general agreement and obvious explanation for part of the extra structures in the bulk exciton bands observed under certain experimental conditions is quite satisfactory in view of the long debates about these additional bands. To further substantiate this point SAILE et al. 1980 have studied the transmission of thin Kr films under non-normal incidence (Fig. 20). In the upper part the spectrum for normal incidence shows the n=1 and n=1' TO-bulk excitons as well as the surface excitons denoted by S. For the n=1 exciton there is some additional feature barely discernible at around 10.3 eV. Upon tilting the sample by 73° degree this feature gains intensity and develops into a separate peak and a new maximum associated with the n=1' peak appears. These two maxima are assigned to the LO-bulk excitons. For restrahlenbands in the intrared it has been shown by BERREMAN (1967) that this effect can be derived from a dielectric theory by solving Maxwell's equations with appropriate boundary conditions for slight surface roughness.

It is worthwhile to point out here that this effect is independent of other types of anomalies that may arise from differences between dielectric properties in the bulk of the material and those near the surface.

Such differences have been proposed by ANDREONI et al. (1978) in order to explain the dip in the reflection stop band between $\hbar\omega_{TO}$ and $\hbar\omega_{LO}$ in terms of spatial dispersion and a dead layer for bulk excitons at the surface.

3.2.3 Core Excited Excitons

SONNTAG (1977) has reviewed the experimental evidence for core excited excitons for pure RGS in detail and since no new experimental material has appeared since that time, we refer to his chapter and give only a few comments here.

An interpretation of the fine structure of the onset of transitions from inner shells (Fig. 21) is possible in terms of the joint density of states where the valence band density of states has to be replaced by dispersionless core states. This approach has been described by RÖSSLER (1976). Thus the optical function is merely a superposition of the conduction band density of states with the spin-orbit splitting and degeneracy of the core levels taken into account (e.g. RÖSSLER 1971, KUNZ and MICKISH 1973). In principle a deconvolution of the optical absorption spectra into the weighted contribution from spin orbit split core levels should yield the density of conduction band states. It turned out, however, that this simple one electron approach applied to the available data does not give meaningful results (SAILE et al. 1977).

We mention a few other theoretical calculations which recently took up the problem. ALTARELLI et al. (1975) calculated the core excitons at the onset of the 2p soft x-ray threshold for solid Ar. The binding energies and relative transition amplitudes for the lowest allowed exciton states were computed by formulating the problem in terms of Wannier functions of the conduction bands and solving the resulting integral equation in the one site approximation already applied successfully to the fundamental exciton spectrum of Ar (ANDREONI et al. 1975). The results obtained allow to locate the onset of interband transitions at an energy a few eV above previous theoretical determinations.

Therefore, the sharp fine structure at the onset of absorption previously interpreted in terms of conduction band density of states was attributed to discrete excitonic transitions. This interpretation had already been strongly suggested by the close analogy of the optical absorption with the atomic absorption in this range (HAENSEL et al. 1969). Using the same approach GROSSO et al. (1978) reexamined the core exciton spectra from 3d levels of Kr and 4d levels of Xe, both in the isolated atoms and in the crystal and found support of the earlier interpretation of these resoncances as due to 1s, 2p and 3p-like excitons.

Finally, we mention the work by RESCA et al. (1978) extending the theory for valence excitons (RESCA 1978a,c) to the calculation of core excitons at the onset of Kr 3d transitions, and Xe 4d transitions, and for solid Ne and Ar at the 2s and 2p, 3s onset respectively. The paper by BARONI et al. (1979) deales with the Ar 3p core excitons within the envelope function formalism.

3.3 Rare Gas Alloys

In this section we deal with impurity excited states in the low concentration limit. We discuss also the few experimental results available for concentrated rare gas alloys. In the discussion, we confine ourselves to rare gas guest atoms. Thus we are concerned with deep impurity states whose binding energies are comparable to the band gap of the host crystal. Most of the information about the energy levels has been obtained by absorption spectroscopy, but we shall use also information obtained from photoemission and luminescence experiments. We shall find this information instrumental to the following discussion of the electron affinity (V_0) scale as well as for an understanding of the dynamical processes discussed in later sections of this review.

3.3.1 Deep dilute impurities in rare gas solids

For dilute rare gas alloys the pertinent experimental data have been summarized and discussed in detail by JORTNER (1974). Here we shall only discuss a few specific examples and point out the salient features. Rare gas guest atoms in a rare gas matrix are the best known examples of deep impurity states in insulators. For a schematic description of the energy levels we refer to Fig. 2. These systems were first studied in absorption experiments by BALDINI and KNOX (1963) (Xe in Ar) and by BALDINI (1965) (Ar, Kr and Xe in Ne; Kr and Xe in Ar; and Xe in Kr). From the more extensive later investigations we mention the work by GEDANKEN et al. (1973) (Xe in Ne, Ar and Kr and C_6H_6, C_2H_4 and CH_3I in Ne, Ar, Kr and Xe) and by PUDEWILL et al. (1976) using synchrotron radiation (Ar, Kr and Xe in Ne).

One of the most informative results for the systems Xe, Kr and Ar in a Ne matrix is illustrated in Fig. 22 (PUDEWILL et al. 1976). Long impurity Wannier series containing up to five lines are observed. In each case two series can be assigned, split by spin orbit interaction and converging to the bottom of the conduction band of the host matrix. For $n = 2$ the energies of the series members are almost perfectly described by a Wannier formula (eq. 3) where now E_n, E_G and B are replaced by the corresponding values for the impurity:

$$E_n^i = E_G^i - \frac{B^i}{n^2} \qquad (3.8)$$

The excellent fit of the excitation energies to this formula is demonstrated graphically in Fig.23 where E_n^i is plotted versus $1/n^2$. Thus, from the convergence of these series the gap energies E_G^i of the impurity states as well as the spin orbit splitting of the guest atoms in the Ne matrix can be derived

with an accuracy of 0.2 eV. A summary of the resulting energy schemes together with the assignments is presented in Table 8. This table includes also results for the heavier rare gas matrices Ar, Kr and Xe and recent values deduced from luminescence excitation spectra (HAHN and SCHWENTNER, 1980).

We note in passing that in the system Xe in Ne the observation of two series including also higher members enabled PUDEWILL et al. (1976) to give a more satisfactory assignment for the impurity exciton series, with the $n = 1$ (3/2) exciton at 9.06 eV and the $n = 1$ (1/2) exciton at 10.05 eV and the $n = 2$ excitons at 11.32 eV (3/2) and 12.59 eV (1/2) respectively, thus avoiding some problems with the earlier interpretations by BALDINI (1965) and RAZ et al. (1971).

PANTOS et al. (1977) and HAHN et al. (1980) have assigned further structures in these spectra to nd-final states. However, some of the spectral features (see Table 8) remain unexplained.

As shown in Fig. 23 the term values $T_n^i = E_G^i - E_n^i$ coincide with those for pure Ne. Deviations are observed only for the $n = 1$ excitations where the electron and hole are fairly localized. It follows that the binding energies B^i determined from excitons $n \geq 2$ excited at the guest atoms reflect the properties of pure Ne and are independent of the individual impurity. This observation very strongly supports the interpretation of the impurity excited states for $n \geq 2$ in terms of a Wannier model. In Table 3 we reproduce the values for E_G and E_G^i and the binding energy B, respectively, the spin orbit splitting of the impurity levels ΔE_{SO}^i and the central cell correction for the $n = 1$ states.

Within the effective mass approximation the binding energy B (eq. 3.3 - 3.5) depends only on the dielectric constant ϵ and the effective mass m^*. For excitons with radii larger than the nearest neighbor distance ($n \geq 2$) and at the low concentrations employed ϵ of pure Ne may be used for the calculation of B^i. In this case electrons excited at the guest atom move in the conduction bands of the host, leading to a common value of m_e, whereas the hole will be bound to the guest atom ($m_h \approx \infty$). PUDEWILL et al. (1976) obtained an upper limit of $B^i = 5.8$ eV taking typical values for m_e from band structure calculations (KUNZ and MICKISH, 1973) and a B value of $B = 5.24$ eV for pure Ne from their experiment with $1/m_h = 0$. In order to determine B^i from the experiment one can use $n = 2$, $n = 3$ and $n = 4$ of the Γ (3/2) exciton series of Ar in Ne and Kr in Ne. One obtains $B^{Ar} = 5.27$ eV and $B^{Kr} = 5.32$ eV (Table 3). The experimental accuracy

for the energy positions is approximately 0.05 eV at 20 eV and results in an uncertainty of 0.5 eV for the B^i values. Thus, the predictions of the Wannier model for the binding energies of $n \geq 2$ excitons of these deep impurity states in solid Ne are in good agreement with the experiment.

Turning now to the energy of the $n = 1$ excitons we observe that the overlap of the lowest excited states with the medium is not sufficiently large to make the approximations valid which are used in the Wannier scheme. The central cell correction Δ determined from the experiments appear in Table 3. The calculated relationship between Δ and B shows a monotonic increase of Δ with binding energy (HERMANSON and PHILLIPS, 1966). In fact, GEDANKEN et al. (1972, 1973) were able to describe their experimental results by a linear relationship $\Delta = \alpha + \beta B^i$ where the constants α and β are determined by the impurity. It is interesting to note that this linear relationship apparently holds only for a range of small B values up to roughly B = 2.5 eV. The Δ value for Xe in Ne (see Table 3) is considerably too low to fit into the linear dependence. Finally, we note that similar as for the pure materials the quantum defect theory has also been applied for the impurity exciton states yielding a nice fit to the experimental data (RESCA and RESTA, 1979).

Next we have to consider the linewidth of the intermediate and Wannier type atomic impurity excitations. Compared to the linewidth of the free gas atom these apparent absorption bands are considerably broadened (see Table 8). To illustrate one broadening mechanism we reproduce in Fig. 24 the change of the lineshape with concentration in a "modified absorption" experiment for the $n = 1$ (3/2) and (1/2) states of a Xe impurity in Ne (PUDEWILL et al., 1976). With higher concentration of the guest atoms the line profile becomes broader, and a splitting of the band into two distinct subbands is observed for the (3/2) $n = 1$ band for Xe in Ne at a concentration of 1% (Fig. 24). This observation strongly suggests that for most of the impurity spectra broadening of the absorption bands due to formation of clusters of the impurity atoms starts already at fairly low impurity concentration around 1%.

As the work by NANBA et al (1974) on Xe in Ar matrices has shown, the study of the intensity variation of different bands with concentration in the low concentration regime is helpful for distinguishing between monomer and dimer absorption bands. For Xe in Ar BALDINI had observed a small shoulder on the low energy side of the $n = 1$ Xe impurity absorption band (see also the low concentration curve in Fig. 25) which is similar to the extra band appearing

in the Xe/Ne mixture discussed above (PUDEWILL et al. 1976). The origin of this band was not clear until NANBA et al. (1974) investigated in detail the intensity variation of this band at about 9.03 eV. It has a quadratic dependence on the Xe concentration over the range 0 - 2% molar fraction of Xe, if one assumes that the $n = 1$ Xe impurity state has a linear intensity variation. Thus, it was concluded that the band at 9.03 eV is due to Xe dimers in the Ar matrix. We shall return to these experiments in the next section.

For a discussion of the lineshapes the following line broadening mechanism, discussed in more detail in Section 6, should be considered:

(1) Inhomogeneous broadening due to distribution of different trapping sites. This broadening effect results in a Gaussian line shape. It appears that in well annealed samples of the molecular solids considered here this effect is small.

(2) Electron-phonon interaction which originates from the displacements of the medium normal modes and from changes in the vibrational frequencies between the ground and the excited state. This problem can be handled by multiphonon theory. For weak electron-phonon coupling a zero phonon line will be exhibited, followed by multiphonon transition on the high energy side, while for strong electron-phonon interaction a Gaussian line shape will result. Experimentally, the zero phonon line has never been observed for rare gas impurities in rare gas matrices. For a molecular impurity, for example, N_2 in Ne, GÜRTLER and KOCH (1980) were able to resolve a detailed fine structure in most of the N_2 absorption bands which they could assign to a zero phonon line, librational modes of the N_2 molecule and a selective coupling (depending on the symmetry of the excited state) to phonon modes of the Ne lattice.

(3) Electronic relaxation between a high Wannier state to lower n states. This electron-phonon relaxation process results in a Lorentzian contribution of the line shape.

For the lowest extravalence atomic impurity excitation only mechanism (2) is important, while for the higher Wannier states mechanisms (2) and (3) prevail. Provided that the electronic-nuclear coupling is strong we expect a Gaussian line shape for the $n = 1$ excitation (KUBO and TOYAZAWA, 1955; MARKHAM, 1959).

The observation of Wannier impurity states is not limited to rare gas host matrices. GEDANKEN et al. (1973) have observed these states for a Xe impurity in solid H_2, D_2 and CF_4. These solids are transparent up to relatively high energies (13.7 eV for CF_4 and 11.8 eV for solid H_2 and D_2). From a theoretical point of view the observation of a Wannier series indicates that the conduction band is free electron like in these solids. Recent theoretical calculations seem to confirm this point for solid H_2. It is interesting to note that in pure solid CF_4 (GEDANKEN 1973) and in pure H_2 and D_2 (GEDANKEN et al. 1973) the corresponding high Wannier exciton states are smeared out due to line broadening which exceeds the vibrational spacing.

3.3.2 Concentrated Rare Gas Alloys

A challenging problem in the theoretical study of mixed molecular crystals involves the understanding of the band structure and the optical properties of heavily doped molecular crystals. Two limiting cases for the different types of mixed crystal systems may be distinguished (ONODERA and TOYOZAWA, 1968, HOSHEN and JORTNER, 1972): (i) in the case of the persistence type mixed crystals the energies of the electronic states of the two constituents remain almost unchanged against the change in composition. Thus, although the mixed crystal itself is homogeneous, the electronic properties corresponding to the two constitutent substances persist. (ii) The second class of mixed crystals is usually called amalgamation type. In this case, only one set of electronic states is observed for the mixed molecular crystal which is characteristic for the new material where the two substances are completely amalgamated to yield another new crystal.

Examples for the persistence type of mixed crystals are provided by excitons in halogen substituted alkali halides, e.g. KBr - KCl and for the amalgamation type by excitons in alkali substituted alkali halides. The phenomenological parameter which determines to which type a given mixed crystal belongs, is the ratio of the difference in the energies of two neighboring valence bands of the two individual components to the width of these bands (ONODERA and TOYOZAWA, 1968). When this ratio is large two energy bands persist. In the opposite limit, when the band width is very large, the two bands merge into a single band characteristic for the amalgamation type systems.

Only a few systems of concentrated rare gas solids have been investigated so far; NAGASAWA et al. (1972) have measured the optical absorption of Ar-Xe solid solutions in the photon energy range 8 eV up to 11 eV, i.e. the range of Xe 5p excitations, whereas HAENSEL et al. (1973) investigated the optical properties of rare gas mixtures in the photon energy range 40 - 260 eV, i.e. in the region of Ne 2s, Ar 2p, Kr 3d and Xe 4d transitions. In addition to these optical investigations NÜRNBERGER et al. (1977) have studied the band formation in Xe-Ar alloys by photoelectron spectroscopy.

In Fig. 25 we reproduce the absorption spectrum for Xe in Ar in the concentration range of 0 - 100 mol% Xe (NAGASAWA et al., 1972). For low impurity concentrations the hydrogen-like $\Gamma(3/2)$ Xe impurity series with terms $n = 1$ up to $n = 4$

dominates the spectrum. Additionally, a shoulder at about 9.03 eV is observed which grows into a distinct separate peak in the 1 mol% spectrum. It has been ascribed to Xe-dimer absorption (see previous section). A gradual change of the spectrum starts at concentrations above 1 mol% Xe. The maxima of the Wannier series are broadened and a new broad maximum appears on the low energy side of the n = 1 peak. When the concentration of Xe increases to about 15 mol%, the spectrum undergoes severe changes and becomes similar to the spectrum of undoped solid Xe. The positions of the resolved structures connect smoothly to those of pure Xe. This observation suggests that the impurity Wannier exciton changes gradually from a localized nature to the band one at higher concentrations up to solid Xe. Further, this observation is consistent with the many optical studies of valence excitons for alkali halide solid solutions. The concentration dependence of impurity absorption spectrum was discussed theoretically by CHO and TOYOZAWA (1969).

The study of the absorption spectra of solid solutions of rare gases in the extreme ultraviolet by HAENSEL et al. (1973) was undertaken to check experimentally the interpretation given for the core level spectra of pure RGS. Selected results for Xe in Kr and Xe in Ar in the range of the Xe 4d excitation appear in Figs. 26 and 27. In most cases a continuous shift of the energetic position of the absorption peaks of the pure RGS upon addition of another rare gas or of N_2 was observed, thus indicating a dilute mixing of both components over the whole range of concentrations.

As mentioned in Section 3.2.3, the core excited spectra of pure RGS show excitonic as well as density of state effects. For instance the features B and C in Figs. 26 and 27 have been interpreted as core excited Frenkel type excitons. By comparing the experimental spectra with the calculated curves for the joint density of states (RÖSSLER 1971), HAENSEL et al. concluded that these Frenkel excitons in Kr 3d and Xe 4d are above the interband transition threshold. This conclusion is supported by the fact that the oscillator strength of these excitons in Kr and Xe is smaller than that of the corresponding gas lines owing to interactions with the underlying continuum. The concept underlying the analysis of core excited optical spectra in terms of the conduction band density of states has been described in Section 3.2.3. In their discussion of the effect of density of states on the spectra of rare gas mixtures, HAENSEL et al. (1973) used the known density of states in the pure crystals. For Xe - Kr as

an example (Fig. 26) we note that the structures D, E, F, G and H and their spin orbit partners shift with changing composition but do not split. They may be classified as almagamation type structures (ONODERA and TOYOZAWA, 1968). Thus the pure Xe spectrum in the lowest part of Fig. 26 should change more and more and become finally the pure Kr spectrum in the upper curve of Fig. 26, a spectrum which is to be understood in terms of the density-of-states of the Kr conduction bands, of course, weighted by the spin orbit splitting of the Xe 4d initial states. A rigorous discussion of theoretical and experimental results is aggravated by the absence of density of states calculations for the mixed crystals. However, a comparison of the maximum shifts of the observed features with calculated maximum shifts of the five lowest conduction bands of Kr (HAENSEL et al. 1973) supports the interpretation of the pure RGS spectra as due to density of states structures.

The Xe - Ar mixtures (Fig. 27) as well as Kr - Ar mixtures exhibit also a widening of the spectra with increasing admixtures of the lighter rare gas. In contrast to this the conduction band density-of-states does not follow this trend when going from Xe or Kr to Ar. For example the first and second density of states maxima as calculated by RÖSSLER (1971) are at lower energy in Ar than in Xe or Kr, and the concept which led to a sound interpretation of the Xe - Kr spectra did not work here with the same success. Thus, we conclude again that the original hopes cherished for core excited spectra as being a tool to map out conduction band density of states, did not materialize. On the other hand, these results stress once more the importance of matrix element and relaxation effects in optical spectra which are beyond the simple one electron picture employed.

More insight into the band formation in rare gas alloy systems can be expected from photoelectron spectroscopy. In Figs. 28, 29 and 30 the results of such a study on Xe - Ar alloys are shown (NÜRNBERGER et al. 1977). In Fig. 28 photoelectron energy distribution curves for concentrations ranging from 0 - 100% are displayed measured by excitation with synchrotron radiation at $h\nu$ = 13.8 eV, 16.5 eV and 18.0 eV. With increasing Xe concentrations the gradual formation of Xe valence bands starting from the atomic Xe $5p_{1/2}$ and Xe $5p_{3/2}$ states is observed. Similarly, with Ar the 3p states are broadened with increasing Ar concentration. The width of the energy bands is comparable to their separation. Nevertheless, the energy bands corresponding to the two

individual constituents are well separated and persist through all concentrations. It was noted by NÜRNBERGER et al. (1977) that rather high concentrations of Xe or Ar are necessary in order to reach the fully developed Xe or Ar valence bands, respectively.

The concentration dependence of the band width has been compared to concentration dependent band structure calculations. The results are displayed in Figs. 29 and 30. For simplicity NÜRNBERGER et al. (1977) used band structure calculations in the tightbinding scheme (SLATER and KOSTER 1954). The parameters $pp\sigma$, $pp\pi$ and the spin orbit splitting ΔE_{SO} needed for the calculation have been determined from the photoelectron energy distribution curves of pure Xe by RÖSSLER (1977) to be $pp\sigma = +0.33$, $pp\pi = -0.038$ and $\Delta E_{SO} = 1.37$ eV. The change of $pp\sigma$ and $pp\pi$ with concentration due to the reduced overlap integral of the wave function has been represented by an exponential decrease with increasing mean separation of the Xe atoms using the nearest neighbor distance in solid Xe d_0 multiplied by α as a reference length. The mean separation has been correlated with the concentration. In Fig. 29 a comparison of the measured valence bandwidth with calculated bandwidths is shown using α as a free parameter. For the calculated bandwidth the energy difference between Γ and X has been used because this is the largest width of the bands in the tight-binding approach given the above parameters. For both the Xe and Ar valence states a value of $\alpha = 2$ agrees satisfactorily with the experimentally determined concentration dependence (Fig. 29).

In Fig. 30 the valence bands along the direction from the center of the Brillouin zone Γ to the X point at the boundary are compared with the measured EDC's for Xe (upper part) and Ar (lower part) at three concentrations using $\alpha = 2$ for the calculation. The common feature in Fig. 30 for the three photon energies is the appearance of two maxima which correlate quite well with the maxima of the density of states of the lower valence band and of the center of the density of states of the split upper valence bands. The maximum of the density of states is expected to lie at the flat region near the X point. The relative shift of the maxima with reduced Xe concentration is well reproduced by the position of the upper and lower bands at X. Changes in the EDC's with photon energy are attributed to structures in the final states. According to Fig. 30 such changes are only significant for pure Xe.

This observation can be taken as a hint that the conduction band states are disturbed by a relatively small concentration of guest atoms.

Similar tendencies were found for the Ar valence bands but the smaller spin-orbit splitting yields a less clear cut case for the separation of the different contributions.

Finally, we mention the calculation by PARINELLO et al. (1977) who have attributed the considerable difference between the calculated bandwidth for Xe and the width of the valence bands observed in photoelectron spectra to different relaxation energies of the relaxed holes for the Xe $5p_{3/2}$ and Xe $5p_{1/2}$ valence states.

On the basis of a two-band Koster-Slater model the following qualitative predictions for doped rare gas samples have been made by PARINELLO et al. (1977): 1) For heavy rare gas atoms (Xe) in light rare gas matrices (Ar) no bound state is expected but at higher concentrations of the heavy atoms (Xe) the 3/2 state should shift to higher energies as observed in the experiment by NÜRNBERGER et al. (1977). 2) On the other hand, a strong bound state is expected for the case of light impurities (Ar) in a matrix of heavy atoms (Xe). Therefore at small Ar concentrations in Xe a large apparent spin orbit splitting is predicted. However, taking a width for the Ar states comparable with that of the Xe states in Ar, a splitting much larger than the real spin-orbit splitting of 0.2 eV does not fit the experimental results.

In summary, there seems to be an inconsistency in so far as absorption experiments favor an amalgamation type classification of rare gas alloys whereas EDC measurements suggest a persistent type model. Both results can, however, be reconciled if we recall that the photoemission experiments sample mainly the initial state density of states, which is persistent (Fig. 28). The absorption bands on the other hand are determined by both the initial and final states where the latter may introduce amalgamation type character.

4. Excitons in Rare Gas Liquids

The central features of bound one-electron excitations in pure RGS and in dilute rare gas alloys are characterized by Frenkel type exciton states, Wannier type excitons, or impurity states converging to the bottom of the conduction band (see previous section). As we have seen, the theoretical treatment of such bound excited states involves essentially the translational symmetry of the crystal lattice (e.g. KNOX 1962, PHILLIPS 1966, RICE and JORTNER, 1967). These solid state concepts break down when excitons and impurity states with extended electron orbits are considered in the liquid phase. The following general questions arise in relation to bound excited electronic states of simple dense fluids:

(i) Do exciton states "exist" in liquids, how should such states be described, and what physical information can be gathered from the optical spectrum? More specifically, can tightly bound excited states of a liquid be described in terms of a dispersion relation appropriate for the disordered system? Such Frenkel type states have a unique parentage the states of the constituents and will thus be definitely experimentally observed. Can Wannier-Mott type exciton and impurity states be experimentally observed in a liquid? Furthermore, if Wannier states exist in a liquid, it is interesting to inquire what is the relation between these liquid electron-hole pair states and the conduction band states in the disordered system.

(ii) How do interatomic interactions affect the spectrum of the stationary states? Studies of the density and temperature dependence of optical spectra from pure and doped liquids may shed some light on this question.

Theoretically, it was suggested by RICE and JORTNER (1966) and by RICE, NICOLIS and JORTNER (1968) that large radius Wannier type exciton states are amenable to experimental observation in a dense fluid where electron-medium interaction is sufficiently weak. Extensive theoretical studies of Frenkel-type tightly bound exciton states in liquids were performed by RICE and coworkers (POPIELAWSKI and RICE, 1967; NICOLIS and RICE, 1967; FISCHER and RICE, 1968).

Pure rare gas liquids and impurities in rare gas liquids provide suitable candidates for the study of excitons in liquids and are of interest in relation

to the above mentioned general problems as well as for the investigation of ionization processes in simple liquids (see e.g. SCHMIDT 1975, TAUCHERT 1975, JORTNER and GAATHON, 1977). For liquid Ar and Kr electron mobility data (SCHNYDERS, RICE and MEYER, 1966; MILLER, HOWE and SPEAR, 1968) indicate that the electron-atom interaction is sufficiently weak and that the transport properties of an excess electron can be quite well described in terms of disorder scattering of a nearly free electron. Although transport properties do not give conclusive evidence about the details of the density of conduction band states in a disordered system (see e.g. EDWARDS, 1965), it appears that a reasonable working hypothesis is that the conduction band states in liquid rare gases can be taken as free electron-like or nearly so.

Furthermore, in rare gas liquids, the weak electron-atom coupling (LEKNER, 1967; COHEN and LEKNER, 1967; SPRINGETT, JORTNER and COHEN, 1968) insures that the line widths of the Wannier states will not be excessive.

Quantitative experimental information concerning Wannier exciton states in liquid rare gases is still meager and only a few groups have tackled this problem so far. A summary of the optical absorption and reflection experiments performed so far on both the pure liquids and impurities in rare gas liquids appears in Table 9. The considerable amount of theoretical and experimental information concerning atomic and molecular type states in liquid He, Kr, Ar and Ne and especially in liquid He will be considered in Section 6 where we shall discuss results from transient absorption and luminescence experiments. In this section, we focus our attention on excitons in pure liquid Xe, Xe impurity states in liquid Kr, Ar and He and in particular on the density dependence of these states studied by optical absorption and reflection measurements. Further, we discuss one example for molecular impurity states in liquid rare gases. Finally, the electron affinities derived from the experimental data for solid and liquid rare gases are compared with calculated V_0-values.

Already a cursory examination of Table 9 shows that, except for a preliminary reflection experiment on liquid He by SURKO et al. (1970), all the experimental data are restricted due to obvious experimental reasons to energies below 10 eV and hence only liquid Xe and Xe impurity states as well as molecular impurity states in liquid rare gases have been studied so far by simple optical

experiments. Clearly, studies of Wannier states of lighter rare gas liquids, though experimentally quite difficult, would be of great value.

4.1 Excitons in Pure Liquid Rare Gases

BEAGLEHOLE (1965) reported the first optical experiment on rare gas liquids in the VUV. Reflection measurements on Xe in a LiF-windowed cell were performed in the region 7.8 - 11.0 eV covering the range of the Wannier type exciton lines observed for solid Xe. The main n = 1 (6p 3/2) exciton line at around 8.4 eV in solid Xe was found to shift to lower energies and to broaden as the temperature was raised becoming quite markedly wider in the liquid. More important was the observation of a weak and unresolved band around 9.0 eV in the liquid, which was taken as evidence for the fact that Wannier states $n \geq 2$ do exist in the liquid phase, however, as expected, in a much broadened form.

Optical spectra of pure liquid Xe have subsequently been studied in detail by STEINBERGER and coworkers (see Table 9). In a careful study by STEINBERGER and ASAF (1973) spectra of solid and liquid Xe covering the range 7.75 eV to 10.3 eV have been obtained at temperatures between 6 K and 160 K. Throughout the temperature range, the peak positions of the n = 1 (3/2) and n = 1 (1/2) excitons as well as the n = 2 and n = 3 (3/2) Wannier excitons were found to shift to lower energies with increasing temperature. STEINBERGER and ASAF inferred from the linear shift of the peak positions as a function of density that these shifts are caused mainly by the change of energy band edges with thermal expansion. In particular, the experimental points for the liquid fit these linear functions very well.

Photoconductivity in liquid Xe has been studied by ROBERTS and WILSON (1973) and ASAF and STEINBERGER (1974). The later authors found in photoconductivity excitation spectra a threshold of 9.20 eV and a dip at 9.45 eV very near the peak of the competing n = 1 (Γ1/1) exciton transition. From these results a band gap $E_g = 9.22 \pm 0.01$ eV was determined for liquid Xenon. This value is very near the estimate (9.24 eV) based on the density change upon melting. Combining the value for E_G with the measured excitation energy of the n = 2 Γ(3/2) exciton yielded an exciton binding energy B = 1.08 eV (see eq. 3.3) and an effective exciton reduced mass $\mu = 0.27$ (in units of electron mass) (see eq. 3.5).

The influence of the density on the optical spectra was further studied for pure liquid Xe in the density range from near the critical point to the triple point by LAPORTE and STEINBERGER (1977). The experiment covered the spectral range from 7.5 to 10.8 eV that is the atomic transitions in Xe which are observed at wavelengths above the MgF_2 cutoff: 8.44 eV (1469 Å), 9.57 eV (1295 Å) and 10.4 eV (1192 Å). For each atomic line, two bands have been observed: one broadened and somewhat red-shifted band corresponding to the atomic transition, and another distinct band corresponding in position to that of the exciton observed in the triple point liquid. These greatly broadened excitonic bands were observed in the liquid near the triple point at 8.12 eV (1526 Å), 9.35 eV (1326 Å) and 10.34 eV (1199 Å) where the values are those of the reflectivity maxima. As an example, we present in Fig. 31 the evolution of the 8.33 eV excitonic band with increasing density. Fig. 31 represents the reflectivity spectra of a Xe/MgF_2 interface at several densities near the critical point as well as near the triple point. The gradual rise of the excitonic band at 8.33 eV at the expense of the perturbed atomic band at 8.12 eV is evident. LAPORTE and STEINBERGER (1977) performed also a dispersion analysis for the two $^3P_1$ bands. They assumed Lorentzians for ε_1 and ε_2 in order to obtain via a fit to the experimental reflectivity data the optical constants ε_1, ε_2, n and k as a function of photon energy (see the solid curve in Fig. 31). They interpreted their results as evidence for exciton transitions appearing in momentary clusters of the fluid.

The only other piece of information concerning optical spectra of excitons in pure rare gas liquids pertains to liquid He. Here the free exciton states are less well known. They can be derived from the one available reflection spectrum taken by SURKO et al. (1969). It shows two maxima, a strong one at 21.4 eV (580 Å) corresponding to the strongly allowed transition to the 2 $p\,^1P$ state (at 584 Å in the gas) and a very weak one at 20.8 eV (597 Å) corresponding to the forbidden $2s\,^1S$ transition (at ..... A^o in the gas).

4.2 Xe Impurity States in Liquid Gases

The identification of "high" n = 2 Wannier type exciton states in liquid rare gases rests on a comparison (perhaps somewhat oversimplified) of the absorption bands with the optical properties of the corresponding solid. In order to establish the nature of Wannier states in dense simple fluids, it is of interest to obtain a continuous description of the electronic excitations of a guest atom or molecule in a host fluid where the fluid density is varied over

a broad density range. In this context, three types of electronic transitions of the guest atom should be considered:

(1) Intravalence excitations. Studies of spectral perturbations of such transitions by foreign gases at low and moderate densities reveal (see e.g. ROBIN et al. 1956, GRANIER 1969): (a) Small red or blue spectral shifts and line broadening, (b) the appearance of "red" or "blue" satellites due to the formation of a van der Waals diatomic molecule as well as (c) symmetry breaking effects, i.e. appearance of symmetry forbidden transitions. At high fluid densities features (a) and (c) are expected to prevail while the spectral satellites and resonance line will merge into a single broad band.

(2) Low extravalence excitations. These transitions are accompanied by a change $n_a = 1$ in the principal atomic quantum number n_a. The features of such transitions (e.g. the $5p^6 \longrightarrow 5p^5$ 6s transition in Xe) of rare gas atoms are: (a) Spectral shifts to the red at low density and to the blue at high density and line broadening (RUPIN et al. 1967, MESSING et al. 1977a-e); (b) Appearance of "blue" spectral satellites, originating from continuum-continuum and bound-continuum transitions between the diatomic adiabatic potential surfaces of the guest-host pair (GRANIER et al., 1967, CASTEX 1974) and (c) Induction of symmetry-forbidden transitions. At higher densities of the host fluid large blue-shifts are exhibited, the satellites are smeared out by overlapping the resonance line, while the symmetry breaking effect (c) is also operative. Apart from quantitative differences regarding the large magnitude of spectral blue-shifts, the gross features of the lowest extravalence transitions of rare gases are qualitatively similar to those of intravalence excitations.

(3) High extravalence excitations. Such transitions are characterized by $n_a = 2$. Only very little is known concerning spectral perturbations of such transitions at moderate and at high densities of the host fluid and questions arise, such as: What are the spectral shifts of higher atomic Rydberg states at low and at moderate densities of the host fluid? Or, can one define a critical density of the host fluid where these high extravalence excitations disappear being replaced by the Wannier type states of the dense medium? Or alternatively, do they converge to the n = 2 Wannier states?

In an attempt to understand these problems, MESSING et al. (1977a) have conducted an extensive experimental study of the absorption spectrum in the energy range 8.3 eV to 10.8 eV of Xe guest atoms perturbed by Ar, Ne and He over a density range of the host from the atomic limit to the liquid density. The VUV absorption spectra of Xe with an initial impurity concentration of 0.5 to 1 ppm in Ar, Ne and He have been studied using the absorption cell as described in Fig. 5. We shall discuss here as an example the results obtained for the Xe/Ar system.

In Figs. 32 and 33 the experimental results for the absorption spectra of Xe in liquid Ar are shown at low and at intermediate densities (ρ = 0 - 0.6 g cm^{-3}, Fig. 32) and at high Ar densities (Fig. 33) respectively. The following electronic excitations of the guest Xe atom were observed in the spectral range from 9.5 eV (1300 Å) to 10.8 eV (1150 Å) in order of increasing energy. The transition energies are given in the atomic limit using Moore's notation (MOORE 1958):

Transition (I) to $6s'[1/2]J = 1(5p^5\{^2P_{1/2}\}\ 6s)$ at 9.57 eV (1296 Å)
Transition (II) to $5d\ [1/2]\ J = 1(5p^5\{^2P_{3/2}\}\ 5d)$ at 9.92 eV (1250 Å)
Transition (III) to $5d\ [5/2]J = 3(5p^5\{^2P_{3/2}\}\ 5d)$ at 10.25 eV (1210 Å)
which is symmetry-forbidden in the atomic limit. (CASTEX 1974).
Transition (IV) to $5d\ [3/2]\ J = 1\ (5p^5\{^2P_{3/2}\}\ 5d)$ at 10.40 eV (1192 Å)
Transition (V) to $7s\ [3/2]\ J = 1\ (5p^5\{^2P_{3/2}\}\ 7s)$ at 10.60 eV (1170 Å).

Transitions (I) - (IV) correspond to the low extravalence excitations with $\Delta n_a = 1$, while transition (V) originates from the second member $\Delta n_a = 2$ of a Rydberg series which starts with the first resonance line $6s\ [3/2]J = 1\ (5p^5\{^2P_{3/2}\}6s)$ at 8.44 eV (1470 Å). The following medium effects have been observed at low and moderate densities (Fig. 32).

1. Satellite bands. In the density range 0.1 - 0.4 g cm^{-3} a single blue satellite band accompanies each of the transitions (I) and (IV). The intensity of these blue satellites increases with increasing density until at Ar density $\simeq$ 0.6 g cm^{-3} they merge together with the corresponding resonance line into a single band.

2. Symmetry breaking effects. The transition (III) to a J = 3 state is symmetry-forbidden in the atomic limit, as is evident from Fig. 32, being induced by the host fluid.

No other symmetry-forbidden, pressure-induced transitions were observed in the spectral region 9.5 eV to 10.8 eV with the possible exception of the broad structureless absorption exhibited around 9.6 eV to 9.8 eV which may originate from pressure induced transitions to states of the $5p^5$ 6p configuration (CASTEX 1974).

3. Medium-induced shifts of the lowest $\Delta n_a = 1$ extravalence excitations. These shifts are summarized in Fig. 34. The Xe resonance lines 6 s [3/2] (not shown in Fig. 32) and 6s' [1/2] (Transition I) are weakly red-shifted at low densities, exhibiting a large blue-shift at higher densities. A similar behavior is observed for transition (IV). These features have been explained in terms of a strongly repulsive Xe-Ar interaction potential in the excited state (MESSING et al. 1976). In contrast, transition (II) exhibits only a small red-shift throughout the low and the intermediate density region.

4. Medium induced shifts of the higher $\Delta n_a = 2$ extravalence excitation. The spectral shift of transition (V) to the 7 s [3/2] state drastically differs from those revealed by the 6s 3/2 and 6 s' [1/2] transitions. While the latter low extravalence excitations exhibit predominantly a large spectral blue shift (Figs. 32, 34), the former "high" extravalence transition reveals an apprciable spectral red-shift, even at high densities, overlapping the blue-shifted band (IV) at a density of $\lesssim 0.4$ g cm^{-3} and appearing as a low energy shoulder of band (IV) at a density of ≈ 0.6 g cm^{-3}.

In the high density range (Fig. 33) the first transition at $\approx$ 9.7 eV (1265 Å to 1290 Å) was assigned by MESSING et al. 1977a to an excitation of the 6s' [1/2] state (transition I) and the third main transition at $\approx$ 10.5 eV (1170 Å to 1190 Å) to the 5d [3/2] state (transition IV). These transitions exhibit large blue-shifts (Fig. 34) at high densities. The most interesting feature of the spectra in Fig. 33 is the absorption band at 9.9 eV to 10.2 eV. This second band centered at 10.12 eV (1225 Å) in the high density fluid was assigned by MESSING et al. (1977a) to an n = 2 Wannier state, because it is close in energy to the n = 2 Wannier impurity state in solid Xe/Ar alloys which peaks at 9.95 eV (1246 Å) (BALDINI, 1965). As MESSING et al. (1977a) pointed out, this is only a qualitative argument in favor of the n = 2 Wannier exciton assignment, and they therefore also considered alternative assignments. They pointed out that the absorption intensity around 10.1 eV in the

Xe/Ar system at high ($>7 \times 10^{-3}$ atoms Å^{-3}) densities is anomalously enhanced indicating the appearance of a new absorption band at these densities. This behavior is unique to the Xe/Ar system and was not observed for Xe/Ne and Xe/He in the same range of atomic densities. It was taken as a strong support for the n = 2 exciton assignment. The assignments are summarized in the correlation diagram in Fig. 35.

The assignment of the n = 2 [3/2] Wannier impurity state of Xe in liquid Ar at 10.12 eV enables one to draw an energy correlation diagram which relates the high extravalence atomic excitations and the "high" Wannier states (Fig. 35).

With the n = 2 exciton, the ionisation energy and polarisation energies for the electrons and Xe ions (hole states) for Xe in liquid Ar have been estimated (see Table 10) (RAZ and JORTNER 1970; MESSING et al. 1977a) (see Table 10). Furthermore, MESSING and JORTNER (1977c) have discussed the density dependence of the polarization energy P_+ of Xe^+ in Ar.

4.3 Molecular Impurity States in Liquid Rare Gases

The observation of intermediate and Wannier type atomic impurity states in RGS and liquids implies that analogous molecular excitations should be amenable to experimental observation. There have been extensive experimental spectroscopic studies of such high-energy electronic excitations of molecular impurities in solid rare gases, which have been reviewed by JORTNER (1974). In this section, we shall discuss only one of the few examples (Table 9) for a molecular impurity in liquid rare gases, namely the perturbation of molecular extravalence excitations of methyl iodide in liquid Ar and Kr as reported by MESSING et al. (1977d).

Of considerable interest are such electronic excitations in a dense fluid where the excited states of the molecular impurity can be roughly classified into three categories analogous to the atomic impurity states:

(A) Intravalence molecular excitations. Most of such valence excitations from a bonding orbital to a nonbonding orbital can be adequately described in terms of the tight binding scheme.

(B) Low molecular extravalence excitations. These correspond in the low pressure limit to the lowest Rydberg states of the molecule, which are

characterized by a change $\Delta n = 1$ of the principal quantum number.
(C) Wannier states. Wannier-type molecular impurity states were identified for CH_3I, C_2H_4 and C_6H_6 in solid rare gases. (KATZ et al., 1969 and GEDANKEN et al., 1972, 1973, JORTNER 1974) and evidence for these highly excited states in a liquid was obtained for CH_3I in liquid Kr by GEDANKEN et al. (1973e).

The detailed experiments of MESSING et al. (1977d) on molecular impurities in liquid Ar and Kr in the spectral range from 6.2 eV (2000 Å) to 10.3 eV (1200 Å) were performed over a broad density range of the host liquid from the low pressure limit ("isolated molecule") up to the liquid density. Three small organic molecules, methyl-iodide, carbon disulfide and formaldehyde were investigated. The absorption spectra of CH_3I in Ar in the low energy range are displayed in Fig. 36. CH_3I is a suitable and interesting molecular system to study because of two reasons. First, the lowest extravalence excitations of this molecule in the gas phase are isoelectronic with the Xe atomic $^1S_0 \longrightarrow {}^3P_1$ and $^1S_0 \longrightarrow {}^1P_1$ transitions. The first Rydberg transitions of the isolated CH_3I molecule originate from the iodine $np\pi$ (5p) nonbonding orbital (PRICE, 1936; HERZBERG, 1966; BOSHI and SAITAHUB, 1972; and TSAI and BAER, 1974). Only the lowest broad and structureless absorption band located at 4.8 eV is assigned to an intravalence $np\pi \longrightarrow \sigma^*$ transition (ROBIN 1974). Most of the absorption bands were assigned to three Rydberg series of different symmetry converging to the same ionisation limit. Each of the Rydberg series is further split into two components because of the strong spin-orbit coupling within the positive hole when the CH_3I^+ ion core is left in either $^2E_{3/2}$ or $^2E_{1/2}$ state. Second in view of the low gas phase ionisation potentials of this molecule, $I^1_{gas} = 9.49$ eV, $I^2_{gas} = 10.11$ eV (e.g. POTTS et al., 1970), the Wannier series in the matrix or liquid should be located at moderately low energies amenable to experimental observation.

The results of the spectroscopic study of CH_3I in liquid Ar and Kr by MESSING et al. (1977a) can be summarized as follows:
(1) Medium induced spectral shifts can provide a diagnostic tool for the distinction between Rydberg type and valence excitations (see also the discussion of this method by ROBIN (1974)). The magnitude of the blue spectral shifts decreases in the following order: (a) The largest blue spectral shifts are exhibited for the lowest $n = 1$ Rydberg transitions of an s or p excited-state configuration, (b) the blue shift for an $n = 1$ type configuration is slightly lower, (c) mixed type valence-Rydberg transitions exhibit even a smaller blue shift and (d) the lowest spectral shift is revealed by a pure valence transition.
(2) Medium effects on large radius $n > 1$ Rydberg transitions can be followed only at moderate densities where these high extravalence molecular excitations can be unambiguously identified. In general, these high excitations in fluid Ar exhibit a red shift which increases with increasing density, being larger for higher term values. This trend implies that in this fluid where $V_0 < 0$ the impurity ionization potential $E_g(\rho)$ decreases with increasing density ρ.
(3) The impurity absorption spectrum at high fluid density is characterized by a small number of broad bands, some of them quite distinct and intense, some of them are diffuse and some appear as shoulders or humps. Only those impurity states originating from the lowest Rydberg transitions ($n = 1$) of different symmetries are amenable to a reliable assignment as they develop continuously from the "isolated" molecule spectrum (see Fig. 33). This definite molecular parenthood justifies the classification of the latter transitions as intermediate states. Some of these intermediate states are accompanied by a vibrational structure persisting up to the highest density (e.g., the $n = 1$ impurity states of CH_3I in Ar at 6.16 eV (2012 Å) (Fig. 33). The relation of these lowest extravalence impurity excitations to the molecular states leads to the conclusion that Liehr splitting of the $n = 1$ states (the splitting of states belonging to s, p, d excited-state configurations) persists up to the liquid density, in contrast to the conventional interpretation of the analoguous solid matrix spectra.
(4) Several impurity absorption bands at high fluid density were interpreted in terms of large radius $n \geq 2$ impurity states. In particular, experimental evidence was obtained for the appearance of an $n = 2$ impurity state in the spectrum of CH_3I in Ar. In the spectra of CS_2 and H_2CO there is a tendency of the molecular $n = 2$ Rydberg transitions originating from different series to converge into a single band in the high density fluid. The significance of this observation is that the Liehr splitting for $n = 2$ states gradually disappears, being vanishingly small in the liquid, as appropriate for a hydrogenic series of impurity states in a dense medium.

In an accompanying study, MESSING et al. (1977b) have also studied the medium effects on the vibrational structure of the low extravalence (Rydberg) excitations of CH_3I and of H_2CO in liquid Ar. The statistical theory was utilized for model calculations of the line shape of the medium-perturbed molecular transitions.

It was concluded from these studies that independent asymmetric broadening of individual vibronic components accounts for the modification of the apparent intensity distribution with increasing density of the host fluid.

4.4 Electron Affinities for Solid and Liquid Rare Gases

The combination of spectroscopic and photoemission data results in a reliable V_0 (= $-E_A$) scale for solid rare gases. In Table 10 we compare these V_0 values obtained for pure and doped RGS with the experimental data for liquid rare gases determined by TAUCHERT (1975) and TAUCHERT et al. (1977). Negative V_0 values mean that energy is released by bringing an electron from the vacuum into the solid.

Interest in V_0 values arises from various problems of electron transport in solids and liquids. According to the simple SJC theory (SPRINGETT et al. 1968), the magnitude of V_0 determines whether an extended or a localized state of the electron in the liquid is energetically the most favorable one. It is apparent from Table 10 that in all cases V_0 in the solid is higher than in the corresponding liquid, indicating that in the former case the contribution of short-range repulsive interactions is somewhat higher. In liquid He the electron medium interaction is repulsive and the localized bubble state is energetically favored. The notion of repulsive e-He interaction is in agreement with the V_0 value (SOMMER, 1964). The positive V_0 values for solid and liquid Ne predicts according to the SJC model localized electron states to be stable which is corroborated by the experimentally observed low electron mobilities. Experimentally in liquid Argon, Krypton and Xenon high electron mobilities were observed (MILLER et al., 1968) and the reported value for liquid Argon (LECKNER et al., 1967) favors the extended electron state. These observeations are consistent with the negative V_0 values determined by TAUCHERT et al. (1977) for these materials.

It is of interest to confront the experimental V_0 data with the prediction of the simple SJC theory (SPRINGETT et al, 1968). As is well known, the energy of the conduction band minimum for the excess electron consists of two contributions, the background polarization potential U_p and the kinetic energy term T arising from multiple scattering from nearest neighbors, so that $V_0 = T + U_p$. The SJC model provides a simple recipe for the estimate of U_p including the screened polarization field of the surrounding atoms and for the evaluation of T by the Wigner-Seitz approximation. Table 10 summarizes the results of such calculations, where the scattering length a of the Hartree-Fock atomic field for He and Ne was.

taken from theoretical scattering data (SPRINGETT et al., 1968), while for Ar, Kr and Xe the value of a was adjusted to fit the liquid V_0 value. These semiquantitative theoretical estimates of V_0 are fraught with difficulties as Table 10 emphasizes how much smaller V_0 is than the T and the U_p terms. These theoretical estimates clearly indicate that the increase of T in the solid is somewhat higher than the corresponding decrease in U_p; however, the SJC model underestimates the relative increase of the short-range repulsive interactions in the solid as is apparent from the result for Ar. Thus, this semiquantitative approach of the SJC model should not be considered as an ultimate theory and further theoretical work in this field is required.

The density dependence of V_0 for liquid Ar has been discussed by MESSING and JORTNER (1977c). They reported on calculations of the adiabatic electrostatic polarization energy P_+ of Xe^+ in fluid Ar over a density range from 0.1 to 1.4 g cm^{-3}. In a phenomenological description P_+ is connected to V_0 by the impurity ionization energy E^i_{TH} of an atom or molecule in a dense fluid and the gas phase impurity ionisation energy I_{gas} via $E^i_{TH} = I_{gas} + P_+ + V_0$ (see e.g. RAZ and JORTNER, 1969). The density dependence of P_+ can be quite well approximated (within 10%) by the Born charging energy with the effective ionic radius being identified with the effective hard-core diameter for the (neutral) solute-solvent separation. The theoretical density dependence of V_0 in liquid Ar as calculated by JAHNKE et al. (1972) was found to be practically independent of the density over a range from ρ = 0.28 g cm^{-3} to ρ = 1.43 g cm^{-3}, the average value being $V_0 = -0.5$ eV. As an upper limit for V_0 in liquid Ar, MESSING and JORTNER (1977c) estimated a value of -0.2 eV based on their calculation of P_+ and spectroscopic data. This value is in even better agreement with the experimental value of $V_0 = -0.22 \pm 0.02$ eV at ρ = 1.4 g cm^{-3} determined by TAUCHERT and SCHMIDT (1975). More interestingly we note that V_0 was found to be practically constant over a wide density range in accord with the theoretical calculation of JAHNKE et al. (1972). The weak density dependence of V_0 in liquid Ar over a broad density range is in contrast to the pronounced increase of V_0 from -0.2 eV in liquid Ar to $+0.3$ eV in solid Ar (Table 10).

Finally, we mention in this context again the photoelectron spectra of heavier Xe clusters by DEHMER and DEHMER (1978a, 1978b) which we briefly discussed in Section 3.1. These spectra show qualitatively how the ionization potential and thus the derived parameters change as the average cluster size is increased.

The threshold energy for photoemission of solid Xe is 9.7 to 9.8 eV, as compared to the ionisation potential of Xe_2 of 11.127 eV. The highest pressure spectrum (Fig. 16) has a threshold energy of $\leq$ 10.5 eV which already is considerably below the ionisation of the dimer. Further experiments along these lines promise to provide a wealth of information on the energy level structure of species which are in the transition region between the gas and solid phases.

5. Metal-Rare Gas Mixtures

Matrix isolation techniques (e.g. PIMENTEL 1958, 1978, McCARTHY and ROBINSON 1959, MEYER 1971) utilize rare-gas matrices (RGM's) as inert host solids for the trapping of a variety of metastable atoms and molecular species. During the last few years extensive studies were reported for binary mixtures of metals (M) and RGSs, explored over the entire composition range, with the metal atomic fraction (X) being varied in the range X = 0 - 1.0. These systems are of interest, because of several reasons:

(1) Matrix isolation at moderate metal concentrations (X = 0.01 - 0.05) results in the production of interesting weakly bound diatomic M_2 or MM' homonuclear and heteronuclear molecules (e.g. OZIN 1977, MILLER et al. 1977, LEUTLOFF and KOLB 1979, DANOR et al. 1979).

(2) Matrix isolation at higher metal concentrations (X = 0.02 - 0.1) results in the stabilization of clusters of metal atoms M_n with n = 3 - 5 trapped in solid rare gases (e.g. SCHULZE et al. 1978, OZIN and HUBER 1978; MOSKOVITZ and SCHULZE 1977, WELKER 1978, WELKER and MARTIN 1979, DANOR et al. 1979) which are of considerable fundamental interest in the fields of nucleation, chemisorption and catalysis.

These two points pertain to interesting but still rather conventional extensions of the traditional matrix isolation techniques. Even more interesting phenomena are exhibited at high metal concentrations:

(3) At concentrations X > 0.1 metal - RGS mixtures provide model systems for disordered amorphous semiconductors (MOTT and DAVIS, 1972).

(4) A well dispersed metal RGS mixture at even higher X can be considered as an expanded metal where the rare gas atoms serve as "spacers" which keep the metal atoms apart. With increasing X the two-component mixture will undergo a metal-nonmetal transition (MNMT) (MOTT, 1974, FRIEDMANN and TUNSTALL, 1978) from a zero conductivity system to a finite conductivity system. Metal-RGS systems are prototypes for the experimental and theoretical studies of the nature of the MNMT induced by composition changes in a disordered material.

(5) At high metal concentrations above the metal composition which marks the MNMT the transport and optical properties of metal - RGS mixtures provide information on the electronic structure and transport in disordered metals (e.g. MOTT 1974, CATE et al. 1970, EVEN and JORTNER 1972, COHEN and JORTNER 1974).

From the foregoing discussion it is apparent that studies of metal - RGS mixtures can yield direct information regarding the electronic states, transport properties and MNMTs in disordered materials, a field of research which has been of considerable recent theoretical and experimental interest (MOTT and DAVIS 1972, MOTT 1974). In metal-RGS mixtures both structural disorder and compositional disorder can prevail. The characteristic structural features of the density of states function of the perfect lattice will be reduced and disappear in disordered systems and, in particular, the van Hove singularities will be smeared out. Gaps in the density of states of the perfect crystal may be filled up with a finite density of states, and sharp band edges are smeared out to form band tails (MOTT 1967, COHEN et al. 1969). However, the concept of density of states is still useful and applicable for disordered materials. The density of states in such disordered systems is characterized by a mixed distribution of localized states and of extended states. The localized electronic states which are specified by an envelope wavefunction which decays exponentially at large distances are associated with finite atom clusters. On the other hand, extended electronic states, where the envelope wavefunction is plane wave-like, extend to infinity, so that for a binary disordered material these states are associated with an infinite cluster. It has been argued that there is no coexistence of localized and extended states at the same energy (MOTT 1967, COHEN et al., 1969). Therefore, there exist a finite number of well defined energies which segregate between localized and extended states. Since at zero temperature the localized states do not contribute to d.c. electronic transport, these energies separating localized and nonlocalized states are referred to as mobility edges. The transport and optical properties of disordered materials stem from the basic differences between extended and localized states.

The nature of the electronic states of disordered materials is determined not only by the general characteristics of disorder but dominated by the microscopic structure of these solids. In RGS mixtures at low X localized states corresponding to single atoms, diatomic molecules and small clusters

will be exhibited. The cardinal question is whether the distribution of the metal atoms is statistical or whether preferential clustering of the metal atoms occurs. Obviously the experimental preparation conditions of the sample have a profound influence on its microscopic structure which is affected by the nature of the substrate, deposition temperature, deposition rate, the kinetic energy of the metal atoms, surface diffusion etc. Two general classes of disordered two-component materials can be distinguished (Fig. 37) in this context:

(1) Microscopically inhomogeneous metal-RGS mixtures. Here clustering is preferential. At low metal concentrations it can happen that a single metal atom cannot be matrix-isolated as efficient surface diffusion prefers the production of M_2 diatomics, as is the case for Be (MILLER et al. 1977). At higher metal concentration the material consists of metallic clusters, i.e. microclusters, embedded in the insulator. At even higher metal concentrations the inhomogeneous metal RGS mixture becomes metallic, its properties are expected to be analogous to those of granular metals (ABELES et al. 1975).

(2) Microscopically homogeneous metal-RGS mixtures. In such randomly substituted material only statistical clustering of metal atoms exists. When increasing the metal concentration, statistical clusters of increasing size will be formed; while at even higher X the homogeneous disordered material will become metallic.

The information currently available regarding the microscopic structure of metal-RGS is meager. A preliminary study using electron diffraction techniques was reported by QUINN and WRIGHT (1976). Thus, the available information regarding the microscopic structure is still indirect. It is derived from the optical and transport data. Figure 38 presents a scheme for the diverse structural and electronic features of metal RGS mixtures over the entire composition range which will provide guidelines for the subsequent discussion of these systems.

5.1 Single Metal Atoms

The pioneering studies of the electronic spectra of single metal atoms in RGS were conducted for Na and Hg by McCARTHY and ROBINSON (1959). Since then more than 40 metal atom systems have been studied (see e.g. the reviews by MEYER 1971, GRUEN 1976, MEYER 1978). A summary of the individual atomic systems studied by optical spectroscopy (e.g. McCARTHY and ROBINSON 1959, WEYHMAN and PIPKIN 1964, MEYER 1965, KUPFERMAN and PIPKIN 1968, ANDREWS and PIMENTEL 1967, BALYEAEVA et al. 1969) and by ESR techniques (COUFAL et al., 1974a, b, c) is presented in Fig. 39. In view of the extensive reviews available, we shall restrict ourselves to a brief selective survey of the energetics and microscopic structure of the single atom M centers in RGS which are pertinent for the subsequent discussion.

Considering absorption spectroscopy two general features should be noted: First, in all cases the optical absorption is exhibited in the proximity of the lowest electronic excitations of the free atom. The proper theoretical treatment for these excitations should rest on the tight binding picture considering small matrix perturbation of the free-atomic levels. This approach is similar to the currently fashionable description of the lowest electronic excitations in pure RGS and rare gas alloys (Section 3). Second, there is no definite evidence currently available concerning higher energy Wannier type excitations of the M center, analogous to those observed for rare gas impurity atoms in RGS. Twenty years ago, an absorption of Na in Ar at 3300 Å was reported (McCARTHY and ROBINSON 1959) which was assigned to a 3s $\rightarrow$ 4p atomic transition. It may be viewed as a n = 2 Wannier state. Such Wannier impurity states will be of interest for determining the ionization energy of the M center and in connection with nonradiative processes between the high energy bound states of this center.

Next, we would like to emphasize that while the general spectroscopic assignment of the observed optical spectra of the M center is straightforward, the interpretation of the details of the structure of these absorption spectra are not yet understood. The optical absorption spectra of the M center reveal broad lines which exhibit fine structure. A characteristic example is shown in Fig. 40 for the spectra of Na in RGSs (BALLING et al. 1978). Those spectra of alkali atoms in RGS reveal two triplets labelled A and B

and one or two additional bands (MEYER 1978). Qualitatively similar effects of broadening and splitting are exhibited in many M centers. The following effects should be considered for an interpretation: (i) Line broadening of individual spectral features, i.e. a single component of an alkali triplet may originate either from intrinsic phonon broadening or from inhomogeneous broadening due to statistical Gaussian distribution of trapping sites. (ii) Site splitting; different trapping sites, e.g. substitutional and interstitial are expected to exhibit different spectral shifts and thus to be characterized by different excitation energies. (iii) Matrix spectral shifts exhibited within each individual trapping site. These can be conventionally attributed to short range repulsive overlap interactions and to long range attractive dispersive coupling. (iv) Crystal field splitting effects within each individual center which are determined by the local symmetry (WEYHMAN and PIPKIN 1964). (v) Jahn Teller coupling effects originating from the coupling of a degenerate vibration (ENGLMAN 1974). (vi) Spin-orbit coupling effects which may be modified by overlap non-orthogonality effects (NAGEL and SONNTAG 1978).

The effects of inhomogeneous broadening and of site splitting have to be sorted out before the intrinsic electronic effects (iii) - (vi) which are all of comparable magnitude as well as the effect of phonon broadening within a single well defined center can be subsequently considered. The techniques of laser induced fluorescence line narrowing (POWELL 1978) can be utilized to discriminate between the effects of inhomogeneous and homogeneous broadening. BALLING et al. (1978) have applied these methods to the M centers of alkali atoms in RGS obtaining definite identification and characterization of individual trapping sites.

By fluorescence spectroscopy of the M center (BALYAEVA et al. 1973, BALLING et al. 1978, LEUTLOFF and KOLB 1979) excited state potential surfaces, relaxation processes and photochemically induced diffusion processes (OZIN and HUBER 1978, OZIN 1978) have been studied. Consider first the relevant energetics. While the attractive interaction between a ground state guest atom and the host is of the weak van der Waals type, the pair interaction between the rare gas and the excited metal atom can lead in many cases to quite a stable molecule M^*R which can be called a heteronuclear excimer. For example, the dissociation energy of the $Na(^2P_{3/2,1/2})$ Ar diatomic molecule is 400 cm^{-1} (SMALLEY et al. 1977 and BAYLIS 1969) (Fig.41). Trapping of an H^*

atom to form a heteronuclear excimer bears a close analogy to the formation of homonuclear excimers via excitation trapping in pure RGSs (Section 6). Provided the excimer is stable and that vibrational relaxation to form the M^* rare gas diatomic molecule is fast on the time scale of the radiative decay of M^*, one expects the emission spectra of many M centers to be characterized by broad structureless excimer emission bands. This expectation is borne out by the emission spectra of Na in Ar, Kr and Xe (BALLING et al. 1978) reproduced in Fig. 42, and of Ag in Kr and Xe (LEUTLOFF and KOLB 1979) which indeed exhibit broad emission bands revealing large ($\approx$3000 cm^{-1} for Na and $\approx$8000 cm^{-1} for Ag) Stokes shifts characteristic of excimer emission. The formation of M^* rare gas excimers requires that from the energetic point of view this molecule is stable while the dynamic point of view requires that vibrational relaxation is effective. A violation of the energetic condition is encountered for Au centers in Kr and in Xe which are characterized by a very narrow emission line (LEUTLOFF and KOLB 1979). It was assigned to an atomic type emission from a d^9s^2 configuration which does not form an excimer. The emission spectrum of Ag in Ar at low temperatures reveals a sharp "atomic" line whose intensity diminishes with increasing temperature (LEUTLOFF and KOLB 1979). Again this sharp line was assigned to emission from a d^9s^2 state. However, this proposal does not explain the remarkable temperature dependence. An alternative interpretation can involve violation of the dynamic condition at low temperatures, so that vibrational relaxation is competing with radiative decay of the atom while at higher temperatures activated vibrational relaxation is effective in producing the excimer.

In systems where the energetic and dynamic conditions for excimer formation are satisfied, the strongly repulsive ground state of the M^* rare gas excimer contributes substantially to the red Stokes shift. Thus, as a consequence of the excimer emission the translational energy of the M-rare gas pair is locally dissipated. Such an energy dissipation process results in local heating of the matrix which will enhance the diffusion of the metal atom. The photoinduced bulk diffusion of atoms in RGS (OZIN and HUBER 1978) originates from this local heating effect. It is worthwhile to point out that the same considerations apply to pure RGSs where excimer radiative decay to the repulsive ground state (Section 6) can result in appreciable local heating and possibly to photo-induced bulk self diffusion in RGS.

Spectroscopic studies provide an important diagnostic tool to probe the microscopic structure of the material. From the concentration dependence of absorption bands information whether the material is microscopically homogeneous or whether preferential clustering occurs can be derived. In Figure 43 (DANOR et al. 1979) the composition dependence of the absorption intensity of a single Hg atom in solid Xe is shown for the 4.85 eV peak, which corresponds to the $^1S_o \rightarrow {}^3P_1$ transition. The concentration (X) dependence can be accounted for in terms of the probability $P_1(X)$ of finding a single Hg atom

$$P_1(X) = X(1-X)^z \qquad (5.1)$$

where z is the coordination number. The Hg/Xe experimental data of Fig.43 (DANOR et al. 1979) can be described by this relation with z = 10 - 12, as appropriate for an amorphous rare gas solid. These experimental data demonstrate that for this system up to X = 0.20 the distribution of the M centers is statistical.

5.2 Diatomic Metal Molecules

The study of homonuclear and heteronuclear diatomic metal molecules in RGS is expected to provide a wealth of new spectroscopic information complementary to that available (HERZBERG 1966) for the spectra of diatomic molecules in the gas phase. The interpretation of the spectra of such diatomic molecules in RGS rests on two types of criteria. First, the vibrational structure (e.g. MILLER et al. 1977) is used and matrix bands are compared to the spectra in the gas phase (e.g. DANOR et al. 1979). Second, one can use a compositional criterion. For materials where the distribution of the metal atoms is statistical the intensity of the absorption band corresponding to a homonuclear dimer is proportional to X^2 at moderately low values of X. Figures 44, 45 and 46 show the concentration dependence of the absorption spectra of Li and Na in Ar (WELKER and MARTIN 1979) and of Hg in Xe (DANOR et al. 1979) which at moderate X = 0.02 - 0.10 metal concentration exhibit M_2 absorption bands. An unambiguous identification of the M_2 bands is crucial. In Fig. 47 an example for the spectroscopic criterion is shown for Hg in Xe (DANOR et al. 1959) where the transitions in the range 4.7 - 5.3 eV are identified. The application of the compositional criterion for the identification is demonstrated in Fig. 48 for Hg_2 (DANOR et al. 1979) and in Fig. 49 for Na_2 in Xe (WELKER and MARTIN 1979).

The absorption bands of M_2 molecules in RGS fall into two distinct classes: (1) unstructured bands as is the case for the spectra of alkali dimers (Figs. 44, 45) and of Hg_2 (Fig. 46) and (2) structured bands which exhibit well defined vibrational structure, as is the situation for matrix isolated alkaline earth metal diatomic molecules (e.g. MILLER et al. 1977). A typical example is reproduced in Fig. 50 for Ca_2. Characteristic vibrational frequencies are 474 cm^{-1} for Be_2, 190 cm^{-1} for Mg_2, 111 cm^{-1} for Ca_2 and 66 cm^{-1} for Sr_2 all recorded in Ar (MILLER et al. 1979). The nature of the matrix exerts small spectral shifts and small modifications of the vibrational frequency. These general features of the absorption spectra can be rationalized in terms of different potential energy curves for the ground and excited state (Fig. 51). When the ground state is characterized by well defined minima due to valence forces as is the case for alkali diatomic molecules the excited state can be either strongly bound (case (a)) or weakly bound or even repulsive (case (b)). The unstructured spectra of the alkali molecules correspond to case (b). For many cases the ground state potential curves are shallow and only stabilized by weak van der Waals forces, as is the situation for alkali earth atoms and for Hg. Again, the excited state can be either shallow (case (c)) or deep (case (d)). For case (c) a well defined vibrational structure will be exhibited provided that the minima of the two potential curves are not too far displaced, as is the case for the alkaline earth diatomics. On the other hand, when in case (c) the minima of the two curves are well displaced (e.g. for some transitions of Hg_2, Fig. 46) an unstructured peak is observed. For case (d) only an unstructured peak is expected.

5.3 Miniclusters

Molecular aggregates M_n (n = 3 - 5) containing a few metal atoms were recently identified by optical spectroscopy in RGS (SCHULZE et al. 1978, DANOR 1979, WELKER and MARTIN 1979). The identification of these species on the basis of the order of their appearance (OZIN and HUBER 1968) with increasing X is not reliable (WELKER and MARTIN 1979). The compositional criterion for the assignment of absorption peaks (SCHULZE et al.1978, WELKER and MARTIN 1979) and of continuous absorption in a certain energy range (DANOR et al. 1979) to specific M_n clusters is more reliable. The application of this compositional criterion to the identification of Na_3 and of Hg_3 and Hg_{4-5} is presented in Figures 49 and 48, respectively. The list of well identified clusters is rather short.

These include Ag_3 and Ag_4 (SCHULZE et al., 1978), Na_3 (WELKER and MARTIN 1979), Li_{3-4} (WELKER and MARTIN 1979), Hg_3 and Hg_{4-5} (DANOR et al. 1979). In all cases broad bands devoid of any vibrational structure are observed.

The understanding of the electronic excitation of such miniclusters provides an interesting problem in the area of molecular physics. Semiemperical calculations of energy levels and optical excitation energies of such clusters (WALKER and MARTIN 1979) provide general correlations for the rationalization of the experimental data. For a qualitative discussion of the general features of such molecular clusters we would like to point out that matrix isolation is expected to give a variety of isomers for any given M_n molecular cluster with a fixed value of $n > 2$. Consider for example the M_3 molecule. It is apparent that the ground state energy, the ionization potential and the excitation energies of the triangular and of the linear M_3 species are different. Since energetically metastable molecules can be trapped in the RGS, we expect a distribution of excitation energies due to different isomers for each size n of the minicluster. Consequently, one cannot just inquire what are the trends of the excitation energy of miniclusters M_n with increasing the size of the metallic molecule without specifying the structure of the clusters. For example, for chains M_n of M atoms, the lowest excitation energy decreases monotonically with increasing n. On the other hand, the lowest excitation energy for a two dimensional structure of a given M_n molecule is in general higher than that for the corresponding linear chain of the same n. These considerations stress the importance of the coordination number in determining the electronic excitations for these molecular miniclusters. With increasing the cluster size the average coordination number is crucial in determining the "transition" from molecular properties to solid-state characteristics which can correspond to those of metallic microclusters or to statistical clustering.

5.4 Microclusters and statistical clustering

When the concentration is increased beyond a few ppm clustering of the metal atoms is expected. In the following discussion microscopically inhomogeneous and microscopically homogeneous systems have to be considered separately.

In microscopically inhomogeneous metal RGS (nonstatistical clustering) the material consists of islands of metal atoms embedded in the insulator. For the "transition" from molecular properties of a minicluster (see below) to metallic properties of the islands, two conditions have to be satisfied (KUBO 1962): Firstly, the size of the metallic regions has to be sufficiently large so that the level spacing of the highly-filled states is small relative to the thermal energy. The particles are locally metallic. Secondly, the correlation length for the metallic regions has to be large relative to the mean free path (or the coherence length) of the conduction electrons in such metallic regions. This situation is analogous to granular mixtures of small metallic particles in insulators (ABELES 1975). As long as the metallic particles are mutually isolated, that is when the concentration is below the percolation threshold (SHANTE and KIRKPATRICK 1971) then the material is an insulator.

A striking characteristic of the optical properties of small metallic particles dispersed in an insulator is the appearance of Mie resonances (MIE 1904, MAXWELL-GARNETT 1906, COHEN et al. 1973, GITTELMAN and ABELES 1977, WEBMAN et al. 1977). At low values of the volume fraction of the metal a Mie resonance is expected at the energy E_{MI} which satisfies the relationship

$$\varepsilon_1^{M}(E_{MI}) = -2\varepsilon_1^{o}(E_{MI}) \qquad (5.2)$$

where ε_1^{M} and ε_1^{o} correspond to the real part of the dielectric functions for the metal and for the insulator, respectively. At higher metal concentrations the Maxwell-Garnett theory (1906) or the effective medium theory (WEBMAN et al. 1977) can be applied. The Mie resonance exhibits only a weak concentration dependence below the percolation threshold. Thus it indicates selective clustering of the metal atoms. An example has been discussed by WELKER and MARTIN (1979) for Ag in Ar (Fig.52). The observed broad Mie resonance bears a close analogy to Mie resonances of granular mixtures of silver particles in Al_2O_3 (COHEN et al. 1973, ABELES et al. 1975).

In microscopically homogeneous metal RGS the metal atoms are statistically clustered. A diagnostic criterion for microscopically homogeneous materials is the lack of Mie resonances in the optical spectra. The average size of the metal clusters in homogeneous materials can be estimated from percolation theory (SHANTE and KIRKPATRICK 1971). The average cluster size is $S = (1-p/p^{*})^{-(j+1)}$ where $j = 11/16$ for a three-dimensional system, p is the fractional site

occupation probability and p^{*} is the percolation threshold. For an amorphous system containing two types of atoms of different size, e.g. a metal and rare gas, it was proposed (DANOR et al. 1979, CHESHNOVSKY 1979) that one can replace (p/p^{*}) by (C/C^{*}) where C is the atomic volume fraction of M while $C^{*} \approx 0.15$ corresponds to the continuous percolation threshold (ZALLEN and SCHEN 1971, WEBMAN et al. 1976). For the Hg/Xe system where a Mie resonance is not observed (CHESHNOVSKY et al. 1979), DANOR et al. (1979) estimated that $S \approx 3 - 4$ at $X \approx 0.4$ while S diverges at the percolation threshold at $X \approx 0.7$. Thus, statistical clustering results in rather small cluster size up to reasonably high $X \approx 0.4$ metal concentration.

DANOR et al. (1979) have assigned the low energy absorption tails of Hg statistical clusters in Xe to charge-transfer excitations within a single cluster. This assignment is of considerable interest as these charge transfer states are analogous to Wannier type states in a large cluster, which will converge to the bootom of the conduction band. When the size of the Hg_n cluster will increase further in the concentration range $X > 0.4$ the excitation energy will be reduced by the gradual increase of the coordination number increasing the charge exchange stabilization energy. Large three-dimensional Hg_n clusters will be characterized by low energy absorption tails which will be then classified as valence-band to conduction-band transitions in the amorphous Hg/Xe material. The charge transfer states in small Hg_n miniclusters are the molecular precursor to the interband optical transition in amorphous semiconductors consisting of a highly doped metal - RGS (DANOR et al. 1979). Thus, microscopically homogeneous metal RGS systems bridge the gap between the molecular description of localized clusters and the band structure model applied to amorphous semiconductors.

5.5 Metal-Nonmetal Transitions in Metal RGS

Metal RGS mixtures undergo a metal-nonmetal transition (MNMT) (MOTT 1974) with increase of the metal concentration. At low metal concentrations the material is an insulator while at high metal concentrations the metal - RGS is an amorphous disordered metal. The metallic state is characterized by a high finite d.c. electrical conductivity in the zero temperature limit. The variation of the electrical transport properties of typical metal - RGS mixtures with changing the metal concentration is demonstrated in Figures 53 and 54. This transition from zero conductivity at low X to metallic conductivity at high X is referred to as the MNMT (MOTT 1974). A complementary and equivalent

description is that metal RGS mixtures are "expanded metals" which, by decreasing X can be continuously expanded from normal, metallic density to very low metal densities, and which undergo a MNMT. The list of such "expanded metals" that have been experimentally studied involves Na (CATE et al. 1970, McNEAL and GOLDMAN 1977), Cs, Rb (PHELPS et al. 1975, PHELPS and FLYNN 1976), Cu (ENDO et al. 1973, HUNDERI and RYDBERG 1975, RYDBERG and HUNDERI 1977), Ga (RYDBERG and HUNDERI 1977), Pb (EATAH et al. 1975) HILDER and CUSAK 1977, QUINN and WRIGHT 1977), Co (QUINN and WRIGHT 1977), In (HILDER and CUSAK 1977), Fe (SHANFIELD et al. 1975) and Hg (RAZ et al. 1972, CHESHNOVSKY et al. 1977, 1979, DANOR et al. 1979). Usually the conductivity has been measured.

The variation of the electrical conductivity σ, with the metal atomic fraction X, falls into two categories:

(1) The abrupt conductivity transition is characterized by a sudden drop of σ at a certain value of X, where $d\sigma/dX$ is discontinuous. The experimental evidence for such an abrupt transition in disordered materials reported for Cu/Ar (ENDO et al. 1973) and for Pb/Ar (Fig. 53) (EATAH et al. 1975) is not conclusive. It may originate from spurious crystallization effects (MOTT 1978).

(2) The continuous conductivity transition is characterized by a gradual decrease of σ with decreasing X. A typical example is presented in Fig. 54. Such a behavior was observed for a variety of systems, e.g. Na/Ar (McNEAL and GOLDMAN 1977), Cs/Xe (PHELPS et al., 1975), Rb/Kr (PHELPS et al., 1975), Hg/Xe (CHESHNOVSKY et al., 1977) and Fe/Xe (SHANFIELD et al., 1975). In general, the conductivity transition was found at $X \approx 0.2 - 0.6$ for monovalent metals and at $X \approx 0.4 - 0.8$ for polyvalent metals. Figure 55 provides an overview of the composition characterizing the conductivity transition in a variety of such materials.

Can the conductivity transition in low temperature metal RGS mixtures be identified with the MNMT? CHESHNOVSKY et al. (1979) have argued that the conductivity transition in metal RGS mixtures cannot be identified in general with the MNMT, as contribution from thermally activated hopping and hopping between large radius localized states cannot be disregarded even at low temperatures. For a meaningful interpretation it is necessary to distinguish again between microscopic inhomogeneous and microscopically homogeneous materials.

The MNMT in inhomogeneous materials containing randomly dispersed finite volumes of conducting materials can be adequately accounted for in terms of classical percolation theory (SHANTE and KIRKPATRICK 1971, KIRKPATRICK 1972, COHEN and JORTNER 1974, COHEN et al. 1979). Classical percolation theory is valid, provided that the correlation length for local clustering exceeds the mean free path of the conduction electrons. In the case of mixtures of conducting and insulating particles, there is a critical concentration of metal above which there is a finite probability for the creation of a conducting path through the sample. This concentration depends only on the topology of the system and marks the MNMT in classical systems. The critical concentration occurs at a metallic volume fraction C, denoted C^*, which is referred to as the percolation threshold. For continuous percolation (ZALLEN and SCHEN 1971, WEBMAN et al., 1976) $C^* \approx 0.15 \pm 0.02$. The d.c. conductivity in the vicinity of C^* is expected to be (KIRKPATRICK 1971)

$$\sigma = 0 \qquad \text{for } C < C^* \tag{5.3}$$

$$\sigma \propto (C - C^*)^p \quad \text{for } C > C^* \tag{5.4}$$

with $p \approx 1.6$. The applicability of the percolation theory for the MNMT requires that the power law (eq. 5.4) is fullfilled. It is plausible on the basis of the optical data (Fig. 52) that the electronic structure, the transport and the nature of the MNMT in Ag/Ar mixtures correspond to a granular metal and can be handled in terms of classical percolation theory.

In this case one should be aware of the disappointing fact that there is no unique mechanism for the MNMT. Notable mechanisms proposed to account for the occurrence of the MNMT (MOTT 1974, FRIEDMAN and TUNSTALL 1978) are the (i) MNMT due to band overlap (WILSON 1931), (ii) MNMT due to electron-electron interaction resulting in short range screening (MOTT 1979), (iii) MNMT due to localization in a disordered material (ANDERSON 1958). In real life, several of these mechanisms combine to induce the MNMT in a particular disordered material. As mentioned above, all the available reliable data show a continuous conductivity transition for metal RGS. Therefore, it is important to outline supplementary experimental evidence for the characterization of the MNMT in metal RGS which are believed, on the basis of admittedly indirect optical evidence, to be microscopically homogeneous:

(A) Screening of Wannier exciton states of the insulator. RAZ et al. (1972) reported that the Wannier excitons of Xe prepared at 40 K in Hg/Xe mixtures (Fig. 56) are smeared out at some high value of $X \simeq 0.55 - 0.60$ indicating the onset of short range screening and thus marking an MNMT. The high deposition temperature raises some serious questions concerning the structure of this material and quantitative conclusion cannot be drawn. On the other hand, this screening effect was not observed in Rb/Kr and in Cs/Xe (PHELPS et al., 1975, PHELPS and FLYNN, 1976) where peaceful existence of Wannier excitons of the rare gas atoms was observed at metal concentrations far aobve the MNMT (Fig. 57). One way out of this contradictory and mutually inconsistent data is to propose that while the Hg/Xe system is microscopically homogeneous, the Rb/Kr and the Cs/Xe samples are microscopically inhomogeneous. However, more work is required to resolve these problems.

(B) Vanishing of the temperature coefficient of the electrical conductivity. The temperature coefficient for the Hg/Xe system (Fig. 54) vanishes at $X_M = 0.79 \pm 0.02$ (CHESHNOVSKY et al., 1977) a concentration high above the onset $X_M = 0.69 \pm 0.02$ of the conductivity transition in this material. Thus, in the composition range $X = 0.69 - 0.79$ d.c. conductivity by thermally activated hopping is exhibited in Hg/Xe at 6 K (CHESHNOVSKY et al., 1977, 1979). The onset of temperature independent conductivity at $X_M = 0.79$ marks the MNMT.

(C) Optical data. The optical data for the Hg/Xe system in the visible and near UV (Fig. 58 and 59) (CHESNOVSKY et al. 1979, 1980) show the features of an amorphous semiconductor, i.e. positive ε, and vanishing low-frequency optical conductivity, at low ($X < 0.70$) and the characteristics of a metallic system at high ($X > 0.83$) concentrations. In particular, the real part of the dielectric function at the lowest energy measured (Fig. 58) exhibits an abrupt discontinuity at $X_M = 0.80 \pm 0.02$ which marks (CHESHNOVSKY et al., 1980) the MNMT, and which is in perfect agreement with the analysis of the temperature coefficient of the conductivity (CHESHNOVSKY et al., 1979).

CHESHNOVSKY et al. (1977, 1979) have proposed that in microscopically homogeneous materials, such as Hg/Xe, the continuous conductivity transition should be interpreted in terms of the Mott-Anderson transition (MOTT 1974) intermediated by low-temperature thermally-activated hopping between large

radius localized states. A different point of view was advanced by PHELPS, AVCI and FLYNN (1975) who proposed for the onset of conductivity a description in terms of a classical percolation theory. This proposal is incompatible with the observation of activated conductivity in Hg/Xe and with the optical properties in the vicinity of the conductivity transition (CHESHNOVSKY et al., 1977, 1979). Recently, CHESHNOVSKY et al. (1980) have attempted to provide a uniform picture for the MNMT in microscopically inhomogeneous metal RGS mixtures. They suggested that with increasing X the topological percolation threshold marks the onset of activated transport corresponding to the conductivity transition while for $X \simeq X_M$ the electronic states become extended. Obviously, more experimental and theoretical work for the characterization of the MNMT transition associated with a continuous conductivity transition is required.

Finally, we would like to speculate on the possibility of observing a discontinuous MNMT in metal RGS. From all the mechanisms proposed for the MNMT only the Mott transition (MOTT 1974) can result in a discontinuous MNMT in a disordered material. It would be very important to test further the discontinuous conductivity transition from the experimental point of view (MOTT 1978).

6. Excited State Dynamics

Up to this point we have been concerned with the electronic structure in pure and doped condensed rare gases. We shall now proceed to discuss dynamic processes in electronically excited states of RGS, alloys, and liquid rare gases. The electronic structure provides the essential input data which serves now as the starting point for the discussion of excited-state dynamics. Optical excitation of an electron in an insulator results in two general effects: (A) The system is produced in a nonequilibrium nuclear configuration so that the balance of interatomic (or intermolecular) interactions is destroyed. (B) The electronically excited state is degenerate with electronic-nuclear excitations (e.g. phonons) of lower electronic configurations including the electronic ground state.

The first effect leads to two important consequences: (A1) Intrastate spectroscopic implications. Simultaneous excitation of electronic and nuclear states, or more generally, simultaneous excitation of various kinds of elementary excitations, e.g. excitons and phonons in a pure solid or a localized electronic state and phonons in an impurity center.
(A2) Intrastate dynamic implications. The medium produced in a nonequilibrium configuration relaxes to a new nuclear equilibrium configuration. Typical examples involve modulation of exciton motion by phonons, exciton trapping in pure solids, lattice relaxation around an electronically excited impurity state and medium relaxation around an electronic excitation in a liquid. These occur within a single electronically excited configuration of excitonic or impurity type and are thus referred to as intrastate dynamic processes.

The central implications of effect (B) are:
(B1) Interstate dynamic implications. Electronic relaxation processes can occur between different electronic configurations. These processes include diverse phenomena which in the order of decreasing energy are:

a) Slowing down of free electrons by electron-electron and electron phonon scattering (Section 7).
b) Autoionization of metastable excitons located above the interband threshold (PHILIPS 1964, JORTNER 1966).
c) Thermal ionization of exciton and impurity states (KUBO and TOYOZAWA, 1955).

d) Electron-hole recombination (KUBO and TOYOZAWA, 1955)
e) Electronic relaxation of exciton and impurity states into lower electronic configurations (JORTNER 1974)
f) Electronic energy transfer between free and localized exciton and impurity states (FÖRSTER 1948, DEXTER 1952, KNOX 1965).

All these interstate relaxation processes between two electronic configurations involve the dissipation of electronic energy into phonon energy.

The relaxation processes can be interrogated by time-resolved measurements, quantum yield studies and for ultrafast (psec or shorter) processes by the uncertainty broadening of spectral lines. Usually, the physical situation is complicated and several elementary relaxation processes occur simultaneously (Fig. 60). Obviously, the basic concepts are interrelated but different for excitons in pure RGS and for impurity states. The problem of exciton-phonon coupling in the pure solid requires in principle a "global" starting point for the description of the electronic states while intrastate medium relaxation around an impurity center in a solid or in a liquid will start from a "local" description. It is still an open question whether intrastate relaxation in a liquid requires a "global" or a "local" description. Starting with intrastate relaxation we shall discuss exciton trapping in pure RGS and then proceed to phonon relaxation in impurity centers in solids and in liquids. Subsequently, interstate processes involving electronic relaxation for localized impurity states and energy transfer between either free or localized exciton states in pure crystals and in localized impurity states will be discussed.

6.1 Modulation of Exciton Motion by Phonons

Following TOYOZAWA (1957, 1959, 1974, KOTANI and TOYOZAWA 1979), we shall consider the implications of exciton-phonon coupling on the nature of exciton states formed by optical excitation in a pure solid. The nth exciton band is described in the tight binding model by the states $|nk\rangle$, the dispersion curve $E_n(k)$ and bandwidth 2B (Fig. 61). Phonon coupling effects are introduced by lattice distortions from equilibrium at each lattice site R_j, the coupling between nuclear and electronic motion being $V = \sum_j V_j = \sum_j \gamma Q_j$, with Q_j being the nuclear coordinate at site R_j while γ determines the local

nuclear distortion upon excitation so that the lattice nuclear relaxation energy is $E_{LR} = \gamma^2/2$. Exciton scattering is determined by the matrix element

$$V_{kk'} = \frac{1}{N} \sum_j \exp\{i(k-k') R_j\} V_j \qquad (6.1)$$

The thermal average of the coupling $\langle V_{kk'} \rangle_T = 0$ for a harmonic lattice. As the average value of the coupling vanished, what is required is the square of the exciton-phonon coupling strength which, by neglecting correlations between different lattice sites, is: $|V_{kk'}|^2 = V_j^2 = \gamma^2 Q_j^2$ and its thermal average, D^2, for a harmonic lattice being

$$D^2 \equiv \langle |V_{kk'}|^2 \rangle_T = 2E_{LR} (\hbar\langle\omega\rangle/2); \quad k_B T << \hbar\langle\omega\rangle \qquad (6.2)$$

$$= 2E_{LR} k_B T; \quad k_B T >> \hbar\langle\omega\rangle$$

where $\langle\omega\rangle$ is the characteristic phonon frequency. D represents the statistical dispersion of the energies of the electronic excitation due to nuclear motion. It is a measure of the thermal fluctuations which damp the band motion of the exciton according to free exciton band in k-space. One can now express the exciton-scattering time τ_k and the linewidth Γ_k in terms of perturbation theory taking an average value for the exciton density of states

$$\frac{\Gamma_k}{2\hbar} = \frac{1}{\tau_k} \approx \frac{2\pi}{\hbar} \frac{D^2}{B} \qquad (6.3)$$

The parameters D and B reflect the local and the band nature of the exciton, respectively. One can distinguish two limiting situations: (1) strong scattering D >> B, when the rate of excitation transfer is slow relative to thermal fluctuations. The modulation of the exciton motion is so extreme that the exciton is essentially localized. (2) Weak scattering D<< B. The exciton stays on a given lattice site only a small fraction of the time required to switch on the nuclear fluctuation, so that the effect of nuclear motion is smeared out.

The local or the band character is reflected in the exciton absorption line shape. In the weak scattering limit the absorption lineshape L(E) for the k = 0 optically accessible exciton at photon energy E is quasi Lorentzian

$$L(E) = \frac{(\hbar/2\pi)\,\tau_0}{(E - E_n(0) - \Delta_0)^2 + (\hbar/2\,\tau_0)^2} \qquad (6.4)$$

where Δ_0 is a level shift and τ_0 is the scattering lifetime of the k = 0 excitation. The linewidth (eq. 6.3, 6.4) exhibits a linear temperature dependence at high T. As pointed out by TOYOZAWA (1956) interesting complications arise when the k = 0 state is located at the bottom of the lowest exciton band with no density of states below it. Under these circumstances eq. 6.3, which was derived for an average density of final states, is inapplicable. Rather, the lineshape is a distorted Lorentzian, the linewidth being now proportional to D^4/B^3 exhibiting at high temperatures a T^2 temperature dependence. In the second extreme case, the strong scattering situation, the lineshape is Gaussian

$$L(E) = \frac{1}{\sqrt{2\pi D^2}} \exp.\ \{-(E - E(0))^2/2D^2\} \qquad (6.5)$$

corresponding essentially to a state localized by phonons. The linewidth is determined by the phonon fluctuation D which at sufficiently high temperatures is proportional to $\sqrt{T}$.

Three diagnostic criteria are applicable to assess whether an excitonic absorption corresponds to the weak scattering limit or to the strong scattering situation. (1) One can examine the relation between B and D. (2) The exciton absorption lineshapes can be analyzed. (3) The temperature dependence of the linewidth is relevant. Regarding pure RGS it should be pointed out that at present the available experimental data are inadequate for the application of criterion (3) and difficult to evaluate regarding (2) as the details of the best available spectra (section 3) for Xe, Ar, Kr and Ne are obscured by surface excitons and by the appearance of longitudinal excitons as well as by the overlap between the $^3P_1$ and $^1P_1$ components for Ne and Ar. Concerning criterion (1) we have to rely on rough order of magnitude estimates. The exciton bandwidths in k-space for the lowest optically accessible n = 1 exciton in RGS vary from 2B = 0.9 eV for Xe to 0.4 eV for Ne (e.g. FUGOL 1978). From the estimates of the lattice relaxation energy due to two-center localization of the diatomic molecule (see Section 6.2) which constitute an upper limit to E_{LR} one can infer from eq. 6.2 that at 50 K, D ≈ 0.4 eV for Ne and D ≈ 0.07 eV for Xe. Thus for Xe, D << B corresponding to the weak scattering limit while for Ne D ≈ B, still on the verge of weak scattering. The experimental absorption spectra for n = 1 excitons in Ar, Kr and Xe reveal a linewidth (FWHM) of 80 meV (SAILE et al. 1977) while for the n = 1 exciton in Ne the linewidth is 200 meV (SAILE and KOCH, 1979). The increase of the linewidth for Ne reflects presumably the

transition from the weak scattering limit in Ar, Kr and Xe towards the strong scattering situation. No evidence for asymmetry of the lineshapes of RGS towards lower energies was observed while TOYOZAWA's theory (1957) for excitation to k = 0 of the lowest exciton band would imply such asymmetry. It should be noted that the n = 1 exciton band having parentage in the $^3P_1$ atomic excitation is not necessarily the lowest exciton state, as the exciton band originating from the $^3P_2$ state may be located below the $^3P_1$ band (KNOX 1963). Interband exciton scattering from the optically accessible $^3P_1$ band to the lower $^3P_2$ band will result in symmetric line broadening and, provided that the weak scattering limit holds, the lineshape will be Lorentzian and proportional to T. We note in passing that in systems where this interband scattering is dominant, the polariton effects proposed recently by KINK and SELG (1980) will not be important.

The local effects which may destroy the band character of the exciton are not restricted to the case of thermal fluctuations. Disorder scattering effects due to either substitutional or positional disorder play a similar role in introducing local effects. These considerations are important for the electronic states of a pure liquid where disorder results in a static spread D_s of the site excitation energy. Provided that $D_S > B$ the electronic excitation is localized. For liquid Xe the linewidth (FWHM) of the n = 1 exciton is ~0.3 eV which provides a rough measure of D_s. We expect the exciton bandwidth in the liquid to be lower than in the solid so that $B < 0.45$ eV. Accordingly $D_s \geq B$ for liquid Xe. Thus, in the liquid the electronic excitation may well belong to the strong scattering situation.

6.2 Selftrapping of Excitons

From the discussion of the optical excitation of an exciton coupled to lattice vibrations, we now proceed to consider the subsequent fate of the exciton. The basic question in this context is whether the exciton will be free or localized. In the strong scattering limit the exciton is localized. On the other hand, the condition $D < B$ for weak scattering is not sufficient to insure that the exciton will remain free on the time scale of its radiative decay (TOYOZAWA 1974). This is apparent as exciton localization lowers the lattice energy by E_{LR} due to nuclear distortions while the energy gain due to exciton motion is B.

Thus the nature of the final relaxed state of the lattice depends on the relative magnitudes of B and E_{LR}; the free state is energetically stable when $B \gg E_{LR}$ while a localized state is formed when $B \ll E_{LR}$ (TOYOZAWA 1969, RASHBA 1976). Exciton dynamics in RGS is of considerable interest here, because long range coupling effects, for example, due to polar modes, are absent. In RGS short range coupling with acoustic phonons prevails. For a system characterized by such a short range interaction, which can be described in terms of a deformation potential, TOYOZAWA (1974) and RASHBA (1976) predicted a discontinuous transition from the free to the localized state when $B \sim E_{LR}$. The localization process due to lattice distortion can be visionalized as splitting off a bound state from the exciton band for a finite value of the lattice distortion (Fig. 61). When E_{LR} is sufficiently large, the localized state will be characterized by a minimum on the adiabatic potential surface which is separated from the free exciton state by a potential barrier. TOYOZAWA and RASHBA (1976) have described selftrapping in terms of an isotropic continuum model where the lattice distoriton corresponds to an elastic dilation. The energy of the electronic excitation is

$$E(\alpha) = B\alpha^2 - E_{LR}\,\alpha^3 \qquad (6.6)$$

where the lattice relaxation energy is $E_{LR} = E_d^2/2Cr_k^3$ with E_d being the deformation potential while C_l is the elastic constant r_k the nearest neighbor distance, and $0 \leq \alpha \leq 1$ represents the orbital exponent of a trial Gaussian electronic wavefunction. $\alpha = 0$ denotes an extended state, while $\alpha = 1$ corresponds to a localized state. The first term in eq. 6.6 accounts for the increase of the kinetic energy with localization while the second term provides a stabilization energy due to dilation of the elastic medium. Although a true minimum of $E(\alpha)$ is not exhibited for $\alpha > 0$, it is obvious from eq. 6.6 that $E(1) < E(0)$ for $E_{LR} > B$. As the continuum approximation breaks down at $\alpha = 1$, an energetically stable localized state with $\alpha = 1$ is formed. The free and the localized states are separated by a maximum of a height

$$H_m = 4B^3/27\,E_{LR}^2 \qquad (6.7)$$

According to this continuum model two conditions have to be satisfied for the observation of selftrapping in a solid. First, $E_{LR} \approx B$ is necessary. Second, dynamic conditions have to be fulfilled which imply that the barrier height (eq. 6.7) is comparable to the Debye phonon frequency $H_m \leq \hbar\omega_D$, so

that nuclear tunnelling from the free state to the localized state is feasible. On the other hand, when $H_m > \hbar\omega_D$ and $H_m > k_BT$, the barrier cannot be overcome and the free state is expected to be stable.

Up to this point the general question of selftrapping was explored on the basis of a continuum model which does not incorporate any details of the microscopic structure. Two stable configurations of the localized state are of particular interest (Fig. 62): (1) The one-center atomic trapped exciton. Here the nearest neighbors displace symmetrically around the excitation. (2) The two-center trapped excitation. Here two neighboring atoms displace axially to trap the excitation.

The question whether the one-center or the two-center trapping is favored should be settled on the basis of energetic and dynamic criteria. Exciton trapping bears a close analogy to hole trapping in alkali halides resulting in the V_k center formation (e.g. DAS et al. 1964, SONG 1968). The starting point for a microscopic model is to express the total energy $E_t(Q)$ of the solid as

$$E_t(Q) = E_e + I(Q) + E_L(Q) \qquad (6.8)$$

where E_e is the electronic energy of the free exciton state, $I(Q)$ is the interaction between the exciton and the lattice displacements, while $E_L(Q)$ is the lattice energy. The potential energy depends parametrically on the lattice coordinates Q. Two lines of attack are now feasible. (i) Excitonic model for one-center and for two-center trapping (SONG 1968). The exciton lattice coupling is expressed in terms of two contributions, the change in the diagonal site energies, U', and the change of the off-diagonal pair interactions V' with lattice displacements. The lattice energy is calculated in the harmonic approximation. It was demonstrated by SONG (1968) that large diagonal deformation energies U' result in one center trapping while large off-diagonal deformation energies V' give two center trapping (Fig. 62). (ii) Molecular model for two-center trapping (DAS et al., 1964). It can be argued that two center localization results in the formation of an ordinary excited diatomic molecule. This point of view is in particular pertinent for RGS where this diatomic homonuclear excited state reveals very similar characteristics to those of the gas phase excimer (JORTNER 1974). One can

then attempt to start from a local approach expressing the electron-lattice coupling I (Q) in terms of the molecular potential curve of the "isolated" diatomic molecule, while the lattice deformation energy $E_L(Q)$ can be calculated along conventional lines provided that potential parameters are available. This approach which disregards part of the excitonic effects, is also applicable to liquids and to impurity pairs.

The two models are not mutually exclusive but rather complementary. A reliable calculation of the exciton localization energy was not yet performed. It should be noted that eq. 6.8 provides the microscopic analogue of the continuum approximation (eq. 6.6). In principle, eq. 6.8 gives the potential surface for free, one-center and two-center localized excitations and the nature of the potential barriers separating these states. Eq. 6.8 can be minimized with respect to nuclear displacements and should provide three energies $E_t(0)$ corresponding to the free state $E_t(Q_1)$ for the minimum of the one-center localized state and $E_t(Q_2)$ for the minimum of the two-center localized exciton. The energetic criterion for localization is $E_t(Q_1)$ and/or $E_t(Q_2) < E_t(Q_1)$ and $E_t(Q_2)$. The dynamic criterion for localization stems from the existence of barriers and considerations of tunnelling probability.

The predominance of the molecular characteristics of the trapped two-center exciton in RGS (JORTNER 1974) strongly suggests but does not prove that the molecular approach to the problem of trapping in these materials should provide a feasible starting point. FUGOL and TARASOVA (1977), FUGOL (1978) have considered the energetic stability of trapped excitons in RGS (see Fig. 63). For two-center trapping they have estimated E_{LR} from the experimental potential surfaces of the diatomic rare gas molecule. The results of their analysis are summarized in Table II. From these estimates they conclude that the two-center trapped exciton, i.e. the diatomic excimer is energetically stable with respect to the free state in all RGS. They have also estimated E_{LR} for one-center trapping. These estimates (Table II) reveal that E_{LR} (one center) > E_{LR} (two center) for all RGS so that according to the energy criterion the two-center state is favored. To assess the dynamic criterion, FUGOL and TARASOWA (1977) utilized a hybrid of the isotropic continuum model (eq. 6.6) together with the molecular estimates of E_{LR} to derive the barrier humps H_m (Table II). These data predict that the barrier height for two-center and one-center localization in Ne and Ar is sufficiently low. In Xe the one-center localized state is energetically instable and the barrier height is

large for two-center localization so that the free state should be observed. These predictions should be considered as preliminary since no estimates of the tunnelling effects are currently available. Solid Xe may provide an interesting example for a system where tunnelling between free and localized exciton states occurs.

6.3 Maxima in the molecular potential curves

The existence of potential barriers in the total potential energy of an excited solid undergoing structural deformation has been described within the continuum theory for exciton localization (see Section 6.2). Starting from the molecular point of view for two-center excitation trapping one should incorporate the molecular potential curve in I(Q) (eq. 6.8). The potential curves for the lowest states of some of these free diatomic excimer rare gas molecules exhibit barriers (MULLIKEN 1964).

These barriers are very pronoucned for the lighter rare gases He_2^* (e.g. GUBERMAN and GODDARD, 1975) and Ne_2^* (e.g. COHEN and SCHNEIDER, 1974). They appear also in some branches of potential curves of heavy rare gases. The origin of these maxima is the Pauli exclusion principle and has to be well distinguished from the solid state effects in Fig. 63. Nevertheless, these maxima have a similar retarding effect for the formation of excimer centers. Thus it is apparent that the molecular potential curves provide some indispensible ingredients which must be incorporated in a complete theory (see the case of solid Ne discussed in Section 6.5).

6.4 Vibrational relaxation in excimer centers

The isotropic continuum theory (RASHBA 1976, TOYOZAWA 1974) implies that the only dynamic restriction for the formation of the diatomic species involves tunnelling over the potential barrier. The hidden assumption involved in this description is that vibrational relaxation of the two center trapped excitation is extremely fast on the time scale of radiative decay, so that once the barrier is overcome the system instantaneously slides down to form the final relaxed diatomic molecule. This vibrational relaxation process essentially corresponds to molecular vibrational relaxation of a diatomic molecule in a RGS (JORTNER 1974). It is now known that vibrational

relaxation of a guest diatomic molecule in a solid can be surprisingly slow (NITZAN et al. 1973). The vibrational relaxation rate is determined by the energy gap $\Delta E_v = (E_n - E_{n-1})$ between adjacent vibrational states. This interconversion of vibrational energy of the diatomic molecule to lattice phonons ($\hbar\omega_p$) is a multiphonon process of order $N = \Delta E_v/\hbar\omega_p$. The zero temperature rate $\gamma_v(0)$ follows the energy gap law

$$\gamma_v(0) = A\exp(-\delta N) \qquad (6.9)$$

where $A \simeq 10^{12}$ sec^{-1} is a coupling constant (JORTNER 1976) and δ a numerical factor of the order of unity. The rate decreases exponentially with N, therefore high order multiphonon processes are expected to be slow. The exponential dependence of the rate on the energy gap implies that the vibrational relaxation rate can decrease by a few orders of magnitude by going from higher to lower vibrational energy levels of the diatomic molecule. These general considerations imply that vibrational relaxation within the diatomic center in Xe, Kr and Ar where the vibrational frequency is low and N small will be fast while for Ne the high order multiphonon vibrational relaxation will be seriously retarded.

6.5 Localization of excitons and vibrational relaxation in solid Ne, Ar, Kr and Xe

Generally, two types of luminescence emission bands are observed in RGS: strong broad bands with a large Stokes shift (1 - 2 eV) and weak sharp bands with some fine structure and much smaller (< 1 eV) Stokes shifts relative to the first exciton absorption band. First we shall discuss the prominent emission bands. In Xe, Kr and Ar most of the luminescence intensity is emitted in broad luminescence bands of nearly Gaussian shape (JORTNER et al., 1964). These bands have been observed in all investigations and a typical set of spectra is shown in Fig. 64. The energies are compiled in Table 12. These luminescence bands are assigned (JORTNER et al., 1965) to emission from vibrationally relaxed electronically excited homonuclear diatomic rare gas molecules which correspond to the trapped two center excitations. Although the prominent molecular character of these bands in solid Ar, Kr and Xe is well established, several complicated features are exhibited in the solid state experimental data. First, trivial complications arise due to

inhomogeneous broadening of the emission due to statistical distribution of trapping sites which cause different spectral shifts. A careful analysis by HEUMÜLLER (1978) of the position and shape of these bands for different temperatures as well as preparation and annealing conditions showed that in most cases these bands are inhomogeneously broadened. The shifts of these bands with temperature reported earlier can be ascribed to annealing. Secondly, a nontrivial temperature dependence is exhibited in the emission spectrum of solid Xe which in the temperature range 60 - 130 K exhibits a second prominent emission band peaking at 7.6 eV (Table 12 and Fig. 65). HEUMÜLLER and CREUZBURG (1978) identified four components in the Xe emission band by a deconvolution with Gaussians (Table 12).

Two new techniques were recently introduced to obtain further detailed information regarding the nature of the emitting molecular species in Ar, Kr and Xe. (1) Time-resolved data. In lifetime measurements for the Xe 7.1 eV emission band, a short temperature-independent lifetime of some nsec and a temperature dependent long lifetime in the μsec regime have been reported (HAHN et al., 1977, Figs. 64 and 66). In these experiments, the long lifetime is shortened by surface quenching. At low temperatures KING et al. (1977) measured a lifetime longer than 10 μsec (Fig. 64). For thin films of Kr and Ar a short component and two temperature dependent long components have been observed by HAHN et al. (1980). Further, HAHN et al. (1980) separated the emission bands of Xe, Kr and Ar into two bands with a splitting ranging from 30 meV to 50 meV by recording the emission spectra with (i) a time window of some nsec just covering the time range of the excitation and (ii) with a time delay excluding the short component. The long components are found at lower energies whereas the fast components are at higher energies (Fig. 64). Time resolved data have also been reported by CREUZBURG and VÖLKL (1977), by COLETTI and HANUS (1977) and CARVALHO and KLEIN (1978) and MONAHAN et al. (1977). (2) Transient absorption data. The selftrapped exciton states are not accessible to usual absorption spectroscopy, because of the limitations imposed by the Frank Condon principle. These states have been studied by transient absorption spectroscopy in solid Xe, Kr, Ar and Ne (SUEMOTO et al., 1977, 1978, 1979). In solid Kr and Ar transitions from the lowest excited triplet state $^3\Sigma_u^+$ to several higher excited states have been identified (Table 13). By comparison with the available calculated molecular potential curves, the spectra for Ar and Kr are correlated to transitions from $^3\Sigma_u$ to $^3\Sigma_g$, $^3\Sigma_g'$ and $^3\Pi_g$ (Fig. 67). The transition energies in this Rydberg series of selftrapped excitons have been calculated by SONG and LEWIS (1979). These authors used two methods; an effective mass approximation including corrections

which were used also for free excitons in RGS by HERMANSON (1966) and a pseudopotential approach which has been applied successfully to F centers and selftrapped excitons in alkali halides. The results, collected in Table 13, agree quite well with the experiment. The only optical experiment reported up to date on solid He (SOLEY et al. 1975) used transient absorption to identify the $^3\Sigma_u$ molecular state. These experimental data provide further support for the molecular description of the selftrapped exciton in the heavy RGS as well as in solid He.

Proceeding with the survey of the prominent emission bands of RGS we note that the emission spectra of solid Ne are exceptional (Fig. 68). They are dominated by a relatively narrow emission band peaking at 16.7 eV which is Stokes shifted by 0.7 eV to lower energies relative to the n = 1 ($^3P_{3/2}$) exciton state. This emission originates from a medium relaxed atomic state (PACKARD et al. (1970), GEDANKEN et al. (1973b) which has been assigned to a one-center trapped exciton. The splittings observed (Fig. 68) in some experiments of this "atomic type" emission into several components have beeen correlated to the $^1P_1$, $^3P_1$ and $^3P_0$ splitting in the free atom. In this context, the excitation method is crucial. VUV light and X-rays do not damage the sample and the penetration depth is large enough to excite mainly the volume. Creation of lattice defects by electrons with energies up to 200 eV is also negligible. But the penetration depth is small and contamination and surface effects will become important. The penetration depth is increasing with electron energy, but the sample damage will be more severe at higher energies. High currents can cause a local heating of the sample. α-particles will induce strong lattice defects due to the large mass which is comparable to the mass of the lattice atoms. More detailed studies involving crystal field, spin orbit coupling and Jahn Teller splitting may be necessary. The assignment of the prominent emission of solid Ne is confirmed by transient absorption spectroscopy (SUEMOTO and KANZAKI, 1979) where besides one transition due to molecular type centers, also several transitions due to the atomic-like centers have been observed. The atomic-like transitions start from the lowest atomic state $^3P_2$ ($1s_5$) terminating at the fine structure components of the higher lying p states (Table 13). Further, solid Ne exhibits a medium intensity broad emission (Fig. 68) towards lower energies which is due to unrelaxed molecular emission (SCHUBERT and CREUZBURG 1975, YAKHOT 1975). This assignment is also borne out by transient absorption experiments.

Next, we survey the weak emission bands from RGS. In solid Ar, Kr and Xe the relative intensities of these emissions (bands a, b, c in Fig. 69) are 10^{-2} to 10^{-3} of the major two-center molecular emission band (band d in Fig. 69). The assignment of these weak bands has to consider whether they are indeed intrinsic and whether they are not due to structural disorder, i.e. emission from excitons trapped at imperfections, vacancies etc., or at surface states. The experimental results are still controversial concerning the number of peaks, the energy positions (Table 14) and the relative and overall intensities. Despite these problems there is now a very detailed experimental investigation of the temperature dependence of the narrow line emission available (COLETTI and BONNOT (1978) Fig. 69). In particular, the optical excitation data of KINK and SELG (1980) provide good evidence that the weak 8.3 eV emission for solid Xe is intrinsic.

The following classification of the emission bands of RGS will be introduced in the order of decreasing energy:

a band; Corresponding to the emission from the free exciton state. This emission can be observed in a system where a free exciton state is stable. Further, in a system where the trapped exciton is energetically and dynamically favored, competition between exciton localization (Section 6.2) and radiative decay of the free exciton will be exhibited. The emission quantum yield Y_f for emission from the free exciton state is in this case

$$Y_f = \tau_t/\tau_R \qquad (6.10)$$

where τ_R is the pure radiative lifetime of the free exciton and τ_t the exciton trapping time.

b band; Corresponding to the localized atomic excitation, i.e. the one-center trapped exciton. The emission peak is red shifted relative to the absorption, because in RGS the short range one-center excitonic interaction term (the matrix spectral shift) is repulsive, i.e. U' (see Section 6.2) is negative. The emission line will be phonon broadened.

c band; Due to emission from a vibrationally hot diatomic R_2^* molecule. In this case exciton trapping has occurred by the two-center mechanism forming the vibrationally excited diatomic molecule. However, vibrational relaxation is inefficient or only partially completed on the time scale of radiative decay.

d band; Assigned to the broad prominent Gaussian bands due to emission from vibrationally relaxed diatomic R_2^* homonuclear molecule as discussed already above.

We shall now discuss the emission spectra of each RGS in more detail. In Table 15 we present a synopsis and a tentative assignment of the emission bands for all RGS. Solid Xe exhibits a weak a-band, $Y_f \sim 10^{-3}$, and a dominant d-emission band. The a-band of Xe reveals an interesting temperature dependence (KINK and SELK 1980, COLETTI and BONNOT, 1978) which is similar to that of the free exciton absorption band, providing support for the assignment of this band. In Kr some evidence for weak a, b and c-emission is present ($Y_f \sim 10^{-2}$) together with the dominant d-band, while Ar reveals very weak a ($Y_f \sim 10^{-4}$) and weak b and c bands ($Y_f \sim 10^{-2}$) together with the strong d band. Finally, for Ne emission d is missing and emission b is strong compared with the broad bands c.

For a detailed interpretation of the molecular type emission spectra (band d and c) of vibrationally relaxed and nonrelaxed R_2^* centers, we use input information from gas phase spectra at low and high pressures. The broad band emission d is very similar to the emission observed in the gas phase at high densities. In the gas phase it is well known that excited RG atoms have attracting potential curves and form excimers R_2^*. At high pressure the molecules decay after complete vibrational relaxation by emitting the second continuum (Fig. 70). At low pressure, the collision rate is smaller and emission of only partially vibrationally relaxed excimers is observed (first continuum, Fig. 70) which corresponds to emission c in the solid phase (JORTNER 1974).

The ground state potential curves involved have been discussed already in Chapter 4, Vol. I of this book. Since the first potential curves for Xe_2^* have been estimated by MULLIKEN (1970, 1974), several calculations for R_2^* and R_2^* molecular states have become available. GILBERT and WAHL (1971) treated Ne_2^* and Ar_2^*. WADT (1979) treated the series Ar_2^*, Kr_2^* and Xe_2^*. Ab initio calculations exist for Ne_2^* and Ne_2^* (COHEN and SCHNEIDER, 1974). Potential curves for excited states of Ar_2^* have been calculated by LORENTZ and OLSEN (1972), by GILLEN et al. (1976), by SAXON and LIU (1976) and by SPIEGELMAN and MALRIEU (1978). Furthermore, potential curves have been calculated for Kr_2^* (ABOUAF et al. 1978), Xe_2^* (WADT et al., 1977) and for

Xe_2^* and Xe_2^* (ERMLER et al., 1978). The equilibrium separations and the dissociation energies have been collected in Table 2. Ar_2^* centers in an Ar crystal have been discussed by SONG (1971). In the following Xe will be used as an example, because new potential curves (ERMLER et al., 1978) and detailed additional information concerning the influence of the crystal are available. This is illustrated in the scheme of Fig. 71. The influence of the symmetry of the surrounding crystal on the potential curves causes the additional splitting into Γ_1', Γ_2', Γ_3' and Γ_4' (MOLCHANOV 1970, 1972).

For radiative decay (d-bands) the lowest Rydberg states $^3\Sigma_u^+$ and $^1\Sigma_u^+$ are important. In the region of the equilibrium separation, i.e. in the lower vibrational levels, Hund's coupling case "c" has to be applied and $^3\Sigma_u^+$ splits into 1_u and 0_u^- whereas $^1\Sigma_u^+$ corresponds to 0_u^+ (Fig. 71). Vibrational relaxation and electronic relaxation between the singulet (0_u^+) and triplet branches (0_u^-, 1_u) will take place in the excimer centers. In Fig. 71 (III) the complications arising from the large variety of states are illustrated. For example, the anharmonicity of the potential curves causes for Xe a reduction of the vibrational spacing from 15 meV to 6 meV. The electronic potential curves of the 0_u^+ and the 0_u^-, 1_u states are separated by about 100 meV which leads to a superposition of the vibrational series. Some of the vibrational levels of different electronic states lie close together and transitions between these electronic states will be accelerated according to the energy gap law. Therefore, emission of singulet and triplet states can be expected with lifetimes which span the range from 10^{-5} to 10^{-9}s, similar to the values observed for the free molecules (Table 16). The lifetimes observed in RGS are collected in Table 17.

There is general agreement that the d bands in Ar and Kr and the 7.2 eV band in Xe are due to radiative decay of the lowest vibrational level of the 0_u^-, $1_u(^3\Sigma_u^+)$ and 0_u^+ ($^1\Sigma_u^+$) branches of the molecular centers. There is a controversy, however, whether the fine structure indicated by at least two different decay components and a splitting of 20 - 50 meV (see Fig. 64) is caused by the two states $^3\Sigma_u^+$, $^1\Sigma_u^+$ or by an additional splitting of $^3\Sigma_u^+$ due to the reduction of the symmetry from $D_{\infty h}$ to D_{2h} for the molecule in the solid (see Fig. 71, IV).

The following tentative explanation for the fine structure and temperature dependent lifetimes of the d bands in Ar and Kr and the 7.2 eV band in Xe is consistent with the experimental results and incorporates earlier proposed models. Part IV of the potential curves in Fig. 71 is based on this interpretation. The emission at higher energy (see Fig. 64) and with the nsec lifetimes (Table 17) corresponds to the strongly allowed transition from 0_u^+ ($^1\Sigma_u^+$) to the groundstate (HAHN et al., 1977). In the D_{2h} symmetry of the crystal the 0_u^+ state becomes Γ_3' and remains strongly allowed. The transitions with long decay times (Table 17) and 30 - 50 m eV lower energies are due to the 0_u^-, 1_u ($^3\Sigma_u^+$) states. In the D_{2h} symmetry 0_u^- and 1_u split further into Γ_1', Γ_2', Γ_4' (MOLCHANOV 1972) where transitions from Γ_1' to the groundstate are strongly forbidden and those from Γ_2', Γ_4' are moderately allowed. The two long decay times of Ar and Kr are attributed to the Γ_1', Γ_2' and Γ_4' sublevels. The temperature dependence of the transition rate for Xe is explained by a thermal depopulation of Γ_1' to Γ_2', Γ_4' yielding an energy separation from Γ_1' to the center of Γ_2', Γ_4' of 5 meV in a single phonon model (HAHN et al., 1977) and of 14 meV with a multiphonon model (KINK et al., 1977). The splitting of Γ_4' and Γ_2' is expected to be in the μeV region as in alkali halides where it has not been resolved (e.g. FISCHBACH, et al. 1973).

One unsettled problem regarding the assignment of the d bands is the appearance of the prominent 7.6 eV emission band of solid Xe around 60 K (Fig. 65). The lifetime of this band is 58 nsec (Table 17). Emission from a special site where lattice relaxation around R_2^* is hindered has been proposed by CHESNOVSKY et al. (1973). This assignment is consistent with the observation of the 7.6 eV emission from Xe_2 impurity pairs in solid Ar (CHESNOVSKY et al., 1973), however, it does not explain the temperature dependence. Alternatively, a phase transition similar to the case of Ne has been discussed by TOLKIEHN (1976). A third explanation has been reintroduced recently by MONAHAN et al. (1976) who attribute the 7.6 eV band to emission from selftrapped n = 2 excitons (MOLCHANOV 1972), because the energy difference of these two bands is similar to that of the n = 1 and n = 2 excitons. The weak but proven emission at 7.6 eV, when only n = 1 excitons are excited (Fig. 65c) is not consistent with this latter explanation for which a change from the n = 1 branch to the n = 2 branch during selftrapping would be required. KINK et al. (1977) assigned the 7.6 eV band to the selftrapped n = 1 exciton at an ideal crystal

site, whereas the 7.2 eV band is due to an excitonic state localized at a defect site. HEUMÜLLER and CREUZBURG (1978) attributed the 7.2 eV band to the ^1_u and 0^+_u states and the 7.6 eV band to the next higher electronic states ^2_g and ^1_g (Fig. 71 III). From the temperature dependence of the relative intensities of the 7.2 eV and 7.6 eV bands, a barrier of 60 meV for the g states has been deduced which governs the temperature dependent branching ratio for the g and u levels. This model is inconsistent with the short (58 nsec) lifetime of this band. We are inclined to assign this band to a d type emission, however, the problem described above is not yet solved.

We shall now proceed to discuss the dynamics of exciton trapping attempting to utilize the theoretical description of Sections 6.1 to 6.4 to account for the following observations:

(1) The efficient trapping of excitons by the two center localization mechanism in solid Ar, Kr and Xe where 99% of the excitation results in the formation of diatomic excimers.

(2) The efficient trapping of the electronic excitation in solid Ne by the one-center trapping rather than by two-center trapping.

(3) The appearance of the free exciton emission in Xe and possibly in Ar but not in Ne.

(4) The inefficient vibrational relaxation of the R^*_2 center in solid Ne.

In attempting to confront theory and experiments several discouraging inconsistencies are immediately apparent: Observation (1) and (2) are inconsistent with the theoretical predictions of Table II (FUGOL and TARAZOVA, 1977) which imply that the two center localized state is expected to be energetically stable in solid Ne. Observation (1) may be in quantitative disagreement with the estimate of the barrier height for solid Xe which for reasonable barrier width will result in a high emission yield from the free exciton in an ideal crystal. Therefore, we shall use the localization theory as means for providing only qualitative guidelines for the understanding of the experimental results. Observation (1) implies that the barrier height separating the free and the two center localized states in Ar, Kr and Xe is sufficiently low to allow for effective tunnelling and stabilization of the diatomic molecule, while observation (2) and (3) imply that for Ne the barrier separating free and one center localized states is small or does not exist at all. This last conclusion is

encouraging in relation to localization theory provided that we can give a good argument for the inefficiency of two center localization in favor of one center localization in solid Ne. The retardation of the formation of the Ne^*_2 center in solid Ne may originate from a molecular effect rather than a solid state effect resulting from a hump in the molecular potential curve (Section 63). Humps appear in the Ne^*_2 potential curves calculated by COHEN and SCHNEIDER (1974). These humps appear at internuclear distances of 2 - 4 Å. They may reduce the probability to form molecular centers by crossing the barrier and may force the formation of a cavity. In this way, atomic-like centers are favored and are stabilized by the molecular potential curve in solid Ne. Using COHEN and SCHNEIDER's potential curves, KUNSCH and COLETTI (1979) have calculated the local structure around the cavity and the resulting transition energies (E_1 and E_3 in Fig. 68). For the cavity an increase in the nearest neighbor separation by a factor of 1.37 has been obtained for the first atomic shell surrounding the excited atom. This deformation extends to distant shells and even for the 16th shell a deformation in the nearest neighbor separation by 1 percent has been calculated.

Perhaps the most interesting feature of exciton dynamics in RGS is the appearance of the weak but well defined free exciton band a ($Y_f \sim 10^{-3}$) in solid Xe. The theoretical concepts described in Section 6.2 support the notion that tunnelling through a barrier may occur in this particular system. To obtain an estimate of the exciton localization time we make use of the emission yield $Y_f \sim 10^{-3}$ which, together with the radiative lifetime $\tau_R \sim 5 \times 10^{-9}$, roughly give $\tau_t \sim 5 \times 10^{-12}$. Exciton localization by tunnelling in solid Xe is corroborated by the temperature dependence of the relative yield of the a band (KING and SELG (1980)). Fig. 72 reveals a temperature independent yield at T < 50 K, which reflects nuclear tunnelling effects although the nature of the tunnelling process cannot be assessed from these data. Further confirmation of the a emission in pure solid Xe will be of considerable interest. In order to distinguish between free exciton emission and the radiative decay of an exciton trapped at an imperfection or at a surface, lifetime measurements must be performed. A trapped exciton will decay on a time scale of ns, while the free exciton will decay on a ps time scale.

Finally, we consider the effects of vibrational relaxation in the R_2^* centers (point 4) which is inefficient in solid Ne to the extent that the vibrationally relaxed R_2^* does not form. The intensities of hot luminescence increasing from Kr to Ne reflect the competition between radiative decay times lying roughly in the ns to μs regions for all RGS (Table 17) and the decreasing vibrational relaxation rates for lighter RGS. This result can be explained in terms of the energy gap law for vibrational relaxation (JORTNER 1974) discussed in Section 6.4. Relaxation starts from the high vibronic levels of the R_2^* molecular states. In Table 17, the largest phonon energies $\hbar\omega_p$ are compared with the vibrational quanta ΔE_v for all RGS (SCHWENTNER 1978). The phonon energies are several times smaller than the vibrational quanta and relaxation has to be a multiphonon process. The order $N = \Delta E_v/\hbar\omega_p$ of this process is increasing from 4 in Xe to 6 in Ar. There is a jump to N = 18 in Ne, which retards the vibrational relaxation process of R_2^* (GEDANKEN et al., 1973). The vibrational relaxation of He_2^* should be ineffective and the relative contribution from the c band should decrease in the order Ne >> Ar >> Kr > Xe. YAKHOT et al. (1976) calculated vibrational relaxation of R_2^* in RGS providing a set of relaxation lifetimes which agree with the radiative yields for the c emission in Ar, Kr and Xe. For solid Ne, YAKHOT et al. (1975) using the ab initio potential curves given by COHEN and SCHNEIDER (1974) considered also the influence of anharmonicity on the vibrational relaxation. From the comparison with the radiative lifetimes (Table 17) emission from the 5th to the 3rd vibrational level is predicted. We note however that in the calculation of YAKHOT et al. (1975) the close proximity of the 0_u^-, 1_u and 0_u^+ states with the possibility of relaxation between these states has not been considered.

6.6 Emission from liquid Ne, Ar, Kr, Xe

The striking similarity between the prominent d emission bands in solid Ar, Kr and Xe and the emission of the corresponding molecular emission spectra has been illustrated in the previous section. It is interesting to see whether liquid rare gases fit into this picture. Further, liquid helium will also be included in this discussion as sufficient emission data on gaseous and liquid helium are available. JORTNER et al. (1965) compared emission spectra of liquid Xe, Kr and Ar obtained by α-particle excitation in all three phases and established excimer formation in the condensed phases. In the course of the search for VUV lasers, emission bands of liquid Xe, Kr and Ar have been investigated with electron excitation by the group of BASOV et al. (1970). CHESNOVSKY et al. (1973) and SUEMOTO (1977) reported emission bands for liquid Kr and CHESNOVSKY et al. (1972) for liquid Ar. The only experiment for liquid Ne has been performed by PACKARD et al. (1970). The emission spectra for liquid He yield information both on radiative decay to the ground state (STOCKTON et al. (1970, 1972), SURKO et al. (1970) and on transitions between excited states of He^* and He_2^* (FITZSIMMONS 1973).

In Fig. 73 and Table 18 we present a collection of spectroscopic data for emission bands of liquid rare gases together with spectra for the gaseous and solid phase. All the emission bands of Xe, Kr, Ar and Ne in the liquid phase are attributed to the decay of excimer-like molecular centers R_2^* from the lowest excited bonding molecular states $^1\Sigma_u^+$ (0_u^+) and $^3\Sigma_u^+$ (1_u) to the ground state $^1\Sigma_g^+$ (0_g^+) (Fig. 71). For Xe and Ar the emission bands in the three phases are almost identical. The differences are smaller as for example the shifts due to temperature broadening (CHESNOVSKY et al., 1973) or due to different preparation conditions observed in the solid phase. For Kr, besides the maximum at 8.42 eV (1472 Å), which is common in the solid and liquid phase, a shoulder appears on the low energy tail at 7.85 eV (1580 Å). This shoulder has been attributed to a Kr Xe* molecule (CHESNOVSKY et al., 1973) which is formed due to the presence of Xe impurities. Thus liquid Ar, Kr and Xe exhibit only the d type molecular emission band.

The emission spectrum for liquid Ne differs dramatically from that of solid Ne (Fig. 68). The b type atomic emission line observed in solid Ne at 16.69 eV (743 Å) is missing in liquid Ne. The absence of the atomic emission

6.7 Emission from Liquid He

We turn to the emission properties of liquid He considering first emission to the electronic ground state. In liquid He a broad emission band centered around 15.5 eV (800 Å) (Fig. 73, Table 18) has been reported by STOCKTON et al. (1970, 1972) and by SURKO et al. (1970). The conversion of excitation energy to VUV light is very efficient. Absolute measurements show that about 30% of the energy of 200 keV electrons is emitted in the 800 Å band. On the basis of these results a VUV lamp has been proposed yielding 3 Watts (10^{10} photons/sec Å) at 800 Å (FITZSIMMONS 1973). The 800 Å band corresponds to transitions from low vibrational levels (v' = 0) of the lowest excited singulet state A $^1\Sigma_u^+$ to the repulsive ground state $^1\Sigma_g^+$ (Fig. 74). In addition, a series of sharp maxima is observed near 20 eV (600 Å) (Fig. 73, Table 18). The limitation of the spectrum to higher energies is due to reabsorption in the liquid He sample. The emission in this region has been attributed by STOCKTON et al. (1970, 1972) to the decay of the v' = 16 vibrational level in the A $^1\Sigma_u^+$ state. The fine structure is caused by the projection of the Franck-Condon distribution in the v' = 16 level onto the strongly repulsive ground state potential. The broad band emission and the fine structure have been observed also in the gas phase. The rapid and selective population of this high vibrational level needs to be explained. v' = 16 and v' = 17 are thetwo highest quasi bound vibrational levels of A $^1\Sigma_u^+$. The v' = 16 level is within 1.2×10^{-2}eV resonant with the 2s ^{1}S metastable atomic state (Fig. 74) which is produced at high rates. This radiative recombination process involves inverse predissociation (HERZBERG 1950). What is remarkable is that this inverse predissociation occurs in the liquid and that the v' = 16, 17 quasibound vibrational states are not damped by vibrational relaxation on the time scale of their radiative decay.

The metastable 2s ^{3}S atomic state decays nonradiatively by a molecular mechanism similar to the decay of the 2s ^{1}S atomic state (Fig. 74). The lifetime of 15 μsec obtained for the state by transient absorption spectroscopy (KETO et al. 1972, 1974) is considerably too short for the radiative decay of this state. The decay of the 2s ^{3}S state gives rise to a buildup of a new transient absorption at 1.92 μm, which is explained by a $a^3\Sigma_u^+$ (v) → $b^3\Pi_g$ (v') transition involving high initial and final vibrational states. Thus, the 2s^{3}S state decays nonradiatively by the formation of vibrationally excited a $^3\Sigma_u^+$ molecular state. Again vibrational relaxation is slow in the liquid.

in liquid Ne suggests that either this center is not formed in the liquid or that it does not live long enough to radiate. In liquid Ne atomic transitions from the $^3P_2$ state have been found in transient absorption spectra, but the lifetime of the $^3P_2$ state is much shorter in liquid than in solid Ne. The radiative lifetimes in both phases are expected to be of the same order. Therefore, the shorter lifetime in liquid Ne is attributed to quenching of Ne^* centers by Ne_2^* excimer formation. In the solid phase, the barrier in the molecular potential curves is sufficiently high to suppress Ne_2^* formation, whereas at the higher temperatures of the liquid these humps may perhaps be crossed. The prominent emission band of liquid Ne is peaking at 16.0 eV (774 Å). It coincides with the c emission in the solid and is attributed to a c band in the liquid.

Additional information regarding these molecular centers in liquids can be derived from lifetimes. In liquid Xe, Kr, Ar and Ne lifetimes have been investigated by KUBOTA et al. (1977), by CARVALHO and KLEIN (1978) and by SUEMOTO et al. (1979). A fast component of some nsec and a slow component have been identified (Table 19). They are attributed to allowed transitions in the R_2^* centers from $^1\Sigma_u^+$ (0_u^+) and transitions from $^3\Sigma_u^+$ (1_u) which becomes more forbidden in going from Ne, Ar to Xe by an admixing of $^1\Pi_u$ character due to increasing spin-orbit coupling. These data support the notion that the R_2^* molecular center is practically identical in the gas phase and in condensed phases. The insensitivity of the R_2^* emission to medium effects can be reconciled with a large medium distortion around this large radius Rydberg state in the liquid as is the case in the solid.

We conclude that the features of excited state dynamics in pure liquid Ne, Ar, Kr and Xe are characterized by three features. First, excited state trapping via two center localization occurs in all liquids. A combination of the molecular approach for the description of the R_2^* potential surface together with a solid state (continuum or microscopic) approach for lattice relaxation is required for a theoretical description of exciton trapping in liquids. Second, medium induced vibrational relaxation of R_2^* in liquid Ar, Kr and Xe is efficient on the time scale of the radiative decay while third in Ne emission is exhibited from vibrationally excited states of Ne_2^* in accord with the energy gap law for vibrational relaxation.

Of considerable interest are the lifetimes of those states which are involved in transitions to the ground state. For the $A\,^1\Sigma_u^+$ state of He_2^* in liquid He experimental lifetimes are not available. The high efficiency of this transition shows that the lifetime is determined mainly by radiative decay. The $A\,^1\Sigma_u^+$ is the lowest state for allowed transitions to the ground state. But the role of the even lower $a^3\Sigma_u^+$ molecular state and of the lowest atomic state $2s^3S$ (Fig. 74) have also to be considered. Both states are metastable, and no radiative decay of these states has been reported. However, interesting dynamic effects of these metastable states were observed. The intensity of the VUV luminescence which is emitted within 10^{-6} sec after α-particle excitation, depends on the sample temperature in the region of 0.2K to 4 K (MOSS and HEREFORD, 1963, FISCHBACH et al., 1969, ROBERTS and HEREFORD, 1973). The explanation of the temperature dependence requires that part of the luminescence intensity (15%) is due to annihilation processes of metastables. These decay processes are influenced by the temperature via the transport properties of liquid He as will be shown below. In addition, SURKO and REIF (1968) found energy transport by neutral excitations in superfluid He between 0.3 and 0.6 K when the sample was irridiated with α-particles. At low temperatures, the neutral excitations travel over distances greater than 1 cm without appreciable attenuation. At higher temperatures, the range is reduced. The neutral excitations carry enough energy to produce electrons and ions at the liquid He surface and at metal surfaces. Due to the amount of energy and the long lifetime, these excitations are attributed to metastable atoms and molecules. These studies have been extended by MITCHELL and RAYFIELD (1971), CALVANI et al. (1972, 1973) and ARRIGHINI et al. (1974). The lifetimes of these metastable states have been investigated by KETO et al. (1972, 1974) using transient absorption spectroscopy. Metastable states with a density of about 10^{12} to 10^{13} per cm^3 have been prepared by electron beam excitation (160 keV). In these experiments, the beam was pulsed with a pulse length of ≈ 3 msec and rise and fall times of 10 nsec. The decay of the population has been probed by observing during and after the excitation an absorption spectrum for transitions from $2s^3S \rightarrow 2p^3P$ at 1.145 eV (1.083 μm) (metastable atoms) and from a $^3\Sigma_u^+$ (v = 0) → $b^3\Pi_g$ (v' = 0) at 0.59 eV (2.1 μm) (metastable molecules) (see Fig. 74). The initial density of metastable states has been changed by varying the electron beam current between 0.1 μA and 4 μA.

In the discussion of these lifetimes we will first be concerned with processes determining the lifetimes of molecules in the $^3\Sigma_u^+$ state. Two experimental facts are pertinent. First, for a fixed temperature and fixed initial concentration, the inverse of the concentration of a $^3\Sigma_u^+$ states increases linearly with time for the time range of 1 μsec up to 100 μsec after excitation. Second, the steady state concentration increases with the square root of the beam current.

These two observations show that the dominating loss process for metastable molecules in liquid He is a bilinear collision process between pairs of metastable states:

$$He_2^* (a^3\Sigma_u^+) + He_2^* (a^3\Sigma_u^+) \xrightarrow{\alpha(T)} He + He + He_2^* \qquad (6.11)$$

The time dependent concentration M of metastable states is described by second order kinetics

$$1/M = 1/M_o + \alpha(T) \cdot t \qquad (6.12)$$

with the steady state concentration M_o and the bilinear reaction rate $\alpha(T)$. M_o is given by the number I_o of initially produced metastable molecules $M_o = \{I_o/\alpha(T)\}^{1/2}$. To provide a quantitative estimate we note that the lifetime of the $a^3\Sigma_u^+$ state due to the bilinear quenching is about 1 msec at a beam current of 1 μA and the lower limit of the radiative lifetime is at least as long as 0.1 sec. A most important experimental observation is that the bilinear reaction rate $\alpha(T)$ increases with decreasing temperature. $\alpha(T)$ is inversely proportional over the higher part of the temperature range to the number density of rotons given by $e^{-\Delta/T}$ with Δ = 8.6 K (KETO et al. 1972, 1974). This interesting temperature dependence reveals that the reaction rate is diffusion limited and determined by scattering with rotons. The energy gap of rotons is pressure dependent. The change of $\alpha(T, P)$ with external pressure P has been measured (KETO et al. 1974). The observed decrease of $\alpha(T,P)$ with pressure agrees with the predictions based on the pressure dependence of Δ.

Some direct implications of the annihilation process (6.11) were recorded. The afterglow observed in the VUV emission of the $A\,^1\Sigma_u^+$ state is due to repopulation of this state in the annihilation process of two metastable

$a^3\Sigma_u^+$ states as follows from the similarity in the rate constants for annihilation $\alpha(T,P)$ and for repopulation. The destruction of metastable molecules feeds the $A^1\Sigma_u^+$ channel as well as higher lying states shown in Fig. 74 (KETO et al., 1974).

Similar results for triplet-triplet annihilation have been obtained by SOLEY et al. (1975) in the only optical experiment reported for solid He. In solid He the molecular absorption band for the $a^3\Sigma_u^+ \rightarrow b^3\Pi_g$ transition (Fig. 74, Table 13) is similar to that in the liquid phase. Also the time dependence of the $A^1\Sigma_u^+$ afterglow, i.e. the bilinear reaction rate $\alpha(T)$ is the same. The common reaction rate is surprising, because α is determined by diffusion of metastable molecules and the transport properties for other species like positive and negative ions are about four orders of magnitude smaller in the solid than in the liquid phase. Thus, mass transport in the solid is excluded. Short range electron exchange interaction (DEXTER 1953, JORTNER et al., 1964) provides an attractive mechanism for triplet migration in solid He. If this is indeed the excitation transport mechanism, the triplet-triplet annihilation in solid He bears a close analogy to triplet-triplet annihilation in aromatic crystals (WOLF 1967).

From the foregoing discussion it is apparent that in liquid He as in other liquid rare gases it is justified to use the gas phase molecular potential surface for He_2^* for the study of energetics and dynamics in liquid He. An interesting feature of the potential curves for the He molecule is that at least up to the $F^1\Sigma_u^+$ singulet and $3d\ ^3\Sigma_u$ triplet states, no antibonding states exist. The potential curves show humps instead of antibonding states, a feature which has been discussed since the early work by MULLIKEN (1964), by GINTER and BATTINO (1970) and has been analyzed in detail by GUBERMAN and GODDARD (1975). This feature of the He_2 potential curves (Fig. 74) differs qualitatively from the general characteristics of the potential curves for the heavy rare gases (Fig. 75). For all heavier rare gas diatomics there are several branches of antibonding potential curves which start from the lowest excited state and which cross higher lying selftrapped exciton states near the minima at the equilibrium internuclear distances of these R_2^* states (Fig. 75). This qualitative difference between He and heavy rare gases influences the dynamics in highly excited states of the corresponding liquids. In the condensed heavy rare gases the highly excited R_2^* centers originating from high electronic states are expected to decay nonradiatively by predissociation as the crossing points of the bonding and antibonding potential

curves lie, for the heavier rare gases, near the minima of the bonding potential curves. Therefore, predissociation is possible even after vibrational relaxation of the diatomic centers. This nonradiative relaxation follows the antibonding potential curves which bridge the gaps between the bonding states. The radiationless processes governing these configurational changes are expected to be very efficient. Thus in condensed rare gases, excited nonselectively by α, x-ray or electron excitation, this cascading results in the formation of the $n = 1$ exciton state on a time scale which is short compared to the radiative decay of high electronically excited states. Accordingly, no emission was observed from high excited states in heavy RGS and liquids. Thus, for liquid He transitions between excited states (Fig. 74) are expected and were identified in the long wavelength emission spectrum (Fig. 76).

Radiative transitions for liquid He are observed in the spectral range from 6000 Å - 11000 Å (2 eV - 1 eV) (DENNIS et al. (1969), KETO et al. (1974) and Fig. 76). Similar to the gas phase, three atomic transitions are observed: $3s\ ^1S \rightarrow 2p\ ^1P$, $3s\ ^3S \rightarrow 2p\ ^3P$ and $2p\ ^3P \rightarrow 2s\ ^3S$ (Fig. 74, 76 and Table 18). Higher states are not expected, because of the HORNBECK MOLNAR (1951) process

$$He^* + He \rightarrow He_2^+ + e \qquad (6.13)$$

which quenches He^* atoms in states above the reaction threshold at 23.0 eV. The transition $2p\ ^1P \rightarrow 2s\ ^1S$ expected at 20581 Å (0.60 eV) with a radiative transition time of 510 nsec (WIESE et al. 1969) has not been observed in the liquid, probably due to the fast (1.8 nsec) radiative depopulation of the $2p\ ^1P$ state to the ground state. The most prominent structures in the emission spectrum (Fig. 76) correspond to molecular transitions. As is shown in Fig. 74 and Table 18, transitions between $C\ ^1\Sigma_g^+ \rightarrow A\ ^1\Sigma_u^+$, $D\ ^1\Sigma_u^+ \rightarrow B\ ^1\Pi_g$ in singulet states and $c\ ^3\Sigma_g^+ \rightarrow a\ ^3\Sigma_u^+$, $d\ ^3\Sigma_u^+ \rightarrow b\ ^3\Pi_g$ and $d\ ^3\Sigma_u^+ \rightarrow c\ ^3\Sigma_g^+$ in triplet states have been identified. All the observed molecular emissions originate from Σ states. Though the emission spectrum demonstrates that the $b\ ^3\Pi_g$ and $B\ ^1\Pi_g$ states are populated effectively in the course of the radiative cascade, no emission from these Π states has been detected in careful experiments (DENNIS et al., 1969). Thus, it is evident that Π states are strongly quenched by nonradiative processes. The details of the emission spectrum show that the emitting states are not in thermal equilibrium with the surrounding liquid. In

C $^1\Sigma_g^+$, emission from a series of vibrational levels v' = 0, 1, 2, 3, 4 and in c $^3\Sigma_g^+$, emission from v' = 0, 1, 2 is observed. Even a rotational fine structure in the D → B, d → b and d → c transitions can be identified from the broadening of the lines as in the gas phase. The population of higher vibrational levels of D and d states (KETO 1974) and a long lifetime of the rotational excitations in the a $^3\Sigma_u^+$ state (HILL et al. 1971) has been proven in transient absorption spectra. A connection of the radiationless quenching rate with the symmetry of the states is obvious. The strong quenching of Π states has been mentioned. The Σ states can be divided into two subclasses concerning symmetry and quenching probability. In all Σ states, the vibrational excitations have a long lifetime. But the rotational excitations are strongly quenched in the pσ orbitals (C, c) whereas they have a long lifetime of 10^{-3}s and more in the sσ orbitals (D, d). The presence of strong nonradiative quenching processes for all higher excited states leading to a population of the lowest emitting state A $^1\Sigma_u^+$ simply follows from intensity considerations. More than 99% of the overall emitted intensity belongs to the A $^1\Sigma_u^+ \rightarrow {}^1\Sigma_g^+$ transition. That part of the population of each of the higher excited states which contributes to the emission spectrum in the visible is about 3 - 4 orders of magnitude smaller than that in the A $^1\Sigma_u^+ \rightarrow {}^1\Sigma_g^+$ radiative decay (KETO et al. 1974). The nonradiative relaxation cascade is much more efficient than the radiative. This follows also from the time dependence of the emission in the visible (KETO 1974). The intensity drops within the response time of the experimental set-up (20 μsec) by one order of magnitude. The further slow decrease is due to repopulation by the annihilation of a $^3\Sigma_u^+$ metastables. The efficiency of the nonradiative cascade can be even increased further by some orders of magnitude by applying static external pressure to liquid He (SOLEY and FITZSIMMONS, 1974). The intensity for all higher excited states is quenched exponentially with increasing pressure (Fig. 77a) and only the A $^1\Sigma_u^+ \rightarrow {}^1\Sigma_g^+$ transition is quenched very little (a factor of two up to 25 atm). The slopes of intensity versus pressure curves on a logarithmic intensity scale are characteristic for the symmetry of the upper state. For transitions starting from p type states C, c, $2s\,^3P$, a common slope is observed which corresponds to a very strong increase in quenching efficiency with pressure (about two orders of magnitude at 15 atm). For the s-type states D, d, $3s\,^3S$ and A the slopes are much smaller. They depend on both, the initial and the final state (Fig. 77a) as shown by the example d → c and d → b with different slopes.

In summarizing the results concerning the balance between radiative and nonradiative relaxation in excited states of liquid He, we can state that the nonradiative processes are by some orders of magnitude faster. Many of the radiationless processes will be faster than 10^{-9} s, because the times for competing radiative processes like $2p\,^3P \rightarrow 2s\,^3S$ or $3s\,^3S \rightarrow 2p\,^3P$ are 9.8×10^{-8}s and 3.6×10^{-8}s, respectively (WIESE et al., 1969). On the other hand, higher vibrational and rotational excitations of molecular states have a lifetime up to milliseconds.

The energy shifts between gas and liquid phase contain salient information about the nuclear configurational changes around excited states in liquid He. HILL et al. (1971) compared the transition energies in emission and in transient absorption of liquid He with gas phase values. They observed shifts to the blue and to the red. All the shifts relative to the gas phase values are very small, of the order of 0.01 eV. For a discussion of these shifts it is important to realize that the 3 Å average interatomic spacing in liquid He is substantially smaller than the diameters of the extended Rydberg states of excited atoms and molecules with diameters of 10 - 20 Å. The small energy shifts are consistent with dramatically large solvent dilatation around the electronically excited state. The large electron - He repulsive interaction in the excited state results in large medium expansion leading to a formation of a "bubble" in analogy with the bubble formed around a free electron in liquid He. These bubbles around free electrons in liquid He have been studied extensively from the experimental and theoretical point of view and the reader is referred to the literature (see for example SCHWARZ 1975, COLE 1974). The origin of both electron bubble and the bubble around the excited species is the repulsive interaction due to the Pauli exclusion principle. The diameter of the bubble corresponds to the balance between these repulsive forces and attractive terms which are given in a simplified picture by the surface tension of the bubble. A sensitive test for this model and its applicability for the more complicated case of electrons in bound excited states follows from the introduction of an additional attractive term given by external pressure. Due to external pressure, the diameter of the bubble should be reduced. The influence of pressure on the transition energies and linewidths can be compared with the predictions of model calculations. SOLEY and FITZSIMMONS (1974) determined pressure shifts of the transitions in absorption and in emission up to pressures of 25 atm. For the emission bands a linear shift with pressure of roughly 3.2 Å/atm. to the blue has been found for all molecular and atomic transitions (Fig. 77b). In

absorption the shifts in transition energies versus pressure show different slopes (Fig. 77c).

The calculation of the spectral shifts and line broadening requires the dependence of the energy of both states, the upper one and the lower one, on the bubble radius with the pressures as parameter in the calculations. These potential curves are nothing but adiabatic potential surfaces. The shapes of the potential curves and the diameters corresponding to the minima in the potential curves are expected to be different for the upper and lower state, because of the larger extension of higher excited states and because of the different symmetries of the states. The symmetry of p-type states may cause even nonspherical bubbles. In the adiabatic approximation, the transitions take place in a time which is short compared to the relaxation time of the bubble and the observed energies correspond to vertical transitions. In transient absorption and in emission the transitions for the same pair of states start from bubbles with different size and shape which cause the observed difference in transition energies. HANSEN and POLLOCK (1972) calculated the pair distribution of ground state He atoms in the vicinity of an excited metastable 2s ^{3}S He atom from Percus-Yevick theory. HICKMAN and LANE (1971) and HICKMAN, STEETS and LANE (1975) adopted the approach of JORTNER et al. (1965) which has been developed for free electron bubbles and modified it to account for bubble formation around electronic excitations. The energy $\langle E \rangle$ of the bubble is divided into two parts

$$\langle E \rangle = E_{cavity} + E_{atom} \qquad (6.14)$$

E_{cavity} describes the energy necessary to form the cavity and contains three terms corresponding to the surface tension, the volume pressure and a kinetic energy which is due to the density gradient at the edge of the cavity. E_{atom} describes the electronic perturbation due to the surrounding liquid. HICKMAN et al. (1975) treated the problem for metastable atoms. E_{atom} has been obtained from a pseudopotential for the system He^{++} plus two electrons interacting with one another and with the rest of the bulk liquid by a variational method. The calculated shifts with external pressure for the $2s^3S \rightarrow 2s^3P$ absorption line agree quite well with the experimental results (Fig. 77c). For the corresponding emission line the initial state has p-symmetry and the bubble will be nonspherical. Therefore, the treatment causes more problems. But the observed shift has been explained by the earlier calculation of HICKMAN and LANE (1971). In the case of n = 2 states

(2s ^{3}S, 2s ^{3}P) the cavity radius of 6 Å is rather small. The model describes very well the increase of the bubble radius with increasing main quantum number. In the case of n = 3 a bubble radius of 11 Å has been calculated for the 3s ^{3}S state and of 13 Å for 3s ^{1}S. The calculated energy shifts for the 3s ^{3}S → 2s ^{3}P emission line (Fig. 77b) are in good agreement with the experimental results. The experimental pressure shifts of the 3s ^{1}S → 2s ^{1}P transition are less accurate in the experiment due to the strong quenching. Beside the shifts also the observed broadening of the lines with increasing pressure has been explained by the bubble model. The method can be applied in principle to molecular centers, but the treatment is more complicated due to the additional interactions inherent in a system of 2 He atoms with 4 electrons. On the basis of the bubble model STEETS et al. (1974) made an attempt to explain the strong quenching of higher excited states with external pressure. They included a more detailed description of the density of the ground state He atoms just at the border of the bubble. Adopting an exponential, pressure dependent distribution function, they have been able to rationalize the experimental slopes of the pressure dependence (Fig. 77a) by processes where only a few (1 - 3) liquid atoms are involved. However, the nature of the quenching process is still obscure.

6.8 Localized excitations and lattice relaxation of impurity states

The cavity model for the localization of an electronic excitation in liquid He implies a considerable nuclear relaxation around the electronically excited state. In this case, the short-range electron He repulsive interaction leads to a rearrangement into a new equilibrium configuration which is characterized by an appreciable increase of the average separation between the electronically excited species and its nearest He atoms. Apart from the name "cavity model" which emphasizes large displacements, such medium relaxation phenomena are common in impurtiy centers in solids and liquids. Optical excitation of such localized impurity states often leads to a high degree of phonon excitation in the electronically excited state. The electronically-vibrationally excited state, populated by vertical transitions, will subsequently relax by phonon emission to a new equilibrium nuclear configuration. A proper description of excitation and relaxation within a localized impurity center is described in terms of the configurational coordinate model sketched in Fig. 78 which portrays the nuclear dependence of the adiabatic potential surfaces. $U_g(Q)$ and $U_e(Q)$ correspond to the ground electronic state and to the electronically excited state respectively, while Q designates the (dimensionless) normal nuclear coordinates. In the harmonic approximation these are

$$U_g(Q) = 1/2 \sum_j \hbar\omega_j \, Q_j^2 \tag{6.15}$$

$$U_e(Q) = U_g(Q) - \sum_j C_j Q_j + \Delta E \tag{6.16}$$

where ΔE is the electronic energy gap, ω_j the phonon frequencies while the coefficients C_j represent the phonon coupling constants so that the displacement of the equilibrium configuration of the jth mode is $\Delta_j = C_j/\omega_j$. The lattice rearrangement energy of the center is

$$E_{LR} = 1/2 \sum_j C_j^2/\omega_j = 1/2 \sum_j \omega_j \, \Delta_j^2 \tag{6.17}$$

being due to nuclear distortions while the Stokes shift between emission and absorption is given by $E_s = 2E_{LR}$. We have already used the notion of lattice distortion energy in relation to exciton trapping, now the same concepts are employed for the simpler case of a localized center. The

quantum energy levels on the two potential surfaces are $|gv\rangle = |g\rangle\,|v\rangle$ and $|ev'\rangle = |e\rangle|v'\rangle$ where $|g\rangle$ and $|e\rangle$ are electronic wavefunctions, while $|v\rangle$ and $|v'\rangle$ denote vibrational states for the ground and excited electronic configurations. The corresponding energies are E_{gv} and $E_{ev'}$. The absorption lineshape is

$$L(E) = \langle \Sigma |\langle ev'|\mu|gv\rangle|^2 \, \delta(E + E_{gv} - E_{ev'})\rangle_T \tag{6.18}$$

where $\langle \quad \rangle_T$ denotes thermal averaging over the ground state vibrational states and μ is the transition dipole operator. The theory of optical lineshapes is well known (KUBO and TOYOZAWA 1955, MARKHAM 1956, PRYCE 1966, MARADUDIN 1966). It is useful to introduce the Huang-Rhys coupling constant

$$G = 1/2 \sum_j \Delta_j^2 \tag{6.19}$$

Two limiting situations are of interest to us:

(1) Weak coupling limit ($G \ll 1$). The electron phonon coupling is weak, i.e. the displacement of the equilibrium configuration in the excited state is small. The optical spectrum consists of a zero phonon line followed by one-phonon and multiphonon contributions at higher energies

$$L(E) = \exp(-1/2 \sum_j \Delta_j^2 \coth(\frac{\hbar\omega_j}{2kT}) \, \delta \, (E - \Delta E) + \text{higher order terms} \tag{6.20}$$

The Debye Waller factor appearing in the exponent in eq. (6.20) determines the relative intensity of the zero phonon line to the rest of the band. This situation is realized for example by N_2 excited impurity states in Ne (GÜRTLER and KOCH, 1980).

(2) The strong coupling limit ($G \gg 1$). The distortion of the equilibrium configuration is large. The absorption lineshape can be expressed in terms of a Gaussian

$$L(E) = \frac{1}{\sqrt{2\pi D^2}} \exp(-\frac{(E - \Delta E - E_{LR})^2}{D^2}) \tag{6.21}$$

$$D^2 = \hbar \sum_j \omega_j \, \Delta_j^2 \coth(\frac{\hbar\omega_j}{2kT}) \tag{6.22}$$

In the limit of low temperatures

$$D^2 = \hbar \sum_j \omega_j \, \Delta_j^2 \qquad k_B T \ll \hbar\omega_j \tag{6.23}$$

while in the high temperature limit

$$D^2 = 2 \, k_B T \, E_{LR} \tag{6.24}$$

The latter expressions describe the local thermal fluctuations of the phonon field around the impurity which were utilized in TOYOZAWA's work (1957) for the description of the modulation of exciton motion (see equations 6.2 - 6.5). Adopting a mean phonon frequency $\langle\omega\rangle$ the optical absorption lineshape in the strong coupling limit is a Gaussian, eq. (6.21), with a linewidth according to

$$H = H_0 \left(\coth \frac{\hbar\langle\omega\rangle}{2kT}\right)^{1/2} \qquad (6.25)$$

where H_0 is the linewidth at T = 0.

The only quantitative data available concerning the lineshape of impurity states in RGS originate from OPHIR's (1970) study of the n = 1 (3/2) and n = 2 (3/2) lineshapes and their temperature dependence for Xe/Ar (Fig. 79). OPHIR found that the lineshape for the n = 1 (3/2) state is Gaussian, so that the strong coupling situation prevails. The half line width H varies from 93 meV ± 1 meV at 33 K to 139 meV ± 1 meV at 80K (Fig. 80). The temperature dependence of the linewidth can be well fitted by the multiphonon theory in the strong coupling limit given by eq. (6.25). The experimental data for H(T) of the n = 1 (3/2) state yield H_0 = 82 meV and $\hbar\langle\omega\rangle$ = 8.2 meV. The electron phonon coupling strength is given by $G = \eta(H_0/\hbar\langle\omega\rangle)^2$ where η = 0.18 is a (T independent) correction factor relating the half linewidth to the second moment of the absorption line (see e.g. PRICE 1966). Thus G = 18 which, indeed, corresponds to the strong coupling situation. The Stokes shift E_s between absorption and emission is given by (KUBO and TOYOZAWA 1955) $E_s = -2\hbar\langle\omega\rangle G = -0.3$ eV resulting in a large red Stokes shift in accordance with the emission data for Xe in Ar (E_S = - 0.39 eV) (CHESHNOVSKY et al., 1972, HAHN and SCHWENTNER, 1980). The simple model cannot quantitatively account for the Stokes shift as it assumes that the phonon frequencies in the two electronic states are identical. Experimental evidence for frequency changes between the two electronic states is obtained for the temperature dependence of the energy maximum of the n = 1 absorption peaks of Xe impurity in Ar and Kr (Fig. 80). Multiphonon theory (PRYCE 1966) predicts that the first moment of the absorption band shifts as

$$E_{max} = E_{max}(0) + \hbar\Delta\omega \coth\left(\frac{\hbar\langle\omega\rangle_g}{2k_BT}\right) \qquad (6.26)$$

where $\langle\omega\rangle_g$ is a characteristic ground state frequency and $\Delta\omega$ is the frequency change. This formula provides a semiquantitative fit of the experimental data (Fig. 80).

In the strong coupling situation a highly excited phonon state is produced by optical excitation. The optically excited "doorway state" (MUKAMEL and JORTNER 1974) is $\mu|gv\rangle$ which is not an eigenstate of the nuclear potential in the electronically excited configuration and will exhibit time evolution. The nonequilibrium "doorway state" will exhibit intrastate phonon relaxation to the equilibrium configuration. Dissipation of the vibrational energy is expected to occur on a time scale of the reciprocal Debye frequency $\sim(\omega_D)^{-1}$ or alternatively be determined by unharmonic interactions. The time scale for lattice relaxation around a single impurity state is $\sim 10^{-13}$ sec.

6.9 Emission from impurity states in rare gas solids

Experimental studies of optical emission from electronically excited states of impurity centers in RGS were conducted for dilute rare-gas alloys. The emitting impurity centers involved a single guest atom or a pair of guest atoms embedded in a host RGS (e.g. CHESHNOVSKY et al. 1972, 1973; GEDANKEN et al. 1973; NANBA et al. 1974; FUGOL and BELOV 1975, 1978; MÖLLER 1976; ACKERMAN 1976; HAHN et al. 1979; HAHN and SCHWENTNER 1980). These studies are of interest because of three reasons. First, the large Stokes shift between absorption and emission provides information on substantial medium phonon relaxation around the electronically excited impurity centers. Second, identification of the emitting states of atomic impurity centers can be conducted by the assignment of a unique atomic parentage to those medium relaxed electronic excitations. Thus, medium perturbations are much smaller in emission than in absorption. Third, the nature of the emitting atomic impurity states resulting from photoselective excitation (HAHN and SCHWENTNER 1980) provide central information on electronic relaxation processes within the impurity center which is coupled to the phonon field. In what follows we shall proceed to discuss the implications of emission spectroscopy to elucidate intrastate medium relaxation processes, while interstate electronic relaxation phenomena will be discussed in Section 6.12.

In early studies of emission from atomic impurity states in RGS (CHESHNOVSKY et al. 1972, 1973, GEDANKEN et al. 1973) α-particle excitation and later electron excitation (e.g. FUGOL and BELOV 1975) and X-ray excitation (e.g. SCHUBERTH and CREUZBURG 1978) has been used (see also Table 20). The spectra of Xe/Ar at 80K excited by α-particles (CHESNOVSKY et al. 1972) were rather simple, exhibiting only the impurity emission from the atomic Xe $1s_5$ state, the molecular emission from Xe_2^* due to impurity dimers and the Ar_2^* emission of the matrix (Fig. 81). Subsequent studies of emission induced by α-excitation of Xe/Ar alloys at 4 - 20 K (GEDANKEN et al. 1973) revealed two distinct trapping sites for the emitting atomic impurity and for the excimer (Table 20). The major drawback of the studies, which involve nonspecific excitation, were surpassed by the utilization of photoselective excitation methods by HAHN and SCHWENTNER (1980) and HAHN et al. (1980) who were able to identify emission from the $1s_2$, $2s_3$ and $1s_4$ states of the Xe impurity (Table 20, 21).

The system Kr in Ar serves as an example for the complications caused by the presence of single guest atoms and pairs of larger clusters of guest atoms as well as for multiple trapping sites. Emission spectra for three optical excitation energies and three concentrations are shown in Fig. 82 (HAHN et al. 1980). For the higher doping concentrations the presence of pairs of guest atoms can be expected in the sample (KREITMAN and BARNETT 1965). These pairs tend to form Kr_2^* excimers in the excited state and a molecular emission band is observed for Kr. In Fig. 82 it is labelled a (Table 20). The emission bands c and h in Fig. 82 appear only for excitation energies which are high enough to excite intrinsic states of the Ar matrix (upper part of Fig. 82, $\hbar\omega$ = 13.8 eV). The bands c and h correspond to the excimer emission of the host Ar_2^* from the vibrational ground state and from the excited vibrational levels, respectively. The excitation spectra II and III in Fig. 82 clearly show that maximum e corresponds to the decay of the n = 1 exciton of Kr atoms in the Ar matrix and maximum g to the n' = 1 excitons. The remaining emission bands b and d (Fig. 82) have been observed also after particle excitation (CHESNOVSKY et al., 1973; FUGOL et al., 1977). They have been ascribed to $(KrAr)^*$ excimers. The emission has also been observed for Kr impurities in liquid Ar (CHESHNOVSKY et al., 1973) supporting the assignment of heteronuclear excimer emission. The assignment of the b and d bands in Fig. 82 to the $KrAr^*$ excimer is yet uncertain in view of the new results of HAHN et al. (1980) using photoselective optical excitation. They found, first, that emission bands b and d can be excited by photon energies below the threshold of absorption of Kr atoms in Ar matrix (curve I in Fig. 82). Second, at low Kr concentration, the emission bands b and d disappear when the sample is annealed for 15 minutes at 15 - 20 K (solid curves in Fig. 82). HAHN et al. (1980) suggested the existence of special sites for a number of Kr atoms in the Ar matrix leading to a smaller threshold for absorption and to lower emission energies. The number of these sites is reduced by annealing.

Solid Ne, which is transparent up to 17.4 eV, provides an excellent matrix for the study of the emission spectra of Ar, Kr and Xe impurity atoms. This host solid has another advantage, namely that heteronuclear excimer states between the electronically excited guest and the host atom are not formed. The emission spectra of dilute Ne alloys resulting from photoselective excitation are presented in Fig. 83 while the energies of the emission bands of Xe, Kr and Ar in solid Ne are summarized in Table 21. Each guest atom exhibits three emission bands which were compared with the radiative transitions

in the free atom (HAHN and SCHWENTNER, 1980). The emission bands can be correlated with the three lowest dipole allowed transitions of the free atom when a Stokes shift of some tenth of an eV to the red is assumed in going from the matrix to the free atom (Table 21). The states associated with these dipole allowed transitions for Ar and Kr are the fine structure components $1s_4$, $1s_2$ and $3d_5$ of the states ns, ns' and (n-1)d (Table 21). For Xe the next higher state $3d_2$ is observed instead of the $3d_5$ state. These assignments are confirmed by a comparison of the radiative lifetimes of the states in the matrix and in the free atom (HAHN and SCHWENTNER 1980, Table 22). The influence of the Ne matrix on the radiative lifetimes of the guest atoms was accounted for in terms of the reduction of the macroscopic radiation field due to the dielectric constant n of the sample and the difference in the effective radiation field E_{eff} at the site of the excited species from the macroscopic field E_o due to the polarizability of the species (BLAIR et al., 1972, FOWLER 1968). The radiative lifetime being

$$\tau^r \text{ (crystal)} = \tau^r \text{ (gas)} / (n \cdot (E_{eff}/E_o)^2) \qquad (6.27)$$

For a guest center in a matrix E_{eff} has been approximated by mean values of the dielectric constant of host and guest (PERSON 1958, DUBOST and CHARNEAU 1976). This treatment did not account for medium effects on the electronic states of the impurity. It is apparent that the medium effects on the radiative lifetimes are small.

In Tables 20 and 21 the assignments of the impurity emission bands in dilute RGS alloys are summarized. Emission bands originating from the following states were observed. (1) In all cases atomic type emission is exhibited, for example from the $1s_4$, $1s_2$ and $3d_5$ states. (2) In addition, emission from special trapping sites for atomic impurity states has been observed. (3) Impurity pairs involving the emission for the lowest excited states of excimers. (4) Impurity pairs in special trapping sites. (5) Heteronuclear excimers, such as Xe^*Kr and possibly Kr^*Ar.

Next we shall discuss the spectroscopic implications of intrastate relaxation. As is evident from the data summarized in Tables 20 and 21, the emission from single impurity states reveals a Stokes shift of $\sim$ 0.2 eV - 1.2 eV relative to the corresponding exciton state seen in the absorption spectrum. This large Stokes shift originates from phonon

relaxation around the excited impurity (CHESHNOVSKY et al. 1972, JORTNER 1974). The observation of these large Stokes shifts is consistent with the notion that the electronic excitation of impurity states in RGS corresponds to the strong electron-phonon coupling limit (Section 6.8), being in good agreement with the results of the analysis of the line broadening data. The experimental Stokes shift for the Xe/Ar system $E_s = -0.39$ eV at 6 K deduced from the emission studies is consistent with the value of $E_s = -0.3$ eV for the Stokes shift deduced (OPHIR 1970) from the temperature dependence of the line broadening in this system, Section 6.8.

The medium dilation around electronically excited impurity states in RGS causing the large Stokes shifts bears a close physical analogy to the bubble formation around electronically excited states in liquid He (Section 6.7). The changes in the equilibrium configuration coordinates for the ground and the excited states can be described semiquantitatively for Xe in Ne. MESSING et al. (1979) measured the dependence of the energy of the atomic absorption bands of Xe atoms for an increasing density of surrounding Ne atoms. They scanned a range of densities from pure Xe up to Xe in liquid Ne. In the middle part of Fig. 84 the energy shifts of the Xe transitions observed in absorption are shown as a function of the mean Xe-Ne nearest neighbor separation together with the energies of the peaks of the excitation spectra of Xe in solid Ne (HAHN and SCHWENTNER, 1980) which continue the trends of the density dependence for the different states. A comparison of the energy positions of the emission bands (right part of Fig. 84) with the absorption maxima shows the larger Xe-Ne nearest neighbor separation due to medium dilation occurring before radiative decay. This guest-host separation increases from 3.2 Å in the ground state configuration to values between 4 Å to 5 Å in the medium relaxed excited state.

The large medium relaxation around impurity states brings the impurity emission close ($\sim$ 0.1 - 0.2 eV in allcases) to the energy of the corresponding atomic emission in the gas phase, as is apparent from Tables 20 and 21. The proper theoretical description of such medium-relaxed electronically excited impurity states should involve a tight binding approach rather than a Wannier picture. The effects of medium dilation around impurity states are exhibited also for excited impurity pairs, as matrix effects on the emission spectra of the excimers are negligibly small.

Finally, we would like to comment on the time scale for intrastate medium relaxation around excited atomic impurity states. The rise time of the emission for the medium-relaxed impurity excited states is shorter than 10^{-11} sec (HAHN and SCHWENTNER 1980). This result is compatible with the theoretical estimates of Section 6.8 for the medium relaxation occurring on the time scale of $\sim 10^{-13}$ sec. We thus expect that the quantum yield for hot luminescence originating from the radiative decay of electronically excited impurity states prior to medium relaxation will be $10^{-4} - 10^{-5}$. Such low quantum yields of hot luminescence induced by photoselective excitation are amenable to experimental observation and are expected to provide pertinent information concerning the dynamics of intrastate medium relaxation.

6.10 Emission from impurity states in liquid rare gases

Emission from impurity states of guest rare gas atoms in host liquid rare gases was excited by α-particles (CHESHNOVSKY et al. 1972,1973; JORTNER 1974, RAZ et al. 1976). The spectroscopic interpretation of the emission spectra of impurity states in liquid rare gases (Table 23) is somewhat simpler than in the corresponding solids, as complications due to multiple trapping sites are not exhibited in the liquid.

The only case of a genuine atomic impurity emission in a liquid recorded up to date involves the emission from the $^3P_1$ state of Xe in liquid Ar shown in Fig.81 (CHESHNOVSKY et al. 1972). The Xe emission is Stokes shifted by 0.4 eV to the red relative to the impurity absorption in the liquid, being very close to the corresponding atomic emission in the gas phase. These features clearly indicate the effects of medium dilation,i.e. cavity formation around the excited impurity state in the liquid (CHESHNOVSKY et al. 1972).

From Fig.81 it is apparent that the molecular impurity emission at low Xe concentrations is much more prominent in the liquid than in the solid. This is not surprising, as formation of Xe_2^* impurity molecules will occur in the liquid by the diffusion controlled "collision" process

$$Xe(^3P_2) + Xe(^1S_o) \rightarrow Xe_2^*(^3\Sigma_u) \qquad (6.28)$$

This process provides an example of the applicability of diffusion controlled kinetics to reactions involving electronically excited atoms or molecules in simple dense fluids.

Emission spectra of Xe/Kr liquid alloys are portrayed in Fig. 85. They reveal three prominent emission bands. The Kr_2^* host emission peaked at 1470 Å, the Xe_2^* impurity pair emission at 1740 Å and an additional band peaked at 1580 Å. This latter band appears at the lowest accessible Xe impurity concentration (10 ppm); its relative intensity reaches a maximum at 100 ppm Xe and starts decreasing in favor of the Xe_2^* 1740 Å emission band at higher Xe concentrations (Fig. 85).This 1580 Å band is assigned

(CHESHNOVSKY et al. 1973) to emission from the heteronuclear $XeKr^*$ diatomic molecule. The Xe_2^* molecule in this system is formed via the reaction

$$XeKr^* + Xe(^1S_o) \xrightarrow{k_F} Xe_2^*(^3\Sigma_u) + Kr(^1S_o) \qquad (6.29)$$

This mechanism requires that the intensity ratio between the 1740 Å emission and the 1580 Å emission is proportional to the Xe impurity concentration. Such a relation is indeed obeyed, as is evident from Fig. 86 which results in the rate constant $k_F = 2 \times 10^{-13}$ $cm^3 sec^{-1}$ for the reaction. This magnitude of the rate constant is compatible with a diffusion controlled process which is characterized by a diffusion coefficient $D = 10^{-6} cm^2 sec^{-1}$.

6.11 Electronic Relaxation

A central feature of excited state dynamics involves interstate radiationless electronic relaxation between different electronic states. In this relaxation process electronic energy is converted into vibrational energy (e.g. KUBO and TOYOZAWA 1956, RISEBERG and MOOS 1968, ENGLMAN and JORTNER 1970, MUKAMEL and JORTNER 1975, FREED 1976, AUZEL 1979). For atomic impurity states in RGS electronic energy of the impurity is dissipated by acoustic phonons. Such a nonradiative process can be described in terms of relaxation between two potential surfaces corresponding to two different electronic configurations (Fig. 78). The coupling which induces the nonradiative processes is given by the nonadiabatic interstate interaction originating from nuclear kinetic energy. The electronic relaxation process is envisioned as a transition from a phonon manifold $|ev'\rangle$ of the initial excited electronic configuration $|e\rangle$ to a set of phonon states $|gv\rangle$ corresponding to the final electronic ground state $|g\rangle$. The microscopic rate constant W_{ev} for the $|ev'\rangle \rightarrow |gv\rangle$ transition can be expressed in terms of the nonadiabatic formalism (KUBO and TOYOZAWA 1956, PERLIN 1963, ENGLMAN and JORTNER 1970) provided that the residual coupling is weak relative to the characteristic phonon frequency $\langle\omega\rangle$ of the system. The nonadiabatic microscopic rate is expressed within the framework of the Condon approximation

$$W_{ev'} = \frac{2\pi}{\hbar} |V_{eg}|^2 \sum_v |\langle v'|v\rangle|^2 \, \delta(E_{gv} - E_{ev'}) \qquad (6.30)$$

where V_{eg} is the nonadiabatic electronic coupling, $\langle v'|v\rangle$ is the nuclear overlap integral, while E_{gv} and $E_{ev'}$ are the energies of the vibronic states. A basic assumption underlying most of the studies of electronic relaxation is that medium-induced vibrational relaxation and excitation within each electronic manifold are fast on the time scale of the electronic process. Thus, for example, in the case of impurity states in RGS one can assert that medium relaxation around electronically excited states is fast ($\sim 10^{-13}$ sec, section 6.8) on the time scale of interstate electronic relaxation. Under these circumstances the transition probability W_{eg} for electronic relaxation can be expressed in terms of a thermal average of the microscopic rates.

$$W_{eg} = \sum_{v'} \exp(-E_{ev'}/k_B T) \, W / \sum_{v'} \exp(-E_{ev'}/k_B T) \qquad (6.31)$$

Before proceeding to discuss any approximate calculations of the rate (6.31) two general limiting cases can be distinguished:

(a) The low temperature limit, when the thermal energy is considerably lower than all the characteristic vibrational (phonon) frequencies of the system. The low temperature rate $W(T \rightarrow 0) = W_{eo}$ is temperature independent over the range $k_B T \ll \hbar\langle\omega\rangle$. The temperature independent rate exhibits the effects of nuclear tunnelling from the zero-point state of the initial nuclear configuration.

(b) The high temperature limit, when the thermal energy considerably exceeds the nuclear vibrational frequency. The high temperature rate

$$W \propto \exp(-E_A/k_B T) \qquad (6.32)$$

assumes an activated rate expression with the activation energy E_A being given by the potential energy of the initial electronic state at the lowest intersection point of the two potential surfaces (see Fig. 78).

Considerable effort was devoted towards derivation of explicit expressions. Moste of these studies (e.g. KUBO and TOYOZAWA 1956, PERLIN 1963, ENGLMAN and JORTNER 1970, AUZEL 1979) treat the nuclear motion in the harmonic approximation considering only linear electron-phonon coupling corresponding to configurational distortion of the origins of the potential surfaces. The physical picture is analogous to the treatment of phonon broadening of impurity absorption lineshapes surveyed in Section 6.8. However, while optical excitation corresponds to nearly vertical transitions at finite photon energy, the non-radiative process corresponds to a horizontal transition in the limit of zero energy.

Within the framework of the simple harmonic picture, the nonradiative rate can be expressed as a product of a nonadiabatic electronic coupling term $|V_{eg}|^2$ and a thermally averaged nuclear Franck Condon overlap term. The latter contribution can be approximately expressed in terms of the electronic energy gap ΔE (see Fig. 78) between the minima of the two potential surfaces, the phonon characteristics frequency $\hbar\langle\omega\rangle$ and the electron phonon coupling strength G (eq. 6.19). Although some general but cumbersome expressions were derived (KUBO and TOYAZAWA 1956, WEBMAN 1976) considering phonon dispersion, a coarse graining procedure over phonon frequencies taking only the characteristic phonon frequency $\hbar\langle\omega\rangle$ into account, leads to great simplifications. The approximate general rate can be expressed in the form (HUANG and RHYS 1953)

$$W = A \exp\left[-G(2\bar{\nu}+1)\right] I_P\left\{2G\left[\bar{\nu}(\bar{\nu}+1)\right]^{1/2}\right\}\left[\frac{\bar{\nu}+1}{\bar{\nu}}\right]^{P/2} \tag{6.33}$$

where the reduced energy gap is

$$P = |\Delta E| / \hbar\langle\omega\rangle \tag{6.34}$$

$I_p\{\}$ is the modified Bessel function of order P, v represents the thermal population of phonon states

$$\bar{\nu} = \left[\exp(\hbar\langle\omega\rangle)/kT) - 1\right]^{-1} \tag{6.35}$$

while the preexponential factor is

$$A = \frac{2\pi}{\hbar^2}\frac{/V_{eg}^2}{\langle\omega\rangle} \tag{6.36}$$

For exothermic processes, $\Delta E < 0$, the low temperature rate for nuclear

tunnelling is obtained for eq. 6.33 in the form

$$W\ (T \to 0) = A \exp(-G)\frac{G^P}{P!} \tag{6.37}$$

while in the high temperature limit eq. 6.33 results in the activated rate

$$W = A\left(\frac{\hbar\langle\omega\rangle}{4\pi G k_B T}\right)^{1/2} \exp - \frac{\Delta E/-G\hbar\langle\omega\rangle}{4G\hbar\langle\omega\rangle k_B T}^2 \tag{6.38}$$

For the intermediate temperature region eq. 6.33 has to be applied.

Of considerable interest is the low temperature rate which for reasonable values of $P > 3G$ can be expressed by the use of Stirling's approximations

$$W(I \to 0) = \frac{A}{(2\pi P)^{1/2}} \exp(-G) \exp(-\gamma P) \tag{6.39}$$

$$\gamma = \ln\left(\frac{P}{G}\right) - 1 \tag{6.40}$$

Eq. 6.39 expresses the energy gap law for electronical relaxation. From eq. 6.39 it is apparent that the following general features of the physical system are expected to affect the low-temperature electronic relaxation rate within the impurity center:

(1) The preexponential factor A. For atomic impurity states in RGS A was roughly estimated to be $A \sim 10^{14}\,sec^{-1}$ (WEBMAN 1976).

(2) The electronic energy gap ΔE. The increase of P with ΔE (eq. 6.34) results in an exponential decrease of W.

(3) The electron phonon coupling G. When $P \simeq G$ we expect that $\gamma \simeq -1$ and the energy gap dependence of W is suppressed. Efficient electronic relaxation can occur for large energy gaps provided that $G \sim P$ (WEBMAN 1976).

WEBMAN (1976) has conducted model calculations for the rates of electronic relaxation in impurity centers in RGS (JORTNER 1974) which rest on a Wannier type description of the electronic excited states. Such an approach indicated that nonradiative cascading from high excited states, characterized by large main quantum members is efficient. However, this treatment is too crude for a detailed theoretical understanding of electronic relaxation within low lying electronically excited impurity states in RGS, which are essentially of atomic parentage.

6.12 Electronic Relaxation within Impurity Centers in RGS

The dynamics of excited states of impurity centers in RGS can be investigated by measurements of emission spectra, excitation spectra, emission quantum yields transient absorption and decay lifetimes. The central experimental information involves the total lifetime τ_I of the Ith electronic state where the nonradiative decay rate $W_I=\Sigma_F W_{IF}$ involves the contribution from all nonradiative decay channels, while the corresponding radiative decay time τ_I^r incorporates radiative decay to all lower lying F states so that $(\tau_I^r)^{-1}=\Sigma_F(\tau_{IF}^r)^{-1}$. The experimental lifetime is given by the well known relation

$$(\tau_I)^{-1} = W_I + (\tau_I^r)^{-1} = \Sigma_F W_{IF} + \Sigma_F (\tau_{IF}^r)^{-1} \qquad (6.41)$$

The partial quantum yield for the radiative $I \rightarrow F$ transition is:

$$Y_{I\rightarrow F}^r = (\tau_I)/(\tau_{IF}^r) \qquad (6.42)$$

while the quantum yield for the nonradiative $I \rightarrow F$ process is

$$Y_{I\rightarrow F}^{nr} = W_{IF} \cdot \tau_I \qquad (6.43)$$

The major experimental effort should be directed towards (i) the elucidation of the nature of the various radiative and nonradiative decay channels, (ii) the quantitative determination of the total decay rates τ_I^{-1}, W_I and $(\tau_I^r)^{-1}$, (iii) the determination of partial radiative and nonradiative decay rates $(\tau_{IF}^r)^{-1}$ and W_{IF} and (iv) determination of quantum yields $Y_{I\rightarrow F}^r$ and $Y_{I\rightarrow F}^{nr}$ for radiative and nonradiative channels, which is complementary to (iii). The theory of electronic relaxation of localized states in insulators (Section 6.11) should provide answers to

the following questions regarding excited states dynamics of impurity states in RGS:

(a) Which states exhibit appreciable esmission? Effective radiative decay of a given state I requires that $W_I \lesssim (\tau_I^r)^{-1}$.

(b) What are the rates of nonradiative cascading from highly excites states which terminate in the emitting states?

(c) What quantitative information can be obtained regarding nonradiative decay rates between specific electronic states?

(d) What information can be obtained concerning details of electronic relaxation processes, such as temperature dependence of individual nonradiative rates?

We shall start with a survey of the experimental information. The early studies (CHESHNOVSKY et al. 1972, GEDANKEN et al. 1973, RAZ et al. 1976) using α-excitation of dilute rare gas alloys, established the occurence of emission from low lying excited states. In all cases emission from the $^3P_1$ state of the guest, while for Xe in Ne emission from the $^1P_1$ state was observed. These results were qualitatively rationalized in terms of the energy gap law for electronic relaxation (JORTNER 1974, RAZ et al. 1976). Much more detailed information was recently obtained by HAHN and SCHWENTNER (1980) using photoselective excitation. The most extensive and informative data were obtained for the emission of Xe, Kr and Ar in solid Ne. Typical experimental results for the excitation spectra, the emission spectra and time-resolved decay are presented in Figures 87 and 88. We have already discussed the assignment of these impurity emission peaks (Table 21) and will now consider the electronic relaxation processes. Excitation of the n = 1 impurity state of Xe, Ar and Kr in solid Ne results in medium relaxation leading to the formation of the $1s_4$ ($^3P_1$) impurity state. On the basis of the experimental data (Table 22) for the radiative decay, it is apparent that the major contribution to the lifetime of the $1s_4$ state originates from the radiative decay channel to the ground state which is much faster than the other two competing radiationless processes, i.e. radiationless relaxation either to the only lower lying excited state $1s_5(^3P_2)$ or to the ground state. The radiationless relaxation to the ground state is hindered by the very large (≈10eV) energy gap. The

separation from $1s_4$ to the $1s_5$ state is 0.1 - 0.2 eV (see Figs. 89, 90) requiring a radiationless transition of the order of P = 10-30. Provided that the electron-phonon coupling is not too large the radiationless $1s_4 \rightarrow 1s_5$ decay will be effectively blocked by the appreciable energy gap. The energy gap law determines in a similar manner the relaxation of the n = 1' impurity states of Xe and of Ar in solid Ne. Excitation of n = 1' excitons leads to the formation of the medium relaxed $1s_2(^1P_1)$ state. The experimental decay lifetimes (Table 22) are again dominated by the pure radiative decay channel, so that radiationless electronic relaxation for $1s_2(^1P_1)$ to the $1s_3(^3P_0)$, $1s_4(^3P_1)$ and $1s_5(^3P_2)$ states are not exhibited on the time scale of 10^{-6} sec.

The energy gaps of 0.2 eV for Ar and 1.1 eV for Xe, due to spin orbit coupling, are sufficiently large to prohibit electronic relaxation. For Kr in solid Ne an interesting complication due to impurity - impurity energy transfer arises. In this system there is an accidental energetic overlap between the medium relaxed $1s_2(^1P_1)$ state and the n = 1$(^3P_1)$ state. The rise and decay times of the emission bands of the $1s_2$ and the $1s_4$ states after excitation of n = 1' excitons indicate that a resonant dipole - dipole energy transfer takes place from an excited Kr atom in the $1s_2$ state to a nearby Kr atom in the ground state (HAHN and SCHWENTNER 1980). The Förster-Dexter radius for this transfer is 21 Å.

Next, we consider the fate of high energy impurity excitations in solid Ne. There are several characteristic differences for the n = 2 exciton relaxation cascades for Xe, Kr and Ar guest atoms in a Ne matrix. The origin is an increasing spread on an energy scale of the (n+1)s, the (n-1)d, the np and the ns' states in going from Xe to Ar. This spread results in groups of close lying levels which are separated by increasing gaps (Figs. 89, 90). Excitation of n = 2 excitons in Xe leads to a population of the medium relaxed $2s_4$ and $3d_2$ states (Fig. 89). The $3d_2$ state is separated from the next state $3d_1$' by a gap of 0.18 eV. It was experimentally established that the $3d_2$ state decays radiatively with a time constant of $1,3 \times 10^{-9}$s as well as nonradiatively to $3d_1$' with a time constant of 1.0×10^{-9}s. We note that in this case radiationless processes of the order of P = 30 can have time constants as fast as 10^{-9}s. This observation is incompatible with the considerations based on the energy gap law and can be rationalized in terms of the cancellation effect which is exhibited when P ≈ G in Eqs. 6.39, 6.40. The energy interval between the $3d_1$' and the $1s_2$ states

is so densely populated with other states (Fig. 89) that the radiationless processes will be extremely fast. Radiative transitions, i.e. the dipole allowed decay from the $3d_5$ state, are not absorved. In the $1s_2$ state the radiationless relaxation cascade terminates as has been previously noted. No relaxation to $1s_3$, $1s_4$ or $1s_5$ is observed.

The relaxation cascade resulting from the n = 2 excitation of Ar in solid Ne (Fig. 90) results in an initial population of the medium relaxed $2s_4$ state which relaxes effectively to the lowest 3d states ($3d_5$ and $3d_6$). The gap between the 3d and (4p, 4p') states is sufficiently large to make non-radiative decay rather slow. Branching occurs between radiative decay of the $3d_5$ state (420×10^{-9}s) and slow nonradiative decay to 4p' and 4p states. The (4p' 4p) states are separated by a large energy gap from the 4s and 4s' levels. Therefore, both the 4p' and 4p states are depopulated radiatively to the 4s as well as 4s' state with similar time constants. The intensity is distributed between radiative channels from the fine structure components of the 4p' to 4s' and the 4p to 4s states with the branching ratios given in Fig. 90.

The relaxation cascade of Kr in solid Ne (Fig. 88) is similar to that of the Ar impurity state (HAHN and SCHWENTNER, 1980). Compared to the energy scheme for Ar (Fig. 90) the main quantum numbers n have to be increased by one and the group of 5p' levels are shifted into the range of the 4d levels. The energy of the n = 2 exciton does not result in radiative decay from the medium-relaxed $2s_4$ or from the $3d_2$ states. Thus electronic relaxation from $2s_4$ and $3d_2$ into the lower 4d states ($3d_5$ and $3d_6$) is fast on the time scale of 10^{-9} s. Subsequently, 4d → 5p electronic relaxation competes with radiative decay of the lower 4d states. The energy gap between the 5p state and the 5s' and 5s states is so large that radiationless processes do not occur. Further, radiative decay from the p symmetric 5p state to the p symmetric ground state is dipole forbidden. Therefore, the 5p states are depopulated by radiative decay to the 5s and 5s' levels. The transitions to the 5s states which are singulet - singulet transitions with transition times of 22×10^{-9}s are favored compared to 5s' transitions (750×10^{-9}s). In this radiative depopulation channels to the 5s states a branching to the fine structure components $1s_4$ and $1s_5$ with equal probability takes place.

The results for the relaxation cascades of impurity states in solid Ne are collected in Table 24. The radiative population efficiencies of the fine

structure components derived in this relaxation cascade agree with the intensities in emission bands found by SCHUBERTH and CREUZBURG (1978) with X-ray excitation. A quantitative theoretical description of these relaxation cascades is not yet available and will be of considerable interest.

Results for atomic impurity states in heavy RGS have been collected in Table 20. Obviously, further experimental and theoretical work concerning the electronic relaxation processes is required. An interesting new result in this field involves the study of the temperature depencence of the electronic relaxation from the $1s_4(^3P_1)$ state of Kr in Ar which is produced by medium relaxation around the $n = 1$ $(^3P_1)$ state (HAHN et al. 1980). The $1s_4$ state is depopulated by radiative decay to the ground state and by nonradiative decay to the $1s_5(^3P_2)$ state. In Fig. 91 the temperature dependence of the decay rate of the $1s_4(^3P_1)$ state is shown which exhibits the temperature independent nuclear tunnelling at low temperatures and temperature activated processes at higher temperatures. Analysis of the data in terms of Eq. 6.33 can be performed taking $\Delta E = 82$ meV and $\hbar\omega_p = 4$ meV, i.e. $P = 20$.

6.13 Electronic Energy Transfer

Some of the most interesting features of the dynamics of electronic excitations in molecular crystals involve energy transfer processes (KNOX 1963). There have been extensive studies of migration of singlet and triplet Frenkel type excitons in organic crystals (e.g. RICE and JORTNER 1967, WOLF 1967, POWELL and SOOS 1975, KEPLER 1976, SILBEY 1978) which led to estimates of the exciton diffusion length and the exciton diffusion coefficient in these molecular crystals. Studies of electronic energy transfer in pure RGS are of interest to establish the possibility of exciton migration on an ultrashort time scale prior to exciton self trapping and in relation to energy transfer from self trapped excitons. The effects of substitutional disorder on energy transfer are manifested for transfer to atomic and molecular impurity states, while some consequences of structural disorder are exhibited for energy transfer in liquid rare gases. The following electronic energy transfer processes in condensed rare gases are of interest (see e.g. JORTNER 1974, RAZ et al. 1976, FUGOL 1978, SCHWENTNER 1978, 1980):

(A) Migration of "free" excitons. The term "free" excitons refers to exciton states prior to selftrapping. In this context two limiting cases of energy transfer should be considered:

(A1) Coherent exciton transport. The limiting situation for weak exciton-lattice coupling involves coherent transfer characterized by the exciton group velocity, so that the displacement of the exciton at time t is proportional to t. This idealized state of affairs is not realized in real life as exciton-scattering mechanisms due to phonons, structural imperfections, etc. prevail even in pure crystals. Coherent exciton transport should be envisioned in terms of a mean free path Λ, which considerably exceeds the lattice spacing a, i.e. $\Lambda >> a$.

(A2) Incoherent exciton transport. When the exciton scattering by phonons, disorder, etc. is strong, the exciton mean free path is comparable to the lattice spacing $\Lambda \approx a$. Exciton transport is now characterized by a diffusion coefficient D which is related to the diffusion length ℓ by

$$\ell = (Dt)^{1/2} \tag{6.44}$$

where τ is the exciton lifetime. For RGS we identify τ with the lifetime ($\tau \sim 10^{-12}$ sec) of the free exciton prior to selftrapping (Section 6.2). Experimental evidence for incoherent, strong scattering diffusive type exciton transport will be discussed in Section 6.13.1 and 6.13.2.

(B) Electronic energy transfer from selftrapped excitons in RGS. On a time scale long relative to the selftrapping time, the exciton energy becomes localized (Section 6.2). Energy migration involving polaron type motion (HOLSTEIN 1959) e.g. $R_2^* + R \rightarrow R + R_2^*$ in solid Ar, Kr and Xe would be accompanied by large nuclear configurational changes. It is unfavorable in view of the large binding energies of the R_2^+ diatomic molecules, and therefore this exciton transport mechanism can be safely neglected. Electronic energy transfer from selftrapped excitons to impurity states in the bulk and to boundaries can occur via:

(B1) Transfer from two center trapped excitons in solid Ar, Kr and Xe where the energy donor is the diatomic R_2^* molecule while the energy acceptor is an impurity center.

(B2) Transfer from a one-center trapped exciton in solid Ne to an impurity center

Mechanisms (B1) and (B2) involve Förster Dexter (FÖRSTER 1948, DEXTER 1952) pairwise electronic energy transfer, where the selftrapped exciton acts as the energy donor which transfers energy to randomly distributed impurity acceptors.

(C) Electronic energy transfer between impurity states. Two types of processes can be distinguished in this context:

(C1) Transfer between impurities of the same type. This energy transfer process which has been frequently observed in liquids since the pioneering work of FÖRSTER (1948) is not commonly exhibited in doped RGS. The large Stokes shift between absorption and emission of atomic impurity states in RGS (poor spectral overlap, Section 6.9) leads in general to a low efficiency of energy transfer from an excited impurity excitation to another impurity of the same type. An interesting case in this category involves energy transfer between different electronic states of impurities of the same type. It is exhibited in the transfer from the medium relaxed n = 1' state of Kr to the n = 1 state of another Kr impurity in solid Ne (HAHN and SCHWENTNER 1980) which was discussed in Section 6.12.

(C2) Transfer between impurities of different type, which involves the conventional Förster-Dexter mechanism. Examples for processes B and C will be discussed in Section 6.13.2 and 6.13.3.

The physical consequences of donor-acceptor electronic energy transfer in RGS can be classified in terms of two types of transitions:

(a) Bound-bound transitions where the energy acceptor is produced in a bound excited state which is located below the ionization energy of this acceptor. The excited state of the acceptor can subsequently decay either radiatively or nonradiatively.

(b) Bound continuum transitions. When the energy of the donor exceeds the solid state ionization potential of the energy acceptor, the energy transfer process will result in the ionization of the acceptor. Such ionization processes in RGS bear a close analogy to Penning ionization in the gas phase. From the foregoing classification it is apparent that two general techniques can be utilized to interrogate the dynamics of energy transfer in RGS. The consequences of transfer resulting in bound-bound transitions can be explored by the techniques of emission spectroscopy. On the other hand energy transfer resulting in ionization can be investigated by photoemission studies monitoring the electronic yield and the photoelectron energy distribution.

6.13.1 Dynamics of "free" excitons in RGS

To explore electronic energy transfer by "free" excitons one has to utilize sensitive interrrogation methods in order to probe processes occuring on the 10^{-12}s time scale . Photoemission yield and energy distribution measurements provide an adequate tool.

In pure RGS two separate photoemission mechanisms are exhibited.

1. In the excitonic energy range $E_{n=1} \leq E < E_{Th}$ only extrinsic photoemission can occur. Here extrinsic means that the photoemission process is mediated by energy transfer of the exciton to a boundary from where a photoelectron is released.

2. Above threshold, i.e. $E > E_{Th}$ the usual intrinsic photoemission takes place (see section 3.1, 7.3 and 7.4). Extrinsic photoemission yield spectra from pure RGS were studied by O'BRIEN and TEEGARDEN 1966, SCHWENTNER et al. 1973, KOCH et al.1974a, 1974b, STEINBERGER et al.1974, OPHIR et al. 1975a, 1975b, PUDEWILL et al.1975, HASNAIN et al.1977 and RUDOLF et al.1980). These studies encompassed all RGS. An example for the pronounced structure in the photoemission yield curves associated with the exciton states is depicted for solid Kr in Fig. 92. Yield spectra are shown for a number of film thicknesses (SCHWENTNER et al. 1980). Direct emission at the surface is forbidden energetically. KOCH et al.1974, OPHIR et al.1975 and PUDEWILL et al.1975 have earlier assigned similar extrinsic photoemission in pure solid Ne, Ar and Xe to the exciton diffusion to the gold substrate (the emitter electrode), followed by electron ejection from the electrode. Several alternative interpretations, such as impurity effects, nonlinear optical processes, ionization of excitons near the surface and long range energy transfer from a trapped excited diatomic molecule to the gold surface could be eliminated. The experimental data for pure Xe, corrected for reflection effects and direct emission from the substrate were analyzed in terms of an exciton diffusion model, involving competition between energy transfer to the substrate and decay of mobile excitons (OPHIR et al.1975). The photoemission yield Y is expressed as $Y = F(\ell,L,\alpha,d)$ where L is the escape length of the electrons (Section 7). L is measured independently, α is the absorption coefficient, and d is the film thickness, while the diffusion length ℓ is given by eq. 6.44. From the thickness dependence of Y (Fig. 93) at several photon energies a diffusion length of $\ell = 300$ Å was determined for solid Xe. Similar yield measurements and the same kind of analysis have been reported for Ne (PUDEWILL et al.1975).

Returning to the case of solid Kr (Fig. 92, SCHWENTNER et al. 1980) we note that the rare gas film is transparent for energies below 9.8 eV. The small photoelectron yield represents the escape probability for electrons from the Au substrate. The strong increase of Y for photon energies in the Kr exciton region above 10 eV is due to the energy transfer to the substrate.

The absolute value of the yield indicates an efficiency for electron emission due to energy transfer of 0.3 - 0.5 electrons per exciton compared with the direct photo yield efficiency of 0.03 - 0.05 electrons per photon. A similar high efficiency is observed in the Penning ionization at metal surfaces by metastable rare gas atoms (e.g. DUNNING et al. 1975). These large efficiencies agree with calculations for the interaction of a metal surface with a dipole in front of it. The interaction mechanism is in this case the coupling of the dipole near field to surface plasmon modes (CHANCE et al.1976). It is interesting to note that the quantitative analysis of the extrinsic photoemission from solid Kr (SCHWENTNER et al., 1980) shows a pronounced energy dependence of the diffusion length (Fig. 94). The diffusion length rises from $\ell = 30$ Å in the low energy tail of the $n = 1$ exciton to $\ell \approx 300$ Å for the $n = 2$ exciton. It is intriguing to inquire whether this monotonous increase of ℓ does reflect a transition from incoherent strong scattering motion at low energies to coherent motion at higher energies.

An independent source of information concerning the dynamics of free excitons in RGS was obtained from exciton induced impurity photoionization. For dilute impurity states three intrinsic photoemission mechanisms can occur: 1. Direct excitation from the impurity above its threshold for $E^{i}_{Th} < E < E_{n=1}$. 2. Impurity photoemission resulting from excitation of the host excitonic series for $E_{n=1} \leq E < E_{Th}$. 3. Intrinsic photoemission from the host matrix at $E > E_{Th}$.

Exciton induced impurity photoionization in RGS was first studied by OPHIR et al.(1974) for C_6H_6 in solid Xe and subsequently extended to dilute rare gas impurities in RGS by SAILE et al.(1974), OPHIR et al.(1975) and PUDEWILL et al. (1975). Benzene in solid Ne, Ar and Kr matrices were studied in photoemission yield experiments by HASNAIN et al.(1977), while photoelectron energy distribution measurements for C_6H_6 in solid Ar, Kr and Xe have been reported by SCHWENTNER et al.(1978). In the following we limit our discussion to the photoemission results obtained for rare gas impurities in rare gas matrices.

The photoelectron yield spectra for Xe atoms in Ar matrices are shown as an example in Fig. 95. At photon energies below 12 eV the matrix is transparent and electrons from the Au substrate and from the Xe guest atoms are emitted. Both contributions are small at all Xe concentrations up to 1%. At photon energies between 12 eV and 13.9 eV light is absorbed by excitons of the Ar matrix. Hence the yield from the Au substrate and from direct absorption by Xe guest atoms is reduced. Nevertheless the yield increases. The observed larger yield in this range originates from the creation of host excitons (n=1, 1', 2 ...). Since these excitons lie below the vacuum level of the matrix, direct photoemission is impossible. The explanation for the photoelectron yield and its strong increase with Xe concentration is energy transfer of Ar excitons to Xe guest atoms leading to ionization of the Xe atoms. The small maxima in pure Ar are due to energy transfer of Ar excitons to the Au substrate. Above $h\nu \approx$ 13.9 eV direct photoemission of the Ar matrix causes a further steep increase of the yield. In Table 25 the matrix exciton energies and the energy of the emission bands are compared for various systems together with the threshold energy E_{Th}^{i} necessary for electron emission from the guest levels. The occurence of energy transfer is marked. The essential result from these experiments is that in all RGS matrices electron emission starts when the energy of primarily excited excitons just exceeds the threshold for photoemission of the guest atom. For Ar and Kr matrices the luminescence emission bands lie below this threshold and energy transfer from trapped excitons cannot lead to photoemission. From the observation of electron emission due to energy transfer in these systems (see Table 25) we conclude that also free excitons are responsible for the energy transfer process. The high yield (Fig. 95) for Xe in Ar proves that at high concentrations this is the dominant transfer process (see also section 6.13.2). By fitting the concentration and thickness dependence, diffusion lengths have been derived. We note that in a Ne matrix both the energy of the free exciton and of the selftrapped excitons exceed the threshold energy for guest ionization (PUDEWILL et al.1977).

Some related additional information regarding exciton dynamics was obtained from energy transfer to boundaries of RGS which are contaminated by impurity molecules. Such processes which are important for luminescence quenching, result in minima in the energy dependence of the luminescence efficiency of RGS (Fig. 96) which coincide with the exciton energies (NAGASAWA and NANBA 1974, NANBA and NAGASAWA 1974, ACKERMAN et al.1976, GERICKE 1976).

Unfortunately, an unambiguous interpretation of these results cannot be provided (ACKERMAN et al.1976) as the energy dependence of the luminescence efficiency can be accounted for both in terms of diffusion of free excitons as well as by Förster-Dexter transfer from localized selftrapped excitons.

In Table 26 we have summarized the available results for the diffusion lengths of "free" excitons in RGS. From these results it is apparent that the diffusion length ℓ considerably exceeds the lattice constant. To obtain a rough estimate for the diffusion coefficient of free excitons in solid Ar, Kr and Xe we take $\tau \approx 10^{-12}$ s which results in $D \approx 0.2 - 1\ cm^2\ s^{-1}$ (eq. 6.44). The question whether the exciton transfer process is diffusive or coherent has not yet been answered definitely. However, the experimental results support the notion that exciton motion is diffusive and hence all authors have analyzed their experiments within a diffusion model. The excitons can be scattered by phonons and crystal imperfections such as grain boundaries. An extensive discussion by FUGOL (1978) arrived at the conclusion that the diffusion lengths derived from the experiments reported so far are limited by scattering of the free excitons by crystal imperfections.

6.13.2 Competition between Relaxation and Energy Transfer

Photoelectron energy distribution measurements (EDC's) on RGS have been used to study exciton dynamics, energy transfer and relaxation processes (SCHWENTNER and KOCH,1976, SCHWENTNER et al.,1978). Detailed information concerning the competition of relaxation and energy transfer has been derived from these experiments. From yield spectra primarily threshold energies for the various processes can be derived. From the analysis of the kinetic energy of emitted electrons toghether with the known vacuum level the transferred energy is determined directly in EDC measurements. EDC's from thin films of solid Ar and Ne each doped with 1% Xe have been presented by SCHWENTNER and KOCH (1976) for several photon energies. In Fig. 97 an overview of EDC's for 1% Xe in Ar is given. On the right hand side the counting rate is plotted versus the kinetic energy of the emitted electrons, where zero corresponds to the vacuum level. The spectra are shifted upwards proportional to the increase in photon energy. In this display, the diagonal lines connect those structures

in different EDC's which are due to the same initial state (see insert). The crosses in the left hand curve show the total number of electrons emitted at a given photon energy. They are compared with a total yield curve of 1% Xe in Ar. At the lowest photon energies (hν = 11 eV and 11.5 eV) only Xe atoms can be excited in the film and the EDC's correspond to the upper Xe $5p_{3/2}$ level. This state and its spin orbit partner Xe $5p_{1/2}$ are seen in all spectra up to hν = 19 eV. At these larger photon energies mainly electrons from the Ar 3p valence band contribute to the EDC. In the photon energy region, where the n=1, 1', 2 and 2' states of Ar are excited, the total emission rate (left hand side) shows strong maxima due to energy transfer to the guest atoms, as has been described before on the basis of yield spectra (see Fig. 95). The EDC's in the excitonic region are shown on an enlarged scale (Fig. 98) using the same kind of display. Upon excitation of the n=1 and n'=1 exciton of the Ar matrix, the EDC's show the same structure at the same energy position as if the Xe atoms would have been excited directly by photons. The energy is transferred by Ar n=1 excitons before relaxation to selftrapped excitons. The difference in kinetic energy for the spectra for n=1' and n=1 excitons also excludes relaxation from n=1' to n=1 before energy transfer. For the n=2 and n=2' excitons of the Ar matrix again the maxima of the Xe 5p states appear in the EDC's at kinetic energies indicating energy transfer from unrelaxed n=2 and n=2' excitons. There is an additional maximum near the vacuum level which is attributed to energy transfer from selftrapped n=2 excitons. This maximum cannot be explained by transfer after relaxation to n=1 and n'=1 excitons.

The situation is quite different for Xe in Ne. The EDC's in Fig. 98 are taken for photon energies corresponding to population of Ne n=2, n=1 excitons and at a somewhat lower energy for direct excitation of the Xe guest atoms (hν = 16 eV). In the latter spectrum emission from the two spin orbit split (Δ_{SO}) Xe 5p states situated in the band gap of Ne is observed. The Xe 5p states are well reproduced when the energy is transferred from the Ne n=1 exciton (hν = 17.5 eV) to the Xe atoms. However, there is a shift of ≈0.7 eV of the total spectrum to lower kinetic energies indicating some relaxation either to the one center selftrapped exciton or to the high vibrational levels of the two center selftrapped exciton before energy transfer.

The striking observation is that in the EDC obtained by exciting the Ne n=2 excitons more than 3 eV are missing. The electrons have the same energy distribution as for excitation of the n=1 Ne excitons. This observation indicates a complete relaxation of the n=2 excitons to n=1 excitons and dissipation of an energy of more than 3 eV before transfer.

These data illustrate the power of EDC measurements yielding direct information about the state of relaxation before transfer. A time scale derived from these experiments for the competition of relaxation and transfer processes is given in Table 27.

Electron energy distribution measurements of electrons produced by energy transfer from Xe, Kr and Ar hosts to benzene molecules were conducted by SCHWENTNER et al. (1978). The spectrum of kinetic energies shows that energy transfer from unrelaxed host excitons in all three matrices is an efficient process.

6.13.3 Energy transfer between localized states

Generally, in optical emission spectra from dilute rare gas alloys (see sections 6.9 and 6.11) the information concerning the primarily transferred energy cannot be recovered, since non radiative relaxation processes are fast on the time scale of the radiative decay. Furthermore, both free and localized exciton can in principle contribute to the emission since the threshold energies discriminating between both in EDC measurements are not relevant for these processes. The energy transfer from localized R_2^* centers of the host to the impurity occurs via the Förster-Dexter mechanism (FÖRSTER 1948, DEXTER 1953). It is determined by the strength of donor-acceptor dipole-dipole coupling and by the spectral overlap between the donor emission and the acceptor absorption. The transition probability for the electronic energy transfer process at the donor (D)-acceptor (A) separation R is

$$W(R) = \alpha \frac{\mu(A)^2 \, \mu(D)^2}{R^6} F \qquad (6.45)$$

α is a numerical constant, μ(A) and μ(D) are the electronic transition moments for the acceptor absorption and the donor emission, respectively,

while F corresponds to the spectral overlap function

$$F = \int f_{Aa}(E)\, f_{De}(E)\, dE \qquad (6.46)$$

where $f_{Aa}(E)$ and $f_{De}(E)$ represent the normalized acceptor absorption and donor emission lineshapes, respectively. The efficiency of the energy transfer process can be specified in terms of the transfer radius, R_q, where the probability, i.e. the reciprocal lifetime τ_o^{-1} for the decay of the donor state (in the absence of the acceptor), is equal to the energy transfer probability so that

$$R_q = (\alpha\mu(A)^2\, \mu(D)^2\, F\tau_o)^{1/6} \qquad (6.47)$$

Now, provided that the major contribution to τ_o^{-1} originates from radiative decay, as is the case for the R_2^* centers, the transfer radius is

$$R_q = \left(\frac{\lambda^3 \mu(A)^2\, F}{8\pi^2}\right)^{1/6} \qquad (6.48)$$

where λ is the (mean) wavelength for the donor emission. Thus R_q is essentially determined by the spectral overlap function.

For atomic impurity states in solid Ar and in solid Kr efficient spectral overlap between the R_2^* emission and the acceptor absorption is effective for Xe impurity in solid Ar and in solid Kr, as is evident from Fig. 99.

Quantitative emission studies of these electronic energy transfer processes (CHESNOVSKY et al.,1972a, 1973b; GEDANKEN et al.,1973a) were conducted and analysed according to FÖRSTER's (1948) formula

$$\frac{\eta^0 - \eta}{\eta^0} = \sqrt{\pi} q \exp(q^2)[1 - \mathrm{erf}(q)] \qquad (6.49)$$

$$q = \tfrac{1}{2}\sqrt{\pi} C/C^* \qquad (6.50)$$

$$C^* = \frac{3}{4\pi R_q^3} \qquad (6.51)$$

where η is the donor emission quantum yield and $\eta = \eta^0$ at the acceptor concentration C=0. A typical plot of η for the Xe/Kr system is portrayed

in Fig. 100. The R_q values thus derived are summarized in Table 28 together with some theoretical data based on eq. 6.48. The temperature dependence of R_q in the Xe/Kr system originates from the temperature dependence of the position and of the width of the Xe atomic impurity band in solid Kr.

Electronic energy transfer to molecular impurities in RGS was studied utilizing the benzene molecule as a prototype (OPHIR et al.,1974, SCHWENTNER et al.,1978, ACKERMANN,1976, HASNAIN et al.,1977). The relevant energy levels and transitions for the free molecule and C_6H_6 in Ar, Kr and Xe matrices are depicted in Fig. 101. HASNAIN et al.(1977a) measured the dependence of the luminescence intensity in the benzene emission bands on the excitation energy. The intensity is much higher for excitation of host excitons than for direct excitation of benzene molecules in the transparent region of the host as is demonstrated for benzene in a Kr matrix (Fig. 102). Evidently, energy transfer from the host to the guest molecules takes place, an observation, made for all rare gas matrices.

ACKERMANN (1976) established that the ratio of host emission intensity to guest emission intensity (Fig. 103) is quite insensitive to changes in the surface quenching rate. A careful study of the concentration and thickness dependence of host and guest emission efficiencies in the excitonic region of the rare gas host indicated that for benzene in Xe and Kr matrices there is an important contribution of selftrapped excitons to the energy transfer for all host exciton states yielding a critical Förster Dexter radius of 28 - 29 Å in a Xe matrix and 21 - 22 Å in a Kr matrix.

In these studies it was difficult to sort out the contribution of electronic energy transfer from free exciton states of the host and that from trapped excitons. Energy migration from localized donor to a molecular acceptor in RGS was explored in the study of energy transfer from Xe atoms to benzene molecules when both partners had been embedded in an Ar matrix (ACKERMANN, 1976). Both centers are fixed in the Ar lattice and exciton diffusion is excluded. The transfer mechanism is exclusively of the Förster Dexter type. Again the intensity in the emission bands of both Xe and C_6H_6 has been measured (Fig. 104)

after excitation of Xe exciton states. More details of the line shape show up in the excitation spectra of the three emission bands at 1640 Å, 1460 Å and 1250 Å of Xe atoms in Ar matrix. The analysis results in a Förster Dexter radius of 24 Å. For the relaxation from n=2 → n=1 a rate constant of 1.2×10^{10} s^{-1} was obtained.

Finally, we mention briefly electronic energy transfer between localized states in liquid rare gases. Electronic energy transfer between Ar_2^* and Kr_2^* donor and Xe acceptor in liquid rare gases was studied by CHESHNOVSKY et al.(1973). In the liquid phase mass diffusion has to be considered. The relative donor emission yield of Kr_2^+ for the Xe liquid Xe/Kr system exhibits a linear dependence on the Xe impurity concentration. This behavior is different from that of the Xe/Kr solid alloys (Fig. 100) and can be accounted for in terms of a simple kinetic scheme with a rate constant $k_{ET}\tau_o = 6 \times 10^{-19}$ cm^3 which, with the value $\tau_o \approx 10^{-6}$ s^{-1} for the radiative decay of the Kr_2^* state, results in $k_{ET} = 6 \times 10^{-13}$ cm^3 s^{-1}. The approximate theoretical treatment of YOKOTA and TANIMOTO (1967) demonstrated that the energy transfer process in the liquid can be expressed in this case by a bimolecular rate constant. Then the rate constant k_{ET} for electronic energy transfer is

$$k_{ET} = 0.51 \cdot 4\pi (R_q^6 \tau_o^{-1})^{1/4} D^{*3/4} \qquad (6.52)$$

With the date $\tau_o = 10^{-6}$ s^{-1} and the relative diffusion coefficient D^* of the donor acceptor pair $D^* = 10^{-6}$ cm^2 s^{-1} (CHESHNOVSKY et al.,1973b) and the experimental value for k_{ET} a transfer radius $R_q = 24$ Å in the liquid was calculated. This value is in agreement with the value $R_q = 21$ Å from eq. 6.45. Thus the energy transfer process between localized states in the liquid involves a long range electronic energy transfer process coupled with diffusive motion.

7. Electron transport and electron-hole pair creation processes

Electronic transport properties have been treated in Chap. 18 in Vol. II of this series by SPEAR and LE COMBER (1977). They discussed the results of electron and hole mobility measurements in solid and liquid rare gases. In mobility experiments electrons or holes are accelerated in an external electric field. Due to the strong elastic and inelastic scattering cross sections, which allow only mean free paths of the order of some Å, the mean kinetic energies of the electrons in the conduction band are restricted to energies below ≈ 1 eV (see Table 29). In this section we report on results for electrons with kinetic energies of some eV's up to MeV's obtained by different techniques.

In a crystal electrons will interact with the lattice by creation or absorption of phonons. The energies of the acoustic phonons ($\lesssim 10$ meV) (Table 2) in RGS are small, compared to electron energies of some electron volts. In the experiments reported here changes in the electron energy by single phonon scattering events are not resolved. Therefore, electron-phonon scattering is described by an excape depth. The escape depth l_p is given by the mean distance after which the electron is scattered below the vacuum level of the sample or is trapped and can no longer escape from the sample into the vacuum.

Inelastic interaction of the probing electron with electrons of the crystal is described by an electron-electron scattering length L. In an inelastic electron-electron scattering event a secondary electron has to be excited in an allowed state above the occupied valence bands. Due to the large band gap, the minimal energy losses will be of the order of some eV's. Unscattered electrons have been separated from scattered electrons in energy distribution measurements of photoelectrons. The derived scattering length L represents the mean free path between inelastic electron-electron scattering events. The relevant scattering processes for different energy ranges following photoexcitation are sketched in Fig. 105.

The energy of high energetic electrons will be diminished by subsequent electron-electron and electron-phonon energy losses. For each electron-electron energy loss a secondary electron is excited from the valence band to an excited state and either a free electron-hole pair or an exciton,

i.e. a bound electron hole pair, has been created. The accumulation of holes and excited electrons is described by a mean energy W which corresponds to a mean value $\bar{N}$ of free electron hole pairs for a primary energy E_o:

$$\bar{N} = \frac{E_o}{W} \qquad (7.1)$$

For practical purposes, when the charge accumulation is used for detectors one is also interested in the r.m.s. fluctuation of the number $\bar{N}$ of pairs produced which is characterized by $\sqrt{F\bar{N}}$ with the Fano factor F (FANO 1947).

The study of these processes in RGS can provide new aspects, for example, concerning the socalled "universal curve" for the electron-electron scattering length L (see e.g. LINDAU and SPICER 1974). The threshold energies and the energy dependence near threshold of electron-electron scattering can be a model case for insulators in view of the large band gaps and the prominent excitonic structure in RGS. Further, because only acoustic phonons with small energies and no dipole moment are present in RGS of fcc structure, both the energy loss per electron-phonon scattering event and the cross-section are expected to be small. Therefore, l_p may reach much larger values than commonly observed in other solids.

Finally, electron energy loss processes are essential for a microscopic description of light and particle excitations in RGS. In many investigations (see e.g. Sections 2 and 6), high energetic particles, such as x-rays, α-particles and electrons are used as excitation sources (see e.g. KUBOTA et al., 1980). Most of the particle energy is converted to highly excited electrons. The slowing down of these electrons and the final partitioning of energy into phonons, luminescence light and slow electrons shall be described here. In this context, we also mention the differences observed in branching ratios for electron and α-particle excitation. They have been attributed to interaction of excited states due to the high density in the α-particle tracks (KUBOTA et al., 1977, CARVALHO and KLEIN, 1978). A fraction of the deposited energy can be reemitted in the form of x-rays. This conversion efficiency shows a monotonic increase with the atomic number Z (e.g. FINK and VENUGOPALA 1974), but considering the high density of the solid and liquid phase, reabsorption has to be taken into account.

For application purposes in high energy particle detectors liquid rare gases may be even more suitable than solid rare gases, because they combine the advantages of the electron scattering mechanisms in RGS, which are similar in liquids, with less preparation problems (e.g. the trapping of charge at grain-boundaries). For particle detection either the luminescence light output (Sect. 6 , KUBOTA et al. 1980) or the amount of charge collected by an external field can be used as a signal. The quantum efficiencies for both processes are expected to be high because of weak nonradiative quenching. The scattering in the mean number of charge per deposited energy should be small (i.e. small Fano factor). Finally, due to the very high mobility of electrons in RG solids and liquids, the response is expected to be extremely fast. Some of the basic results fundamental for the development of fast high energy particle detectors with high efficiency and high energy resolution using rare gas liquids will be discussed here.

After a short compilation of basic concepts describing electron-electron scattering (Section 7.1), experiments providing information about electron-phonon scattering l_p are discussed (Section 7.2). The threshold behavior of electron-electron scattering (Section 7.3) is basic for the charge multiplication processes (Section 7.5). Further, results for the energy dependence of the electron-electron scattering length L are presented in Section 7.4.

7.1 Concepts for the description of electron scattering

Theories of the inelastic scattering of electrons with atoms go back to BOHR (1913, 1915) and BETHE (1930). They have been modified for the solid state first by FERMI (1939). Here we will only summarize the background for understanding experimental results obtained for solid and liquid rare gases and refer the reader to the many reviews of this subject.

The theoretical framework is quite elaborate for energies of primary electrons large compared to the energy losses, i.e. when the first Born approximation holds. The differential scattering cross section per atom for an energy loss $\hbar\omega$ and momentum transfer q can be expressed by:

$$\frac{d^2\sigma}{d\omega\, dq} = \frac{2e^2}{\pi N \hbar v^2} \frac{1}{q} \mathrm{Im}\left[\frac{-1}{\varepsilon(\omega, q)}\right] \qquad (7.2)$$

where N is the density of atoms, v the velocity of the incident electron and $\varepsilon(\omega,q)$ the complex dielectric constant. The connection of optical experiments and electron energy loss experiments is given by Im $(1/\varepsilon(\omega,q))$ in the "optical limit" of hero momentum transfer q. For RGS it has been discussed in Chapter 17 of Vol. II of this series. Following, the treatment of POWELL (1974) the attenuation length $d^2\sigma/d\omega \cdot dq$ can be integrated for a limited energy loss range, corresponding to a particular excitation process n with mean energy ΔE_n by introducing the generalized oxcillator strength $f_n(q)$. The integration concerning the momentum transfer q requires in principle the q dependence of $f_n(q)$ which is difficult to obtain. Therefore, $f_n(q)$ is replaced by $f_n(0)$ and a constant C_n accounts for the functional form of $f_n(q)$:

$$\sigma_n = \frac{\pi e^4}{E_o} \frac{f_n(o)}{\Delta E_n} \ln \frac{4E_o C_n}{\Delta E_n} \qquad (7.3)$$

For plasmon excitation, for example C_n will be unity. Using the cross-section σ_n for specific excitations n and taking C≥1, an approximate expression for the total inelastic scattering cross-section σ_T can be written in the form:

$$\sigma_T = \frac{\pi e^4}{E_o} \sum_n \frac{f_n(o)}{\Delta E_n} \ln\left(\frac{4E_o}{\Delta E_n}\right) \qquad (7.4)$$

If the spectrum of characteristic excitation processes, which would for example consist of the K, L, M .... shell excitations and plasmons and the corresponding oscillator strengths $f_n(0)$, are not available, the energy dependence of the scattering cross-sections can be estimated from

$$\sigma_T = \frac{\pi e^4}{E_o} \sum_i \frac{N_i}{\Delta E_i} \ln\left(\frac{4E_o}{\Delta E_i}\right) \qquad (7.5)$$

N_i is the number of electrons in the ith shell available for excitation and ΔE_i is an average excitation energy which will always be greater than the corresponding binding energy. In this equation, differences between the gas phase cross-section and σ_T in the solid phase can only be

accounted for by different average binding energies ΔE_i, and typical solid state effects like plasmons do not appear explicitly.

BATTYE et al. (1974, 1976) have shown for typical insulators like alkali-halides and Al_2O_3 that the atomic ionisation cross-section describes the experimental results within the limits of the experimental accuracy quite well. In general, empirical formulas are applied which follow the calculations by BETHE (1930) and e.g. RUDGE and SCHWARTZ (1966). They use the following ansatz for single ionisation of the ith subshell:

$$\sigma_i = \frac{a_i N_i}{E_o P_i} \ln\left(\frac{E_o}{P_i}\right) \quad \text{for } E_o \geq P_i \qquad (7.6)$$

with an empirical constant a_i and the ionisation potential P_i. Values for the constants and tabulated stopping powers from 1 KeV to 100 KeV are given by BROWN (1974). The total atomic ionisation cross-section follows from

$$\sigma_T = \sum_i \sigma_i \qquad (7.7)$$

These formulas are valid only for electron energies large compared to the ionisation potentials. LOTZ (1967) has presented a modified formula with three free parameters a_i, b_i and c_i which describes satisfactorily the atomic ionisation cross-section also near threshold and up to some KeV:

$$\sigma_T = \sum_i \frac{a_i N_i}{E_i P_i} \ln\left(\frac{E_o}{P_i}\right) \left\{1 - b_i \exp\left[-c_i (E_o/P_i - 1)\right]\right\} \text{ for } E_o \geq P_i \qquad (7.8)$$

with σ_T in cm^2. The constants are listed in Table 30.

The mean free path L for electron-electron scattering in the solid phase is calculated from the total atomic ionisation cross-section by

$$L(E_o) = \frac{1}{\sigma_T(E_o)} \cdot \frac{A}{L \cdot \rho} \quad [cm] \qquad (7.9)$$

with the atomic weight A, the density ρ and the Loschmidt number L.

In Fig. 106 the calculated energy dependence of L(E) for Ar is shown in the region of 10 eV to 1000 eV using e.q. 7.8 and 7.9, the gas phase ionization energy P_1 and the constants listed in Table 30. In the solid phase the threshold energies are lower as in the gas phase. Therefore,

L(E) has also been calculated for Xe, Kr, Ar and Ne (Fig. 105) by replacing P_1 by P_1'. P_1' (Table 30) is the energy of the lowest exciton (n=1) which, as will be discussed later, is the most probable threshold for scattering (SCHWENTNER et al. 1973, SCHWENTNER 1974, 1976b).

In this approximation the influence of the particular properties of the solid phase on the scattering process is neglected. Differences between the solid state cross-section and the atomic cross-section are expected to show up strongly near threshold. For this region a different approximation has been proposed. In the solid state description a primary electron with momentum k and energy E will be scattered to the momentum k' and E' by exciting a second electron from the valence band with k" and E" to k"' and E"'. Momentum conservation requires

$$k - k' = k'' - k''' + k_o \tag{7.10}$$

and energy conservation requires

$$E - E' = E'' - E''' \tag{7.11}$$

where k_o is a principal lattice vector (which may be zero). This problem has been formulated by BERGLUND and SPICER (1964) and an extended calculation for silicon has been given by KANE (1967). The matrix elements are obtained from a screened Coulomb interaction with a frequency and momentum dependent dielectric function. The density in k space for all relevant k vectors follows from the band structure. KANE confirmed by his calculation that the complex scattering problem can be strongly simplified without changing the numerical results significantly by ignoring the restrictions due to momentum conservation. This simplification works because of the averaging effect of the large variety of possible scattering events contributing to L(E). The transition probability P_s (E, E') for scattering a primary electron at E to a lower energy E' is then given by an integration over several densities of states:

$$P_s(E,E') = \frac{2\pi}{\hbar^2} \int_{VB} |M|^2 \, \mathcal{S}_{CB}(E') \, \mathcal{S}_{VB}(E'') \, \mathcal{S}_{CB}(E''') \, dE'' \tag{7.12}$$

where $\mathcal{S}_{CB}$ (E'), $\mathcal{S}_{CB}$ (E"') are the final densities of states of the primary and secondary electrons respectively and $\mathcal{S}_{VB}$ (E") is the initial density of states of the secondary electron and M is the matrix element.

The inverse lifetime or total scattering probability P(E) follows as:

$$P(E) = \int P_s(E, E') \, dE' \tag{7.13}$$

and the mean free path L(E):

$$L(E) = v_g(E) \,/\, P(E) \tag{7.14}$$

where v_g is the electron group velocity. SCHWENTNER (1976) proposed a further simplified evaluation for rare gas solids in the region near threshold. The matrix element has been taken constant in the limited energy range of $\approx$ 10 eV above threshold, the width of the valence bands has been neglected for the integration of E" and parabolic conduction bands have been used

$$\mathcal{S}_{CB} \propto (E-E_G)^{1/2} \tag{7.15}$$

where E_G is the gap energy. Then the integrations can be solved analytically yielding

$$P(E) = C(E-2E_G)^2 \tag{7.16}$$

and

$$L(E) = C(E-E_G)^{1/2} \, (E-2E_G)^{-2} \tag{7.17}$$

with a free parameter C. The assumption of parabolic conduction bands is reasonable for the lower s type conduction bands. The structures due to the higher lying d bands (see Section 3) may be smeared out. The strong excitonic structures will change both, the density of states and the scattering threshold as will be discussed in Section 7.4.

The scattering of electrons for mean kinetic energies smaller than $\approx$1 eV has been treated in Chapter 18 in Vol. II of this series using the results of mobility measurements (LE COMBER et al. 1976). The cross-sections in the solid and liquid phase are nearly identical, therefore, it is sufficient to discuss here the results for the liquid phase. For the mean free path the density change has to be considered which causes differences in the mobilities for solid and liquid phase. Electrons in the conduction bands can be treated as free electrons. For low electric fields the experimental results have been excellently predicted by the theory of LEKNER (1967). This theory gives the mean free path for both, the energy loss Λ_o which corresponds in our case to inelastic electron-phonon scattering and for the momentum transfer Λ_1 which means elastic scattering (COHEN and LECKNER 1967) (see Table 29). At higher fields the mobility saturates. This has

been ascribed to changes in the effective mass of the electrons caused by structures in the conduction bands. The limiting average kinetic energies of about 1 eV are reached for electric field strengths of 10^5V/cm (see LE COMBER et al. 1976 and YOSHINO et al. 1976).

Electron phonon scattering is the dominant process at least up to the onset of inelastic electron-electron scattering around 10 eV (Fig. 105 and Table 30). Above about 1 eV theoretical cross-sections for electron phonon scattering are not available for RGS. For other insulators such as alkalihalides the energy dependence of the electron-phonon mean free path has been calculated for optical phonons e.g. by LLACER and GARWIN (1969) yielding an approximately linear increase of the mean free path with electron kinetic energy. Typical experimental values for alkalihalides scatter between 10 Å and 100 Å. For the interaction of electrons with the acoustic phonons of RGS's similar calculations are not available. Therefore, only the scarce experimental data presented in Section 7.2 can be discussed.

For larger energies electron-electron scattering becomes an additional and important mechanism. In order to explain the dissipation of the primary energy by successive electron-electron and electron-phonon scattering events, the energy and space distribution of the avalanche of primary and secondary electrons has to be evaluated. This is a problem encountered in all photoemission experiments (see e.g. CARDONA and LEY 1978). Several attempts have been made in analysing photoemission data (e.g. BERGLUND and SPICER 1964, KANE 1966) using empirical models, Monte Carlo calculations and others. Furthermore, a variety of empirical formulas have been developed to describe the deposition rate of energy versus penetration depth in cathode luminescence work (e.g. FANO 1940, KINGSBLEY and PRENER 1972).

A quantity which is relevant for energy deposition is the average energy W necessary to create an electron hole pair (eq. 7.1). In semiconductors an empirical relation between W and the band gap E_G is known (ALIG and BLOOM 1975) which has been explained in the free particle approximation using conservation of energy (SHOCKLEY 1961) and of momentum (KLEIN 1968). It is assumed that as long as energetically possible the electron energy is used to create electrons and holes. Finally, below a threshold energy E_M the energy is insufficient for exciting another electron hole pair. Then the remaining excess energy above E_G is lost by phonon emission. Since W must

be the sum of the band gap energy and the mean excess energy of electrons and holes we get, with the density of states proportional to $\sqrt{E}$ in the free particle limit:

$$W = E_G + 2\int_0^{E_M} E\sqrt{E}\,dE \Big/ \int_0^{E_M} \sqrt{E}\,dE = E_G + 6\,E_M/5 \qquad (7.18)$$

When both energy conservation and momentum conservation are fully fulfilled

$$E_M = 3\,E_G/2 \qquad (7.19)$$

and the general relation for semiconductors follows as:

$$W = 2.8\,E_G \qquad (7.20)$$

This relation has been applied for solid and liquid rare gases (see Chapter 18 in Vol. II, HOWE et al. 1968, and Table 31).

In a series of careful investigation, the evaluation of Shockley's formula has been modified for liquid rare gases (DOKE et al. 1976). In this case exciton excitation (bound electron hole pairs) is an energy loss process competitive to free electron hole pair creation and has to be incorporated in the mean energy W (PLATZMAN 1961):

$$W = E_G + \bar{E}_{ex}\,(\bar{N}_{ex}/\bar{N}_{e\text{-}h}) + \int_0^{E_1} E\,(dN/dE)\,dE \Big/ \int_0^{E_1} (dN/dE)\,dE \qquad (7.21)$$

In addition to the exciton losses with a mean exciton energy $\bar{E}_{ex}$ and the ratio of the number of excitons to the number of electron hole pairs $(\bar{N}_{ex}/\bar{N}_{e\text{-}h})$ both derived from optical data, further essential changes have to be noted: The hole kinetic energy has been accounted for by adding half of the valence band width to E_G which explains the missing factor of 2. The free particle density of states $\sqrt{E}$ has been replaced by that derived from the band structure. More important, the mean excess energy E_M has been replaced by E_1, i.e. the energy of the lowest exciton, because momentum conservation has been ignored. These calculated values (Table 31) are approximately a factor of two lower than those derived from the empirical law for semiconductors. We shall return to this point when discussing the experimental data. We note that DOKE et al. (1976) have also calculated the Fano-factors (FANO 1947, see eq. 7.1) for rare gas liquids.

7.2 Electron-phonon scattering

Electron phonon scattering in RGS has been studied for electron energies below the threshold of electron-electron scattering which means for electrons at the bottom of the conduction band up to $\approx$ 10 eV. The escape depth l_p has been derived from three types of photoelectron yield experiments:

In the first type of experiment (process 1 in Fig. 105), photoelectrons from a metal substrate (usually Au) are injected into an RGS overlayer of known thickness d. The electrons are excited by photons with energies smaller than the first absorption line of the RGS film but larger than the work function of the substrate. The yield of electrons penetrating through the RGS film is measured. From the thickness dependence of the yield the escape depth l_p is calculated. In Fig. 107 experimental results are compiled. The thickness dependence can be divided into three parts. For very thin film thicknesses (0 - 50 Å) the yield is sensitive to the cleanliness and hence to the work function of the substrate. An increase as well as a decrease with film thickness both up to a factor of 2 have been observed. This behavior has been attributed to changes in the work function of the layer system. For lager thicknesses of 50 Å $\leq$ d $\leq$ 300 Å a steep decrease in the yield is observed for Ar, Kr and Xe. Finally, for d $>$ 300 Å the slope of the decrease on a logarithmic scale becomes gradually smaller. The second and third range can be used to derive the escape depth l_p. Usually, an experimental escape probability for the yield Y of the form

$$Y(d) = Y_o \, e^{-d/l_p} \qquad (7.22)$$

has been assumed. Evidently, the results in Fig. 107 cannot be explained by a straight line with the slope l_p. Equation 7.22 would be correct, if the electrons would be lost for detection after one scattering process. Of course, this model is too simple for a description of the yield experiments and a number of microscopic processes have to be considered: electrons can be scattered below the vacuum level in the case of Xe and Kr by successive phonon emission. Also phonon absorption plays a role.

In Ar and Ne the vacuum level lies below the bottom of the conduction band (see Section 3) and all free electrons should be able to excape as far as their energy is concerned. The decrease of the yield indicates trapping of electrons at grain boundaries, at dislocations and at impurities. An

important loss process diminishing the yield is elastic and inelastic backscattering of electrons to the substrate. This loss can be larger near the substrate i.e. at small film thicknesses than at larger separation from the substrate. Further, when the electron is near the substrate a positive image charge will be formed. Due to inelastic scattering processes the electron energy can be reduced below the ionisation limit for the system electron plus image charge and the electron will be recaptured by the substrate.

Quantitative model calculations to explain the thickness dependence have not been published. Nevertheless, in order to obtain a rough estimate for the escape depth, the curves in Fig. 106 have been approximated by straight lines in the region of 50 to 200 Å and from 200 Å up to the larger thicknesses (Table 32). A mean free path for inelastic electron phonon scattering can be estimated from equation 7.23 (BARAFF 1964).

$$\Lambda_o = 3 l_p \sqrt{\frac{\bar{E}_{ph}}{3\bar{E}_o}} \qquad (7.23)$$

With a mean electron kinetic energy $\bar{E}_o$ of $\approx$ 1 eV (see insert in Fig. 107) a mean phonon energy $\bar{E}_{ph} \approx 5$ meV and l_p = 1000 Å a mean free path of 150 Å was obtained (SCHWENTNER 1976). It should be kept in mind that this value can only be regarded as a crude estimate in view of the various processes contributing to l_p.

In a second type of yield experiments (processes 3, 4 in Fig. 105) the photoelectrons are created by photoabsorption in the rare gas film (Fig. 108). The yield depends on the absorption doefficient k and the escape depth. For isotropic excitation of electrons and for an exponential escape probability the following thickness dependence is expected (see e.g. SCHWENTNER 1976 and references therein):

$$Y = \frac{1}{2} \frac{k \, l_p}{1+k} \, 1_p \quad (1 - \exp - (d \, (k+1/l_p)) \qquad (7.24)$$

Interference effects and reflectivity losses have been neglected. The calculated yield using several escape depths as a parameter is compared with the experimental result for pure Ne in Fig. 108 suggesting an escape depth of $l_p \approx 3500$ Å.

Due to the factor 1/2, which results from the assumption that 50% of the electrons will run towards the substrate and 50% towards the surface, the efficiency is restricted to values below 0.5 electrons per photon in this simple model. For Ar (Fig. 108) an increase of the yield above 0.6 electrons per photon has been measured. This high yield can be explained by either including secondary electrons from the substrate or by taking into account the increased density of electrons at the surface due to the absorption process. Electrons reaching the metal substrate can produce secondary electrons quite efficiently (PETRI 1926). These secondary electrons have been detected in energy distribution measurements of photoelectrons (see Section 7.5). The solid curves in Fig. 108 show fits for Ar for two escape depths l_p including secondary electrons with different emission coefficients β. Further, the enhancement of the yield caused by the nonuniform distribution of electrons follows from a random walk model calculation with three different values for Λ_o and $\beta = 0$ (dashed lines Fig. 108). For thick films, the random walk contribution will be more important than secondary electrons. A combination of both processes with l_p between 1000 - 2000 Å, β between 0.2 to 0.3 and Λ_o between 5 Å to 500 Å fits the experiments.

Escape depth have been determined in a third way by HASNAIN et al.(1977e). In doped RGS photoelectron emission is observed below the threshold for host emission due to energy transfer from host excitons to impurity centers and escape of an electron (see Section 6.13). Using a similar type of analysis as described above, HASNAIN et al. (1977e) derived escape depths from the experimental thickness dependence of the yield in the excitonic region of Kr and Ar matrices doped with 0.01% C_6H_6. Within the experimental uncertainties they fit to the other results (Table 32).

Summarizing we note that the escape depth for all RGS is unusually large in the order of 1000 Å for electrons below the electron-electron scattering threshold. These large values are mainly attributed, as has been mentioned before, to the small cross-section and small energy losses for the emission of the acoustic phonons and to the small electron affinities which are even negative in Ar and Ne. These escape depths exceed by far all values reported for other materials.

7.3 Threshold for electron-electron scattering

The threshold for electron-electron scattering E_{sc} can be referenced either to the bottom of the conduction band, or to the vacuum level or to the top of the valence bands. In order to get a consistent picture including the results of photoluminescence and photoelectron emission measurements, where electron excitation energies from the valence bands are essential, we use the top of the valence bands as a common reference energy for E_{sc}.

From electron energy loss data one obtains immediately the smallest energy losses possible. The pertinent experimental results have been collected by SONNTAG (1977) together with excitation energies from optical spectra in Tables IV, V, VI and VI of Chapter 17 in Vol. III of this series. Despite different selection rules causing changes in the overall shape of the spectra, the lowest energy losses (for both high and small primary electron energies) and the lowest absorption lines correspond to the n=1 excitons (Table 33). Of course, the details of the onset would require an extrapolation of the low energy tail of the n=1 excitons. Neglecting this latter point, the scattering onset E_{sc} is given by

$$E_{sc} = E_G + E_1 \qquad (7.25)$$

when an excited valence electron in the conduction band is inelastically scattered to the bottom of the conduction band by exciting another valence electron to the n=1 exciton state.

The threshold energy has been studied in photoelectron emission and luminescence experiments. In these experiments the primary electron is created together with a hole by photoabsorption whereas in energy loss experiments an excess electron is injected and the corresponding hole is missing. Consequentely, a difference in the threshold could be expected from a process corresponding to a recapture of a primary electron by one of the holes and the subsequent decay into two excitons in photoabsorption experiments. In this case E_{sc} would be smaller:

$$E_{sc} = 2\, E_1 \qquad (7.26)$$

Other processes which deserve attention in this context are double excitations, since they could mask the onset of scattering processes.

Double excitation processes as well as scattering processes result in two low energy electrons or excitons where the sum of the energies is equal to $\hbar\omega$. Therefore, they cannot be distinguished immediately. If their respective threshold energies are different, they can be identified easily. More detailed criteria could be obtained from the thickness dependence of the ratio of unscattered and scattered electrons.

A special type of double excitation, i.e. the formation of an "electronic polaron complex" has been discussed by DEVREESE et al. (1972) and KUNZ et al. (1972) and applied to alkalihalides. The optical transition leads to an electron hole pair dressed by an electronic polarisation cloud and an additional exciton. Two different types of electronic polaron complexes have been distinguished: in the bound complex the dressed electron is coupled to the dressed hole via Coulomb interaction, in the free complex this Coulomb interaction is neglected. The cross-sections for the polaron complex in rare gas solids should be similar to those for alkalihalides, because the coupling constants are of the same order. The treshold for the free complex lies at $E_G + E_1$ and for the bound complex near $2\,E_1$ on the basis of this model MÖLLER et al. (1976) have estimated the cross-sections for both processes in Ar.

In the photoelectron yield curves (SCHWENTNER et al. 1973) and the more recent curves by SCHWENTNER (1974) a decrease at a photon energy E_x is observed for solid Kr and Xe, while it is absent in the yield spectra for solid Ar. E_x can be identified with the threshold energy E_{sc} for electron-electron scattering (Table 33). For solid Kr and Xe just above threshold part of the primary electrons will be scattered below the vacuum level. Also near threshold the secondary electrons can only by excited to an exciton state or to the bottom of the conduction band below the vacuum level. Thus, both scattering partners are lost for the yield. In solid Ar the vacuum level lies below the bottom of the conduction band. Therefore, the primary electron can escape in any case and no significant decrease is observed at $E_x = E_{sc}$.

A luminescence yield spectrum up to $\hbar\omega = 55$ eV has been reported by MÖLLER et al. (1976) (Fig. 109). In luminescence any electron-electron scattering will cause an increase of the yield. The luminescence channel due to the self-trapped excitons is fed by excitons and conduction band states, i.e.

from any possible state of the primary and secondary electrons. The first pronounced increase is observed at $\hbar\omega = 25.5 \pm 0.5$ eV (m = 1 in Fig. 109) and lies within the experimental accuracy at $E_{sc} = E_1 + E_G$. At these excitation energies only a doubling of the holes due to electron-electron scattering is possible. MÖLLER et al. were able to exlain the yield spectrum (Fig. 109) in detail: The shape of the onset at around 27 eV is due to the energy dependent scattering cross-section as derived by SCHWENTNER (1976); the increase of the yield by more than a factor of two is due to the higher efficiency of the low energy, once scattered, electrons. At higher photon energies two additional pronounced thresholds are observed, denoted by m=2 and m=3. The experimental values of $E_{m=2}$ = 37,5 $\pm$ 1 eV and $E_{m=3}$ = 50 $\pm$ 2 eV correspond nicely to $E_G + 2\,E_1$ = 38.3 eV and to $E_G + 3\,E_1$ = 50.3 eV. Therefore, the final states at these thresholds are predominantly one electron hole pair plus m excitons per primary electron.

The onset of electron-electron scattering has also been identified in photo electron energy distribution curves. These curves will be discussed in more detail in Section 7.4 to derive the energy dependence of the electron-electron scattering length. With increasing excitation energy the kinetic energy of the unscattered electron increases (Fig. 110). The onset of electron-electron scattering manifests itself in two features: a sudden decrease in the high energy part of unscattered electrons (maximum A) and a strong increase in the dashed region due to scattered electrons which are concentrated near zero kinetic energy. The corresponding photon energies have been collected in Table 33. Further, the onset can be taken from a fit of the energy dependence of the scattering length (Fig. 112). These values are approximately 1 eV lower than those obtained from Fig. 110. Both sets of E_{sc} values are in agreement if one notes that the fit corresponds to an extrapolation to $L \to \infty$, whereas the former set corresponds to the well observable onset.

Summarising the results for the threshold values for electron exciton scattering E_{sc} one observes a general agreement with the value expected from electron energy loss experiments. This shows that scattering of primary electrons to the bottom of the conduction band and excitation of an m=1 exciton is the dominant process, whereas the bound polaron complex with threshold energy $2E_1$, can be excluded.

The free polaron complex can not be excluded on the basis of its threshold energy. The thickness dependence has been studied only in the case of electron energy distribution curves for Ar (SCHWENTNER 1974). The maximum cross-section for the polaron complex is expected at $E_G + 1.2\ E_I = 28.6$ eV (DEVRESE et al. 1972). In this energy region one observes an increase of the ratio of scattered to unscattered electrons with sample thickness, in contrast to the prediction for double excitation. Thus, although one cannot exclude the free polaron complex from these rough estimates, its contribution has to be small.

7.4 Energy dependence of electron-electron scattering mean free path

Electron energy distribution curves in the region of electron-electron scattering have been reported by SCHWENTNER (1974, 1976). In Fig. 110 the EDC's of solid Ar, Kr and Xe are shown for photon energies between an energy somewhat below twice the band-gap energy and 30 eV where electron-electron scattering is important. For Ar and Xe, EDC's have been measured for several thicknesses between 10 and 300 Å. Each spectrum can be divided into two parts. The first part with high kinetic energies (A, B) is due to unscattered electrons which have been directly excited from the valence bands of the rare gas. The structure (A, B) contains information about the band structure as discussed in Section 3. After an inelastic electron-electron scattering event an electron excited from the valence bands will appear in the second part (the hatched region) of the EDC's. The kinetic energy of an electron which has been excited from the top of the valence band (right arrow) and has suffered an energy loss corresponding to the excitation of an exciton is marked by E'. A maximum appears below E' showing the strong increase of the scattering cross-section with photon energy. Also, at photon energies below E_{sc} there are low energy electrons observed which are due to two processes:

(i) Hot electrons from the Au substrate excited by transmitted photons and penetrating through the rare gas film (see process 1 in Fig. 105 and Section 7.2). The intensity and shape of EDC's from the substrate support this explanation.

(ii) Approximately 50% of the electrons excited in the rare gas film reach the Au substrate and produce secondary electrons with an efficiency increasing with electron energy from 20% to 40%. The secondaries will partly leave the sample yielding an energy distribution similar to an EDC from the Au substrate (process 3 in Fig. 105).

The energy dependence of the electron-electron scattering length L (E) has been derived (SCHWENTNER 1976) in several ways from the EDC's (Fig. 110):

(i) from the decrease of the counting rate of unscattered electrons associated with a distinct initial energy when the electron kinetic energy is varied by means of varying $\hbar\omega$ (Fig. 111 left part);

(ii) from the thickness dependence of the counting rate of unscattered electrons for the different photon energies (Fig. 111 right part);

(iii) from the ratio of counting rates within the part of unscattered electrons in one EDC (for example ratio of maximum A to maximum B in Fig. 110) for different photon energies.

(iiii) The consistency of the evaluation has been checked by a comparison of counting rates at equal kinetic energies in spectra obtained with different photon energies.

The results for L(E) for solid Ar, Kr and Xe are shown in Fig. 112 (SCHWENTNER 1976). L(E) decreases from very large values near the scattering onset within 2 eV to values of about 10 Å and within 10 eV down to 1-5 Å. The main sources for errors are uncertainties in the absorption constant. The independent ways of calculating L allow for averaging. The influence of electron phonon scattering on L(E) is considered to be small. Due to the small phonon energy, the phonon scattered electron would be still in the unscattered region of the EDC. An electron phonon scattering event would only increase the path of the electron to the surface in a random walk process.

The experimental results have been compared with the models discussed in 7.2. The full lines in Fig. 112 have been calculated for the best fit from the following equation:

$$L(E) = C(E-E_G)^{1/2}\ (E-E_{sc})^{-2} \qquad (7.27)$$

with the constants C and E_{sc} as parameters. In this relation, E_G in the second term (eq. 7.17) has been replaced by E_{sc} to account for the energy losses due to excitons. The calculated curves follow the experimental values with the E_{sc} values from Table 33. A calculation according to the gas phase ionisation cross-sections (eq. 7.8) as well as an integration of

the loss function as proposed by POWELL (1974) (eq. 7.5) do not fit the experimental scattering length data equally well (SCHWENTNER 1976).

A comparison of L(E) for rare gas solids with some other materials has been made by SCHWENTNER (1976). The striking, though not unexpected point is the large energy range where electron-electron scattering does not occur and the very steep decrease of L(E) near threshold. Some eV above the threshold L(E) follows the so-called "universal curve" (see e.g. LINDAU and SPICER 1974).

7.5 Generation of electron hole pairs by high energy particles

As mentioned in the introduction to this section, liquid rare gases have found wide application as detector media in high energy particle detectors. Thus, the processes underlying the occurrence of electron avalanches in liquid rare gases have been investigated in several papers (KUBOTA et al. 1976, 1980, TAKAHASHI et al 1975, DOKE et al 1976, and references cited herein). Electrons with energies of 0.48 MeV, 0.55 MeV, 0.976 MeV and 1.05 MeV from radioactive materials have been used to excite liquid Xe, Ar, Xe doped Ar and Kr doped Ar. A fast ionisation chamber for electron collection has been filled with carefully purified liquid rare gases. Positive ions have been shielded by grids. The voltage pulses at the collector for each exciting particle have been amplified and the distribution of pulse-heights was stored in a multichannel analyser. From the position of the maxima in the pulse-height spectrum it could be shown that the number of electrons (i.e. pulse-height) is proportional to the energy of the exciting particles. Therefore, the spectra (Fig. 113) represent the energy distribution of the exciting particles. The scaling factor of the energy scale (i.e. the proportional constant) is the mean electron-hole pair creation energy W. Evidently W is smaller for Xe doped Ar than for pure Ar and therefore the energy scale is enlarged in the doped liquid (Fig. 113). From a comparison with the known pair creation energy of a gas chamber filled with Ar (95%) + CH_4 (5%) (W_{gas} = 26.09 ± 0.13 eV), the pair creation energies for liquid Ar and Kr have been derived. The experimental values agree excellently with the calculated value of DOKE et al. (1976) (Table 31). These values seem to be more reliable than the larger ones measured in the course of mobility experiments (Table 31).

The experimental support for the model calculation of DOKE et al. (1976) shows that this model is appropriate for insulators whereas the generally accepted rule used for semiconductors fails. Further, the assumptions made in DOKE's calculation (see Section 7.1 and eq. 7.21) are justified. The assumed loss in efficiency due to exciton excitations has been verified independently in the experiment on Xe doped Ar. In this case, the exciton energy of Ar is sufficient to ionize the Xe dopand (see also section 6). Via this process the loss due to Ar excitons can be eliminated. Indeed the increase in ionisation yield observed for Xe doped liquid Ar (Fig. 113) corresponds to the calculated $\tilde{N}_{ex}/\tilde{N}_{e-h}$ ratio (eq. 7.21). With the W values also the calculated Fano factors have been corroborated.

The interest in liquid Xenon as a detector medium is motivated by the large electron mobility and the large atomic number. In addition, the efficiency due to the low W values and the energy resolution due to the small Fano factors in the liquid phase are better than in the gas phase. For 1 MeV gamma rays a resolution of 3 keV FWHM is expected which is near the actual energy resolution of 1.5 keV of conventinal Ge(Li) detectors with large volume (DOKE et al. 1976).

8. Concluding Remarks

The understanding of the electron structure of the ground and excited states in condensed rare gases is fairly complete for pure RGS. In this chapter we have attempted to shift the focus of interest to structurally and compositionally disordered rare gases including solid rare gas alloys, metal-rare gas solid mixtures, liquid rare gases and liquid rare gas alloys. The basic experimental results concerning the electronic states of these materials have been surveyed. The theory of the electronic structure of disordered systems does not provide general unified concepts, comparable to the Bloch theorem for ideal crystalline solids. We have not attempted to wrench the diverse systems of disordered condensed rare gases from their natural settings. The current theoretical interpretation relies in many cases on conventional solid state concepts, e.g. band structure, densities of states, Wannier and Frenkel exciton states. Impurity states in alloys behave more as impurity states in crystalline materials. Excitons in liquids were considered within the framework of solid state approach, while metal-rare gas solids were discussed in terms of metal-nonmetal transitions from a heavily doped disordered semiconductor to an amorphous metallic material.

We have encountered some rather exotic systems. Medium relaxed electronically excited states and, in particular, bubble states in liquid Helium are examples for novel phenomena in isolated centers. Metal-rare gas solid mixtures provide a nice demonstration for the effects of microscopic clustering and metal-nonmetal transitions in "expanded" low-temperature metals. Recently even pure metallic xenon at 330 kilobars has been prepared (NELSON and RUOFF 1979).

Complementary and supplementary to the information concerning electronic structure is the new and diverse information concerning excited state dynamics in condensed rare gases. During the last few years this field has made an impressive experimental progress. While until recently all the information concerning excited state relaxation phenomena originated from optical emission and electron emission studies under steady state conditions, new experiments in this field advanced photoselective excitation and time resolved interrogation methods on a time scale of $\approx$ 100 ps. Further experimental progress in time resolved studies will undoubtedly unveil the nature

of a variety of interesting nonradiative relaxation phenomena involving exciton selftrapping, vibrational relaxation, electronic relaxation and energy transfer in these materials.

It has often been stated that the conceptually simple intermolecular interactions in RGS render them to be useful prototypes for the description of insulators and molecular crystals. These materials will also serve as prototypes for the understanding of radiationless processes. The description of relaxation processes in excited states is relatively simple, in view of the simplicity of the phonon states in these materials, where interconversion of electronic energy into vibrational energy involves only acoustic phonons. However, the achievements of the theory of electronic relaxation in insulators are still fragmentary and phenomenological. Further experimental and theoretical progress is required to establish models and concepts for a more complete and unified description of excited state dynamics in insulating materials.

The present survey of electronic excitations in condensed rare gases illustrates the interplay between molecular and solid state concepts. Solid state theoretical concepts were extensively utilized for the description of band structure and electronic excitations in pure RGS as well as in the alloys and liquids. Nevertheless, even in that domain a tight binding type approach resting on the "molecular" properties of the constituents proved a useful starting point. The analysis of medium-relaxed excited states requires the molecular approach both for the selftrapped excitons in the pure materials as well as excited impurity states in doped solid and liquid rare gases. The experimental and theoretical studies of rare gas clusters may lead to a merging between the molecular and solid state points of view. Studies of molecular clusters in supersonic beams will extend this interesting research area to finite systems.

Acknowledgments

We wish to thank our colleagues from the laboratories at the Institute for Experimental Physics, University of Kiel, the Hamburg Synchrotron Radiation Laboratory HASYLAB at DESY and the Department of Chemistry, Tel Aviv University for their support. We especially are indebted to O. Cheshnovski, U. Even, A. Gedanken, R. Haensel, U. Hahn, I. Messing, Z. Ophir, P. Rabe, B. Raz, V. Saile, M. Skibowski, B. Sonntag, W. Steinmann and G. Zimmerer to whom we are grateful for rewarding cooperation. We have enjoyed many stimulating and interesting discussions with them.

Special thanks go to H. Lehmann, A. Schmidt and U. Steusloff for their patience and skill in carefully typing the manuscript and tables.

REFERENCES

Abeles, B., Ping Sheng, Coutts, M.D. and Arie, Y. (1975)
Adv. Phys. 24, 407.
Abeles, B., Pinch, H.L. and Gittleman, J.I. (1975)
Phys. Rev. Lett. 35, 247.
Ackermann, Ch. (1976)
Thesis, Universität Hamburg.
and DESY Internal Report F41-76/04.
Ackermann, Ch., Brodmann, R., Tolkiehn, G., Zimmerer, G., Haensel, R. and Hahn, U. (1976a)
J. Luminescence 12/13, 315.
Ackermann, Ch., Brodmann, R., Hahn, U., Suzuki, A. and Zimmerer, G. (1976b)
phys. stat. sol. (b) 74, 579.
Alig, R.C. and Bloom, S. (1975)
Phys. Rev. Lett. 35, 1522.
Altarelli, M., Andreoni, W. and Bassani, F. (1975)
Solid State Comm. 16, 143.
Anderson, P.W. (1958)
Phys. Rev. 109, 1492
Andreoni, W., Altarelli, M. and Bassani, F. (1975)
Phys. Rev. B11, 2352.
Andreoni, W. Perrot, F. and Bassani, F. (1976)
Phys. Rev. B14, 3589.
Andreoni, W., Crescenzi, M. De, and Tosatti, E. (1978)
Solid State Comm. 26, 425.
Andrews, L. and Pimentel, G.C. (1967)
J. Chem. Phys. 47, 2905.
Antoniewicz, P.R. (1977)
Phys. Rev. Lett. 38, 374.
Asaf, U. and Steinberger, I.T. (1971)
Phys. Lett. 34A, 207.
Asaf, U. and Steinberger I.T. (1974)
Phys. Rev. B10, 4464.
Atzmon, R. Cheshnovsky, O., Raz, B. and Jortner, J. (1974)
Chem. Phys. Lett. 29, 310.
Avci, R. and Flynn, C.P. (1976)
Phys. Rev. Lett. 37, 864.
Avci, R. and Flynn, C.P. (1978)
Phys. Rev. Lett. 41, 428.
Bakale, G., Sowada, U. and Schmidt, W.F. (1976)
J. Phys. Chem. 80, 2556.
Baldini, G. (1962)
Phys. Rev. 128, 1562.
Baldini, G. and Knox, R.S. (1963)
Phys. Rev. Lett. 11, 127.
Baldini, G. (1965)
Phys. Rev. 137A, 508.
Balling, L.C., Havey, M.D. and Dawson, J.E. (1978)
J. Chem. Phys. 69, 1670.
Baroni, S., Grosso, G., Martinelli, L. and Pastori Parravicini, G. (1979)
Phys. Rev. B20, 1713.

Baraff, G.A. (1964)
Phys. Rev. 135A, 528
Barker, I.A. (1976)
in Rare Gas Solids, edited by M.K.Klein and J.A.Venables,
Vol. I, p.212, Academic Press, London.
Basov, N.G., Bogdankevich, O.V., Danylichev, V.A., Devyatkov, A.G.,
Kashnikov, G.N. and Lantsov, N.P. (1968)
JETP Letters 7, 317.
Basov, N.G., Balashov, E.M., Bogdankevich, O.V., Danilychev, V.A.,
Kashnikov, G.N., Lantzov, N.P. and Khodkevitch, D.D. (1970)
J. Luminescence 1, 2, 834
Basov, N.G., Danilychev, V.A., Molchanov, A.G. Popov, Yu.M. and
Khodkevich, D.D. (1973)
Isv.Ak.Nauk. SSR, Ser. Fiz. 37, 494.
Battye, F.L., Jenkin, J.G., Liesegang, J., Lechey, R.C.G. (1974)
Phys. Rev. B9, 2887.
Battye, F.L., Liesegang, J., Lechey, R.C.G. (1976)
Phys. Rev. B13, 2646.
Beaglehole, D. (1965)
Phys. Rev. Lett. 15, 551.
Belov, A.G., Fugol, I.Ya. and Savchenko, E.V. (1973)
Solid State Comm. 12, 1.
Belyaeva, A.A., Predtechenskii, Y.B. and Shcherpa, L.D. (1969)
Bull. Acad. Sci. USSR Phys. Ser. 33, 825.
Berglund, C.N. and Spicer, W.E. (1964)
Phys. Rev. 136, A 1030, A 1044.
Berreman, D.W. (1967)
Phys. Rev. 163, 855.
Bethe, H. (1930)
Ann. Phys. (5) 5, 525.
Blair, M., Pooley, D., Smith D. (1972)
J. Phys. C 5, 1537.
Boehmer, W., Haensel, R., Schwentner, N. and Boursey, E. (1980)
Chem. Phys. 49, 225.
Bohr, N. (1913)
Phil. Mag. 25, 10.
Bohr, N. (1915)
Phil. Mag. 30, 581.
Bonifield, T.D., Rambow, F.H.K., Walters, G.K., McCuskers, M.V.,
Lorents, D.C. and Gutcheck, R.A. (1980)
Chem. Phys. Lett. 69, 290 and J. Chem. Phys. 72, 2914.
Bonnot, A., Bonnot, A.M., Coletti, F., Debever, J.M. and Hanus, J.(1974)
J. Phys. (France) C3 35, 49.
Boschi, R.A. and Salahub, D.R. (1972)
Mol. Phys. 24, 289.
Boursey, E., Roncin, J.Y. and Damaney, M. (1970)
Phys. Rev. Lett. 25, 1279
Boursey, E., Castex, M.-C. and Chandrasekharan, V. (1977)
Phys. Rev. B16, 2858.
Brodmann, R., Haensel, R., Hahn, U., Nielsen, U. and Zimmerer, G. (1974)
Chem. Phys. Lett. 29, 250.
Brodmann, R., Haensel, R., Hahn, U., Nielsen, U. and Zimmerer, G.
in Vacuum Ultraviolet Radiation Physics, ed. by E.E. Koch, R. Haensel,
and Kunz, C., Vieweg-Pergamon, Braunschweig (1974), p. 344.
Brodmann, R. (1976)
Thesis, Universität Hamburg and DESY Internal Report F41-77/02.

Brodmann, R., Tolkiehn, G. and Zimmerer, G. (1976)
phys. stat. sol. (b) 73, K99.
Brodmann, R. and Zimmerer, G. (1977)
J. Phys. B: Atom. Molec. Phys. 10, 3395.
Brodmann, R. and Zimmerer, G. (1978)
Chem. Phys. Lett. 56, 434.
Brown, D.B. (1974)
in: Handbook of Spectroscopy, Vol. I, p. 248 ff., edited by
J.W. Robinson, Cleveland.
Cardona, M. and Ley, L. (1978)
editors, Photoemission in Solids, Vol. I and Vol. II,
Topics in Applied Physics, Vol. 26, 27, Springer, Berlin.
Carvalho, M.J. and Klein, G. (1978)
J. Luminescence 18/19, 487.
Castex, M. C. (1974)
Chem. Phys. 5, 448.
Castex, M.C. (1977)
Extended Abstracts, 5th Intern. Conf. on VUV Radiation Physics,
Montpellier, Vol. I, p. 123.
Cate, R.C., Wright, J.G. and Cusack, N.E. (1970)
Phys. Lett. 32A, 467.
Chançe, R.R., Prock, A. and Silvey, R. (1976)
J. Chem. Phys. 65, 2527.
Chandrasekharan, V. and Boursey, E. (1978)
Ber. Bunsenges. Phys. Chem. 82, 49.
Chandrasekharan, V. and Boursey, E. (1978)
Phys. Rev. B. to be published.
Chesnovsky, O., Raz, B. and Jortner, J. (1972a)
Chem. Phys. Lett. 15, 475.
Chesnovsky, O., Raz, B. and Jortner, J. (1972b)
J. Chem. Phys. 57, 4628.
Cheshnovsky, O., Raz, B. and Jortner, J. (1973a)
J. Chem. Phys. 59, 5554.
Cheshnovsky, O., Gedanken, A., Raz, B. and Jortner, J. (1973b)
Chem. Phys. Lett. 22, 23.
Cheshnovsky, O., Gedanken, A., Raz, B. and Jortner, J. (1973c)
Solid State Commun. 13, 639.
Chechnovsky, O., Even, U. and Jortner, J. (1977)
Solid State Comm. 22, 745.
Chesnovsky, O., Even, U. and Jortner, J. (1979)
Phys. Lett. 71A, 255.
Cho, K. and Toyozawa, Y. (1969)
J. Chem. Soc. Japan 26, 71.
Cho, K. and Toyozawa, Y. (1971)
J. Chem. Soc. Japan 30, 1555.
Cohen, M.H. and Lekner, J. (1967)
Phys. Rev. 158, 305.
Cohen, M.H., Fritzche, H. and Ovshinsky, S.R. (1969)
Phys. Rev. Lett. 22, 1065.
Cohen, M.H. (1970)
Proc.Sym. on Semiconductor Effects in Amorphous Solids,
North Holland Publishing, Amsterdam.
Cohen, M.H. and Jortner, J. (1973)
J. de Physique 35, C4-345.

Cohen, M.H. and Jortner, J. (1974)
Phys. Rev. A 10, 978.
Cohen, M.H., Jortner, J. and Webman, I. (1978)
"1st Conference on the Electrical Transport and Optical Properties of Inhomogeneous Media"
AIP Conf. Proc. No. 40, 63.
Cohen, M.H., Jortner, J. and Webman, I. (1978)
Phys. Rev. B 17, 4555.
Cohen, R.W., Cody, G.D., Coutts, M.D. and Abeles, B. (1973)
Phys. Rev. B8, 3689.
Cohen, J.S. and Schneider, B. (1974)
J. Chem. Phys. 61, 3230.
Cole, M.W. (1974)
Review of Modern Physics 46, 451.
Coletti,F. and Hanus, J. (1977)
Extended Abstracts, 5th Intern. Conf. on VUV Radiation Physics, Montpellier, Vol. I, p. 78.
Coletti, F. and Bonnot, A.M. (1978)
Chem. Phys. Lett. 55, 92.
Coufal, H.J., Nagel, U., Bürger, M. and Lüscher E. (1974)
Phys. Lett. A47, 327.
Coufal, H.J., Nagel, U., Lüscher E. (1978)
Ber. Bunsenges. Phys. Chem. 82, 133.
Creuzburg, M. and Teegarden, K. (1968)
Phys. Rev. Lett. 20, 593.
Creuzburg, M. (1971)
Solid State Comm. 9, 665.
Creuzburg, M. and Völkl, G. (1977)
Extended Abstracts, 5th Intern. Conf. on VUV Radiation Physics, Montpellier, Vol. I, p. 74.
Dagens, L. and Perrot, F. (1972)
Phys. Rev. B5, 641.
Danor, R., Cheshnovsky, O., Even, Y. and Jortner, J. (1979)
Phil. Mag. B39, 99.
Danilychev, V.A., Kashnikov, G.N. and Popov, Yu.M. (1970)
Preprint No. 136, Lebedev Institute, Moscow.
Davis, H.T., Rice S.A. and Meyer, L. (1962)
Phys. Rev. Lett. 9, 81.
Davydov, A.S. (1971)
Theory of Molecular Excitons, Plenum Press, New York.
Debever, J.M., Bonnot, A., Bonnot, A.M., Coletti, F. and Hanus, J. (1974)
Solid State Commun. 14, 989.
Dehmer, P.M. and Dehmer, J.L. (1978a)
J. Chem. Phys. 68, 342.
Dehmer, P.M. and Dehmer, J.L. (1978b)
J. Chem. Phys. 69, 125.
Dexter, D.L. (1953)
J. Chem. Phys. 21, 836.
Dexter, D.L. (1958)
Solid State Phys. 6, 353.
Devreese, J.T., Kunz, A.B., Collins, T.C. (1972)
Solid State Comm. 11, 673.
Doke, T. Hitachi, A., Kubota, S., Nakamoto, A., Takahashi, T. (1976)
Nucl. Instr. Methods 134, 353.
Dressler, K. (1970)
Memories de la Societé Royale des Sciences de Liège, Vol. 20, 357.

Druger, S.D. and Knox, R.S. (1969)
J. Chem. Phys. 50, 3143.
Dubost H., Charneau R. (1976)
Chem. Phys. 12, 407.

Eatah, A.I., Cusack, N.E. and Wright, J.G. (1975)
Phys. Lett. 51A, 149.
Economou, E.N., Cohen, M.H., Freed, K.F. and Kirkpatrick, E.S. (1974)
in "Amorphous and Liquid Semiconductors" edited by Tauc, J., p. 101, Plenum Press, London.
Edwards, S. (1965)
Proc. Phys. Soc. 85, 1.
Endo, H., Eatah, A.I., Wright, J.G. and Cusack, N.E. (1973)
J. Phys. Soc. Japan 34, 666.
Ermler, W.C., Lee, Y.S., Pitzer, K.S. and Winter, N.W. (1978)
J. Chem. Phys. 69, 976.
Even, U. and Jortner, J. (1972)
Phil. Mag. 25, 715.

Fano, U. (1940)
Phys. Rev. 58, 544.
Fano, U. (1947)
Phys. Rev. 72, 26.
Farrell, H.H., Strougin, M. and Dickey, J.M. (1972a)
Phys. Rev. B6, 4703.
Farrell, H.H. and Strougin, M. (1972b)
Phys. Rev. B6, 4711.
Fermi, E. (1939)
Phys. Rev. 56, 1242.
Filinski, I. (1972)
phys. stat. sol. (b) 49, 577.
Fink, R.W., Venugopala, P. (1974)
Handbook of Spectroscopy, Vol. I, edited by J.W. Robinson, CRC Press, Cleveland, p. 219.
Fischbach, J.U., Fröhlich, D. and Kabler, M.N. (1973)
J. Luminescence 6, 29.
Fischer, S. and Rice, S.A. (1968)
Phys. Rev. 176, 409.
Flynn, C.P. (1976)
Phys. Rev. B14, 5294.
Förster, Th. (1943)
Ann. Phys. 2, 55.
Forstmann, F., Kolb, D.M. and Schulze, W. (1976a).
J. Chem. Phys. 64, 2552.
Forstmann, F., Kolb, D.M., Leutloff, D. and Schulze, W. (1977)
J. Chem. Phys. 66, 2806.
Forstmann, F. and Kolb, D.M. (1978)
Ber. Bunsenges. Phys. Chem. 82, 30.
Fowler, W.B. (1963)
Phys. Rev. 132, 1591.
Fowler, W.B. (1968)
in: Physics of Color Centers
Academic Press, London.

Frenkel, J. (1931a)
Phys. Rev. 37, 17.
Frenkel, J. (1931b)
Phys. Rev. 37, 1276
Frenkel, J. (1936)
Physik. Z. Sowjetunion 9, 158.
Friedman, L.R. and Tunstall, D.P. (1978), editors
"The Metal-Non-Metal Transition in Disordered Systems"
Proceeding of the 19th Scottish Universities Summer School in Physics,
SUSSP Publication, Edinburgh.
Fugol, I. Ya., Savchenko, E.V. and Belov, A.G. (1972)
ZhETF Pis. Red. 16, 245.
Fugol, I. Ya., Belov, A.G., Savchenko, J.V. and Poltoratskii, Yu.B. (1974)
Solid State Commun. 15, 525.
Fugol, I. Ya. and Belov, A.G. (1975)
Solid State Comm. 17, 1125.
Fugol, I.Ya., Belov, A.G., Savchenko, E.V. and Poltoratski, Yu. B. (1975)
Fiz.nizh.temp. USSR 1,2, 203, Sov, J. Low Temp. Phys. 1,2, 98.
Fugol, I.Ya., Belov, A.G., Poltoratski, Yu. B. and Savchenko, E.V. (1976)
Fiz.nizh.temp. USSR 2, 400.
Fugol, I.Ya. and Tarasova, E.I. (1977)
Fiz. nizh. temp. USSR 3, 366.
Fugol, I. Ya. (1978)
Advances in Physics 27, 1.

Gedanken, A., Raz, B. and Jortner, J. (1972a)
Chem. Phys. Lett. 14, 172.
Gedanken, A., Raz, B. and Jortner, J. (1972b)
Chem. Phys. Lett. 14, 326.
Gedanken, A., Raz, B. and Jortner, J. (1973a)
J. Chem. Phys. 58, 1178.
Gedanken, A., Raz, B. and Jortner, J. (1973b)
J. Chem. Phys. 59, 1630.
Gedanken, A., Raz, B. and Jortner, J. (1973c)
J. Chem. Phys. 59, 2752.
Gedanken, A. Raz, B. and Jortner, J. (1973d)
J. Chem. Phys. 59, 5471.
Gedanken, A., Karsch, Z., Raz, B. and Jortner, J. (1973e)
Chem. Phys. Lett. 20, 163.
Gerick, U. (1977)
Diplomarbeit, Universität Hamburg
Gilbert, T.L. and Wahl, A.C. (1971)
J. Chem. Phys. 55, 5247.
Gillen, K.T., Saxon, R.P., Lorentz, D.C., Ice, G.E. and Olson, R.E. (1976)
J. Chem. Phys. 64, 1925.
Gittleman, J.I. and Abeles, B. (1977)
Phys. Rev. B15, 3273.
Gleason, R.E., Bonfield, T.D., Keto, J.W. and Walters, G.K. (1977)
J. Chem. Phys. 66, 1589.
Granier, R., Castex, M.-C., Granier, J. and Romand, M.J. (1967)
Compt. Rend. Acad. Sci. (Paris) 264B, 778.
Granier, R. (1969)
Ann. Phys. 4, 383.

Grobman, W.D. (1975)
Comments on Solid State Phys. 7, 27.
Grosso, G., Martinelli, L. and Pastori Parravicini, G. (1978a)
Solid State Comm. 25, 435.
Grosso, G., Martinelli, L. and Pastori Parravicini, G. (1978b)
Solid State Comm. 25, 835.
Gruen, D.M. (1976)
in: M. Moskovitz and G.A. Ozin "Cryochemistry"
John Wiley-Interscience, Chapt. 10
Gruzdev, P.F., Longinov, A.V. (1975)
Opt. Spectrosc. 38, 611.
Gürtler, P. and Koch, E.E. (1980)
J. Molec. Structure 60, 259.
Guse, M.P. and Kunz, A.B. (1975)
phys. stat. sol. (b) 71, 631.

Haensel, R. and Kunz, C. (1967)
Z. Angew. Physik 23, 276.
Haensel, R., Keitel, G., Schreiber, P. and Kunz, C. (1969a)
Phys. Rev. Lett. 22, 398.
Haensel, R., Keitel, G., Schreiber, P. and Kunz, C. (1969b)
Phys. Rev. 188, 1375.
Haensel, R., Keitel, G., Koch, E.E., Skibowski, M. and Schreiber, P. (1969c)
Phys. Rev. Lett. 23, 116.
Haensel, R., Keitel, G., Kunz, C., Schreiber, P. and Sonntag, B. (1970a)
Mem.Soc.Roy.Sci.Lg.5 série 20, 169.
Haensel, R., Keitel, G., Kunz, C. and Schreiber, P. (1970b)
Phys. Rev. Lett. 25, 208.
Haensel, R., Keitel, G., Koch, E.E., Skibowski, M. and Schreiber, P. (1970c).
Opt. Comm. 2, 59.
Haensel, R., Keitel, G., Koch, E.E., Kosuch, N. and Skibowski, M. (1970d)
Phys. Rev. Lett. 25, 1281.
Haensel, R., Keitel, G., Kosuch, N., Nielsen, U. and Schreiber, P. (1971)
J. Phys. (France) 32, C4-236.
Haensel, R., Kosuch, N., Nielsen, U., Sonntag B. and Rössler, U. (1973)
Phys. Rev. B7, 1577.
Hahn, U., Schwentner, N. and Zimmerer, G. (1977)
Opt. Comm. 21, 237.
Hahn, U. (1978)
Thesis, Universität Hamburg
Hahn, U., Schwentner, N. and Zimmerer, G. (1978)
Nucl. Instr. Methods 152, 261.
Hahn, U., Jordan, B. and Schwentner, N. (1978c)

Hahn, U. and Schwentner, N. (1979)
J. Luminescence 18/19, 23.
Hahn, U. and Schwentner, N. (1980)
Chem. Phys. 48, 53.
Hahn, U., Jordan, B., Schwentner, N., Sommer, K. and Zimmerer, G. (1980)
to be published.
Halpern, B. and Gomer, R. (1965)
J. Chem. Phys. 43, 1069.

Hanus, J., Coletti, F., Bonnot, A.M. and Debever, J.M. (1974)
In: Vacuum Ultraviolet Radiation Physics, edited by E. E. Koch, R. Haensel and C. Kunz, Vieweg, Pergamon, Braunschweig, New York, p. 341.
Harmsen, A., Koch, E.E., Saile, V., Schwentner, N. and Skibowski, M. (1974)
In: Vacuum Ultraviolet Radiation Physics, edited by E. E. Koch, R. Haensel and C. Kunz, Vieweg, Pergamon, Braunschweig, New York, p. 339.
Harmsen, A. (1975)
Diplomarbeit, Universität Hamburg.
Hasnain, S.S., Hamilton, T.D.S., Munro, I.H., Pantos, E. and Steinberger, I.T. (1977a)
Phil. Mag. 35, 1299.
Hasnain, S.S., Brint, P., Hamilton, T.D.S. and Munro, I.H. (1977b)
Phil. Mag. 36, 629.
Hasnain, S.S., Hamilton, T.D.S. and Munro, I.H. (1977c)
Nuovo Cimento 39, 500.
Hasnain, S.S., Munro, I.H. and Hamilton, T.D.S. (1977d)
J. Phys. C: Solid State Phys. 10, 1097.
Hasnain, S.S., Hamilton, T.D.S. and Munro, I.H. (1978a)
J. Phys. C11, L 261.
Hasnain, S.S., Brint, P., Hamilton, T.D.S. and Munro, I.H. (1978b)
Chem. Phys. Lett. 56, 134.
Hasnain, S.S., Brint, P., Hamilton, T.D.S. and Munro, I.H. (1978c)
J. Molec. Spectroscopy
Hasnain, S.S., Hamilton, T.D.S., Munro, I.H. and Pantos, E. (1978d)
J. Molec. Spectroscopy
Hasnain, S.S., Hamilton, T.D.S., Munro, I.H. and Brint, P. (1978e)
J. Luminescence 18/19
Herbst, J.F. (1977)
Phys. Rev. B15, 3720.
Hermanson, J. (1966)
Phys. Rev. 150, 660.
Herzberg, G. (1950)
Molecular Spectra and Molecular Structure, Vol. I, II, III
Van Nostrand Reinhold Company, New York (1950 ff).
Heumüller, R. and Creuzburg, M. (1978)
to be published.
Heumüller, R. (1978)
Thesis, Universität Regensburg.
Hilder, G. and Cusack, N.F. (1977)
Phys. Lett. 62A, 163.
Hill, J.L., Heybey, O. and Walter, G.K. (1971)
Phys. Rev. Lett. 26, 1213.
Hingsammer, J. and Lüscher, E. (1968)
Helvetia Physica Acta 41, 914.
Horn, K., Scheffler, M. and Bradshaw, A.M. (1978)
Phys. Rev. Lett. 41, 822.
Horton, G.K. (1968)
Am. J. Phys. 36, 93.
Hoshen, J. and Jortner, J. (1972)
J. Chem. Phys. 56, 933, 4138, 5550.
Howe, S., Le Comber, R.G. and Spear, W.E. (1968)
unpublished.
Hsu, Y.P. and Johnson, P.M. (1973)
J. Chem. Phys. 59, 136.
Huber, E.E., Emmons, D.A. and Lerner, R.M. (1974)
Opt. Comm. 11, 155.
Hunderi, O. and Ryberg, R. (1975)
Phys. Lett. 51A, 167.

Jahnke, J.A., Holzwarth, N.A.W. and Rice, S.A. (1972)
Phys. Rev. A5, 463.
Jen, C.K., Bowers, V.A., Cochran, E.L. and Foner, S.N. (1962)
Phys. Rev. 126, 1749.
Jordan, B., Hahn, U., Schwentner, N., Sommer, K. and Zimmerer, G. (1978)
unpublished.
Jortner, J., Meyer, L., Rice, S.A. and Wilson, E.G. (1965)
J. Chem. Phys. 42, 4250.
Jortner, J. (1974)
In Vacuum Ultraviolet Radiation Physics, edited by E. E. Koch, R. Haensel and C. Kunz, Vieweg Pergamon, Braunschweig, New York, p. 263.
Jortner, J. and Cohen, M.H. (1976)
Phys. Rev. B 13, 1548.
Jortner, J. and Gaathon, A. (1977)
Can J. Chem. 55, 1801.
Jortner, J. and Leach, S. (1980)
J. de Chimie Physique 77 (1), 7.

Kane, E.O. (1966)
Phys. Rev. 147, 335.
Kane, E.O. (1967)
Phys. Rev. 159, 624.
Katz, B., Brith, M., Sharf, B. and Jortner, J. (1969)
J. Chem. Phys. 50, 5195.
Kepler, R.G. (1976)
In: Treatise on Solid State Chemistry, Vol. 3, p. 615, edited by N.B. Hannay, Plenum Publishing Corp., New York.
Keto, J.W., Gleason, R.E. and Walters, G.K. (1974a)
Phys. Rev. Lett. 33, 1365.
Keto, J.W., Soley, F., Stockton, H. and Fitzsimmons, W.A. (1974b)
Phys. Rev. 10, 872 and 887.
Keto, J.W., Gleason, R.E., Bonfield, T.D., Walters, G.K., Soley, F.K. (1976)
Chem. Phys. Lett. 42, 125.
Keto, J.W., Gleason, R.E., Soley, F.K. (1979)
J. Chem. Phys. 71, 2676.
Kimura, T. and Freeman, G.R. (1974)
J. Chem. Phys. 60, 4081.
Kingsley, J.D. and Prener, J.S. (1972)
J. Appl. Phys. 43, 3073.
Kink, R., Lohmus, A., Selg, M. and Soovik, T. (1977)
phys. stat. sol. (b) 84, K61.
Kink, R. et al. (1980)
to be published.
Kirkpatrick, S. (1971)
Phys. Rev. 27, 1722.
Kittel, C. (1971)
Introduction to Solid State Physics, Wiley, New York.

Klein, C.A. (1968)
J. Appl. Phys. 39, 2029.
Knox, R.S. and Bassani, F. (1961)
Phys. Rev. 124, 652.
Knox, R.S. (1963)
Theory of Excitons, Academic Press, New York.
Koch, E.E., Raz, B., Saile, V., Schwentner, N., Skibowski, M. and Steinmann, W. (1974a)
Japan. J. Appl. Phys. Suppl. 2, Pt 2, 775.
Koch, E.E., Saile, V., Schwentner, N. and Skibowski, M. (1974b)
Chem. Phys. Lett. 28, 562.
Koch, E.E., Nürnberger, R. and Schwentner, N. (1978)
Berichte Bunsenges. Phys. Chemie 82, 110.
Kovalenko, S.I., Indan, E.I., Solodovnik, A.A. and Krupski, I.N. (1975)
Soviet. Phys. Low Temp. 1, 1027.
Kovalenko, S.I., Indan, E.J. and Khudoteplaya, A. A. (1972)
phys. stat. sol. A 13, 235.
Kramer, B. (1976)
in Physics of Structurally Disordered Solids ,
Proceedings of an advanced NATO Study Institute, edited by Mitra S.S.,
p. 291, Plenum Press, New York and London.
Kreitman, M. and Barnett, E.E. (1965)
J. Chem. Phys. 43, 364.
Kubo, R. and Toyozawa, Y. (1955)
Prog. Theoret. Phys. 13, 160.
Kubo, R.J. (1962)
J. Phys. Soc. Japan 17, 975.
Kubota, S., Nakamoto, A. Tokahashi, T., Konno, S., Hamada, T. Miyajima, M., Hitachi, A., Shibamura, E. and Doke, T. (1976)
Phys. Rev. B13, 1649.
Kubota, S., Hishida, M. and Raun, J. (1978a)
J. Phys. C, Solid State Phys. 11, 2645.
Kubota, S., Nakamoto, A., Tabahashi, T., Hamada, T., Shibamura, E., Miyajima, M., Masuda, K. and Doke, T. (1978b)
Phys. Rev. B17, 2762.
Kubota, S., Hishida, M. and Gesa, K. (1979)
to be published.
Kunsch, P.L. and Coletti, F. (1979)
J. Chem. Phys. 70, 726.
Kunz, A.B., Devreese, J.T. and Collins, T.C. (1972)
J. Phys. C: Solid State 5, 3259.
Kunz, A.B. and Mickish, D. (1973)
Phys. Rev. B8, 779.
Kunz, A.B., Collins, T.C., Esterling, D., Licciardello, D.C. and Mickish, D.J. (1975a)
Phys. Rev. B11, 3210.
Kunz, A.B., Mickish, D.J., Mirmira, S.K.V., Shima, T., Himpsel, F.-J., Saile, V., Schwentner, N. and Koch, E.E. (1975b)
Solid State Comm. 17, 761.
Kunz, C. (1979)
editor, Synchrotron Radiation, Techniques and Applications ,
Springer, Berlin, Heidelberg, New York.
Kupferman, S.L. and Pipkin, F.M. (1965)
Phys. Rev. 166, 207.

Laporte, P. and Steinberger, I.T. (1977)
Phys. Rev. A15, 2538.
Leckner, J. (1967)
Phys. Rev. 158, 130.
Leckner, J., Halpern, B., Rice, S.A. and Gomer, R. (1967)
Phys. Rev. 156, 351.
Le Comber, P.G., Wilson, J.B. and Loveland, R.J. (1976)
Solid State Comm. 18, 377.
Leichner, P.I. (1973)
Phys. Rev. A 6, 815.
Lilly, R.A. (1976)
J. Opt. Soc. Am. 66, 245.
Lindau, I. and Spicer, W.E. (1974)
J. Electron. Spectrosc. 3, 409.
Lipari, N.O. (1970)
phys. stat. sol.(b) 40, 691.
Lipari, N.O. and Fowler, W.B. (1970)
Phys. Rev. B2, 3354.
Lipari, N.O. (1972)
Phys. Rev. B6, 4071.
Llacer, J. and Garwin, E.L. (1969)
J. Appl. Phys. 40, 2766 and 2776.
Lorentz, D.C. and Olson, R.E. (1972)
Semiannual Technical Report, No. 1, Stanford Res. Inst., Menlo Park, Calif.
Lotz, W. (1967)
Zeitschrift für Physik 206, 205.
Lotz, W. (1967, 1968)
J. Opt. Soc. Am. 57, 873; 58, 236; 58, 915.
Loveland, R.J., Le Comber, P.G. and Spear, W.E. (1972)
Phys. Lett. 39A, 225.
Luchner K. and Micklitz,H. (1978)
J. Luminescence to be published
Luetloff, D. and Kolb, D.M. (1979)
Berichte Bunsenges. Phys. Chem. 83, 666.

Mann, B. and Behrens, A. (1978)
Ber. Bunsenges. Phys. Chem. 82, 136.
Maradudin, A.A. (1966)
Solid State Physics 18, 273.
Markham, J.J. (1959)
Review of Modern Physics 31, 956.
Martin, M., Rice S.A. (1970)
Chem. Phys. Lett. 7, 94.
Martin, M. (1971)
J. Chem. Phys. 54, 3289.
Martin, T.P. (1977)
Phys. Rev. B15, 4071.
Martin, T.P. (1978)
J. Chem. Phys. 69, 2036.
Martinelli, L. and Pastori Parravicini, G. (1977)
J. Phys. C: Solid State Phys. 10, L687.

Mattheis, L.F. (1964)
Phys. Rev. A 133, 1399.
Matthew, J.A.D. and Devey, M.G. (1976)
J. Phys. C 9, L 413.
Matthias, E., Rosenberg, R.A., Poliakoff, E.D., White, H.G., Lee, S.T. and Shirley, D.A. (1977)
Chem. Phys. Lett. 52, 239.
Maxwell-Garnett, J.C. (1904)
Phil. Trans. Roy. Soc. London 203, 385;
ibid. 205, 237.
McCarty, M. and Robinson, G.W. (1959)
Molecular Physics 2, 415.
McNeal, N.A. and Goldman, A.M. (1977)
Phys. Lett. 61A, 268.
Messing, I., Raz, B. and Jortner, J. (1977a)
Chem. Phys. 23, 23.
Messing, I., Raz, B. and Jortner, J. (1977b)
Chem. Phys. 23, 351.
Messing, I. and Jortner, J. (1977c)
Chem. Phys. 24, 183.
Messing, I., Raz, B. and Jortner, J. (1977d)
Chem. Phys. 25, 55.
Messing, I., Raz, B. and Jortner, J. (1977e)
J. Chem. Phys. 66, 2239.
Messing, I., Raz, B. and Jortner, J. (1977f)
J. Chem. Phys. 66, 4577.
Meyer, B. (1965)
J. Chem. Phys. 43, 2986.
Meyer, B. (1971)
Low Temperature Spectroscopy, Elsevier, New York.
Meyer, B. (1978)
Ber.Bunsenges. Phys. Chemie 82, 24.
Miller, J.C., Ault, B.S. and Andrews, L. (1977)
J. Chem. Phys. 67, 2478.
Miller, L.S., Howe, S. and Spear, W.E. (1968)
Phys. Rev. 166, 871.
Millet, P.,Birot, A., Brunet, H., Galy, J., Pons-Germain, B. and Teyssier, J.L. (1978)
J. Chem. Phys. 69, 92.
Miyakawa, T. and Dexter, D.L. (1969)
Phys. Rev. 184, 166.
Möller, H. (1976)
Diplomarbeit Universität Hamburg and DESY Internal Report F41-76/14.
Möller, H., Brodmann, R., Zimmerer, G. and Hahn, U. (1976)
Solid State Commun. 20, 401.
Molchanov, A.G. (1972)
Fiz. Tverd: Tela 4, 9.
Monahan, K., Rehn, V., Matthias, E. and Poliakoff, E. (1976)
SSRP Report No. 76/10.
Moore, C.E. (1949, 1952, 1958)
Atomic Energy Levels, Washington, NBS Circular 467.
Moskovits, M. and Ozin, G.A. (1976)
Editors, Cryochemistry, Wiley, New York.
Moskovits, M. and Hulse, J.E. (1977)
J. Chem. Phys. 67, 4271.

Mott, N.F. (1949)
Proc. Phys. Soc. A62, 416.
Mott, N.F. (1966)
Phil. Mag. 13, 989.
Mott, N.F. (1967)
Adv. in Phys. 16, 49.
Mott, N.F. and Davis, E.A. (1971)
Electronic Processes in Non-Crystalline Solids.
Oxford University Press.
Mott, N.F. (1972)
Phil. Mag. 26, 1249.
Mott, N.F. (1974)
Metal-Insulator Transitions, Taylor and Francis, London.
Mott, N.F. (1975)
Phil. Mag. 31, 217.
Mott, N.F. (1978)
Phil. Mag. B 37, 377.
Mulliken, R.S. (1970)
J. Chem. Phys. 52, 5170.
Mulliken, R.S. (1974)
Radiation Research 59, 357.
Nagasawa, N., Karasawa, T., Miura, N. and Nanba, T. (1972)
J. Phys. Soc. Japan 32, 1155.
Nagasawa, N. and Nanba, T. (1974)
Optics Comm. 11, 152.
Nagel, D. (1976)
Diplomarbeit Universität Hamburg
Nagel, D. and Sonntag, B. (1978)
Ber. Bunsenges. Phys. Chemie 82, 38.
Nanba, T., Nagasawa, N. and Ueta, M. (1974)
J. Phys. Soc. Japan 37, 1031.
Nanba, T. and Nagasawa, N. (1974)
J. Phys. Soc. Japan 36, 1216.
Nanba, T., Miura, N. and Nagasawa, N. (1974)
J. Phys. Soc. Japan 36, 158.
Ng, C.Y., Trevor, D.J., Mahan, B.H. and Lee, Y.T. (1977)
J. Chem. Phys. 66, 446.
Nicolis, G. and Rice, S.A. (1967)
J. Chem. Phys. 46, 4445.
Nürnberger, R., Himpsel, F.-J., Koch, E.E. and Schwentner, N. (1977)
phys. stat.sol. (b) 81, 503.

O'Brien, J.F. and Teegarden, K.J. (1966)
Phys. Rev. Lett. 17, 919.
Oka, T., Rao, K.V.S.R., Redpath, J.L. and Firestone, R.F. (1974)
J. Chem. Phys. 61, 4740.
Ophir, Z. (1970)
Master Thesis, Tel-Aviv University.
Ophir, Z., Raz, B. and Jortner, J. (1974)
Phys. Rev. Lett. 33, 415.
Ophir, Z., Schwentner, N., Raz, B.- Skibowski, M. and Jortner, J. (1975a)
J. Chem. Phys. 63, 1072.

Ophir, Z., Raz, B., Jortner, J., Saile, V., Schwentner, N., Koch, E.E. Skibowski, M. and Steinmann, W. (1975b)
J. Chem. Phys. 62, 650.
Ophir, Z. (1976)
Thesis, Tel Aviv University.
Onodera, Y. and Toyozawa, Y. (1968)
J. Phys. Soc. Jap. 24, 341.
Ozin, G.A. (1977)
Catal. Review Science Eng. 16, 191.
Ozin, G.A. and Huber, H. (1978)
Inorg. Chem. 17, 155.

Packard, R.E., Reif, F. and Surko, C.M. (1970)
Phys. Rev. Lett. 25, 1435.
Pantos, E., Hasnain, S.S. and Steinberger, I.T. (1977)
Chem. Phys. Lett. 46, 395.
Parinello, M., Tossatti, E., March, N.H. and Tosi, M.P. (1977)
Lettre al Nuovo Cimento 18, 341.
Peierls, R.E. (1932)
Ann. Physik (5) 13, 905.
Pendry, J.B. (1974)
in Low Energy Electron Diffraction, Academic Press, London.
Person, W.B. (1958)
J. Chem. Phys. 28, 319.
Petry, R.L. (1926)
Phys. Rev. 28, 362.
Phelps, D.J., Avici, R. and Flynn, C.P. (1975)
Phys. Rev. Lett. 34, 23.
Phelps, D.J. and Flynn, C.P. (1976a)
Phys. Rev. B14, 5279.
Phelps, D.J., Tilton, R.A. and Flynn, C.P. (1976b)
Phys. Rev. B14, 5254.
Phillips, J.C. (1966)
Solid State Physics 18, 55.
Pimentel, G.C. (1958)
J. Am. Chem. Soc. 62, 80.
Pimentel, G.C. (1978)
Ber. Bunsengesellschaft Phys. Chem. 82, 2.
Platzman, R.L. (1961)
Int. J. Appl. Rad. Isotopes 10, 116.
Popielawski, J. and Rice, S.A. (1967)
J. Chem. Phys. 47, 2292.
Posener, D.W. (1959)
AustralianJ. Phys. 12, 184.
Potts, W.A., Lempka, H.J., Streets, D.G. and Price, W.C. (1970)
Phil. Trans. Roy. Soc. 268A, 59.
Powell, C.J. (1974)
Surface Science 44, 29.
Powell, R.C. and Soos, Z.G. (1975)
J. Luminescence 11, 1.
Powell, B.M. and Dolling, G. (1977)
in: Rare Gas Solids, ed. by M. Klein and J.A. Venables, Vol. II, p.921,
Academic Press, London.
Powell, R.C. (1978)
in: Luminescence of Inorganic Solids, edited by B. DiBartolo,
Plenum, New York.

Price, W.C. (1936)
J. Chem. Phys. 4, 547.
Prigogine, I. (1957)
The Molecular Theory of Solutions, Chapt. 9
Amsterdam: North Holland.
Pryce, M.H.L. (1966)
in: Phonons in Perfect Lattices and in Lattices with Point
Imperfections, ed. by R.W.H. Stevenson, Oliver and Bryd,
Edinburg, London, p. 403.
Pudewill, D., Himpsel, F.-J., Saile, V., Schwentner, N., Skibowski, M.
and Koch, E.E. (1976a)
phys. stat. sol. (b) 74, 485.
Pudewill, D., Himpsel, F.-J., Saile, V., Schwentner, N., Skibowski, M.
Koch, E.E. and Jortner, J. (1976)
J. Chem. Phys. 65, 5226.

Quinn, J.J. and Wright, J.G. (1977)
Liquid Metals 1976, p. 430,
Inst. Phys. Conf. Ser. No. 30, Bristol and London.

Raether, H. (1965)
Springer Tracts in Modern Physics 38, 85.
Raether, H. (1974)
in: Vacuum Ultraviolet Radiation Physics, edited by E.E. Koch,
R. Haensel and C. Kunz, Vieweg Pergamon, Braunschweig, New York, p.591.
Raether H. (1980)
Excitation of Plasmons and Interband Transitions by Electrons,
Springer Tracts in Modern Physics, Springer Berlin, Heidelberg, New York.

Rashba, E.I. (1976)
Izv. AN SSR, Ser. Fiz. Vol. 40, 535.
Raz, B. and Jortner, J. (1970a)
Proc. Roy. Soc. London A 317, 113.
Raz, B. and Jortner, J. (1970b)
Chem. Phys. Lett. 4, 511.
Raz, B. and Jortner, J. (1971)
Chem. Phys. Lett. 9, 222.
Raz, B., Gedanken, A., Even, U. and Jortner, J. (1972)
Phys. Rev. Lett. 28, 1643.
Raz, B., Gedanken, A., Even, U. and Jortner, J. (1972)
J. Phys. Rev. Lett. 28, 1643.
Raz, B., Cheshnovsky, O. and Jortner, J. (1976)
In: Molecular Energy Transfer, edited by R.D. Levine and J. Jortner;
J. Wiley and Sons, New York, 237.
Reilly, M.H. (1967)
J. Phys. Chem. Solids 28, 2067.
Resca, L., Resta, R. and Rodriguez, S. (1978a)
Phys. Rev. B 18, 696 and 18, 702.

Resca, L., Resta, R. and Rodriguez, S. (1978)
Sol. State Comm. 26, 849.
Resca, L. and Rodriguez, S. (1978)
Phys. Rev. B 17, 3334.
Resca, L. and Resta, R. (1979)
Phys. Rev. B 19, 1683.
Resca, L. and Resta, R. (1980)
Phys. Rev. B 21
Resta, R. (1978)
phys. stat. sol. (b) 86, 627.
Rice, S.A. and Jortner, J. (1966)
J. Chem. Phys. 44, 4470.
Rice, S.A. and Jortner, J. (1967)
in: Physics and Chemistry of the Organic Solid State, edited by
F. Fox, M. Labes and A. Weissberger, Interscience Publishers,
New York, Vol. III, Chapt. 4.
Rice, S.A., Nicolis, G. and Jortner, J. (1968)
J. Chem. Phys. 48, 2484.
Rimbey, P.R. (1977)
J. Chem. Phys. 67, 698.
Riseberg, L.A. and Moos, H.W. (1968)
Phys. Rev. 174, 429.
Roberts, I. and Wilson, E.G. (1973)
J. Phys. C, Sol. State Phys. 6, 2169.
Robin, J. Bergeon, R., Galatry, L. and Vodar, B. (1956)
Discussions Faraday Soc. 22, 30.
Robin, M.B. and Kuebler, N.A. (1970)
J. Mol. Spectrosc. 33, 247.
Robin, M.B. (1974)
Higher Excited States of Polyatomic Molecules, Vol. I, Vol. II,
Academic Press, New York.
Rößler, U. (1970)
phys. stat. sol.(b) 42, 345.
Rößler, U. (1971)
phys. stat. sol. (b) 45, 483.
Rößler, U. and Schütz, O. (1973)
phys. stat. sol.(b) 56, 483.
Rößler, U. (1976)
In Rare Gas Solids, edited by M.K. Klein and J.A. Venables,
Vol. I, 505, Academic Press, London.
Rudge, M.R.H. and Schwartz, S.B. (1966)
Proc. Phys. Soc. (London) 88, 563.
Rupin, J.M., Morlais, M. and Robin, S. (1967)
Compt. Rend. Acad. Sci. (Paris) 265B, 1177.
Ryberg, R. and Hunderi, O. (1977)
J. Phys. C., Solid State Phys. 10, 3559.

Saile, V., Skibowski, M., Steinmann, W., Gürtler, P., Koch, E.E.
and Kozevnikov, A. (1976a)
Applied Optics 15, 2559.
Saile, V., Skibowski, M., Steinmann, W., Gürtler, P., Koch E.E. and
Kozevnikov, A. (1976b)
Phys. Rev. Lett. 37, 305.
Saile, V. (1976)
Thesis, Universität München.
Saile, V., Steinmann, W. and Koch, E.E. (1977)
Extended Abstracts, 5th Intern. Conf. on VUV Radiation Physics,
Montpellier, Vol. I, p. 74.
Saile, V. and Wolff, H.W. (1977)
Proc. 7th Intern. Vac. Congr. and 3rd Intern. Conf. Solid Surfaces,
Vienna, p. 391.
Saile, V. and Koch, E.E. (1979)
Phys. Rev. B20, 784.
Saile, V. and Koch, E.E. (1980a)
Phys. Rev. B21, 4892.
Saile, V. and Koch, E.E. (1980b)
to be published.
Saile, V. (1980)
Applied Optics, in press.
Samson, J.A.R. (1967)
Techniques of Vacuum Ultraviolet Spectroscopy, Wiley, New York.
Sando, K.M. (1971)
Mol. Phys. 21, 439.
Saxon, R.P. and Liu, B. (1976)
J. Chem. Phys. 64, 3291.
Scharber, R.S. and Webber, S.E. (1971)
J. Chem. Phys. 55, 3985.
Scheffler, M., Horn, K., Bradshaw, A.M. and Kambe, K. (1978)
Phys. Rev.
Scher, H. and Zallen, R. (1970)
J. Chem. Phys. 53, 3959.
Schmidt, W.F. (1974)
in: Electron Solvent Interactions, edited by L. Kevon,
Elsivier Publ.
Schneider, B. and Cohen, J.S. (1974)
J. Chem. Phys. 61, 3240.
Schnepp, O. and Dressler, K. (1960)
J. Chem. Phys. 33, 49.
Schnyders, H., Rice, S.A. and Meyer, L. (1966)
Phys. Rev. 150, 127.
Schörner, R., Schuberth, E. and Creuzburg, M. (1977)
Extended Abstracts, 5th Intern. Conf. on VUV Radiation Physics,
Montpellier, Vol. I, p. 181.
Schörner, R. (1977)
Diplomarbeit Universität Regensburg.
Schuberth, E. (1976)
Thesis, Universität Regensburg.
Schuberth, E. and Creuzburg, M. (1975)
phys. stat. sol. (b) 71, 797.
Schuberth, E., Creuzburg M. and Müller-Lierheim, W. (1976)
phys. stat. sol. (b) 76, 301.

Silbey, (1978)

Slater, J.C. and Koster, G.F. (1954)
Phys. Rev. 94, 1498.
Smalley, P.E., Auerbach, D.A., Fitch, P.S.H., Levy, D.H. and Wharton, L. (1977)
J. Chem. Phys. 66, 3778.
Soley, F.J., Leach, R.K. and Fitzsimmons, W.A. (1975)
Phys. Lett. 55, 49.
Sommer, W.T. (1964)
Phys. Rev. Lett. 12, 271.
Sommer, K., Hahn, U., Jordan, B., Schwentner, N. and Zimmerer, G. (1978)
unpublished.
Song, K.S. (1969)
J. Phys. Soc. Jap. 26, 1131.
Song, K.S. (1971)
Can. J. Phys. 49, 26.
Song, K.S. and Lewis, C.J. (1979)
J. Luminescence 18/19, 521.
Sonnenblick, Y., Alexander, E., Kalman, Z.H. and Steinberger, I.T. (1977)
Chem. Phys. Lett. 52, 276.
Sonntag, B. (1977)
in Rare Gas Solids, edited by M.K. Klein and J.A. Venables, Vol. II,
p. 1021, Academic Press, London.
Sowada, U. Schmidt, W.F. and Bakale, G. (1977)
Can.J.Chem.
Spear, W.E. and LeComber, P.G. (1977)
in: Rare Gas Solids, edited by M.K. Klein, J.A. Venables, Vol. II, p. 1119,
Academic Press, London.
Spiegelman, F. and Malrieu, J.P. (1978)
Chem. Phys. Lett. 57, 214.
Springett, B.E., Jortner, J. and Cohen, M.H. (1968)
J. Chem. Phys. 48, 2720.
Steinberger, I.T. and Schnepp, O. (1967)
Sol. State Comm. 5, 417.
Steinberger, I.T., Atluri, C. and Schnepp, O. (1970)
J. Chem. Phys. 52, 2723.
Steinberger, I.T. and Asaf, U. (1971)
in: Proc. 2nd Intern. Conf. on Conduction in Low Mobility Materials,
edited by N. Klein, D.S. Tannhauser, and M. Pollak, Taylor Francis,
London, p. 453.
Steinberger, I.T. and Asaf, U. (1973)
Phys. Rev. B8, 914.
Steinberger, I.T. (1973)
J. Appl.Opt. 12, 614.
Steinberger, I.T., Munro, I.H., Pantos, E. and Asaf, U. (1974)
in: Vacuum Ultraviolet Radiation Physics, edited by E. E. Koch, R. Haensel,
and C. Kunz, Vieweg, Pergamon, Braunschweig, New York;
see also Phys. Lett. 47A, p. 299.
Steinberger, I.T., Pantos, E., Hasnain, S.S., Munro, I.H. and Hamilton,
T.D.S. (1976)
in: Molecular Spectroscopy of Dense Phases, Elsevier Scient. Publ.
Comp. Amsterdam, p. 467.

Schuberth, E. ( )
phys. stat. sol. (b) 84, K91.
Schuberth, E. and Creuzburg, M. (1978)
phys. stat. sol. (b) 90, 189.
Schulze, W. and Kolb, D.M. (1974)
J. Chem. Soc. Faraday Transactions II 70, 1098.
Schulze, W., Kolb, D.M. and Gerischer, H. (1975)
J. Chem. Soc. Faraday Transactions II, 71, 1763.
Schulze, W., Kolb, D.M. and Klipping, G.
5th Intern. Cryogenic Engineering Conf. p. 268.
Schulze, W., Becker, H.U. and Abe, H. (1978)
Ber. Bunsenges. Phys. Chem. 82, 138.
Schwarz, K.W. (1975)
in Advances in Chemical Physics XXXIII, edited by I. Prigogine and
S.A. Rice, Wiley, New York.
Schwentner, N., Skibowski, M. and Steinmann, W. (1973)
Phys. Rev. B8, 2965.
Schwentner, N. (1974)
Thesis, Universität München.
Schwentner, N., Himpsel, F.J., Koch, E.E., Saile, V. and Skibowski, M. (1974a)
in: Vacuum Ultraviolet Radiation Physics, edited by E.E. Koch, R. Haensel
and C. Kunz, Vieweg, Pergamon, Braunschweig, New York, p. 355.
Schwentner, N., Koch, E.E., Saile, V., Skibowski, M. and Harmsen, A. (1974b)
in: Vacuum Ultraviolet Radiation Physics edited by E.E. Koch, R. Haensel
and C. Kunz, Vieweg, Pergamon, Braunschweig, New York, p. 792.
Schwentner, N., Himpsel, F.J., Saile, V., Skibowski, M., Steinmann, W.
and Koch, E.E. (1975)
Phys. Rev. Lett. 34, 528.
Schwentner, N. and Koch, E.E. (1976a)
Phys. Rev. B14, 4687.
Schwentner, N. (1976b)
Phys. Rev. B14, 5490.
Schwentner, N. (1978)
in: Luminescence of Inorganic Solids edited by B. Di Bartolo and D. Pacheco,
Plenum Press, New York, p. 645.
Schwentner, N., Koch, E.E., Ophir, Z. and Jortner, J. (1978)
Chem. Phys. 34, 281.
Schwentner, N., Hahn, U., Einfeld, D. and Mühlhaupt, G. (1979)
Nuclear Instr. and Meth. 167, 499.
Schwentner, N. (1980)
Applied Optics, in press
Schwentner, N., Rudolf, H.W. and Martens, G. (1980)
phys. stat. sol. submitted.
Shanfield, Z., Montano, P.A. and Barett (1975)
Phys. Rev. Lett. 35, 1789.
Shante, V.K.S. and Kirkpatrick, S. (1971)
Adv. Phys. 20, 325.
Shockley, W. (1961)
Solid State Electron. 2, 35.
Siegbahn, K., Nordling, C., Fahlman, A., Nordberg, R., Hamrin, K., Hedman, J.,
Johansson, G., Bergmark, T., Karlsson, S.E., Lindgren I. and Lindberg, B. (1967)
Nova Acta Regiae Soc. Sci. Usal., Ser. IV, Vo. 20, Uppsala.
Siegbahn, K., Nordling, C., Johansson, G., Hedman, J., Hedén, P.F., Hamrin, K.,
Gelius, U., Bergmark, T., Werme, L.O., Manne, R. and Baer, Y. (1969)
ESCA Applied to Free Molecules, North-Holland, Amsterdam.

Steinberger, I.T., Maaskant, P. and Webber, S.E. (1977)
J. Chem. Phys. 66, 4722.
Stock, M., Smith, E.W., Drullinger, R.E., Hessel, M.M. and Pourcin, J.(1978)
J. Chem. Phys. 68, 1785.
Stockton, M., Keto, J.W., Fitzsimmons, W.A. (1970)
Phys. Rev. Lett. 24, 654.
Stockton, M., Keto, J.W. and Fitzsimmons, W.A. (1972)
Phys. Rev. A5, 372.
Suemoto, T., Kondo, Y. and Kanzaki, H. (1977)
Physics Letters 61A, 131.
Suemoto, T. (1977)
Thesis, University of Tokyo.
Suemoto, T., Kondo, Y. and Kanzaki, H. (1978)
Solid State Comm.
Suemoto, T. and Kanzaki, J. (1979)
J. Phys. Soc. Japan. 46, 1554.
Surko, C.M. and Reif, F. (1968)
Phys. Rev. 175, 229.
Surko, C.M., Packard, R.E., Dick, G.J. and Reif, F. (1970)
Phys. Rev. Lett. 24, 657.
Swyler, K.J. and Creuzburg, M. (1976)
J. Luminesc. 1,2, 842.

Takahashi, T., Konno, S., Hamada, T., Miyajima, M., Kubota, S.,
Nakamoto, A., Hitachi, A., Shibamura, E. and Doke, T. (1975)
Phys. Rev. A12, 1771.
Tauchert, W.K. (1975)
Thesis, Freie Universität Berlin.
Tauchert, W. and Schmidt, W.F. (1975)
Z. Naturforsch. 30a, 1085.
Tauchert, W., Jungblut, H. and Schmidt, W.F. (1977)
Can. J. Chem. 55, 1860.
Thompson, C.E. (1965)
J. Opt. Soc. Am. 55, 1184.
Thonnard, N. and Hurst, G.S. (1972)
Phys. Rev. A5, 1110.
Tilton, R.A., Phelps, D.J. and Flynn, C.P. (1974)
Phys. Rev. Lett. 32,1006.
Tilton, R.A. and Flynn, C.P. (1975)
Phys. Rev. Lett. 34, 20.
Tilton, R.A., Phelps, D.J. and Flynn, C.P. (1976a)
Phys. Rev. B14, 5265.
Tilton, R.A. and Flynn, C.P. (1976b)
Phys. Rev. B14, 5289.
Tolkiehn, G. (1976)
Diplomarbeit, Universität Hamburg.
Toyozawa, Y. (1974)
in: Vacuum Ultraviolet Radiation Physics, edited by E.E. Koch, R. Haensel
and C. Kunz, Vieweg, Pergamon, Braunschweig, New York, p. 317.

Tsai, B.P. and Baer, T. (1974)
J. Chem. Phys. 61, 2047.

Ueba, H. and Ichimura, S. (1976)
J. Phys. Soc. Jap. 41, 1974.
Ueba, H. (1977)
J. Phys. Soc. Japan 43, 353.

Waclawski, B.J. and Herbst, J.F. (1975)
Phys. Rev. Lett. 35, 1594.
Wadt, W.R. (1979)
to be published.
Wannier, G.H. (1937)
Phys. Rev. 52, 191.
Webber, S.E., Rice, S.A. and Jortner, J. (1965)
J. Chem. Phys. 42, 1907.
Weber, G. (1979)
Physica Scripta 20, 240.
Webman, I., Jortner, J. and Cohen, M.H. (1975)
Phys. Rev. B11, 2885.
Webman, I., Jortner, J. and Cohen, M.H. (1976)
Phys. Rev. B13, 713.
Webman, I., Jortner, J. and Cohen, M.H. (1976)
Phys. Rev. B14, 4737.
Webman, I. (1976)
Thesis, Tel Aviv University.
Webman, I., Jortner, J. and Cohen, M.H. (1977)
Phys. Rev. B15, 5712.
Welker, T. (1978)
Ber. Bunsenges. Phys. Chem. 82, 40.
Welker, T. and Martin, T.P. (1979)
J. Chem. Phys. 70, 5683.
Wenck, H.D. (1979)
Diplomarbeit, Universität Hamburg.
Wenck, H.D., Hasnain, S.S., Nikitin, M.M., Sommer, K. and Zimmerer, G. (1979)
to be published
DESY SR-79/07
Weymann, W. and Pipkin, F.M. (1965)
Phys. Rev. A 137, 490.
Wiese, W.L., Smith, M.W., Miles, B.M. (1969)
in: Atomic Transition Probabilities, II, 192 NS RDS-NBS 22
Wilcke, H. (1979)
Diplomarbeit, Universität Kiel.
Wolf, H.C. (1967)
in: Advances in Atomic and Molecular Physics, edited by D.R. Bates,
Academic Press, New York, London, Vol. 3, p. 119.

Wolff, H.W. (1977)
Extended Abstracts 5th INtern. Conf. on VUV Radiation Physics,
Montpellier, p. 214.
Wolff, H.W. (1979)
Thesis, Universität Hamburg.
Wright, M.R., Frosch, R.P. and Robinson, G.W. (1960)
J. Chem. Phys. 33, 934.

Yakhot, V., Berkowitz, M. and Gerber, R.B. (1975)
Chem. Phys. 10, 61.
Yakhot, V. (1976)
Chem. Phys. 14, 441.
Yoshino, K., Sowada, U. and Schmidt, W.F. (1976)
Phys. Rev. A14, 438.
Younger, S.M., Wiese, W.L. (1978)
Phys. Rev. 17, 1944.

Zallen, R. and Scher, H. (1971)
Phys. Rev. B4, 4471.
Zimmerer, G. (1976)
in: Proc. of Intern. Summer School on Synchrotron Radiation Research
Ed. A.N. Mancini and L.F. Quercia, Alghero, Vol. I, p. 453.
Zimmerer, G. (1977)
in: Luminescence of Inorganic Solids, edited by B. Di Bartolo and
P. Pacheco, Plenum Press, New York, p. 627.
Zimmerer, G. (1979)
J. Luminescence 18/19, 875.

Table

Binding Energies of the occupied levels of the rare gas atoms obtained from photoemission spectroscopy.
The binding energies are given in electron volts [eV] relative to the vacuum level. Some optical data as
given by Moore (a) and Lotz (c) are also included.

	$1s_{1/2}$ K	$2s_{1/2}$ L_{I}	$2p_{1/2}$ L_{II}	$2p_{3/2}$ L_{III}	$3s_{1/2}$ M_{I}	$3p_{1/2}$ M_{II}	$3p_{3/2}$ M_{III}	$3d_{3/2}$ M_{IV}	$3d_{5/2}$ M_{V}	$4s_{1/2}$ N_{I}	$4p_{1/2}$ N_{II}	$4p_{3/2}$ N_{III}	$4d_{3/2}$ N_{IV}	$4d_{5/2}$ N_{V}	$4f_{5/2}$ N_{VI}	$4f_{7/2}$ N_{VII}	$5s$ O_{I}	$5p_{1/2}$ O_{II}	$5p_{3/2}$ O_{III}	$5d_{3/2}$ O_{IV}	$5d_{5/2}$ O_{V}
$_{1}H$	24.580[a]																				
$_{10}Ne$	870.2[b]	48.42[b]	21.66[c]	21.564[c]																	
		48.47[b]	21.656[d]	21.559[d]																	
$_{18}Ar$	3205.9[b]	326.3[b]	250.56[b]	248.45[b]	29.3[b]	15.94[c]	15.56[c]														
						15.933[d]	15.755[d]														
$_{36}Kr$	14324[b]	1921[b]	1730.9[b]	1678.4[b]	292.8[b]	222.2[b]	214.4[b]	94.9[b]	93.7[b]	27.5[b]	27.5[b]	14.66[b]	14.08[b]								
								95.04[d]	93.81[d]			13.996[e]									
$_{54}Xe$	34561[b]	5453[b]	5104[b]	4782[b]	1148.7[b]	1002.1[b]	940.6[b]	689.0[b]	676.4[b]	213.2[b]	155[c]	145.5[b]	69.5[b]	67.5[b]	-	233[b]					
										1208[d]	1938[d]	879[d]	636[d]	603[d]	299[d]		234[d]	200[d]	153[d]	80[d]	
$_{86}Rn$																					

a) Moore, Atomic Energy Levels, Washington, NBS Circ. 467; 1949, 1952, 1958
b) Siegbahn et al., ESCA applied to free Molecules, North Holland, Amsterdam, 1969
c) Lotz, JOSA 57, 873 (1967); 58, 236 (1968); 58, 915 (1968); from optical data
d) Siegbahn et al., Nova Acta Regia Soc. Sci. Upp. Ser. IV, Vol. 20, Uppsala, 1967

Table 2 (crd.)

a) Powell and Dolling (1977
b) Kittel (1971)
c) Barker (1976)
d) Sando (1971
e) Cohen and Schneider (1974)
f) Saxon and Liu (1976)
g) Ermler, Lee, Pitzer and Winter (1978)
h) Gilbert and Wahl (1971)
i) Ng, Trevor, Mahan and Lee (1977)
l) Wadt (1979)

Table 2

Energies and structural parameters of RGS and rare gas molecules. T_o: meeting point at 760 torr; $\hbar\omega_p$: largest energies of transversal-acoustic phonons TA(X) and longitudinal-acoustic phonons LA(X); D_K: binding energy per atom in a crystal; D_o, D_*, D_+: dissociation energies of rare gas molecules in the ground state, the excited state and of the molecular ions respectively (see Fig. 3); r_K: nearest neighbour separation in a crystal; r_o, r_*, r_+: internuclear distance of rare gas molecules in the fround state, the excited state and of the molecular ions respectively (see Fig. 3).

		He	Ne	Ar	Kr	Xe
T_o (K) [a]			24.6	83.7	115.8	161.3
$\hbar\omega_p$ (eV) [a]	TA(X)		0.0046	0.0059	0.0043	0.0038
	LA(X)		0.0068	0.0086	0.0062	0.0054
D_K (eV/Atom) [d]			0.02	0.08	0.116	0.17
D_o (eV) [c]		0.00095	0.0036	0.0012	0.0017	0.0024
D_* (eV)		2.5[d]	0.5[e]	0.68[f]		0.79[g]
D_+ (eV)		2.67[h]	1.2[e]	1.25[h]	1.15[i]	0.99[g]
r_K (Å) [k]			3.156	3.755	3.992	4.335
r_o (Å) [c]		2.96	3.102	3.761	4.006	4.361
r_* (Å)		1.04[d]	1.79[e]	2.42[f]		3.04[g]
r_+ (Å)		1.06[h]	1.75[e]	2.43[h]	2.79[l]	3.04[g]

Table 3

Parameters for the band structure and for excitons of pure RGS and for impurity states in rare gas matrices. All energies in eV. A superscript "i" denotes values for the impurity states. E_G, E_G^i: band gap energy; E_{Th}, E_{Th}^i: threshold energy for photoelectron emission ≡ vacuum level; $V_o \equiv E_G - E_{Th}$: electron affinity; ΔE_{so}, ΔE_{so}^i: spin orbit splitting of the valence bands and of impurity states with j = 3/2 and j = 1/2; W_{VB}: total width of the valence bands; B, B^i: binding energy of excitons; Δ, Δ^i: central all correction of n = 1 excitons and δ, δ^i quantum defect. We have attempted to gire a consistent set of values from the presumably most reliable data. The binding energies B, B^i depend on the applied model (see e.g. B in Ne corresponds to 5.00 eV in the Wannier model and 6.93 eV in the quantum defect model[a]).

	E_G, E_G^i	E_{TH}, E_{TH}^i	V_o	ΔE_{so}, ΔE_{so}^i	W_{VB}	B, B^i	Δ, Δ^i	δ, δ^i
Ne	21.58[a]	20.3 [b]	+1.3	0.09[a]	1.3[b]	5.00-6.93[a]	0.86[a]	0.28[a]
Ar in Ne	16.1 [d,e]	15.05[f]	+1.1	0.34[g]		"	1.39[e]	0.40[e,l]
Kr in Ne	14.6 [d,e]	13.48[f]	+1.1	0.61[g]		"	1.03[e]	0.31[e,l]
Xe in Ne	12.6 [d,e]	11.60[f]	+1.0	1.27[g]		"	1.53[e]	0.43[e,l]
Ar	14.16[h]	13.9 [b,c]	+0.3	0.18[h]	1.7[b]	2.36[h]	0.26[h]	0.21-0.28[k]
Kr in Ar	12.5 [i]	12.2 [i]	+0.3				0.5	
Xe in Ar	10.54[i,m]	10.23[i]	+0.3	1.08[i]			1.0 [m]	
Kr	11.61[h]	11.9 [b,c]	-0.3	0.69[h]	2.3[b]	1.53[h]	0.09[h]	0.08-0.17[k]
Xe in Kr	10.1 [i]	10.30[i]	-0.2				0.4	
Xe	9.33[h]	9.7 [b,c]	-0.4	1.3	3.0[b]	1.02[h]	0.06[h,m]	-0.03-0.06[k]

Table 3 (ctd.)

a) Saile and Koch (1979)
b) Schwentner, Himpsel, Saile, Skibowski, Steinmann and Koch (1975)
c) Schwentner, Skibowski and Steinmann (1973
d) Hahn and Schwentner (1980)
e) Böhmer, Haensel and Schwentner (1980)
f) Himpsel, Saile, Schwentner, Skibowski, Koch and Jortner (1976)
g) Pudewill, Himpsel, Saile, Schwentner, Skibowski and Koch (1976)
h) Saile, Steinmann and Koch (1977a)
i) Ophir, Raz, Jortner, Saile, Schwentner, Koch, Skibowski and Steinmann (1975)
j) Schwentner and Koch (1976)
k) Resca, Resta and Rodriguez (1978)
l) Resca, Resta (1979)
m) Gedanken, Raz and Jortner (1973)
n) Baldini (1965)

Table 4

Radii of the n = 1 excitons for Ne, Ar, Kr and Xe in comparison with the nearest neighbor distances r_K in a fcc-lattice (see Table 2)..

	Ne	Ar	Kr	Xe
$r^{n=1}_{(\mathring{A})}$ (a)		1.8	2.5	3.2
r_K $_{(\mathring{A})}$ (b)	3.156	3.755	3.992	4.335

(a) after SAILE (1976) calculated with equation (3.7)

(b) Horton (1968)

Table 5

Comparison between experimental transition energies for bulk excitons in solid neon and other parameters with theoretical calculations $B_1 = E_G - E(n=1)$ are the real binding energies of the n = 1 - excitons and μ is the effective mass. The other notations are the same as in table 1. All energies are in eV.

	Experiment		Theory				
	Ref. a		Ref. b	Ref. c	Ref. d	Ref. e	Ref. f
J	$^3/_2$	$^1/_2$					
n = 1	17.36			17.50	17.65	17.75	17.58
		17.50		17.63	17.75	17.85	17.79
2	20.25		19.98			20.32	20.24
		20.36	20.08			20.42	20.35
3	20.94		20.93			20.94	20.91
		21.02	21.13			21.04	21.03
4	21.19		21.25			21.19	21.19
		21.29	21.34			21.29	21.31
5	21.32		21.40			21.31	21.33
			21.50			21.41	21.45
E_G	21.58		21.67			21.55	21.61
		21.62	21.77			21.65	21.73
B_1	4.22		4.16				
		4.12	3.81				
Δ_{so}	0.09		0.10			0.10	0.12
δ	0.28					0.35	~0.5
		0.24				0.35	~0.5
μ	0.8		0.8			0.8	0.97
		0.7					

a) Saile and Koch (1979)

b) Andreoni, Perrot and Bassani, Phys. Rev. B 14, 3589 (1976)

c) Boursey, Castex and Chandrasekharan, Phys. Rev. B 16, 2858 (1977)

d) Resca and Rodriguez, Phys. Rev. B 17, 3334 (1978)

e) Resta, Phys. Stat. Sol. (b) 86, 627 (1978); gap energies are obtained by a fit of the experimental data and Δ_{so} is the atomic value. From these gap energies the theoretical exciton binding energies have been subtracted.

f) Resca, Resta and Rodriguez, Sol. State Comm. 26, 849 (1978), and Phys. Rev. B 18, 696 (1978)

Table 6

Exciton energies of bulk and surface excitons.

Exciton energies at 20 K (Xe, Kr, Ar) and 8 K (Ne) in rare gas solids in the Wannier notation n = 1, 2, ... j = 3/2 and 1/2 indicates the spin-orbit of the series and L is the longitudinal exciton. For Ne an adsorbate state A at 16.91 eV has been observed. All values are in eV. The accuracy is better or equal to 0.01 eV for peak positions.

		$Xe_{(a)}$ 5p		$Kr_{(a)}$ 4p		$Ar_{(a)}$ 3p		$Ne_{(b)}$ 2p	
j =		3/2	1/2	3/2	1/2	3/2	1/2	3/2	1/2
bulk excitons	n = 1	8.37	9.51	10.17	10.86	12.06	12.24	17.36	17.50
	2	9.07		11.23	11.92	13.57	13.75	20.25	20.36
	3	9.21		11.44	(12.21)	13.87	14.07	20.94	21.02
	4			11.52		13.97		21.19	21.29
	5							21.32	
	L	8.43		10.29	10.95		12.50		17.75
surface excitons									A 16.91
	1	8.21		9.95	10.68	11.71	11.93		17.15
				10.02		11.81			
	2			11.03		12.99			
						13.07			

a) Saile, Steinmann and Koch (1977)

b) Saile and Koch (1979)

Table 7

Longitudinal transverse splittings for bulk excitons in RGS.

	Ne		Ar		Kr		Xe	
n = i	3/2	1/2	3/2	1/2	3/2	1/2	3/2	1/2
width of the reflectance band	-	$\sim 0.3^a$	0.06^b	0.32^b	$\sim 0.2^b$	$\sim 0.17^b$	0.2^b	0.15^b
opt. Δ_{LO-TO}	-	0.27^a	-	0.26^c	0.12^c	0.09^c	0.06^c	-
calc. Δ_{LO-TO}	0.04^e 0.236^f	0.232^e 0.252^f						

a) Saile and Koch (1979)

b) see the review by Sonntag (1977)

c) Saile et al. (1981)

d) Chandrasekharan and Boursey (1978)

e) Perrot and Bassoni (1976)

Table 8

Exciton energies of Xe, Kr and Ar guest atoms in Ne, Ar and Kr matrices obtaines from absorption (a,b,c) and luminescence excitation spectra (d). The halfwidth is given in brackets.

matrix

		Ne				Ar		Kr	
guest	exciton	a)	b)	c)	d)	a)	b)	a)	b)
Xe	n = 1	9.08 (0.135)	9.12	9.06	9.10	9.22 (0.095)	9.2	9.01 (0.07)	9.0
	n = 1'	10.04 (0.095)	10.08	10.05	10.06	10.53 (0.085)	10.6		
		10.40	10.51		10.35				
			10.69		10.95				
	n = 2	11.28 (0.115)		11.32	11.31	9.97 (0.075)	10.0	9.76 (0.065	9.8
					11.53				
					11.75				
					11.84				
	n = 3				12.00	10.25	10.3		
	n = 4				12.19	10.36			
	n = 5				12.43				
	n = 2'			12.59	12.60	10.80	10.8		
					12.83				
	n = 3'			13.32	13.34				
Kr	n = 1	10.62 (0.15)		10.68	10.60	10.79 (0.11)			
					10.85				
	n = 1'	11.22 (0.14)		11.29	11.22	11.36 (0.10)			
					11.54				
					13.12				
	n = 2			13.45	13.32				
	n = 2'			14.06	13.94				
	n = 3			14.14	14.05				
					14.18				
	n = 4			14.55	14.48				
Ar	n = 1	12.5 (0.2)		12.59	12.48				
	n = 1'	12.7 (0.2)		12.80	(12.74)				
	n = 2			14.97	14.84				
					15.00				
					15.17				
	n = 2'			15.31	15.25				
	n = 3			15.67	15. 1				
	n = 4			15.90	15.75				
	n = 3'			16.04	15.90				

a) Baldini (1965)

b) Gedanken, Raz and Jortner (1973)

c) Pudewill, Himpsel, Saile, Schwentner, Skibowski and Koch (1976)

d) Hahn and Schwentner (1980)

Table 9

Absorption-, reflection- and photoconductivity experiments on pure rare gas liquids and atomic and molecular impurity states in rare gas liquids. For the spectroscopic results see text.

System	Method	Spectral range	Technical remarks	Reference
pure liq. He	reflectance	12.4eV - 23.9eV	windowless reflectance cell, He bath	SURKO et al. (1969)
pure liq. Xe	reflectance	7.8eV - 11.0eV	LiF window, 165 K	BEAGLEHOLE (1965)
	reflectance	7.9eV - 9.6eV	LiF window	ASAF and STEINBERGER (1971)
	reflectance	7.7eV - 10.3eV	LiF window, temperatur dependence of exciton line positions	STEINBERGER and ASAF (1973)
	photoconductivity	6.5eV - 10.0eV	LiF window, variation of electric field and light intensity	ROBERTS and WILSON (1973)
	photoconductivity	8.0eV - 10.3eV	MgF_2 window, interlaced combs of gold electrodes	ASAF and STEINBERGER (1974)
	reflectance	7.5eV - 10.8eV	MgF_2 window, density dependence line shape analysis	LAPORTE and STEINBERGER (1977)
Xe in liq. Ar in liq. Kr	absorption	8.4eV - 10.6eV	LiF window	RAZ and JORTNER (1970a,b)
Xe in liq. Ar	absorption	8.2eV - 9.1eV	MgF_2 window, Ar density variation 0.1 - 1.4 g cm^{-3}	MESSING et al. (1972e)
Xe in liq. Ar in liq. Ne in liq. He	absorption density dependence high pressure	7.7eV - 10.5eV	MgF_2 window, T = 24 - 300 K pressures up to 400 atm.	MESSING et al. (1977a,f)
CH_3I in liq. Kr	absorption	6.1eV - 8.3eV	LiF window	GEDANKEN et al. (1973e)
CH_3I in liq. Ar H_2CO in liq. Ar	absorption	6.1eV - 7.3eV	MgF_2 window, Ar density variation 0.1 - 1.4 g cm^{-3}, T = 90 - 300 K, medium effects on vibrational structure	MESSING et al. (1977b)
CH_3I in liq. Ar in liq. Kr CS_2 in liq. Ar H_2CO in liq. Ar	absorption	6.1eV - 10.3eV	MgF_2 window, medium density variation, perturbation of molecular extravalence excitations	MESSING et al. (1977d)

Table 10

Experiment V_o scale for solid and liquid rare gases obtaines from optical and photoemission experiments (see table 3) compared to the calculation of V_o based on the SPRINGETT, JORTNER, COHEN (SJC) (1968) theory. A superscript i denotes values for the impurity states. $V_o = E_G - E_{TH} = U_p + T$. U_p: background polarisation potential; T: kinetic energy term.

System		Reference	Experiment	Theory (a) (b)		
			V_o(eV)	T (eV)	Up (eV)	V_o (eV)
liquid ^{4}He	4.2 K	(c)	+1.05	1.66	-0.3	+1.28
solid Ne	4 K	(f)	+1.3	2.44	-1.85	+0.60
liquid Ne	25 K	(d)	+0.67 ±0.05	1.91	-1.46	+0.45
Ar in solid Ne		(f)	+1.1			
Kr in solid Ne		(f)	+1.1			
Xe in solid Ne		(f)	+1.0			
solid Ar	6 K	(f)	+0.4	3.46	-3.54	-0.08
liquid Ar	87 K	(d) (e)	-0.2 ±0.02	2.53	-2.73	-0.20
Kr in solid Ar		(f)	+0.3			
Xe in solid Ar		(f)	+0.3			
solid Kr		(f)	-0.3	3.84	-4.05	-0.21
liquid Kr	123 K	(d)	-0.45 ±0.05	2.73	-3.11	-0.38
Xe in solid Kr		(g) (f)	-0.2			
solid Xe			-0.4	4.12	-4.64	-0.52
liquid Xe	165 K	(d)	-0.61 ±0.05	2.85	-3.46	-0.61

References for Table 10

(a) B.E. Springett, M.H. Cohen and J. Jortner, J.Chem.Phys. 48, 2720 (1968)

(b) J. Jortner and A. Gaathon, Canad.J.Chem. 55, 1801 (1977)

(c) W.T. Sommer, Phys.Rev.Letter 12, 271 (1964)

(d) W.K. Tauchert, Ph.D.Thesis, Freie Universität Berlin, Berlin, W. Germany, 1975, and W.K. Tauchert and W.F. Schmidt, Z.Naturforsch. 30a, 1085 (1975)

(e) J. Leckner et al., Phys.Rev. 156, 351 (1972)

(f) see table 3

Table 12

The broad emission bands "d" of solid Ar, Kr and Xe (in eV).

Reference	Ar		Kr		Xe			
Jortner et al., 1965		9.84		8.25		7.19		
Chesnovsky et al., 1972, 1973 and Gedanken et al., 1973		9.72		8.38	7.56	7.19		
Basov et al., 1970				8.42	7.56	7.08		
Creuzburg, 1971			8.66	8.45	7.60	7.24	6.93	6.53
Heumüller 1978 and Heumüller and Creuzburg, 1978	9.80	9.70	8.60	8.45	7.61	7.44	7.22	7.02
Fugol' 1978		9.63		8.33	7.6	7.1		
Hanus et al., 1974 and Coletti and Hanus 1977		9.76		8.43	7.65	7.21		
Huber et al., 1974		9.61		8.38				
Nanba et al., 1974		9.30		8.0		6.97		
Brodmann et al., 1974 and Ackermann et al., 1976		9.80		8.25	7.6	7.05		
Tolkiehn 1976 and Gerick 1977		9.72			7.6	7.1		
Hahn et al., 1977						7.2		
Hahn et al., 1979, Zimmerer 1979	9.86	9.83	8.46	8.4		7.07	7.03	
Kink et al., 1977					7.6	7.2		

Table 11

Parameters for localized excitons from Fugol' (1978) in eV.
$\hbar\omega_D$: Debeye energies; 2B: exciton band width; S: Stokesshift between absorption and emission; S^*: dissociation energy of the center; E_{LR}: lattice relaxation energy; Λ: coupling parameter; Π_m: barrier height.

	excimer centers R_2^*				atomic centers R^*			
	Ne	Ar	Kr	Xe	Ne (Γ 1/2)	Ne (Γ 3/2)	Ar (Γ 3/2)	Xe (Γ 3/2)
$\hbar\omega_D$	0.0064	0.0080	0.0062	0.0055				
2B	0.4	0.7	0.9	0.9				
S	3.7	2.46	1.8	1.3	1.1	0.9	0.5	-0.06
S^*	1.85	1.5	0.93	0.4	1.05	0.85	0.32	-0.4
LR	2.0	1.86	1.38	0.85	1.25	1.05	0.77	0.05
Λ	10	5.3	3.1	1.9	6.25	5.25	2.2	0.11
Π_m	0.0003	0.002	0.01	0.02	0.0008	0.001	0.01	5.6

Table 14

The narrow emission bands "a", "b" and "c" of solid Ne, Ar, Kr and Xe (in eV).
The assignement is partly tentative.

	Ne			Ar			Kr		Xe
	a	b	c	a	b	c	a	b	a
Fugol' (1978)		16.95, 16.87, 16.76, 16.68, 16.62, 16.56	16.2	12.1	11.64, 11.58	11.37			8.33, 8.18
Hanus et al. (1974)									
Coletti and Hanus (1977)	17.01, 16.91, 16.80, 16.79, 16.74, 16.66, 16.64, 16.49, 16.1			11.67, 11.61, 11.56, 11.53, 10.99, 10.89, 10.74 10.58			10.13, 10.12, 10.02, 9.92, 9.69		9.4 , 9.2 , 9.0 , 8.36, 8.34, 8.24, 8.18
Coletti and Bonnot (1978), Kink et al. (1979									
Packard et al. (1970)	16.97, 16.79	16.85, 16.67	16.91, 16.73, 16.53, 16.18, 15.04	11.58	11.83, 11.62		10.15	10.65, 10.04	8.35
Brodmann et al. (1974, 1976)									
Gerick (1977)	temperature dependence of emission bands see fig. 59								
Schubert and Creuzburg (1975)		16.7	16.0 , 14.0						
Heumüller (1978)						11.1			8.2
					11.85 11.6	11.3			
	16.9, 16.8, 16.7, 16.65, 16.1, 14.0								
							10.14, 9.99		8.33, 8.26

Table 13

Transitions observed in transient absorption spectra.

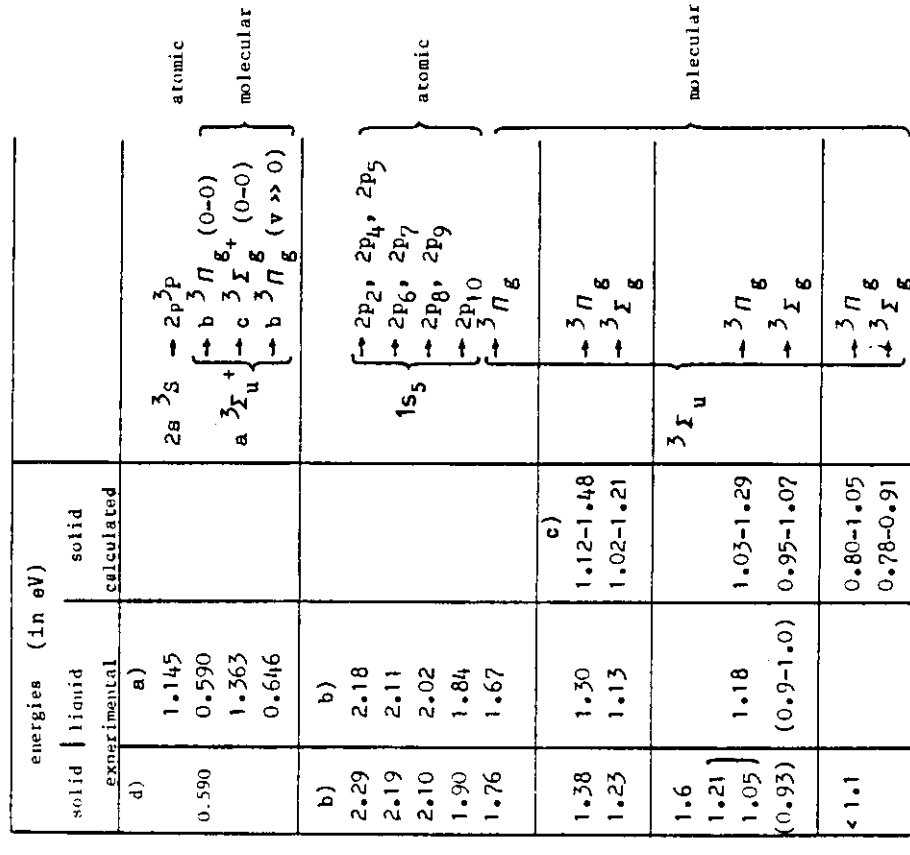

a) Hill, Beyhey and Walter (1971)
b) Suemoto and Kanzaki (1979)
c) Song and Lewis (1979)
d) Soley, Leach and Fitzsimmons (1975)

Table 15

Tentative assignment of emission due to free exditons (a), one center selftrapped excitons (b), vibrationally excited two center selftrapped excitons (c), and vibrationally relaxed two center selftrapped excitons (d). The relative intensities of the bands have been estimated from the area of the emission bands and are only reliable within an order of magnitude:

	energy				relative intensity			
	a	b	c	d	a	b	c	d
Ne		16.5	13-16			1.0	1.0	
Ar	12.1	11.64, 11.58	11.37	9.8	$1x10^{-4}$	$3x10^{-2}$	$5x10^{-2}$	1.0
Kr	10.15	10.05	9.7	8.4	$5x10^{-3}$	$5x10^{-3}$	10^{-2}	1.0
Xe	8.35			7.6, 7.1	10^{-3}			1.0

Ne: Schuberth and Creuzburg (1975)

Ar and Xe: Fugol' (1978)

Kr: Zimmerer (1977), Hahn et al. to be published.

Table 16

Radiative lifetimes of rare gas excimer states (not complete).

	$^1\Sigma_u$ (10^{-9} sec)	$^3\Sigma_u$ (10^{-6} sec)	
Ne_2^*	2.8	11.9	a
		5.1	b
		6.62	c
Ar_2^*	4.2 ± 0.13	3.2 ± 0.3	d
		3.22	c
		2.8	e
Kr_2^*	3.4 ± 0.3	0.264	f
		0.35	c
	5.2	0.15	g
Xe_2^*	6.22 ± 0.8	0.100 ± 2	h
		0.102 ± 2	i
		0.101 ± 1	k
	4.6 ± 0.3	0.99 ± 2	f

a) Schneider and Cohen (1974)
b) Leichner (1973
c) Oka, Rao, Redpath and Firestone (1974)
d) Keto, Gleason and Walters (1974)
e) Thonnard and Hurst (1972)
f) Bonifield, Rambow, Walters, McCusker, Lorentz and Gutcheck (1980)
g) Wenck, diplomwork Hamburg (1979)
h) Keto, Gleason, Bonifield, Walters and Soley (1976)
i) Millet, Birot, Brunet, Galy, Pons-Germain and Teyssier (1978)
k) Wenck, Hasnain, Nikitin, Sommer and Zimmerer (1979)

Table 18

Emission bands in liquid rare gases.

Xe a)	Kr a)	Ar b)	Ne c)	He to ground state d) Å	eV		He between excited states e) Å	eV	
1767 Å	1472 Å	1295 Å	774 Å	800	15.5	$A^1\Sigma_u^+(v'=0) \rightarrow X^1\Sigma_g^+$	10400	1.192	$d^3\Sigma_u^+ \rightarrow c^3\Sigma_g^+$
7.02eV	8.42eV	9.57eV	16.02eV				9182	1.350	$c^3\Sigma_g^+ \rightarrow a^3\Sigma_u^+$
			(900 Å)	(600)	(20.66)		6400	1.937	$d^3\Sigma_u^+ \rightarrow b^3\Pi_g$
				604	20.52				
				608	20.39				
				613	20.23				
				619	20.02		9136	1.357	$C^1\Sigma_g^+ \rightarrow A^1\Sigma_u^+$
				627	19.77	$A^1\Sigma_u^+(v'=16) \rightarrow X^1\Sigma_g^+$			
				636	19.49		6600	1.878	$D^1\Sigma_u^+ \rightarrow B^1\Pi_g$
				648	19.13				
				665	18.64				
				686	18.07		10911	1.136	$2p^3P \rightarrow 2s^3S$
				707	17.53		7270	1.705	$3s^3S \rightarrow 2p^3P$
							7060	1.756	$3s^1S \rightarrow 2p^1P$

a) Basov, Balashov, Bogdankevitch, Danilychev, Kashnikov, Lantzov and Khodkevitch (1970)

b) Jortner, Meyer, Rice and Wilson (1965)

c) Packard, Reif and Surko (1970)

d) Stockton, Keto and Fitzsimmons (1972)

e) Keto, Soley, Stockton, Fitzsimmons (1974)

Table 17

Relaxation time constants in RGS.

τ_1, τ_2, τ_3: experimental lifetimes: τ_4: calculated vibrational relaxation time constants of R_2^* centers; ΔE: vibrational energy spacings; $\hbar\omega_p$: maximum of transverse acoustic phonon energies; $N = \Delta E/\hbar\omega_p$: order of vibrational relaxation processes; τ_5: selftrapping time constant.

		τ_1 (in nsec) $^1\Sigma_u$	τ_2 (in nsec) $^3\Sigma_u$	τ_3	temp.(K)	band.	τ_4 (nsec)	ΔE (meV)	$\hbar\omega_p$ (meV)	N	τ_5 (sec) exp.	τ_5 (sec) theor.
Xe	a	3	150- 900		30 - 6	7.2 eV						
	b		20-15000		100 - 6							
	c		2000		6		0.005	15[l]	3.8	4	10^{-12}	10^{-12}
	d		30		148							
	p		58		80	7.6 eV						
	d		26 - 29		136 - 65	7.2 eV						
	d		15 - 16		136 - 65	7.6 eV						
Kr	e	8	100 - 5000	300-15000	20 - 5							
	c		300		6		0.05	23[m]	4.3	5		
	d		90		83							
Ar	e	4	2000- 3000	5000-15000	10 - 5							
	c		1400		6							
	f	3.2	1100		83		1.5	35[n]	5.9	6		
	d		1410		80							
Ne	e	9	1000					70[o]	4.6	15		
	c		500			16.53 eV	10^{10}	1 → 0 67				
	c		2000			16.18 eV	10^7	2 → 1 61				
	d		3900			molecular	4×10^5	3 → 2 56				
	d		560000			atomic	400	4 → 3 51				
							8	5 → 4 46				
							g, h	h			i	k

a) Hahn et al. (1977)
b) Kink et al. (1977)
c) Coletti and Hanus (1977)
d) Suemoto and Kanzaki (1979)
e) Hann et al. (1979)
f) Carvalho and Klein (1978)
g) Yakhot (1976)
h) Yakhot et al.(1975)
i) Zimmerer (1976)
k) Martin (1971)
l) Ermler et al. (1978)
m) Jortner (1974)
n) Saxon and Liu (1976)
o) Cohen and Schneider (1974)
p) Monahan et al. (1976)
q) Keto, Gleason and Soley (1979)

Table 20

Emission bands in rare gas alloys except He matrix and the assignment ($^3P_1 \triangleq {}^1S_4$, $^3P_2 \hat{=} {}^1S_5$, $^1P_1 \triangleq {}^1S_2$) given by the authors. s means emission from special sites.

	electrons a)	x-rays b)	α particles c)	d)	e)	vacuum UV light f)	g)	stokesshift g)
Kr^* in Ar	9.26 Ar Kr^*	9.33 Ar Kr^* 8.90 Ar Kr^*	10.92 s $^3P_1$ 10.33 $^3P_1$ 9.32 Ar Kr^*				10.95 $^1P_1$ 10.5 s 10.4 $^3P_1$ 9.9 s 9.3 s	0.39 0.39
Kr_2^* in Ar	8.42 8.30	8.53	8.55				8.55	
Xe^* in Ar	8.63, 8.56 s 8.52, 8.46 s 8.40 s 8.38 $^3P_1$ 8.28 $^3P_2$ 7.5 Ar Xe^*	9.88 $^1P_1$ 8.36 $^3P_1$ 8.28 $^3P_2$	8.67 s $^3P_1$ 8.38 $^3P_1$	8.32	9.80 9.61 $^1P_1$ 9.40 8.70 8.44 $^3P_1$, $^3P_2$ 8.27	9.9 $^1P_1$ 8.50 8.36	9.7 $^1P_1$ n=2 8.83 $^3P_1$ 8.42 s 8.32 s	0.25 0.39
Xe_2^* in Ar	7.08	7.24 7.04	7.56 7.18	7.56 7.21	7.56 7.21	7.54 7.25		
Xe^* in Kr	8.40 $^3P_1$ 8.30 $^3P_2$ 7.95 Kr Xe^* 7.4 Kr Xe^*	8.75 Kr Xe^* 8.10 7.87 Kr Xe^* 7.71 Kr Xe^*	8.49 $^3P_1$ 7.94 Kr Xe^*					
Xe_2^* in Kr	7.1	7.65, 7.45 7.26, 7.06	7.70 7.20					

a) Fugol', Belov (1975) and Fugol' (1978)
b) Heumüller and Creuzburg (1978) and Heumüller (1978)
c) Gedanken, Raz and Jortner (1973)
d) Nanba, Nagasawa and Ueta (1974)
e) Möller (1976)
f) Ackermann (1976)
g) Hahn, Jordan, Schwentner, Sommer and Zimmerer (1930)

Table 19

Experimental lifetimes τ_1, τ_2 (in 10^{-9} s) and intensity ratios A_1/A_2 for liquid rare gases.

liquid	τ_1 $^1\Sigma_u^+$, $^0{}_u^+$ a	τ_2 $^3\Sigma_u^+$, $^1{}_u$ a	τ_2 $^3\Sigma_u^+$, $^1{}_u$ b	A_1/A_2 a	$\tau_1 A_1/\tau_2 A_2$ a
Ne			2900		
Ar	5.0 ± 0.2	860 ± 30	1110	7.8	0.45
Kr	2.1 ± 0.3	80 ± 3	110	0.9	0.02
Xe	2.2 ± 0.3	27 ± 1		0.6	0.05

a) Kubota, Hishida, Raun (1978)
b) Suemoto and Kanzaki (1979)

Table 22

Radiative lifetimes of free atoms and of guest atoms in Ne matrix (in 10^{-9} s).

		radiative lifetime in Ne matrix	atomic radiative lifetime	
Xe	$6s$, $1s_4$	2.4 ± 0.2	3.46 ± 0.09	a)
	$6s'$, $1s_2$	3.5 ± 0.2	3.44 ± 0.07	
	$5d$, $3d_2$	1.3 ± 0.2	1.40 ± 0.07	
Kr	$5s$, $1s_4$	2.5 ± 0.2	3.18 ± 0.12	a)
	$5s'$, $1s_2$	3.1 ± 0.5	3.11 ± 0.12	
	$4d$, $3d_5$	13.0 ± 2	44.5	b)
Ar	$4s$, $1s_4$	5.8 ± 0.3	8.4	c)
	$4s'$, $1s_2$	1.2 ± 0.2	2.0	
	$3d$, $3d_5$	420 ± 20	?	

a) Matthias, Rosenberg, Poliakoff, White, Lee and Shirley (1977)
b) Gruzdev and Loginov (1975)
c) Wiese, Smith, Miles (1969)

Table 21

Energies of emission bands (E) and comparison with the corresponding states in absorption (A) and in the free atom (G). Energies in eV.

	emission bands in Ne matrix (E) a)		b)	c)	atomic levels (G)			absorption bands in Ne matrix (A) a)		(A)-(E) STOKES SHIFT	(G)-(E) Matrix SHIFT
Xe/Ne	I	8.61	8.43	8.34; 8.47 8.61	$6s$	$1s_5$ $1s_4$	8.31 8.44	n = 1	9.06	0.45	- 0.16 - 0.17
	II	9.80	9.56	9.77	$6s'$	$1s_3$ $1s_2$	9.45 9.57	n = 1'	10.05	0.25	- 0.11 - 0.20
	III	10.78			$5d$	$3d_2$	10.40	n = 2	11.32	0.54	- 0.38
Kr/Ne	I	10.10	10.03	10.02 10.16	$5s$	$1s_5$ $1s_4$	9.91 10.03	n = 1	10.6	0.5	- 0.11 - 0.13
	II	10.78			$5s'$	$1s_3$ $1s_2$	10.51 10.64	n = 1'	11.22	0.44	- 0.14
	III	12.12			$4d$	$3d_5$	12.04	n = 2	13.35	1.23	- 0.08
Ar/Ne	I	11.70	11.61	11.63 11.71	$4s$	$1s_5$ $1s_4$	11.54 11.62	n = 1	12.51	0.81	- 0.07 - 0.09
	II	11.92		11.81 11.92	$4s'$	$1s_3$ $1s_2$	11.72 11.83	n = 1'	12.74	0.82	- 0.09 - 0.09
	III	13.93			$3d$	$3d_5$	13.86	n = 2	14.82	0.89	- 0.07

a) Hahn and Schwentner (1980)
b) Gedanken, B. Raz and Jortner (1973)
c) Schuberth and Creuzburg (1978)

Table 23

Emission spectra of liquid rare gas alloys (doping concentration $10-14^4$ ppm) at 85K (Xe/Ar, Kr/Ar) and 120K (Xe/Kr) after Chesnovsky et al. (1972, 1973) and Raz et al. (1976).

Assignment	Xe/Ar	Xe/Kr	Kr/Ar
Ar_2^*	9.69		9.69
Xe $^3p_1$	8.32		
Kr_2^*		8.32	8.38
Xe Kr*		7.85	
Ar Kr*			9.18
Xe_2^*	7.12	7.12	

Table 24

Experimental relaxation times between excited guest atom states in Ne matrix (in 10^{-9}s); n.o. means: not observed.

	$n=2 \rightarrow 1s_2$	$n=2 \rightarrow 1s_3$	$n=2 \rightarrow 1s_4$	$n=2 \rightarrow 1s_5$	$1s_2 \rightarrow 1s_3, 1s_4, 1s_5$	$1s_4 \rightarrow 1s_5$
Xe	1.0	n.o.	n.o.	n.o.	n.o.	n.o.
Kr	750	?	22	22	n.o.	n.o.
Ar	71	82	63	32	n.o.	n.o.

Table 25

Comparison of energies which are transferable by the matrix either in the selftrapped exciton states ($E_{R_2}^*$) or in the free exciton states n=1 ($E_{n=1}$) and n=1' ($E_{n=1'}$) with the lowest excitation energies ($E^i_{n=1}$) and ionisation energies E^i_{Th} of guest atom. E_{Th}: ionisation energy of the matrix. + and - means observation or absence of energy transfer in electron emission spectra (energies in eV).

matrix	guest	E_{Th} e)	E^i_{Th}	$E^i_{n=1}$ f)	$E_{R_2^*}$	$E_{n=1}$	$E_{n=1'}$	
Ne		20.3			16.80	17.36	17.50	
	Xe		11.60	9.08	+	+	+	c, d
	Kr		13.48	10.62		+	+	c
	Ar		15.05	12.5		+	+	c
Ar		13.8			9.80±0.44	12.06	12.24	
	Xe		10.2	9.22	-	+	+	b, d
	Kr		12.2	10.79	-	-	+	b
Kr		11.9			8.45±0.32	10.17	10.86	
	Xe		10.3	9.1	-	-	+	a,b

a) Ophir, Raz and Jortner (1974)

b) Ophir, Raz, Jortner, Saile, Schwentner, Koch, Skibowski and Steinmann (1975)

c) Pudewill, Himpsel Saile, Schwentner, Skibowski, Koch and Jortner (1976)

d) Schwentner and Koch (1976)

e) Schwentner, Himpsel, Saile, Skibowski, Steinmann and Koch (1975)

f) Baldini (1965)

Table 26

Diffusion lengths for energy transfer to guest atoms and to boundaries (in Å).

	excitons	photoelectron emission: guest atom	photoelectron emission: boundary	luminescence: guest atom	luminescence: boundary
Ne	n = 1,1',2	2500 ± 500 a)	observed a)		
Ar	n = 1,1'				50 1)
	n = 2,2',3	120 b)	observed b)		100 1) 50 g)
Kr	n = 1		10 - 100		
	n = 1'	observed b)	150 - 250 d)		200 - 250 f)
	n = 2		150 - 350	300 f)	200 g), h)
Xe	n = 1,2	170 c)	300 e)	25 - 260 f)	150 - 1000 1) 500 f)

a) Pudewill, Himpsel, Saile, Schwentner, Skibowski, Koch and Jortner (1976)

b) Ophir, Raz, Jortner, Saile, Schwentner, Koch, kibowski and Steinmann (1975)

c) Ophir, Raz and Jortner (1974) corrected for electron escape depth of a), Ophir (1976)

d) Schwentner, Rudolf and Martens (1980)

e) Ophir, Schwentner, Raz, Skibowski and Jortner (1975)

f) Ackermann (1976)

g) Ackermann, Brodmann, Tolkiehn, Zimmerer, Haensel and Hahn (1976)

h) Ackermann, Brodmann, Hahn, Suzuki and Zimmerer (1976)

i) Gerick (1977)

Table 27

Time hierarchy for the competition of energy transfer and relaxation. The time constants τ (in s) have the following meaning: τ_1: radiative decay of R_2^* or R^* centers of the matrix; τ_2: vibrational relaxation of R_2^* centers; τ_3: localization of excitons; τ_R ($i \rightarrow j$): electronic relaxation of exciton i to exciton j; τ_T: energy transfer. (After Schwentner and Koch, 1976)

		time hierarchy from electron emission experiments	time hierarchy including results of table 13
1 % Xe in Ar			
n = 1	$\tau_1 > \tau_2 > \tau_T$	$\tau_1 \sim 10^{-5} - 10^{-9} > \tau_2 \sim 10^{-9} - \tau_T$	
n = 1'	τ_R (1' $\rightarrow$ 1) $> \tau_T$		
n = 2	$\tau_1 > \tau_R$ (2 $\rightarrow$ 1) $> \tau_T \sim \tau_3$	$\tau_1 \sim 10^{-5} - 10^{-9} > \tau_R$ (2 $\rightarrow$ 1) $> \tau_T \sim \tau_3 \sim 10^{-12}$	
1 % Xe in Ne			
n = 1	$\tau_2 > \tau_1 > \tau_T > \tau_3$	$\tau_2 \sim 10^{-5} > \tau_1 \sim 10^{-6} - 10^{-8} > \tau_T > \tau_3 \sim 10^{-12}$	
n = 2	$\tau_2 > \tau_1 > \begin{cases} \tau_R\ (2 \rightarrow 1) \\ \tau_3 \end{cases}$	$\tau_2 \sim 10^{-5} > \tau_1 \sim 10^{-6} - 10^{-8} > \tau_T > \begin{cases} \tau_R(2 \rightarrow 1) \\ \tau_3 \quad 10^{-12} \end{cases}$	

Table 28

Critical transfer radii Rq (in Å) for electronic energy transfer to guest atoms and boundaries in solid (s) and liquid (l) rare gas matrices.

Host	Temperature	Guest			Boundary
	K	Species	Rq(exp.)	Rq(cal.)	Rq(exp.)
Ar (s)	6-20	Xe	18[a]		
		Kr	6[b]		
Kr (s)	60	Xe	17[a]	10[a]	
(s)	110	Xe	25[a]	15[a]	
(l)	120	Xe	24[a]	21[a]	
(s)	5	C_6H_6	21-22[c]		
(s)					25-29[c]
(s)					22[d]
Xe (s)	5-15	C_6H_6	24-29[c]		
(s)					40[c]

a) Chesnovsky, Gedanken, Raz and Jortner (1973)

b) Gedanken, Raz and Jortner (1973)

c) Ackermann (1976)

d) Ackermann, Brodmann, Hahn, Suzuki and Zimmerer (1976)

Table 29

Calculated mean free path and mean kinetic energies of electrons in mobility experiments for liquid Ar at 84 K after Lekner (1967).

electric field (V/cm)	drift velocity (cm/usec)	mean linetic energy (eV)	mean free path for energy transfer Λ_0 (Å)	mean free path for momentum transfer Λ_1 (Å)
10	0.0039	0.011	6.6	136
10^2	0.037	0.011	6.6	136
10^3	0.21	0.028	6.7	140
10^4	0.47	0.51	8.7	140
10^5	(0.25)	(2.4)	(9.0)	(60)

Table 30

Parameters a, b, c for the calculation of atomic ionisation cross sections (W. Lotz 1967) and of the mean free path for electron-electron scattering. (a in 10^{-14} cm^2 (eV)^2) N_i and P_i: number and binding energy of electrons in shell i. A: atomic weight. ϱ : density (g/cm^3).

	P_1	N_1	P_2	N_2	P_3	N_3	a	b	c	P_1'	A	ϱ
Ne	21.6	6	48.5	2			2.8	0.92	0.19	17.6	20.2	1.504
Ar	15.8	6	29.2	2			4.0	0.62	0.40	12.08	40	1.771
Kr	14.0	6	27.5	2	93	10	4.0	0.71	0.76	10.23	83.8	3.094
Xe	12.1	6	23.4	2	67	10	4.0	0.54	0.64	8.4	131.3	3.782

P_1': threshold energy in the solid state (eV).

Table 31

Mean energies W (in eV) for the production of free electron hole pairs.

	W calculated		W experimental		
	2.8 E_G Gl.5.20	Doke et al. (1976) Gl.5.21	solid	liquid	liquid
			Spear and leComber(1977)		Doke et al.(1976)
Xe	26	15.4	24 ± 1	33 ± 2	15.6 ± 0.3
Kr	32	19.5	25 ± 1	25 ± 1	
Ar	40	23.3	27 ± 1	27 ± 1	23.6 ± 0.3

Table 32

Escape depth lp of RGS (lp and film thickness d in Å).

	l_p from fig. 63		l_p from fig. 64	l_p from equ. 5.26
	50 _ d _ 200	500 d 5000		
Xe	250	950		
Kr	250	4000		2900
Ar	200	3000	1000	1400 - 1700
Ne		5000	3500	

Table 33

Threshold energies E_{sc} for electron-electron scattering.
E_1: n = 1 exciton; E_G: band gap (in eV).

	$2E_1$	E_G+E_1	$2E_G$	E_{sc} a)	E_{sc} b)	E_{sc} c) threshold	E_{sc} c) extrapolation
Xe	16.74	17.70	18.66	17.6		18	17.0
Kr	20.34	21.78	23.22	21.5		21.56	20.5
Ar	24.12	26.22	28.32		25.5 ± 0.5	26.10	24.5
Ne	34.72	38.86	43.00				

a) Photoelectron yield
Schwentner, Skibowski, Steinmann (1973)

b) Luminescence yield
Möller, Brodmann, Hahn, Zimmerer (1976)

c) Photoelectron energy distribution
Schwentner (1976)

Figure Captions

Fig. 1 Energy regions for excited-state photophysical and chemical processes in molecular crystals (after Jortner and Leach, 1980).

Fig. 2 Schematic scheme of the energy levels of an atomic impurity state in a solid rare gas matrix depicted for the case of Xe in Ar. The energies given are discussed in the text.

Fig. 3 Potential curves for a diatomic rare gas molecule. The nomenclature is explained in the text.

Fig. 4 Schematic scheme for various relaxation and energy transfer processes discussed in the text. Case I, selftrapping of excitons and nonradiative relaxation; Case II, recapture of free electrons and formation of luminescence centers; Case III, competition of nonradiative relaxation and radiative decay in exciton states of guest atoms; case IV, energy transfer of free and selftrapped host excitons to guest atoms and boundaries.

Fig. 5 Absorption cell for high pressure vacuum ultraviolet optical experiments (from Messing et al. (1977)). A: pipe leading to the gas handling system; B: sample preparation chamber; C: electrical feed-through; D: vacuum chamber cover flange; E: thermocouple; F: cooling coil; G: heating element; H: closing nut; and I: optical axis.

Fig. 6 Liquid Ar barrel shower counter for the CELLO high energy particle detector used at the Deutsches Elektronen-Synchrotron DESY.

Fig. 7 Crystal growing device for the preparation of neon crystals. (a) Crucible removable for observation in the vacuum ultraviolet; (b) Temperature measurement inside the crystal by a thermocouple led through a stainless steel tube which also supports the crystal (from Schuberth and Creuzburg (1975)).

Fig. 8 Device for luminescence experiments in liquid He by excitation with high energetic electrons (after Fitzsimmons 1973). 1: electron gun; 2: vacuum pumps; 3: sample chamber; 4: main cryostat; 5: electron beam; 6: cryogenic helium; 7: liquid nitrogen; 8: monochromator; 9: sodium salicylate and photomultiplier.

Fig. 9 Experimental setup for simultaneous measurement of transient absorption spectra after excitation with a 5 x 10^{-9}s pulse of 500 keV electrons and registration of luminescence emission spectra and decay curves (after Wilcke 1979).

Fig. 10 Typical photon flux of monochromatized synchrotron radiation at the sample (upper panel). Time structure of the synchrotron light pulses provided by the storage ring DORIS in Hamburg (after Hahn et al. 1978) (lower panel).

Fig. 11 Setup for simultaneous VUV-reflection and photoemission experiments on condensed gases. Synchrotron light (SR) enters the sample chamber (SC) from the monochromator (M) with concave grating (G) via the exit slit (ES). A cryostat (K) with two cryoshields(CS) and an insulated sample substrate (I), an open electrostatic photomultiplier (D1), a gashandling system (GH), and a photoelectron energy analyzer (EEA) with a channeltron as detector (CH) are incorporated into the sample chamber. Photoelectron analysis: V_o to V_5, lens voltages; V_p: sample voltage; EM: emitter follower; D: discriminator; MCA: multichannel analyzer; DAC: digital-analog converter. Channel advance is triggered by a reference signal via lock-in amplifier (LIA), analog-digital converter (ADC) and a preset counter (PC). The reflectance as a function of wavelength is measured by D1. Film thickness is determined by comparing the reflectance $R_1(t)$ at λ_1(VUV) and $R_2(t)$ at λ_2 (laser wavelength, laser (L) via detector D2) simultaneously during evaporation time t (from Schwentner et al. 1974).

Fig. 12 Experimental arrangement for simultaneous measurement of the VUV reflection, luminescence excitation and transmission spectra. The radiation shield is used as a collecting electrode for photoemission yield measurements. Synchrotron radiation is dispersed with a 1.5 m horizontal Wadsworth monochromator. S is the exit slit of the monochromator (from Hasnain et al. 1977).

Fig. 13 Experimental arrangement for time-resolved luminescence experiments with selective excitation. Upper panel: experimental arrangement consisting of: MP: primary monochromator; FS: focusing mirror; P: sample holder; L: luminescence light; MS: secondary monochromator; PM: photomultiplier; VK: cryostat; GE: gas inlet tube. Lower panel: electronics for time resolved luminescence spectroscopy consisting of: DORIS: storage ring; BT: bunch trigger; DL: delay line; CD: constant fraction discriminator; TAC: time to amplitude converter; ADC: analog to digital converter; MC: multichannel analyser; PL: plotter. (From Hahn and Schwentner, 1980).

Fig. 14 Comparison of some representative photoelectron energy distribution curves for solid Xe (at $h\nu$ = 13.78 eV), Kr (at $h\nu$ = 19.84 eV), Ar (at $h\nu$ = 19.07 eV) and Ne (at $h\nu$ = 26.72 eV) with calculated valence bands (from Schwentner 1974).

Fig. 15 The plot of characteristic parameters of the valence and conduction bands (+, width of valence bands; •, valence band splitting; Δ, spin orbit splitting; o, width of conduction band; x, lattice constant) on a linear band gap scale shows a continuous change of these parameters from Xe to Ne (from Schwentner 1974).

Fig. 16 Comparison of photoelectron spectra for the Xe 5p levels of atomic Xe (Turner et al., 1970), Xe-clusters in the gas phase (Dehmer and Dehmer, 1978) and Xe embedded in an Ar and Ne matrix (Schwentner et al. 1975). The binding energy scales have been aligned at the Xe $5p_{3/2}$ maximum.

Fig. 17 The spectra of the imaginary part of the dielectric constant ε_2 for solid Ar, Kr, and Xe in the region of the valence excitons. The spin orbit splitting in the n = 1 excitons Δ_1, the assignments of the higher members of the exciton series and the band gap E_G are indicated. For the Ne-spectrum see Fig. 18 (from Saile 1976).

Fig. 18 Optical density (~ ln I/I_0) of solid neon at 6K in the excitonic range of the spectrum. The main features can be grouped into two series split by spin orbit interaction which converge to the band-gap. For the assignment see text. In the insert results of a surface coverage experiment for solid neon in the range of the n = 1 exciton are shown. Curve A is the optical density of a clean neon sample. Upon evaporation of a thin Ar coverlayer the structure denoted by S disappears whereas the band shape of the remaining peak remains unchanged. In the lower part of the insert, the difference spectrum B-A is shown and the smooth and structureless Ar background is indicated by the broken line (from Saile and Koch 1979).

Fig. 19 High resolution absorption spectra for solid Ar, Kr and Xe in the range of the valence excitons. Volume and surface excitons are observed for all three samples. For Ar and Kr the results of surface coverage experiments are also shown. For Xe the experimentally determined spectrum in the range of the n = 1 surface and volume exciton is displayed on an expanded scale together with a lineshape analysis using two Lorentzians (after Saile 1976).

Fig. 20 Absorption spectrum for thin Kr films (d = 30 Å). The n = 1 and n = 1' transverse TO volume excitons as well as the surface excitons (S) can be seen in the spectrum for normal incidence in the upper panel. At non-normal incidence (lower panel) two new features associated with the n = 1 and n = 1' longitudinal (LO) bulk excitons appear. (From Saile et al., 1980).

Fig. 21 Absorption coefficient of solid (solid line) and gaseous (dashed line) Kr determined by reflectance (Haensel et al. 1970c; Skibowski 1971) and absorption measurements (Haensel et al. 1969b). (..... Samson, 1963; ooo Rustgi et al., 1964; ■ Lukirskii et al., 1964; ·–·–· Cook and Metzger, 1965; ------ (between 15 and 20 eV) Huffmann et al., 1963) (from Sonntag, 1977).

Fig. 22 Reflectance spectra of Ne films doped with 1% Xe, d = 2000 Å (upper panel); 1% Kr, d = 1700 Å (middle panel); and 1% Ar, d = 1800 Å (lower panel) (d: film thickness) evaporated onto a gold substrate. The spin-orbit-split impurity exciton series are indicated on top of each spectrum. (From Pudewill et al., 1976).

Fig. 23 Excitation energies of excitons in pure Ne (E_n) and of the impurity states of Ar, Kr and Xe in a Ne matrix (E_n^i) plotted versus $1/n^2$ according to the Wannier model. (From Pudewill et al., 1976).

Fig. 24 Reflectance of Ne films doped with ≈ 0.1% (solid line), ≈1% (dashed line) and ≈ 5% (dash-dotted line) Xe respectively evaporated onto a gold substrate in the range of the n = 1 Xe impurity excitations.

Fig. 25 Optical absorption spectra of thin solid films of Ar - Xe mixtures deposited onto LiF plates cooled at liquid He temperature. The number at the right side of each curve indicates the Xe concentration in mol%. The ordinate of each curve is shifted for the convenience of comparison. Upward arrows ↑ indicate the position of the localized Wannier exciton bands due to the Xe impurity (Baldini 1965) and downward arrows ↓ mark the intrinsic Wannier exciton bands of the undoped Xe solid (Haensel et al., 1970) (from Nagasawa et al., 1972).

Fig. 26 Fine structure of the Xe-4d absorption in the energy range 64-90 eV for different Xe : Kr mixtures ranging from 100 at.% to 1 at.% Xe. The corresponding peaks are connected by dashed lines (from Haensel et al., 1973).

Fig. 27 Fine structure of the Xe-4d absorption in the energy range 64-80 eV for different Xe : Ar mixtures ranging from 100 - 10 at.% Xe. The corresponding peaks are connected by dashed lines (from Haensel et al., 1973).

Fig. 28 Photoelectron energy distribution curves for Xe/Ar alloys for three different photon energies with the Xe concentration as a parameter. All spectra are normalized to the same maximum counting rate. The estimated background is indicated by the dashed lines. The energy scale for all EDC's has been fixed at the Xe 5p(1/2) maximum. The arrows indicate the onset of photoemission at $E_{kin} = 0$. The dash-dotted curve for pure Ar ($h\nu = 18.37$ eV) was taken from Schwentner et al. (1975). (From Nürnberger et al., 1977).

Fig. 29 Comparison of the measured total valence band widths in eV for Xe (W_{Xe}) and Ar (W_{Ar}) as a function of concentration including estimated errors (crosses) with calculated band widths. The free parameter α is used in the following expression: $pp\pi\ (c) = pp\pi\ (o) \cdot e^{-d/\alpha \cdot d_o}$ and an analogous expression for $pp\sigma$, with (c) and (o) denoting the band structure paramters at a given concentration and for the pure material. d_o is the Xe nearest neighbor distance in pure Xe.

Fig. 30 Comparison of the experimentally determined photoelectron energy distribution curves for Xe at $h\nu = 13.8$, 16.5 and 18.0 eV (upper part) and for Ar at $h\nu = 16.5$ and 18 eV (lower part) for three different concentrations with the calculated valence bands between the Γ and X-point using $\alpha = 2$ for the calculation. (From Nürnberger et al., 1977).

Fig. 31 The reflection of fluid Xenon in the range of the 6s 3/2 excitation at various densities. The experimental values are given by the points. The full curves represent the results of a dispersion analysis. The curves a to g correspond to densities ranging from 182 to 500 amagat. The corresponding densities (amagat) pressures (bar) and temperatures (K) are: a: 182, 61.8, 292.7; b: 241, 65.7, 293.9; c: 283, 61.8, 287.8; d: 306, 61.8, 283.4; e: 338, 61.8, 274.4; f: 350, 83.4, 275.0 and g: 500, 0.8, 163.0 (from Laporte and Steinberger, 1977).

Fig. 32 The absorption spectra of Xe in fluid Ar in the low and intermediate Ar density range. The absorption curves are horizontally shifted, all being displayed on the same optical density (OD) scale. (From Messing et al., 1977a).

Fig. 33 The absorption spectra of Xe in fluid Ar at high Ar density and in solid Ar. The Xe concentration is roughly 1 ppm. The absorption curves are horizontally shifted, all being displayed on the same optical density (OD) scale. (From Messing et al., 1977a).

Fig. 34 The density dependence of the energies of the maxima of the absorption bands relative to the unperturbed atomic transition energy for the absorption lines of Xe in fluid Ar observed in the spectral range 8.5 eV (≈ 1460 Å) to 10.8 eV (1150 Å); see Figs. 32 and 33. The spectral lines are designated by the conventional atomic notation. (From Messing et al., 1977a).

Fig. 35 Energy correlation diagram of the unperturbed atomic states of Xe, Xe impurity states in liquid Ar and of Xe impurity states in solid Ar. The correlation of the $7s[3/2]$ atomic state is rather tentative as denoted by the dashed line. (From Messing et al., 1977a).

Fig. 36 Absorption spectra of CH_3I in liquid Ar in the low energy range 5.9 eV (≈ 2100 Å) to 8.0 eV (≈ 1550 Å). The absorption curves are horizontally shifted, all being displayed on the same optical density (OD) scale. (From Messing et al., 1977b).

Fig. 37 Scheme for inhomogeneous and homogeneous disordered two-component materials.

Fig. 38 Flow diagram for the different structural features of metal RGS mixtures developing with increasing metal concentration.

Fig. 39 Summary of UV absorption spectra of matrix isolated metals. m or c means that also diatomic molecules or clusters have been studied (after B. Meyer 1979).

Fig. 40 Normalized scans of the absorption of white light by Na atoms trapped in Ar, Kr and Xe at 10 K. The arrows indicate the position of absorption peaks determined by laser excitation (from Balling, Havey and Dawson, 1978).

Fig. 41 Ground and lowest excited electronic states of NaAr as calculated by Baylis (from Smalley et al., 1977).

Fig. 42 Normalized luminescence of Na atoms in Ar at 10 K for excitation in different absorption bands A, B and C (from Balling, Havey and Dawson, 1978).

Fig. 43 Composition dependence of the height of the single Hg atom absorption. The experimental points represent the peak height above the background absorption. Solid curve given by eq. 5.1 with Z = 10. (From Danor et al., 1979).

Fig. 44 Optical transmission of lithium in various stages of aggregation. The indicated concentration of lithium vapor is mixed with Xenon and the mixture condensed onto a 5 K substrate. As the concentration of lithium increases, the degree of aggregation increases. (From Welker and Martin, 1979).

Fig. 45 Optical transmission of sodium in various stages of aggregation. The indicated concentration of sodium vapor is mixed with Xenon and the mixture condensed onto a 5 K substrate. (From Welker and Martin, 1979).

Fig. 46 Absorption spectra of Hg/Xe samples at 6 K for X = 0.1 - 0.4 (from Danor et al., 1979).

Fig. 47 Potential curves for the lowest u-type states of Hg_2 from Stock et al. (1978). Allowed transitions are marked by arrows (from Danor et al., 1979).

Fig. 48 Dependence of the absorption coefficient of Hg/Xe samples on the Hg concentration at several energies (see Fig. 46). (From Danor et al., 1979).

Fig. 49 Concentration dependence of the integrated optical absorption of sodium clusters in Xenon. The dotted lines have slopes equal to one and two. The absorption spectrum (right hand side) shows the line assignments. (From Welker and Martin, 1979).

Fig. 50 Absorption spectra of Ca_2 in an argon matrix before (a) and after (b) annealing. (From Miller et al., 1977).

Fig. 51 Scheme of combinations (a, b, c, d) of weakly and strongly bound potential curves for the ground state and the excited state (see text).

Fig. 52 Optical transmission of silver in various stages of aggregation. The indicated concentration of silver vapor is mixed with argon and the mixture condensed onto a 5 K substrate. (From Welker and Martin, 1979).

Fig. 53 Conductivity versus composition for mixtures of lead and argon deposited at 4.2 K (after Eatah, Cusack and Wright, 1975).

Fig. 54 The composition dependence of the conductivity (•) and of the temperature coefficient of conductivity (o) in Hg/Xe mixtures at 6^{o} K. Three scales of Mercury concentrations are presented: X - the atomic fraction of Hg, C - the volume fraction of Hg and C_a - the atomic volume fraction of Hg. (From Chesnovsky et al., 1977).

Fig. 55 Composition of the conductivity transition for several systems. The ordinate is the metal atom radius ÷ gas atom radius (from Hilder and Cusack, 1977).

Fig. 56 Vacuum UV absorption spectra of Hg/Xe solid films deposited at 40^{o}K and measured at 10^{o}K. The spectra were practically temperature independent in the range 10 - 40^{o}K. The percentages represent the mole fractions of Hg. The spectra were vertically displaced on the optical density scale; the residual absorption at 1550 Å in each case was 0.1 - 0.2 optical-density units. (From Raz et al., 1972).

Fig. 57 Optical absorption per Kr atom in thin Rb Kr films spanning the composition of the metal-insulator transition (from Phelps and Flynn, 1976).

Fig. 58 The real part $\varepsilon_1(E)$ of the dielectric function for Hg/Xe mixtures at 6 K for different atomic fractions of mercury (from Chesnovsky et al. 1979, 1980).

Fig. 59 The optical conductivity $\sigma(E)$ of Hg/Xe mixtures at 6 K for different atomic fractions of mercury. $\sigma(E) = \omega\, \varepsilon_2(E)/4\pi$ where E is the photon energy while $\omega(s^{-1})$ is the angular frequency. Solid line: Experimental data from transmission measurements. Broken line: Extrapolation to the D.C. conductivity values which are marked by dots (from Chesnovsky et al., 1979, 1980).

Fig. 60 Schematic sketch for the relaxation cascade of a free electron-hole pair in a RGS. A: excitation; B: scattering in the conduction bands; C: radiative and radiationless relaxation in free and localized exciton states; D: radiative decay to the ground state; E: energy transfer to guest atoms and boundaries.

Fig. 61 Configuration coordinate models for a localized exciton and an exciton band in a rigid lattice (after Toyozawa 1974).

Fig. 62 a) Schematic lattice rearrangement for one center selftrapping (left) and two center selftrapping (right) of excitons in RGS after Song (1968, 1971) and Jortner (1974).
b) Map of zones of stable states of excitons for alkalihalides in the plane $X = U'/\sqrt{\alpha|V|}$, $Y = V'/\sqrt{\alpha|V|}$ (from Song 1968). For α, V, V' and U' see text.

Fig. 63 Schematic potential curves and lattice distortions describing the localization of free excitons in atomic and excimer centers (after Fugol' 1978).

Fig. 64 Results of time-resolved luminescence experiments for the main luminescence bands of solid Xe, Kr and Ar. Full lines in the intensity curves (upper panel) correspond to the component with short decay times (10^{-9} s region), dashed lines to long decay times. Emission bands and decay curves for Kr and Ar are taken from Hahn et al. (1980). The decay times for Xe were determined by Hahn et al., 1977, Kink et al., 1977 (from Zimmerer 1979).

Fig. 65 a) Emission spectra for solid Xe excited by α-particles and VUV light (Zimmerer 1976). b) Intensity ratio of the 7.6 eV emission band to the 7.05 eV emission band for different temperatures. Circles: electron excitation (Basov et al., 1970); crosses: α-particle excitation (Chesnovsky et al., 1973); points: α-particle excitation (Zimmerer 1976). c) Luminescence efficiency in the 7.05 eV and 7.6 eV band of solid Xe for a spectrum of excitation energies (Ackermann et al., 1976).

Fig. 66 Decay curves for solid Xe. Left insert, temperature dependence of the long and short components; right insert, emission bands for different times after deposition of the sample (Hahn et al., 1977).

Fig. 67 Transient absorption of solid Ar (Suemoto and Kanzaki, 1979) and calculated potential curves of Ar_2^* molecules (Spiegelman and Malrieux 1978). The assignment of the observed features is indicated by vertical arrows.

Fig. 68 Comparison of luminescence emission spectra for solid Ne for different excitation conditions. In the left set of spectra (1) - (5) the full emission spectrum is shown. In the right set of spectra (7) - (10) the high energy part is shown on an expanded scale.
1: calculated R_2^* center emission (Yakhot 1975); 2 and 7: x-ray excitation (Schuberth and Creuzburg, 1975); 3: β-excitation (Packard, Reif and Surko, 1970); 4: light excitation (Zimmerer 1978); 5 and 10: 300 eV e^--excitation (Fugol' 1978); 6: calculated R^* center emission (Kunsch and Coletti, 1979); 8: 5 keV e^--excitation, low current (Coletti and Bonnot 1978); 9: 200 eV e^--excitation, high current (Coletti and Hanus, 1977).

Fig. 69 In the lower part an overview of the complete emission spectra for solid Xe, Kr, Ar and Ne is shown with an assignment of the individual features; a: free excitons; b: atomic centers; c: vibrationally excited excimer centers R_2^*; d: vibrationally relaxed R_2^* centers. The Xe and Ar spectra have been obtained by electron excitation at 5K (Fugol 1978); the spectrum for Kr by electron excitation at 5K (Hahn et al., 1980); the spectrum for Ne by X-ray excitation at 5K (Schuberth and Creuzburg, 1975). In the upper part, the temperature dependence of the emission bands a and b excited by 5 keV electrons is displayed on an expanded scale (Coletti and Bonnot, 1978).

Fig. 70 (1) Absorption spectrum of solid Xe (Baldini, 1962)
(2) Emission spectrum of solid Xe (Fugol' 1978)
(3) Xe gas emission at low pressure (Stewart et al., 1970)
(4) Xe gas emission at high pressure (Kashnikov 1971)
(5) Xe atomic resonance lines (after Fugol' 1978).

Fig. 71 Potential curves for Xe excitons.
I: Atomic centers R^* (after Fugol 1978). For the definition of S_1^o, S_1^+ and H_m see text. The dashed region corresponds to free excitons; II: Molecular centers R_2^* depicted according to the calculation of Ermler et al. (1978) for the free molecule; III: Potential curves of the free molecule (II) on an enlarged scale; IV: Experimental results for the potential curves of R_2^* centers in the crystal on the scale of III. a, b, c and d indicate emission of free excitons, of atomic center R^*, of vibrationally excited R_2^* and of vibrationally relaxed R_2^* centers.

Fig. 72 a) Temperature dependence of the peak position of the resonant emission (solid line) and of the reflectivity (dashed line).
b) Temperature dependence of the intensity of the resonant emission ($\hbar\omega$ = 8.35 eV) (after Kink and Selg, 1980).

Fig. 73 Compilation of emission bands in liquid rare gases together with solid and gas phase spectra. Xe gas: Jortner et al., 1965; Xe solid and liquid: Basov et al., 1970; Kr: Chesnovsky et al., 1973; Ar: Chesnovsky et al., 1972; Ne: Packard et al., 1970; He: Stockton et al., 1972.

Fig. 74 Observed transitions in liquid He. The potential curves have been adopted from Ginter and Battino (1970), except the singulet states above $C\,^1\Sigma_g^+$ (Guberman and Goddard, 1975). Transitions to the ground state: Stockton et al. (1972); radiative decay between excited states: Dennis et al. (1969); transient absorption: Soley and Fitzsimmons (1974).

Fig. 75 Relaxation cascade in the excitonic states of heavy RGS (e.g. Xe). a: localization of free excitons; b: electronic relaxation; c: vibrational relaxation; d: predissociation. The potential curves have been drawn according to the work by Molchanov (1972) for excimer centers and Fugol' (1978) for atomic centers.

Fig. 76 Emission spectrum of liquid He in the long wavelength region (after Keto, Soley, Stockton and Fitzsimmons, 1974).

Fig. 77 Upper panel: decrease of the emission intensity with external pressure in liquid He; middle panel: wavelength shifts in the emission spectra from liquid He with external pressure, and lower panel: wavelength shifts in transient absorption spectra from liquid He with external pressure. Experimental points are connected with solid lines. Dashed lines show the results of calculations by Hickman et al. (1975). The numbers refer to the following transitions:

1) $A\,^1\Sigma \rightarrow X\,^1\Sigma$; 2) $d\,^3\Sigma \rightarrow c\,^3\Sigma$; 3) $3\,^3S \rightarrow 2\,^3P$
4) $d\,^3\Sigma \rightarrow b\,^3\Pi$; 5) $D\,^1\Sigma \rightarrow B\,^1\Pi$; 6) $c\,^3\Sigma \leftrightarrow a\,^3\Sigma$
7) $C\,^1\Sigma \rightarrow A\,^1\Sigma$; 8) $2\,^3P \leftrightarrow S^3S$; 9) $b\,^3\Pi \rightarrow a\,^3\Sigma$

Fig. 78 Configuration coordinate diagram for an impurity center. U_g is the energy of the ground state (for absorption) or the energy of any state below the state with energy U_e (for electronic relaxation) and U_e the energy of an excited state versus the configuration coordinate Q. E_{LR} is the lattice rearrangement energy and ΔE the energy difference of the minima of the potential surfaces. E_A is the activation energy given by the crossing of the potential surfaces.

Fig. 79 Experimental absorption line shape (points) of the n = 1 exciton of Xe guest atoms in an Ar matrix at 56 K and fits with a Gaussian (solid line) and Lorentzian (dashed line) line shape. The center of the line E_{max} corresponds to 9.156 eV and the halfwidth (fwhm) H is 119 meV. (After Ophir 1970).

Fig. 80 Temperature dependence of the position of the n = 1 excitons of Xe guest atoms in Ar (circles) and Xe guest atoms in Kr matrix (crosses) (upper part) and of the corresponding halfwidth H (lower part). The result of Baldini (1965) is shown by B. The solid (Ar matrix) and dashed (Kr matrix) lines correspond to fits with equ. 6.25 (lower part) and equ. 6.26 (upper part). (After Ophir 1970).

Fig. 81 Emission spectra of Xenon doped liquid argon at 87 K (a) and Xenon doped solid argon at 80 K (b) (after Chesnovsky et al., 1972).

Fig. 82 Left hand panels: Emission spectra of Kr guest atoms in an Ar matrix for several excitation energies A of 13.8 eV, 11.37 eV and 10.70 eV and for several Kr concentrations: - - - 3% Kr, - · - · 0.3% Kr, ——— 0.03 % Kr.
Right hand panels: I, II and III are excitation spectra of the emission bands "b" (site with energy lower than the relaxed Kr n = 1 exciton), "e" (relaxed Kr n = 1 exciton) and "g" (relaxed n' = 1 exciton), respectively. The identification of the emission bands is shown in the left hand panels. - · - · 3% Kr, — 0.3 % Kr, - - - 0.03 % Kr (from Hahn et al. 1981).

Fig. 83 Emission spectra for Xe, Kr and Ar atoms in the Ne matrix with emission band I, II and III. The atomic states are also shown. Long bars correspond to dipole-allowed, short bars to dipole-forbidden transitions. The absolute positions of the atomic transitions have been shifted by 0.23 eV, 0.14 eV and 0.09 eV for Xe, Kr and Ar, respectively. (From Hahn and Schwentner, 1980).

Fig. 84 Dependence of the energy position of the lowest states of Xe atoms on the density of surrounding Ne atoms. The density is expressed by the mean nearest neighbor separation between an Xe atom and surrounding Ne atoms. The Ne density ranges from 0 through liquid to the solid phase. For solid Ne (density 1,44 $\{g\ cm^{-3}\} \triangleq 3.13$ Å) the maxima of the excitation spectra (left hand side) have been included. The density around relaxed Xe atoms follows from a comparison with the emission spectra (right hand side, horizontal lines). (From Hahn and Schwentner, 1980).

Fig. 85 Emission spectra of liquid Krypton doped with Xe at various concentrations (T = 120 K) (from Chesnovsky et al., 1973).

Fig. 86 Dependence of the intensity ratio of the heteronuclear excited Kr Xe* molecule emission to the excited homonuclear diatomic Xe_2^* emission upon the concentration in liquid Kr. (From Chesnovsky et al., 1973).

Fig. 87 Excitation spectra (emission intensity versus excitation energy) for Xe in Ne (hatched curves) for each of the three emission bands I, II and III (see also Fig. 83). The emission bands are shown for each of the corresponding excitation spectrum at lower photon energies. Prominent maxima in the excitation spectra are marked by a, b, c, d, e. Further, the positions of excitonic states n = 1, 2, 3, 4 and n = 1', 2', 3', 4' are marked. The inserts at the right hand side provide a survey of the time dependence of the intensity in the emission bands at prominent excitation energies. The insert on the left shows the complete emission spectrum (from Hahn and Schwentner, 1980).

Fig. 88 Excitation spectra (emission intensity versus excitation energy) for Kr in Ne similar to Fig. 87. (From Hahn and Schwentner, 1980).

Fig. 89 Left part: experimental radiative (⇝) and nonradiative (⟶) electronic relaxation pathways and time constants (in nanoseconds) for Xe in Ne in a configuration coordinate diagram. The excitation channels n = 1, n' = 1 and n = 2 and the matrix relaxation (⇝) are included. Right part: atomic energy levels (Paschen notation) for Xe with some lifetimes for radiative transitions to the ground

state (~~~~). Long bars correspond to states with allowed, short bars to forbidden transitions to the ground state (from Hahn and Schwentner, 1980).

Fig. 90 Relaxation cascade for Ar in Ne similar to the results shown in Fig. 89. Important radiative transitions between excited atomic transitions are included ( ). (From Hahn and Schwentner, 1980).

Fig. 91 Temperature dependence of the transition rate of Kr n = 1 excitons in an Ar matrix. Crosses, experimental points; solid line, fit with equ. 6.33. (From Hahn et al., 1980).

Fig. 92 Photoelectron yield from Kr layers with thickness d due to energy transfer to the gold substrate normalized to the photoelectron yield of the substrate. The n = 1, n' = 1 and n = 2 exciton bands of Kr ar marked. In the insert, the absorption coefficient for Kr versus photon energy is given (From Rudolf and Schwentner, 1980).

Fig. 93 Thickness dependence of the photoelectron yield from the n = 1 exciton of Xe due to energy transfer to the gold substrate. Points represent experimental data, the curve shows a fit with a diffusion length of 300 Å and an electron escape depth of 850 Å as parameters (from Ophir et al. 1975).

Fig. 94 Diffusion length of Kr excitons versus exciton energy derived from Fig. 92. In the upper panel, the absorption coefficient in the exciton bands is shown. (From Schwentner et al., 1980).

Fig. 95 Dependence of the photoelectric yield of Xe doped Ar films on the Xe concentration. The film thickness is 60 Å. The spectra are not corrected for the hot electron contribution from the gold substrate and the reflectivity. Photoelectric yield curves for the gold substrate and for pure Ar films are also shown (From Ophir et al., 1975).

Fig. 96 Luminescence efficiency of the R_2^* bands for solid Ar, Kr and Xe at 5K for excitation energies in the exciton region. The dashed curves represent results from model calculations. (From Zimmerer, 1978).

Fig. 97 Right part: photoelectron energy-distribution curves (EDC's) (counting rates versus kinetic energy) from films of 1 at.% Xe in Ar for a spectrum of photon energies. The film thickness was 50 Å. For convenience the relevant energy levels are shown in the insert. Left part (yield): The crosses represent the total number of emitted electrons from the EDC's. For comparison the yield spectrum of 1 at.% Xe in Ar of a 60-Å thick film is shown (solid line). The two sets of data were adjusted at hν = 11 and 11.5 eV (gold substrate). The energies of the n = 1, 1' and 2' exciton states are marked. (From Schwentner and Koch, 1976).

Fig. 98 Photoelectron energy distribution curves (counting rates versus kinetic energy) from films of 1% Xe in Ar and 1% Xe in Ne for several excitation energies (below and within the n = 1 and n = 2 host exciton bands) Δ_{so}: spin orbit splitting of the Xe 5p levels. (After Schwentner and Koch, 1976).

Fig. 99 Superposition of the absorption spectrum of solid Xe in Ar (1 ppm Xe) (full line) and the emission spectrum of pure solid Ar (dashed line) at 80 K. (From Chesnovsky et al., 1972).

Fig. 100 Dependence of the ratio of Kr donor emission to Xe acceptor emission upon the acceptor concentration (• experimental points; solid line: fit of Förster's theoretical curve). (From Chesnovsky et al., 1973).

Fig. 101 a) One electron molecular orbital scheme for benzene. A simple presentation with one fixed vacuum level for all initial states as frequently used in solid state physics and molecular orbital pictures is shown. In such a picture neither the superposition of excitations from strongly bound levels with the continuum transitions from weakly bound levels nor correlation effects can be depicted but it indicates immediately where the final states are expected relative to the host levels when benzene is doped into a rare gas matrix. In

the left part (i) the photoelectron energy distribution curves for pure C_6H_6 (from Turner et al., 1970) indicating the initial states and (ii) the absorption coefficients for gaseous benzene indicating allowed transitions to final states are sketched.
b) Energy level diagram for benzene in solid Xe, Kr and Ar matrices as derived from photoelectron energy distribution measurements. (After Schwentner et al., 1978).

Fig. 102 Luminescence excitation spectrum of a benzene-doped Krypton film. The film is totally absorbing above 6 eV. The position of the benzene absorption bands (Katz, Brith, Sharf and Jortner, 1970; Gedanken, Raz and Jortner, 1973) are indicated. (From Hasnain et al., 1977a).

Fig. 103 Dependence of the ratio of host emission intensity to guest emission intensity in benzene doped Xenon on the C_6H_6 concentration for several photon energies. The dashed curve describes the result expected for the diffusion model, the dash-dotted curve describes the result for the dipole model. (From Ackermann, 1976).

Fig. 104 Emission spectra from benzene/Xe doubly doped Ar matrices for several excitation energies $\hbar\nu$ = 10.48; 9.95; 9.2 and 9.0 eV, respectively. The concentration of Xe was kept fixed at 0.22% while the C_6H_6 concentration has been varied from 0 to 500 ppm. (From Ackermann, 1976).

Fig. 105 Scheme for important electron and exciton scattering processes at different energy regions ($\hbar\omega$) of the exciting photons. (From Schwentner, 1974).

Fig. 106 Mean free path for electron-electron scattering in solid Xe, Kr, Ar and Ne according to equations 7.8 and 7.9; dashed curve: P_1 from Table 30; solid curves: P_1' from Table 30.

Fig. 107 Hot electron current from an Au substrate versus thickness of the RGS overlayer; Ne: $\hbar\nu$ = 16 eV (Pudewill et al., 1976); Ar: $\hbar\nu$ = 10 eV (Schwentner et al., 1980); Kr: $\hbar\nu$ = 9 eV (Schwentner et al., 1980); Xe: $\hbar\nu$ = 7.9 eV (Ophir et al., 1975; Schwentner, 1976). In the insert the energy distribution of photoelectrons from the Au substrate is shown.

Fig. 108 Photoelectron yield from films of solid Ne and Ar. Circles represent the experimental electron yield for Ne at $\hbar\nu$ = 25 eV and Ar at $\hbar\nu$ = 18 eV. For Ne (left) the lines are calculated from equ. 7.24 for several escape depths l_p. 1: l_p = 1000 Å; 2: l_p = 2000 Å; 3: l_p = 3000 Å; 4: l_p = 5000 Å. (From Pudewill et al., 1976). For Ar (right) the solid lines are calculated from equ. 7.24 including a contribution due to secondary electrons with the secondary electron coefficient; 5: l_p = 2000 Å β = 0; 6: l_p = 1000 Å, β = 0.2; 7: l_p = 2000 Å, β = 0.3; the dashed lines are calculated using a random walk model with an electron - electron scattering length L = 10 000 Å and several electron - phonon mean free paths Λ_o; 8: Λ_o = 400 Å; 9: Λ_o = 100 Å; 10: Λ_o = 5 Å; (After Schwentner, 1976).

Fig. 109 Excitation spectrum of the R_2^* luminescence band of solid Ar. The thresholds for electron - electron scattering are indicated by m = 1, 2, 3. The dashed line shows a fit to the experimental spectrum (see text). (After Möller 1976).

Fig. 110 Photoelectron energy distribution curves from solid Ar, Kr and Xe films for a spectrum of photon energies. The film thicknesses have been d_1 = 14 Å and d_2 = 228 Å for Xe (the region of scattered electrons is not shown), d = 50 Å for Kr and d_1 = 30 Å, d_2 = 84 Å, d_3 = 140 Å and d_4 = 300 Å for Ar. The spectra have been multiplied by the attached factors (from Schwentner 1976).

Fig. 111 Left part: Dependence of the intensity of maximum A and B of Fig. 110 on the electron kinetic energy for Kr. Zero corresponds to the vacuum level of Kr. Right part: The points show the thickness dependence of the intensity of unscattered electrons from Fig. 110 and the solid lines are calculated curves. (From Schwentner, 1976).

Fig. 112 Electron mean free path versus electron energy measured from the top of the valence bands for Ar, Kr and Xe. The points show the experimental results. The solid curves represent a fit according to equ. 7.27. $E_{s\,c}$ is the electron-electron scattering onset determined by the use of equ. 7.27. I corresponds to twice the n = 1 exciton energy, II to the sum of band gap and n = 1 exciton energy, and III to twice the band gap for Ar, Kr and Xe, respectively. (From Schwentner, 1976).

Fig. 113 Pulse-height spectrum of ^{207}Bi conversion electrons measured with the liquid Ar ionization chamber with and without Xe at an electric field of 13.7 kV/cm. (From Kubota et al., 1976).

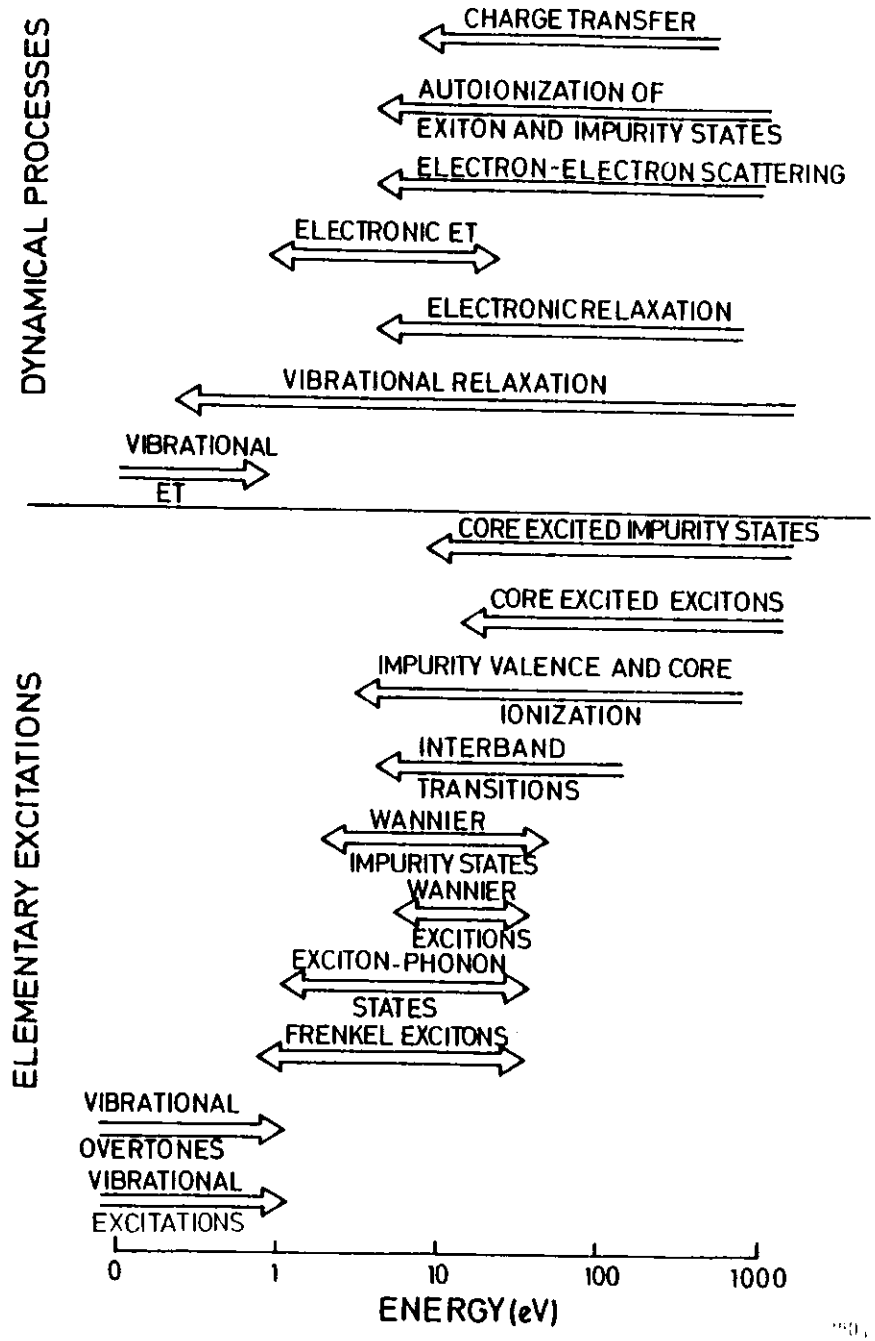

Fig. 1

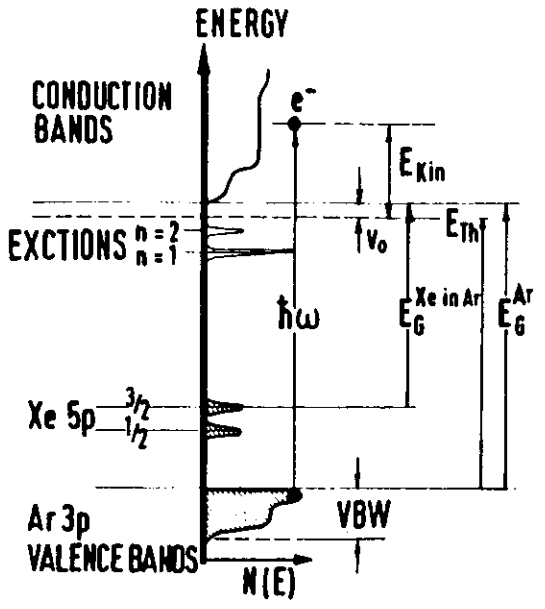
ENERGY
CONDUCTION BANDS
e⁻
E_Kin
EXCTIONS n = 2
n = 1
V_o
E_Th
ħω
E_G Xe in Ar
E_G Ar
Xe 5p 3/2 1/2
Ar 3p
VALENCE BANDS
VBW
N(E)

Fig. 2

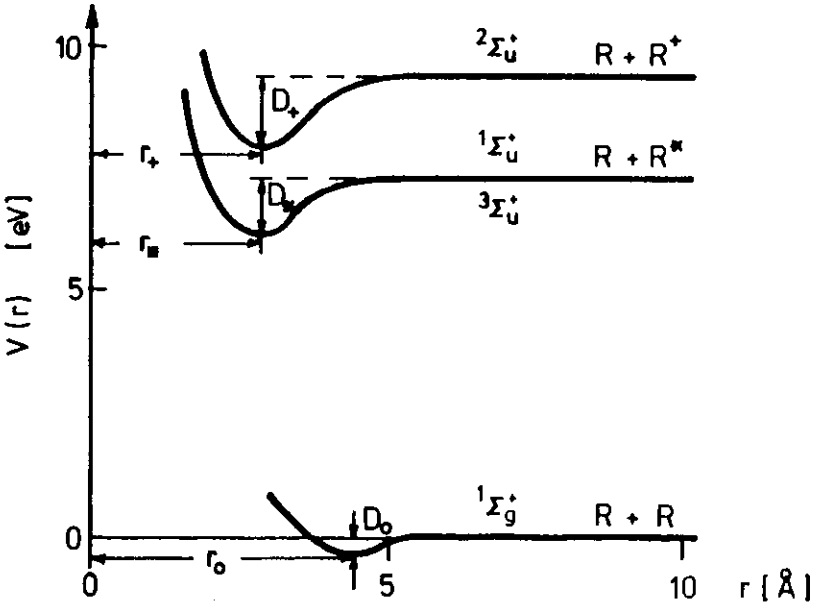
10
5
0
V(r) [eV]
$^2\Sigma_u^+$
R + R⁺
$^1\Sigma_u^+$
R + R*
$^3\Sigma_u^+$
$^1\Sigma_g^+$
R + R
D₊
D*
D₀
r₊
r*
r₀
0
5
10
r [Å]

Fig. 3

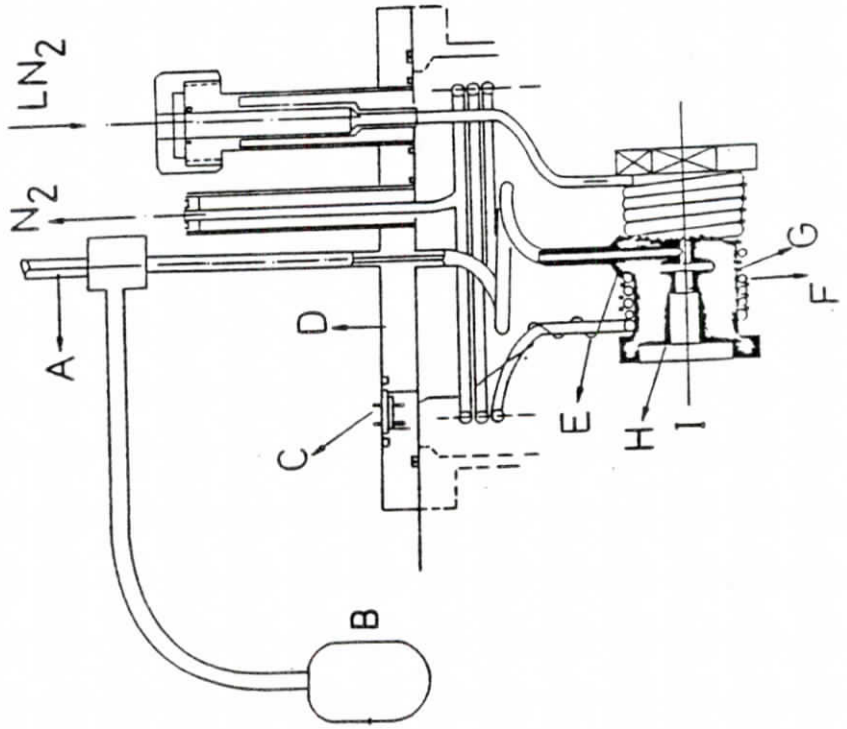
LN2
N2
A
B
C
D
E
F
G
H
I

Fig. 5

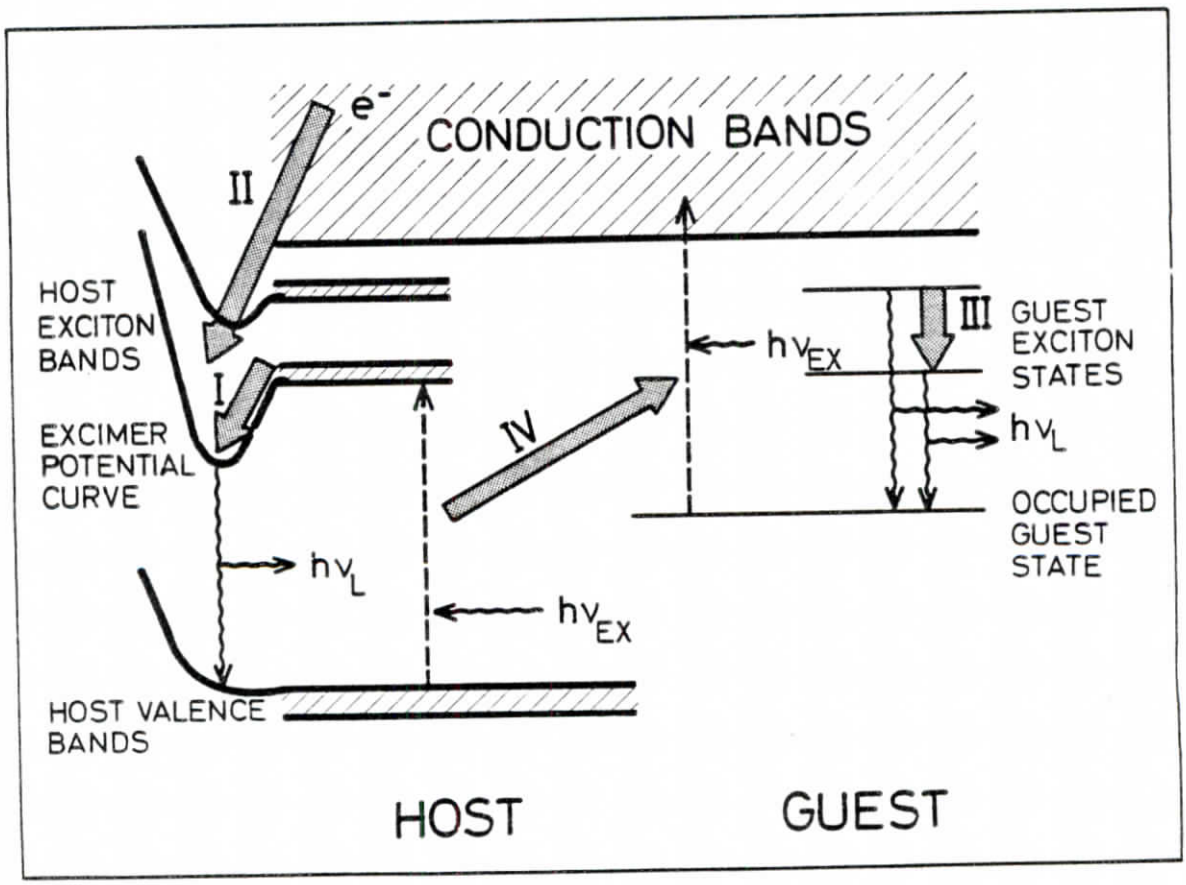
e⁻
CONDUCTION BANDS
II
HOST
EXCITON
BANDS
I
EXCIMER
POTENTIAL
CURVE
hν_L
HOST VALENCE
BANDS
IV
hν_EX
hν_EX
III
GUEST
EXCITON
STATES
hν_L
OCCUPIED
GUEST
STATE
HOST
GUEST

Fig. 4

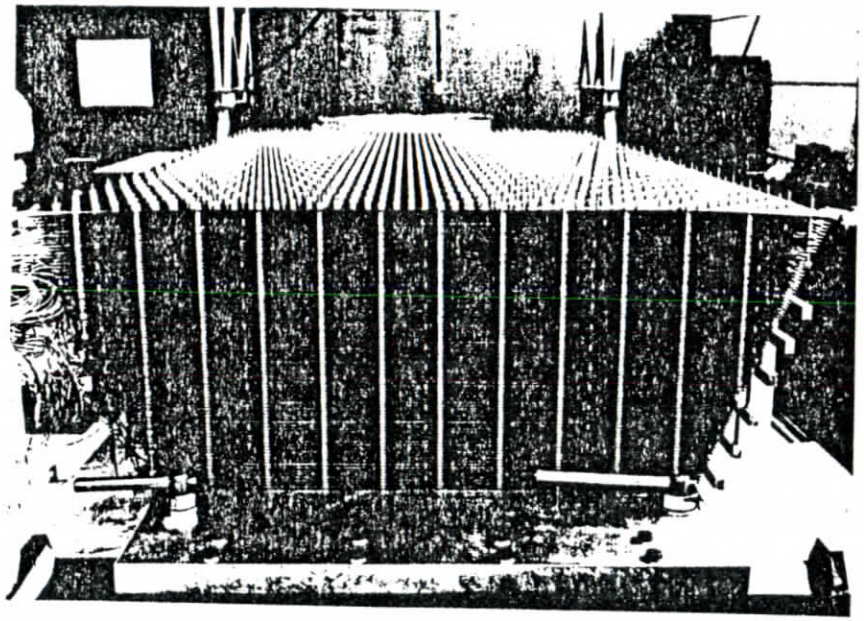

Fig. 6

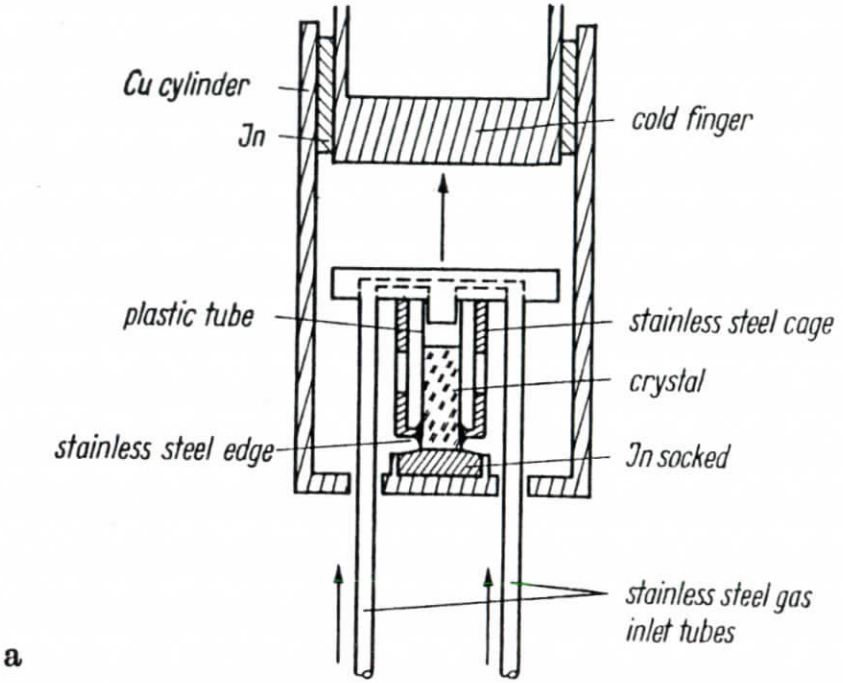
Cu cylinder
In
cold finger
plastic tube
stainless steel cage
crystal
stainless steel edge
In socked
stainless steel gas
inlet tubes

a

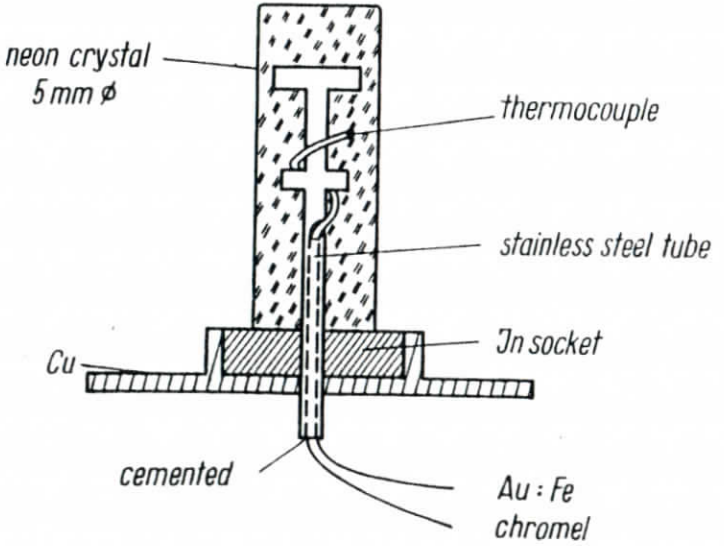
neon crystal
5 mm ø
thermocouple
stainless steel tube
In socket
Cu
cemented
Au : Fe
chromel

b

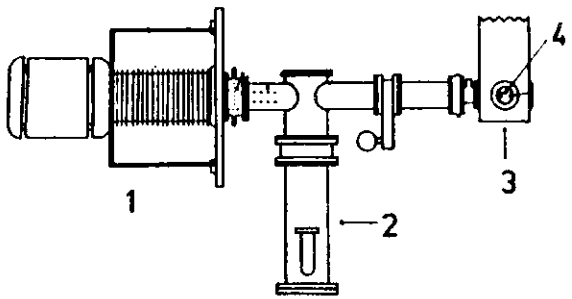
1
2
3
4

Fig. 8

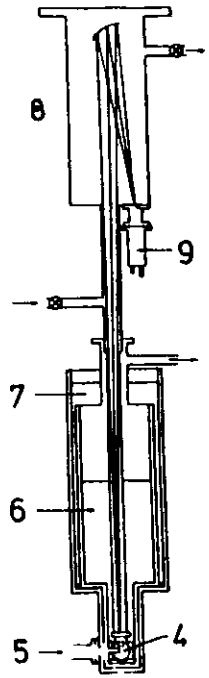
8
9
7
6
5
4

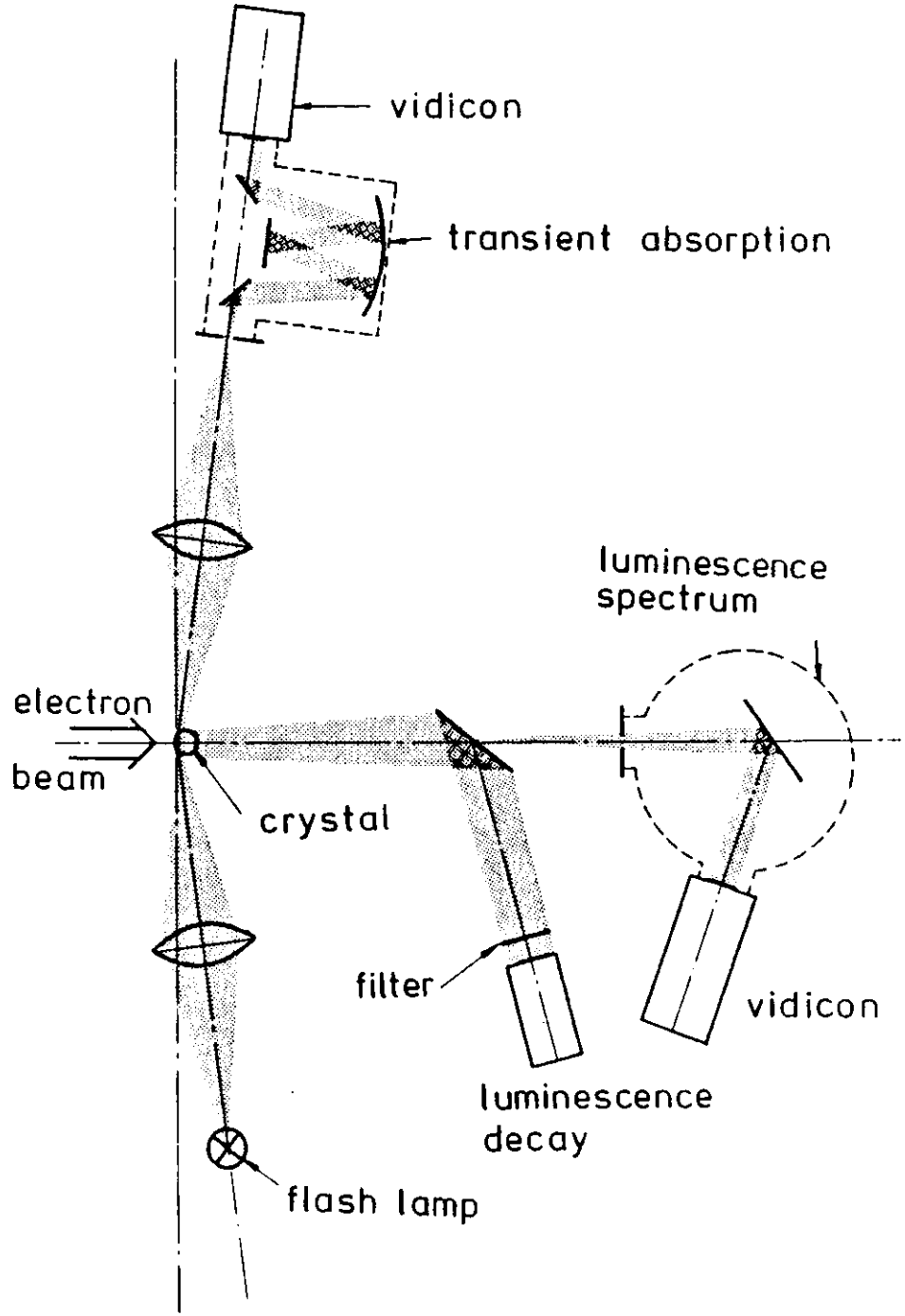
vidicon
transient absorption
luminescence
spectrum
electron
beam
crystal
filter
vidicon
luminescence
decay
flash lamp

Fig. 9

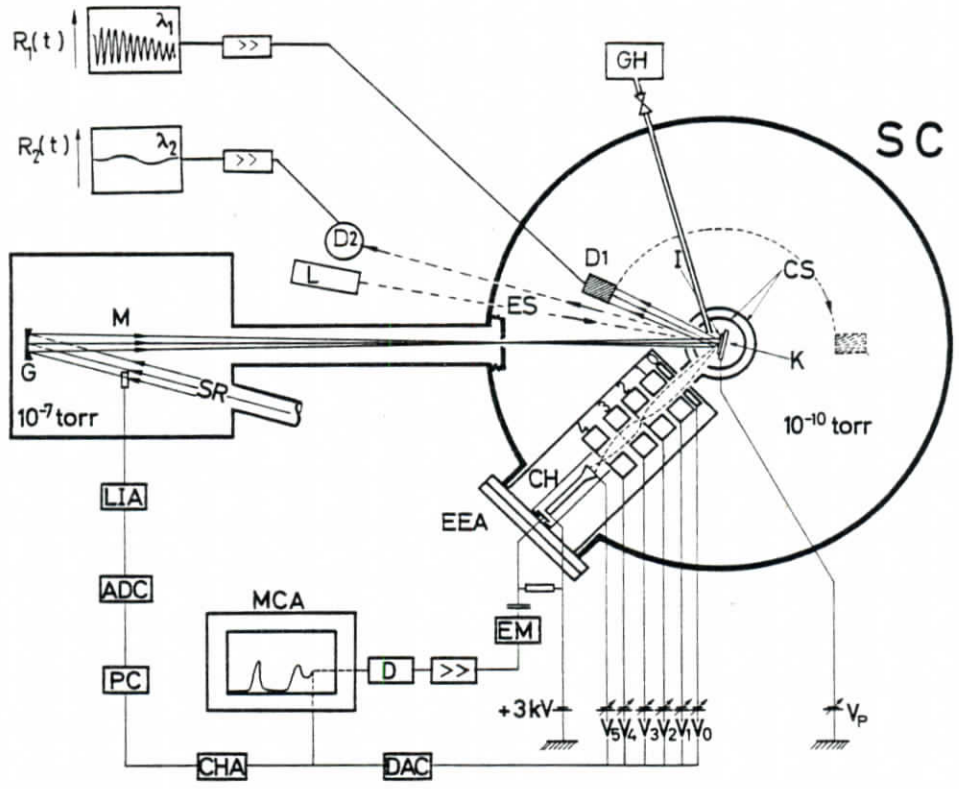
R1(t)
λ1
R2(t)
λ2
>>
D2
L
GH
SC
D1
I
CS
ES
M
G
SR
K
10-7 torr
10-10 torr
CH
EEA
LIA
ADC
MCA
EM
PC
D
>>
+3kV
V5 V4 V3 V2 V1 V0
Vp
CHA
DAC

Fig. 11

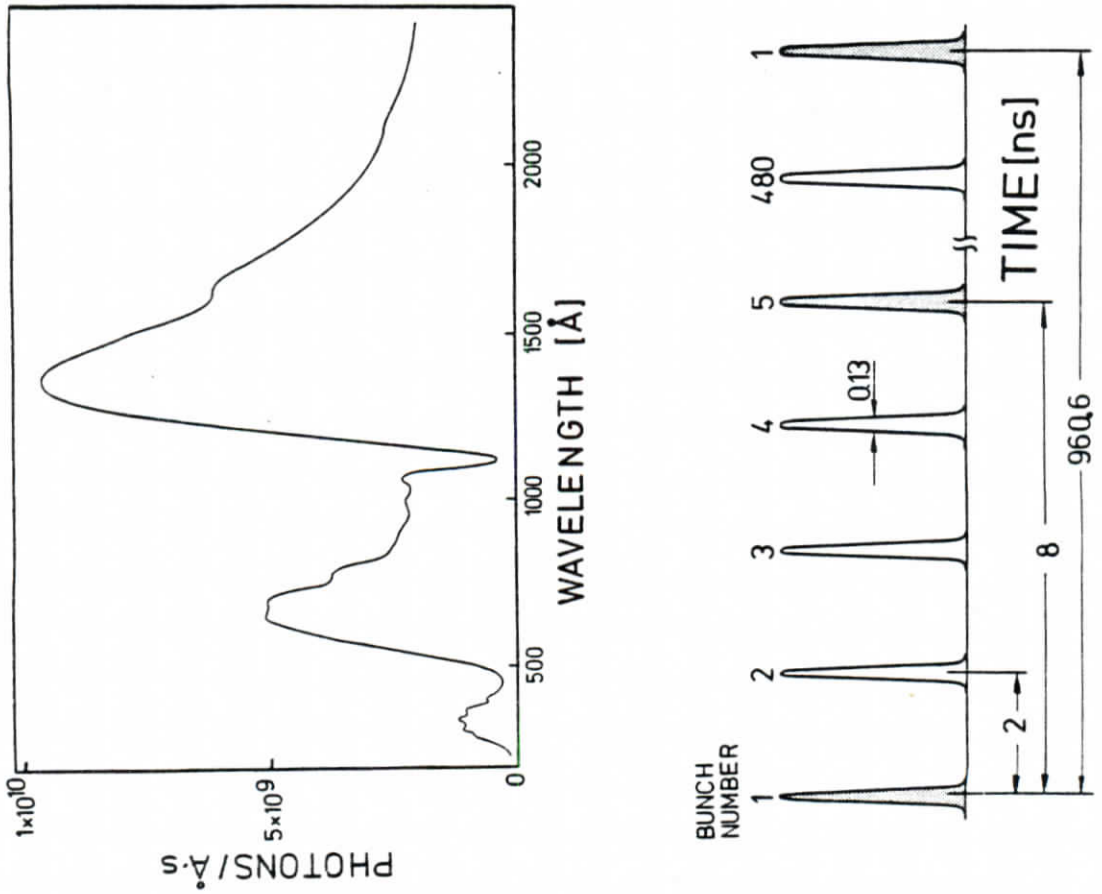
PHOTONS/Å·s
1×10^10
5×10^9
0
500
1000
1500
2000
WAVELENGTH (Å)
BUNCH NUMBER
1
2
3
4
5
480
1
0.13
2
8
TIME[ns]
96.6

Fig. 10

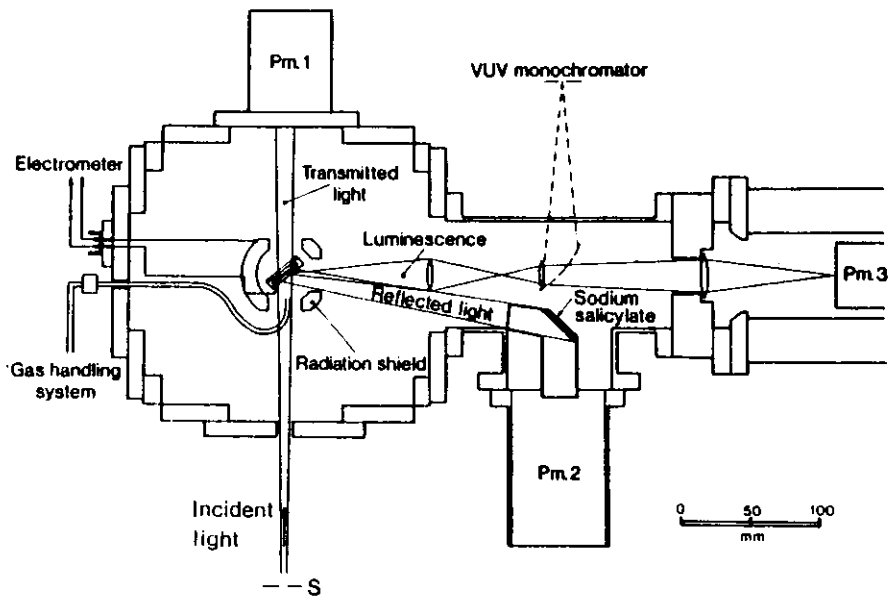
Pm.1
VUV monochromator
Electrometer
Transmitted light
Luminescence
Pm.3
Reflected light
Sodium salicylate
Gas handling system
Radiation shield
Pm.2
Incident light
S
0
50
100
mm

Fig. 12

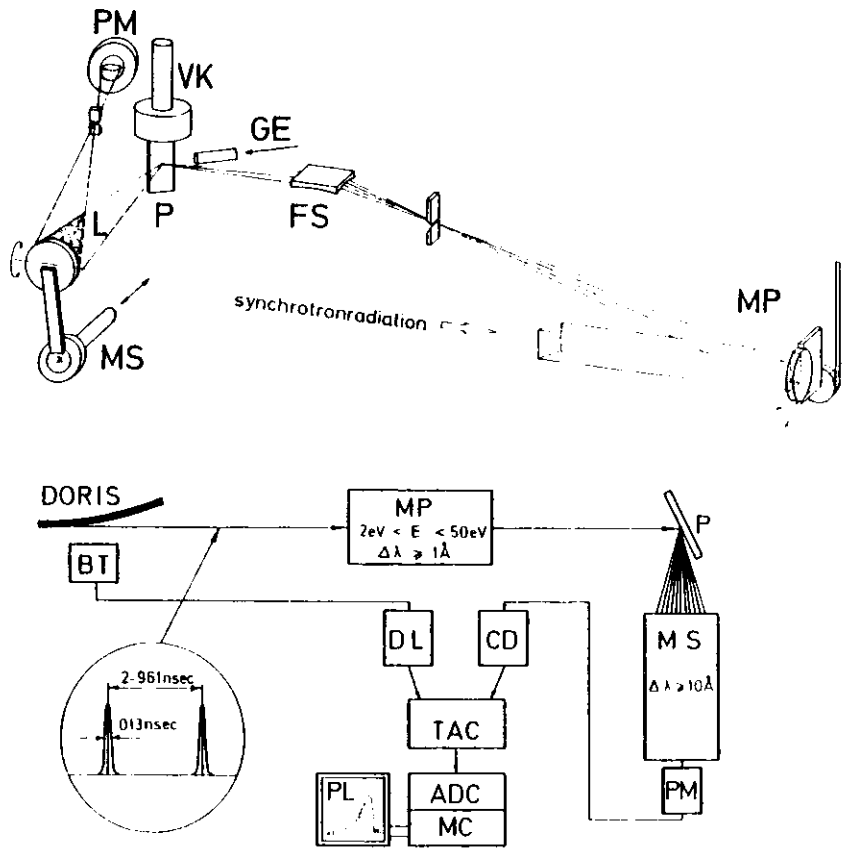
PM
VK
GE
P
FS
L
synchrotronradiation
MP
MS
DORIS
MP
2eV < E < 50eV
Δλ ≥ 1Å
P
BT
DL
CD
MS
Δλ ≥ 10Å
2-961nsec
013nsec
TAC
PL
ADC
MC
PM

Fig. 13

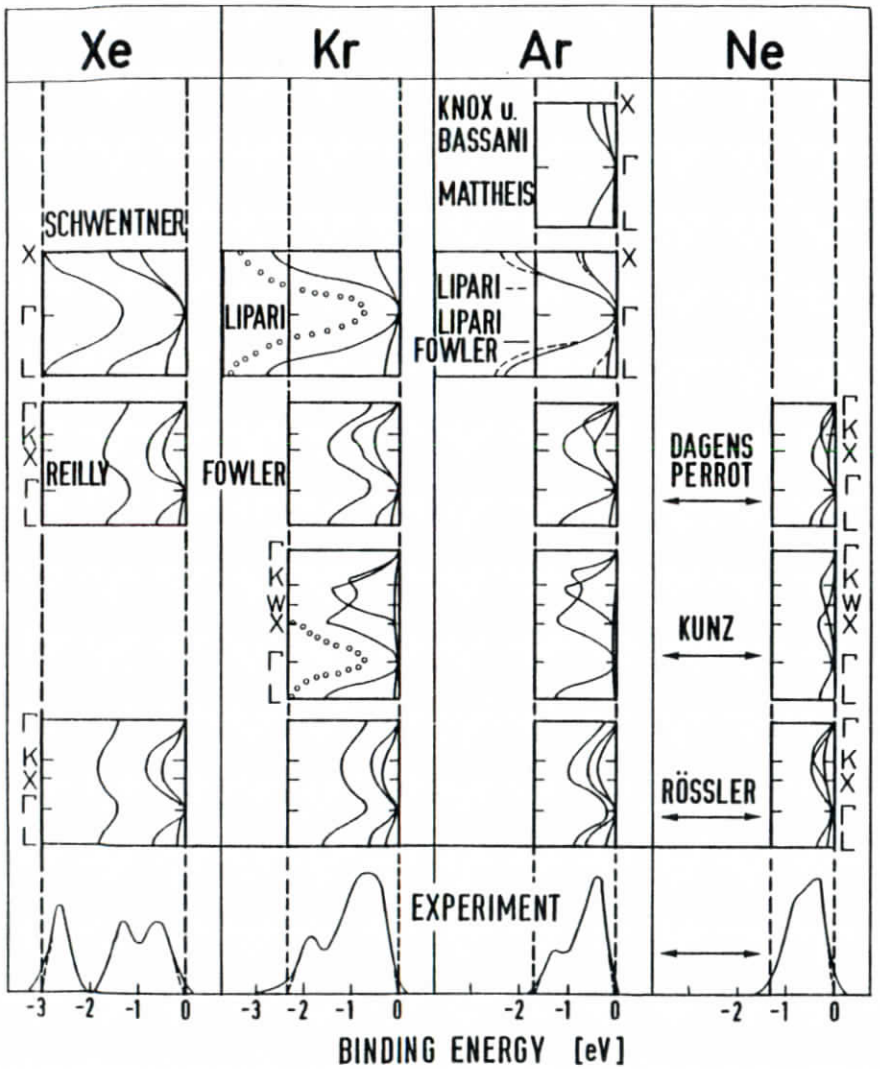
Xe
Kr
Ar
Ne
SCHWENTNER
REILLY
LIPARI
FOWLER
KNOX u. BASSANI
MATTHEIS
LIPARI
LIPARI
FOWLER
DAGENS
PERROT
KUNZ
RÖSSLER
EXPERIMENT
BINDING ENERGY [eV]

Fig. 14

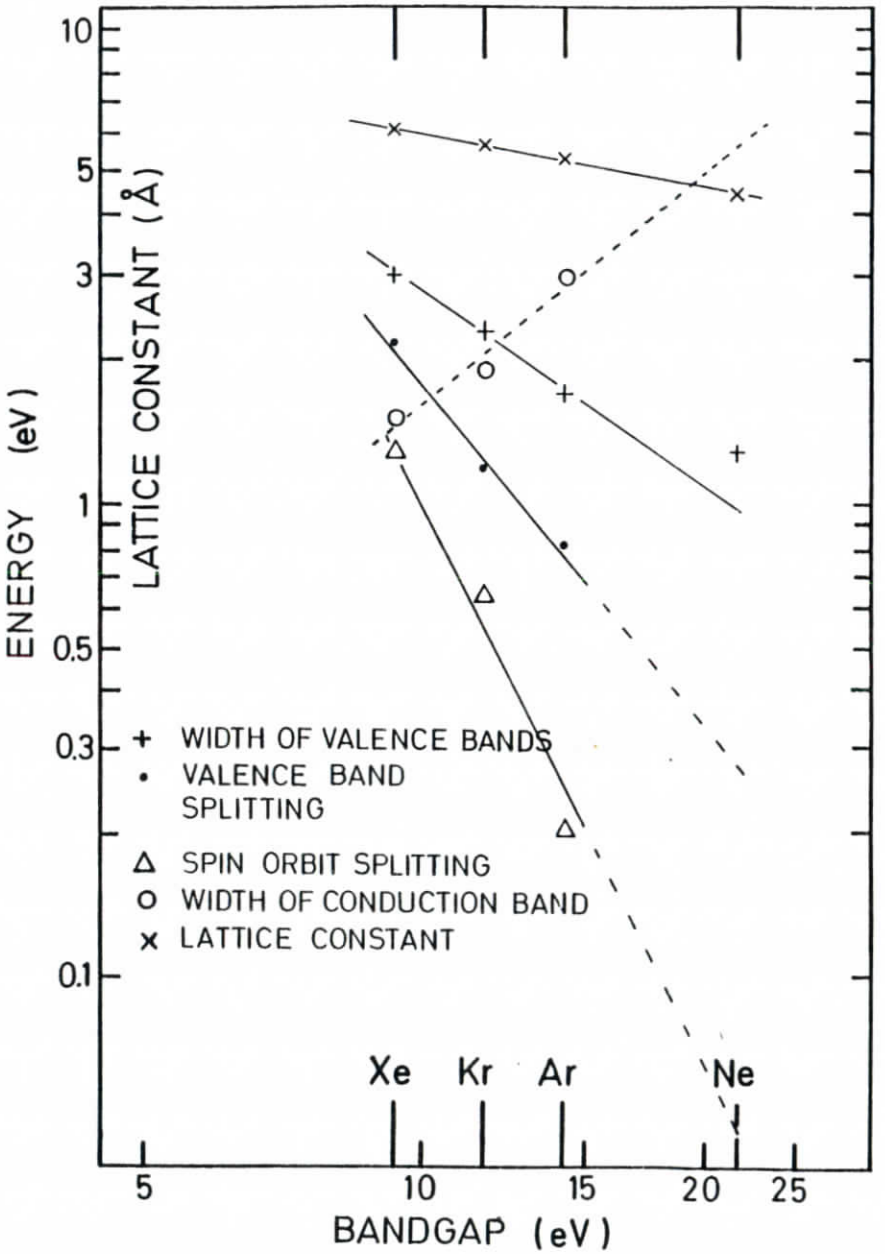
ENERGY (eV)
LATTICE CONSTANT (Å)
BANDGAP (eV)
WIDTH OF VALENCE BANDS
VALENCE BAND SPLITTING
SPIN ORBIT SPLITTING
WIDTH OF CONDUCTION BAND
LATTICE CONSTANT
Xe
Kr
Ar
Ne

Fig. 15

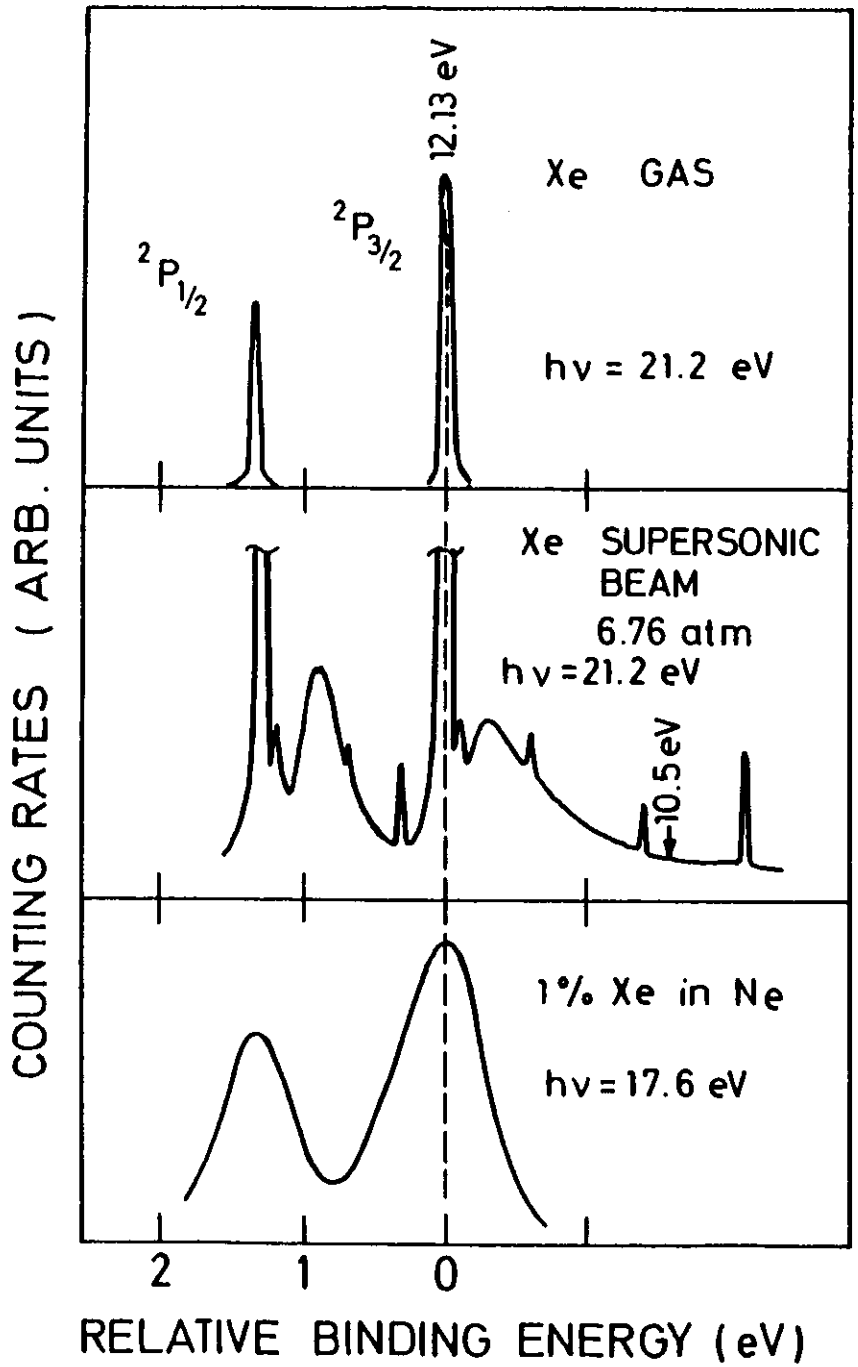
COUNTING RATES (ARB. UNITS)
12.13 eV
$^2P_{1/2}$
$^2P_{3/2}$
Xe GAS
hν = 21.2 eV
Xe SUPERSONIC BEAM
6.76 atm
hν = 21.2 eV
10.5 eV
1% Xe in Ne
hν = 17.6 eV
2
1
0
RELATIVE BINDING ENERGY (eV)

Fig. 16

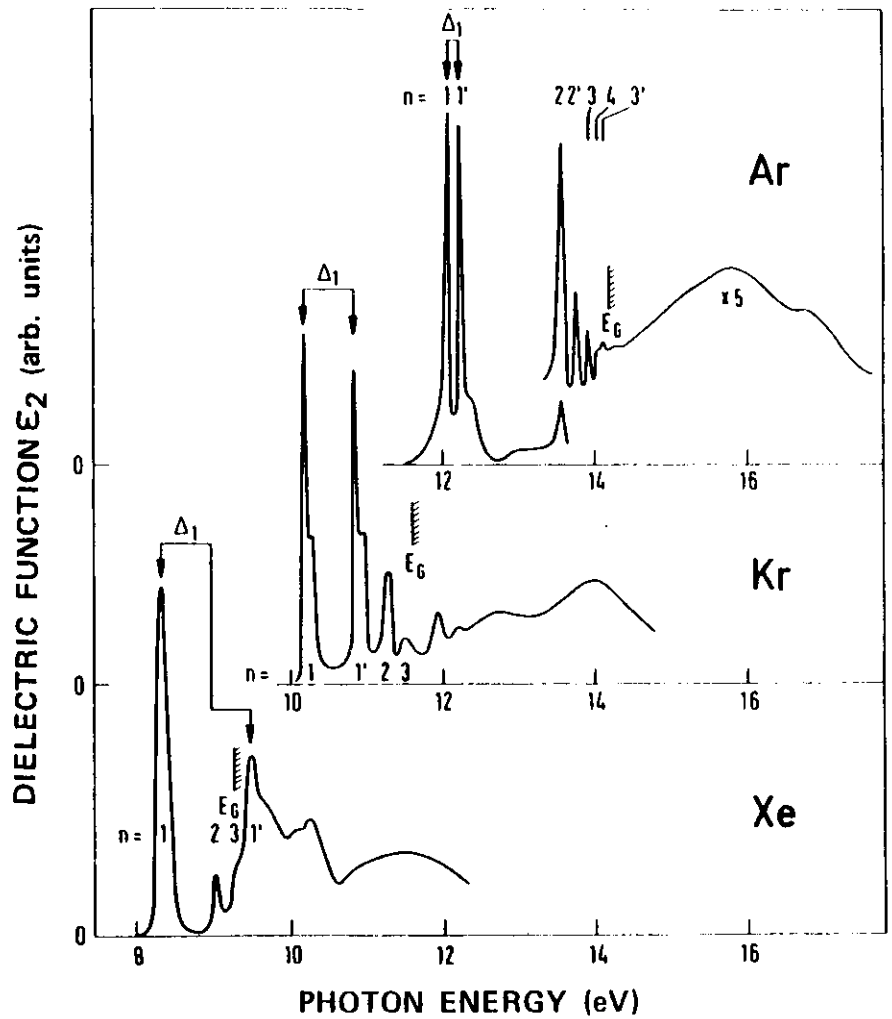
DIELECTRIC FUNCTION ε_2 (arb. units)
Ar
Kr
Xe
Δ_1
E_G
n = 1 1' 2 2' 3 4 3'
x 5
PHOTON ENERGY (eV)

Fig. 17

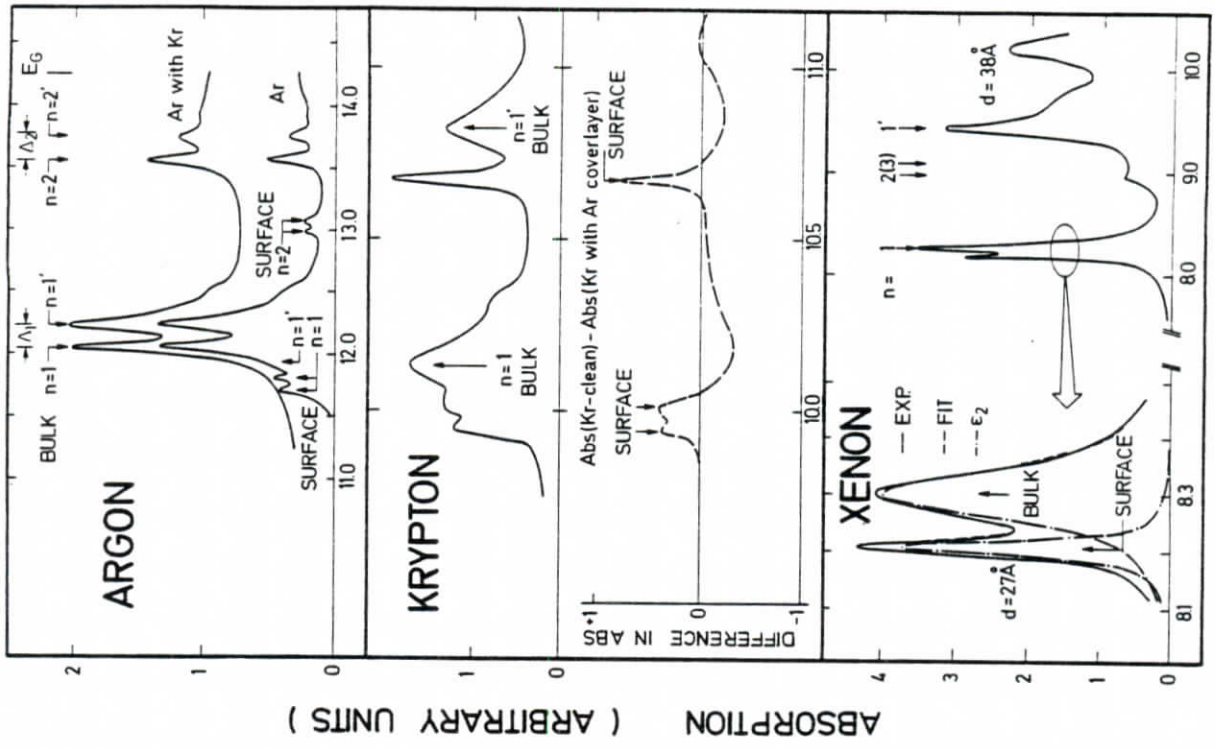
ARGON
KRYPTON
XENON
BULK
SURFACE
Ar with Kr
Ar
Abs(Kr-clean) - Abs(Kr with Ar coverlayer)
DIFFERENCE IN ABS
EXP.
FIT
d = 38Å
d = 27Å
ABSORPTION (ARBITRARY UNITS)
PHOTON ENERGY (eV)

Fig. 19

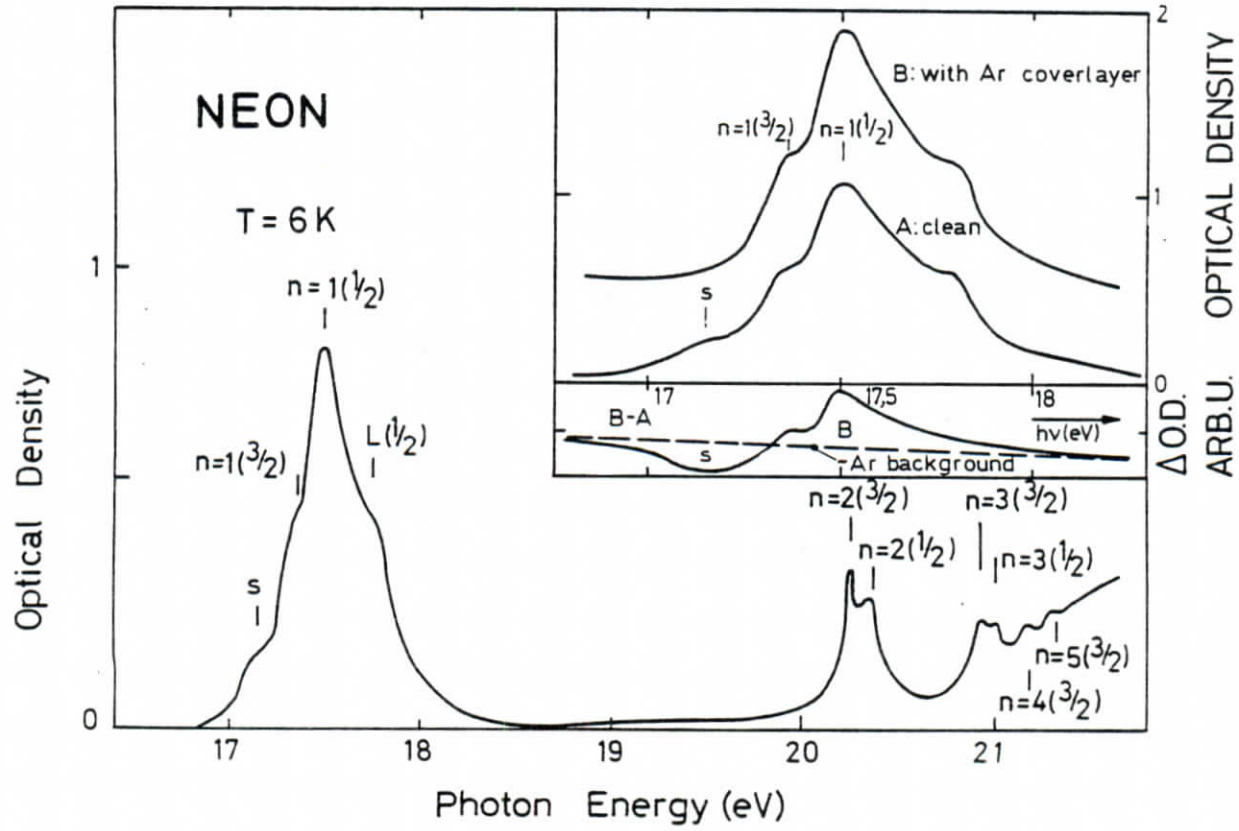
NEON
T = 6 K
B: with Ar coverlayer
A: clean
B-A
Ar background
Optical Density
ΔO.D.
ARB.U. OPTICAL DENSITY
Photon Energy (eV)

Fig. 18

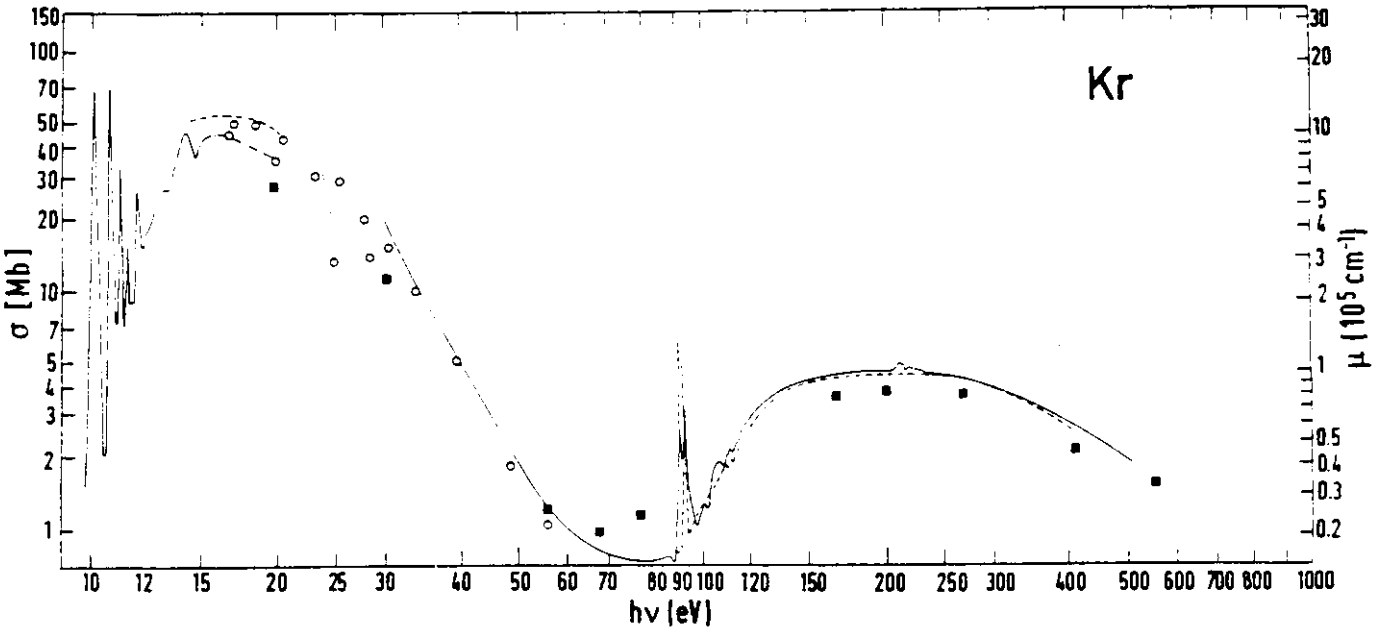
Kr
σ [Mb]
μ [10⁵ cm⁻¹]
hν [eV]

Fig. 21

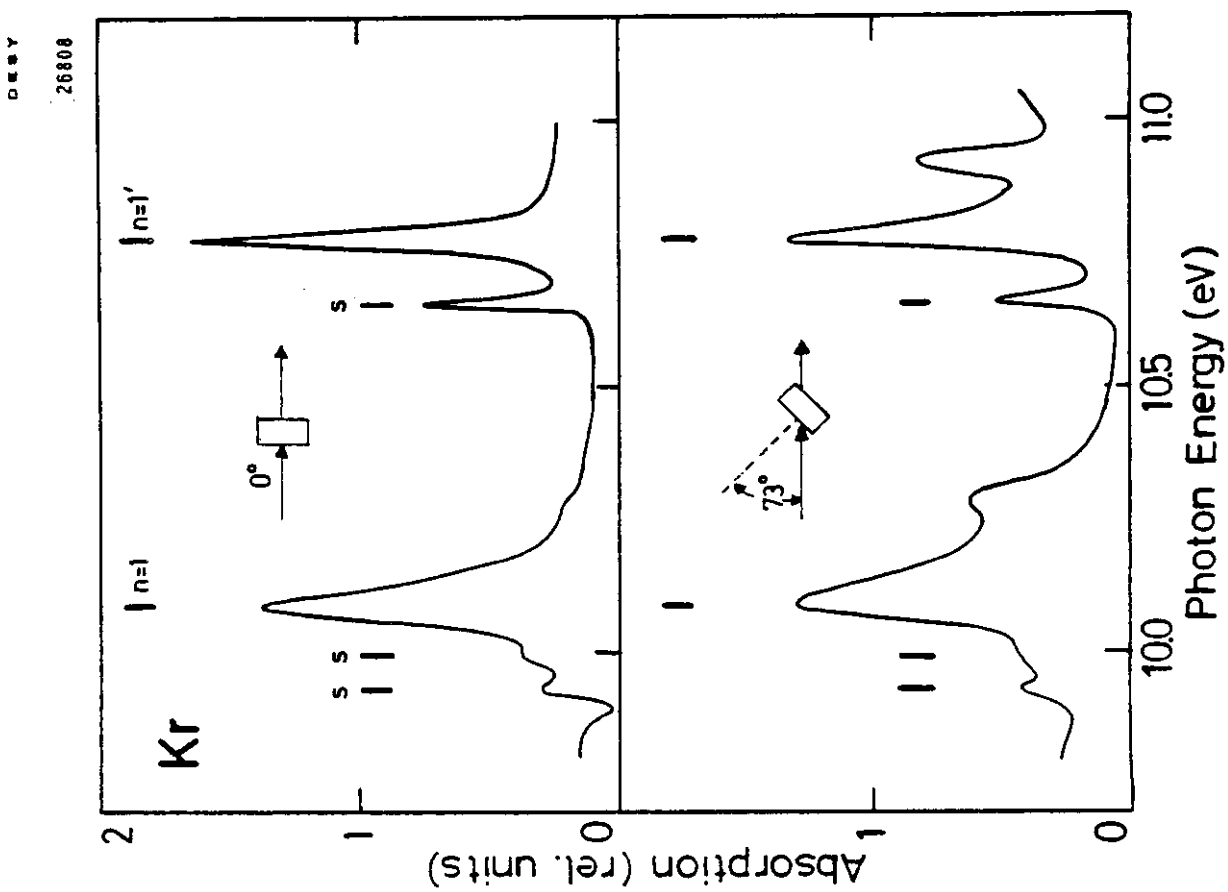
Kr
n=1
n=1'
s s
s
0°
73°
Absorption (rel. units)
Photon Energy (eV)

Fig. 20

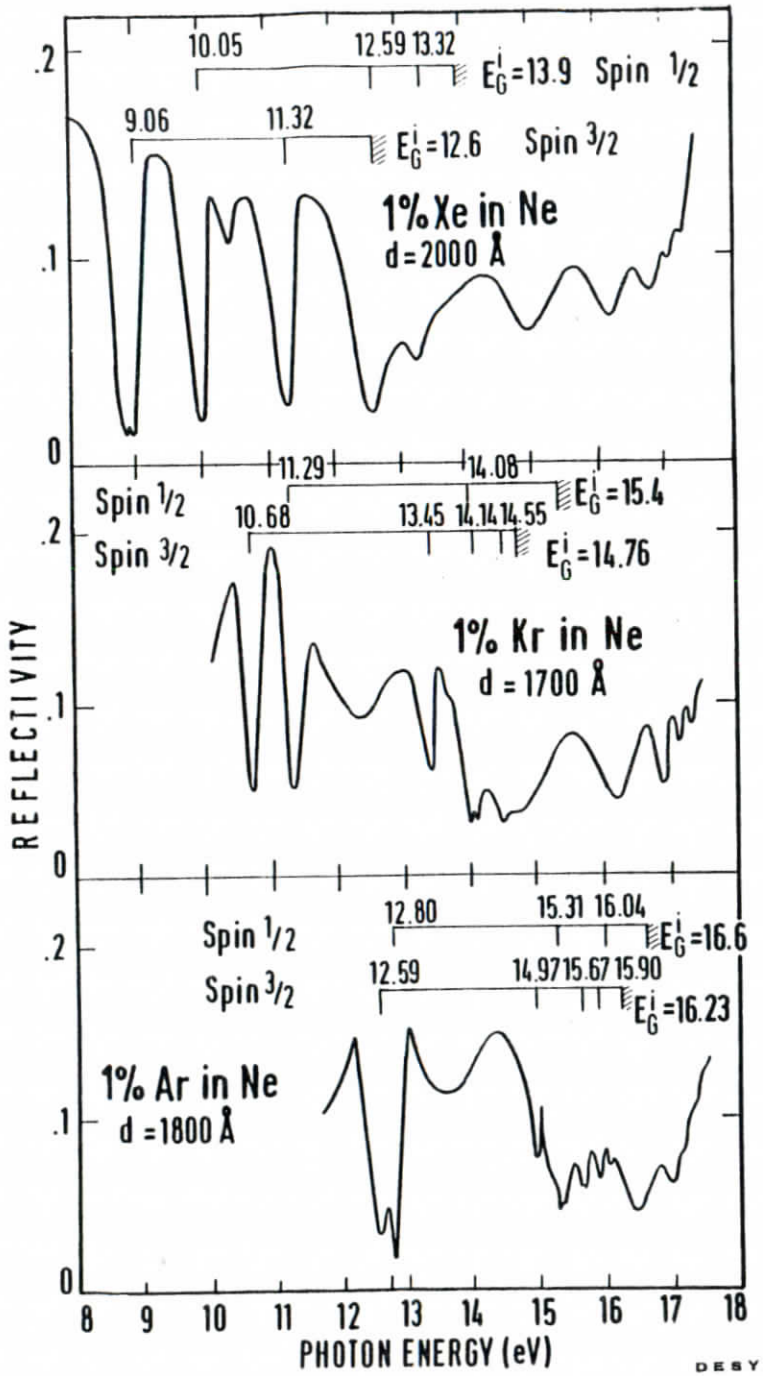
10.05
12.59 13.32
E_G^i=13.9 Spin 1/2
9.06
11.32
E_G^i=12.6 Spin 3/2
1% Xe in Ne
d=2000 Å
11.29
14.08
E_G^i=15.4
Spin 1/2
10.68
13.45 14.14 14.55
E_G^i=14.76
Spin 3/2
1% Kr in Ne
d = 1700 Å
12.80
15.31 16.04
E_G^i=16.6
Spin 1/2
12.59
14.97 15.67 15.90
E_G^i=16.23
Spin 3/2
1% Ar in Ne
d =1800 Å
REFLECTIVITY
PHOTON ENERGY (eV)
DESY
24140

Fig. 22

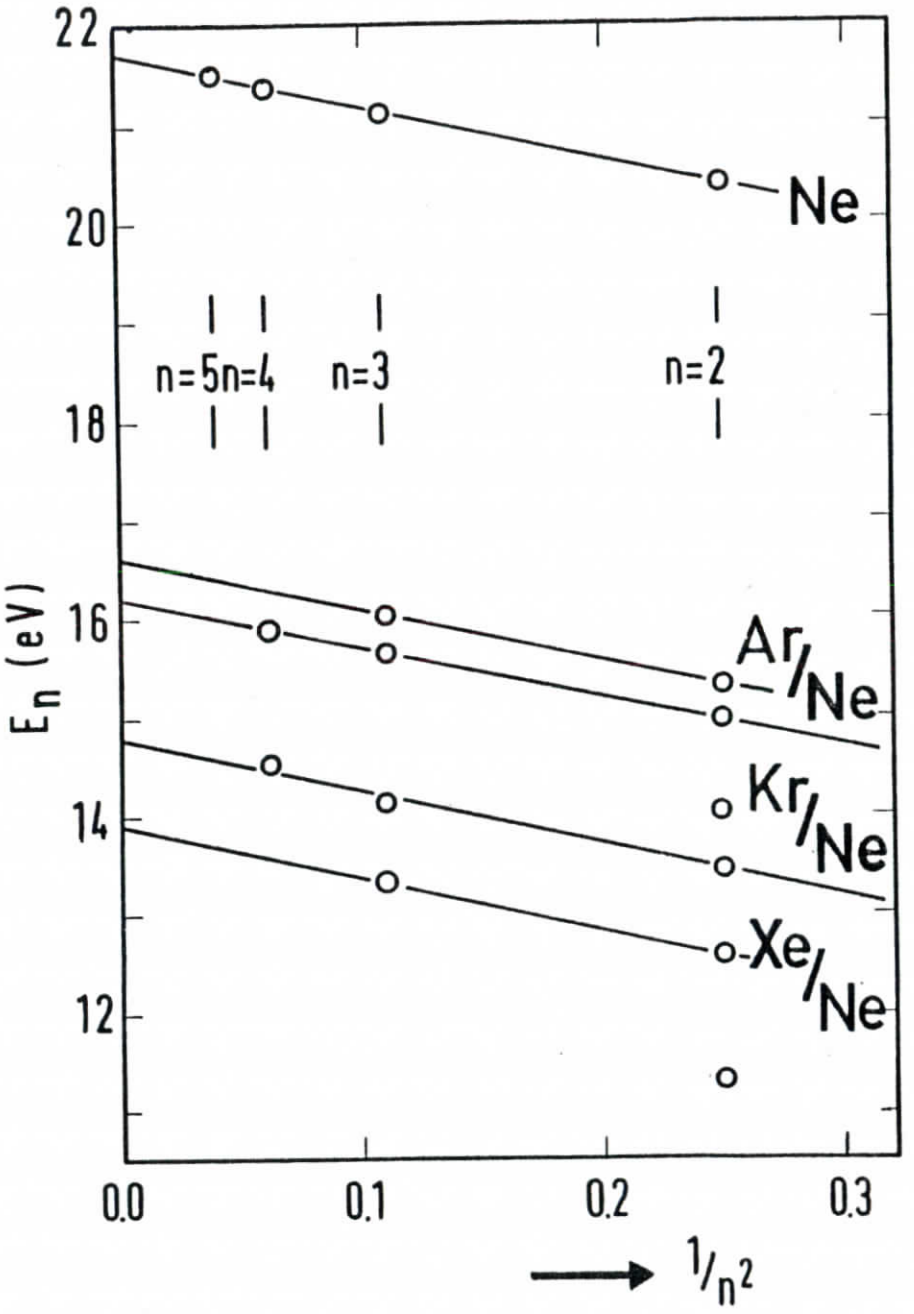
Ne
n=5 n=4
n=3
n=2
Ar/Ne
Kr/Ne
Xe/Ne
E_n (eV)
$1/n^2$

Fig. 23

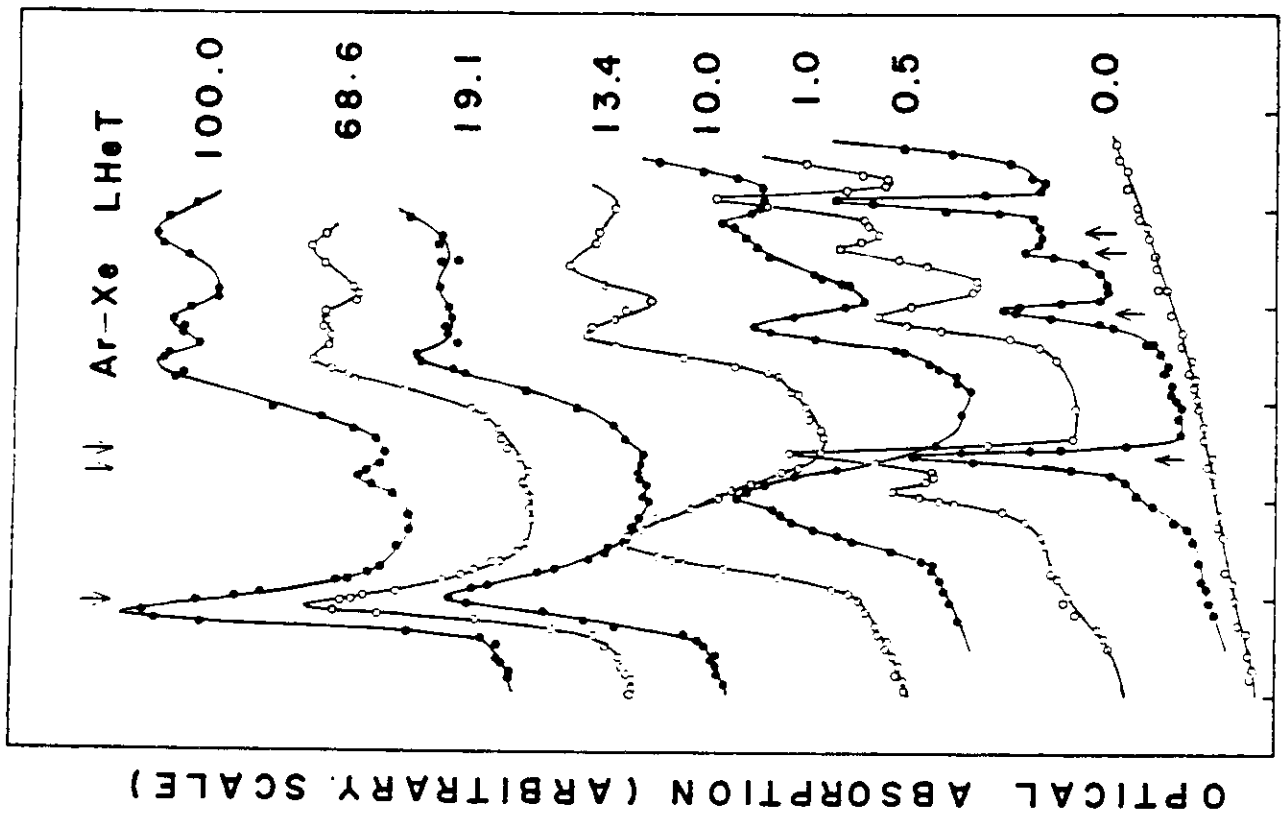
Ar–Xe LHeT
100.0
68.6
19.1
13.4
10.0
1.0
0.5
0.0
8.0
9.0
10.0
11.0
PHOTON ENERGY (eV)
OPTICAL ABSORPTION (ARBITRARY SCALE)

Fig. 25

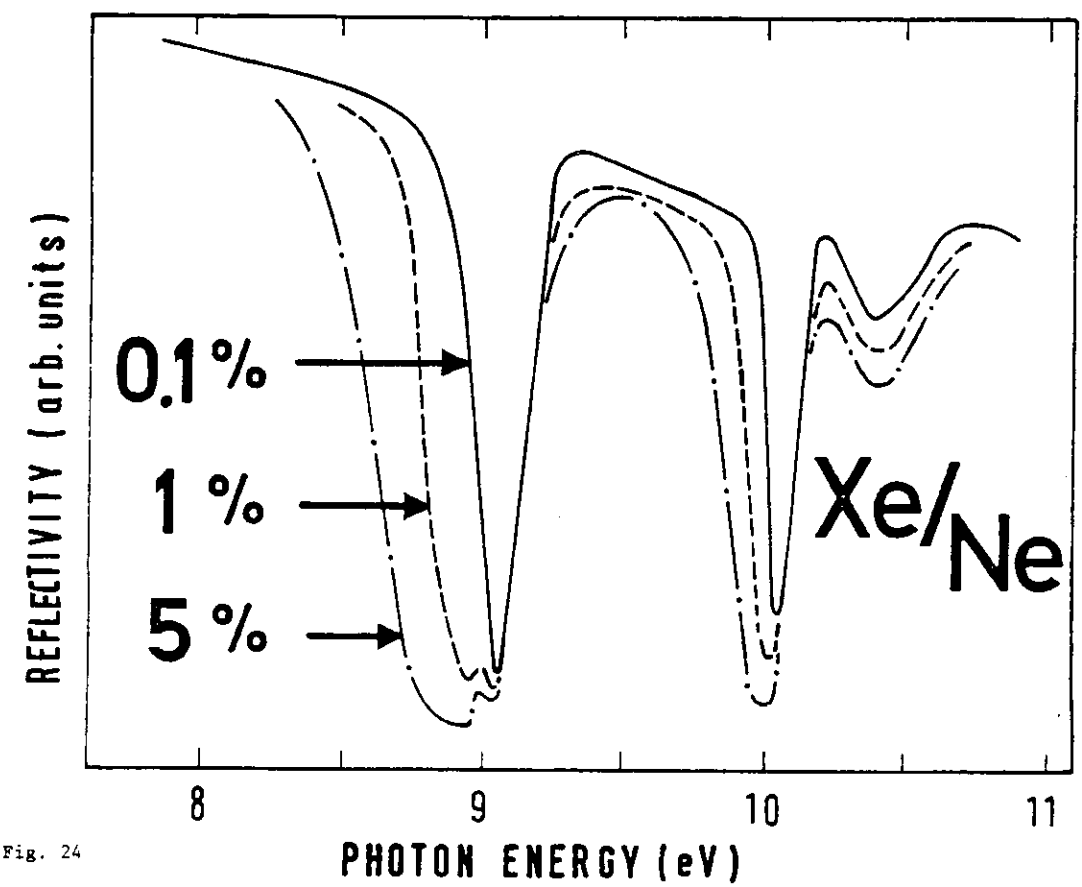
0.1%
1%
5%
Xe/Ne
REFLECTIVITY (arb. units)
8
9
10
11
PHOTON ENERGY (eV)

Fig. 24

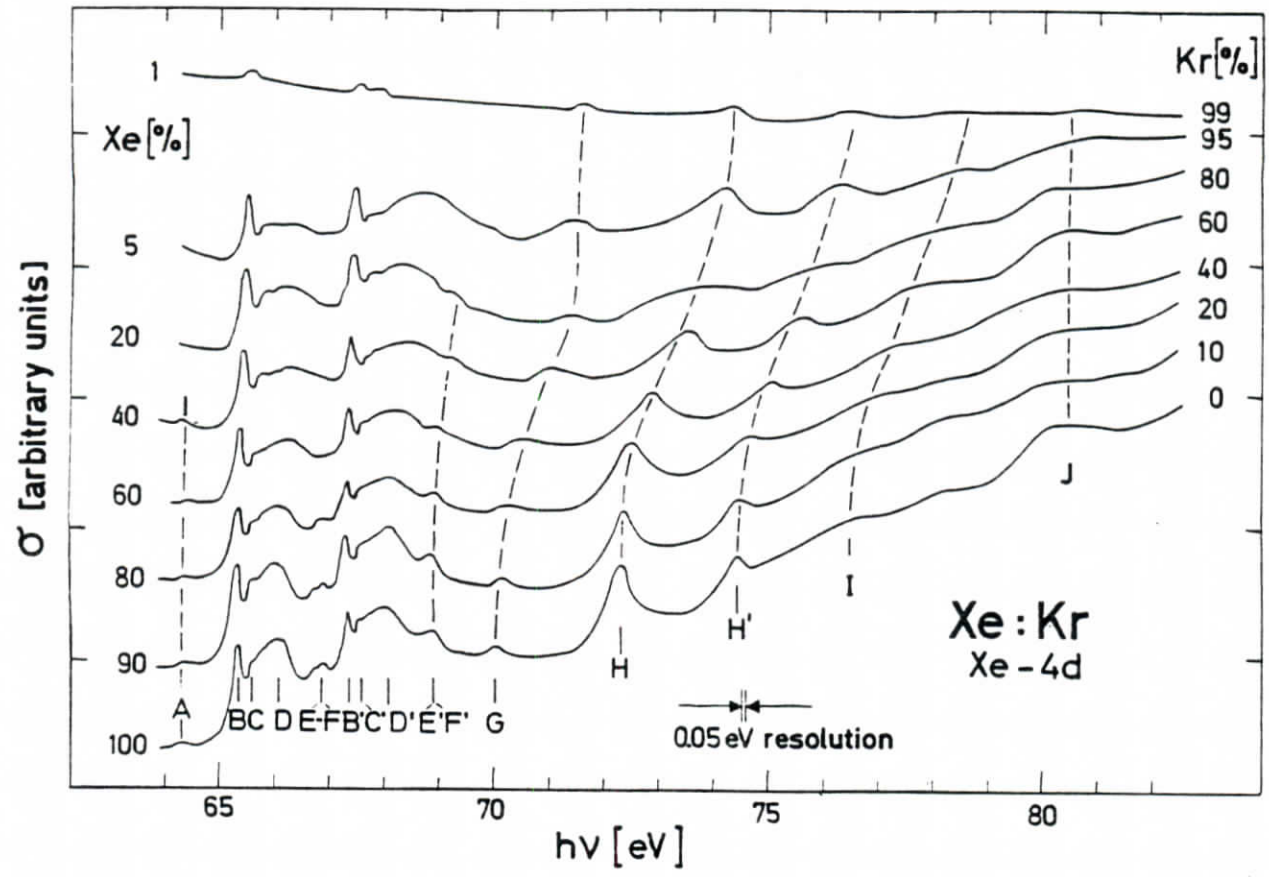
Kr[%]
Xe[%]
1
99
95
5
80
20
60
40
40
20
60
10
80
0
90
100
σ [arbitrary units]
A
BC D E-F B'C' D' E' F' G
H
H'
I
J
Xe : Kr
Xe - 4d
0.05 eV resolution
65
70
75
80
hν [eV]

Fig. 26

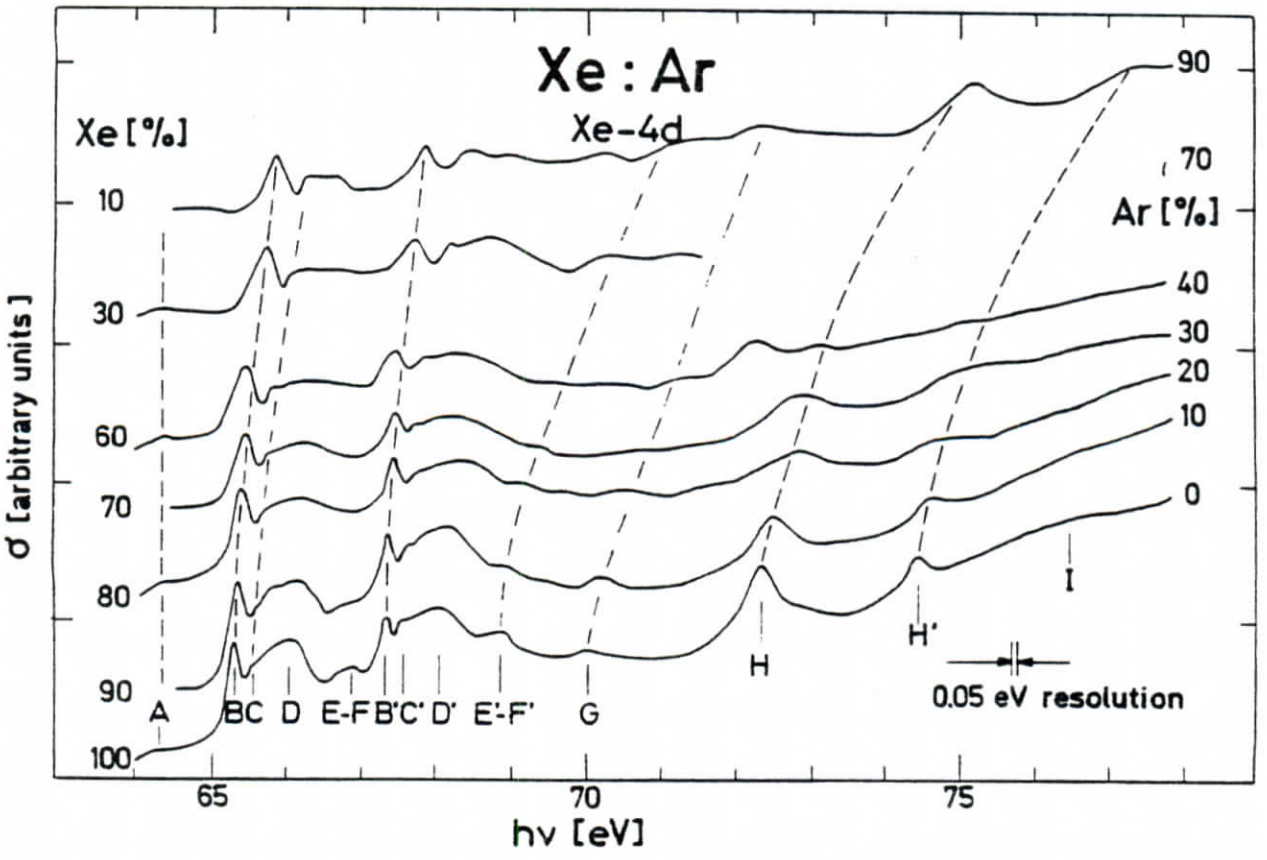
Xe : Ar
Xe-4d
Xe [%]
10
90
70
Ar [%]
30
40
30
60
20
70
10
80
0
90
100
σ [arbitrary units]
A
BC D E-F B'C' D' E'-F' G
H
H'
I
0.05 eV resolution
65
70
75
hν [eV]

Fig. 27

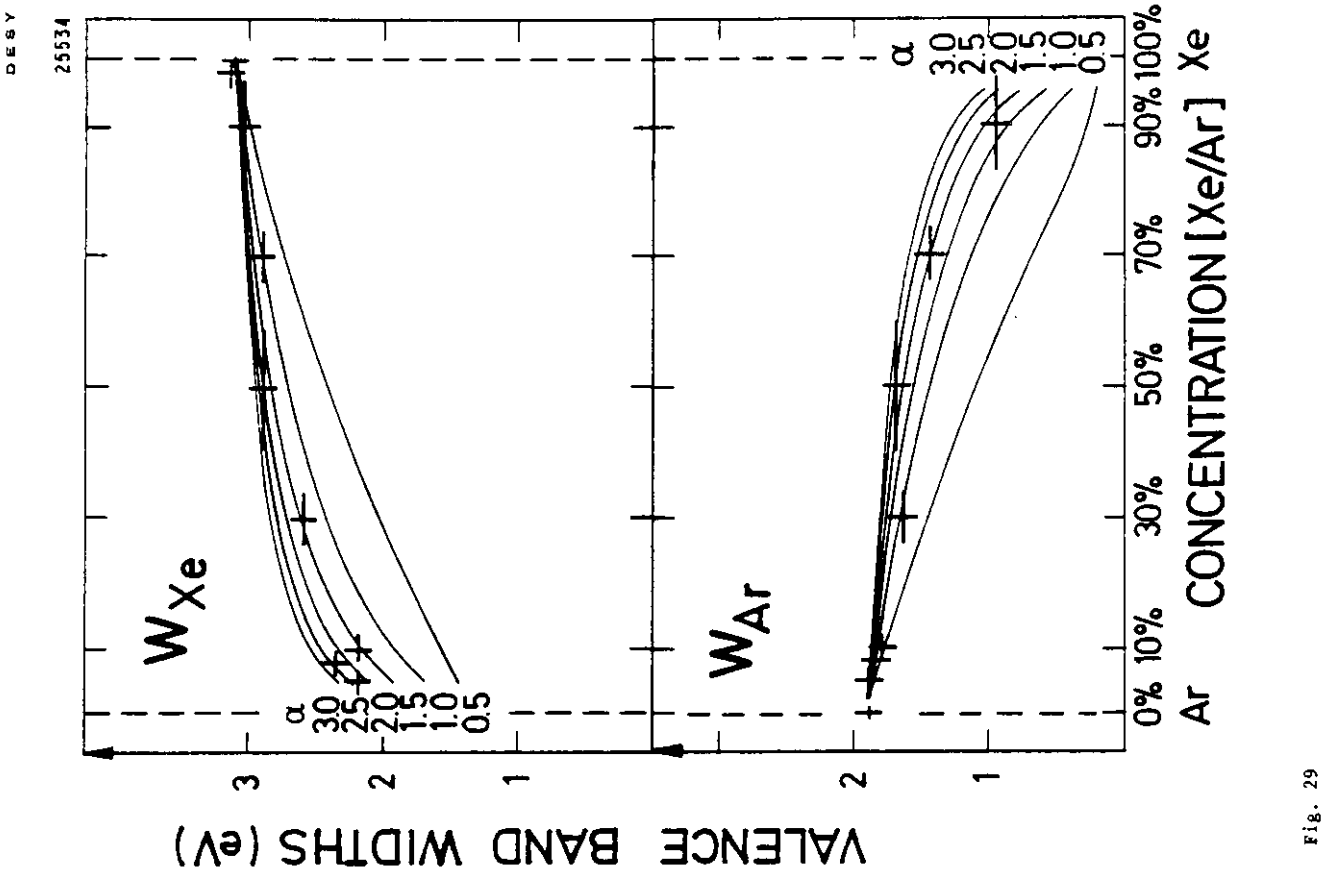
DESY 25534
W_{Xe}
W_{Ar}
α 3.0 2.5 2.0 1.5 1.0 0.5
VALENCE BAND WIDTHS (eV)
Ar CONCENTRATION [Xe/Ar] Xe
0% 10% 30% 50% 70% 90% 100%

Fig. 29

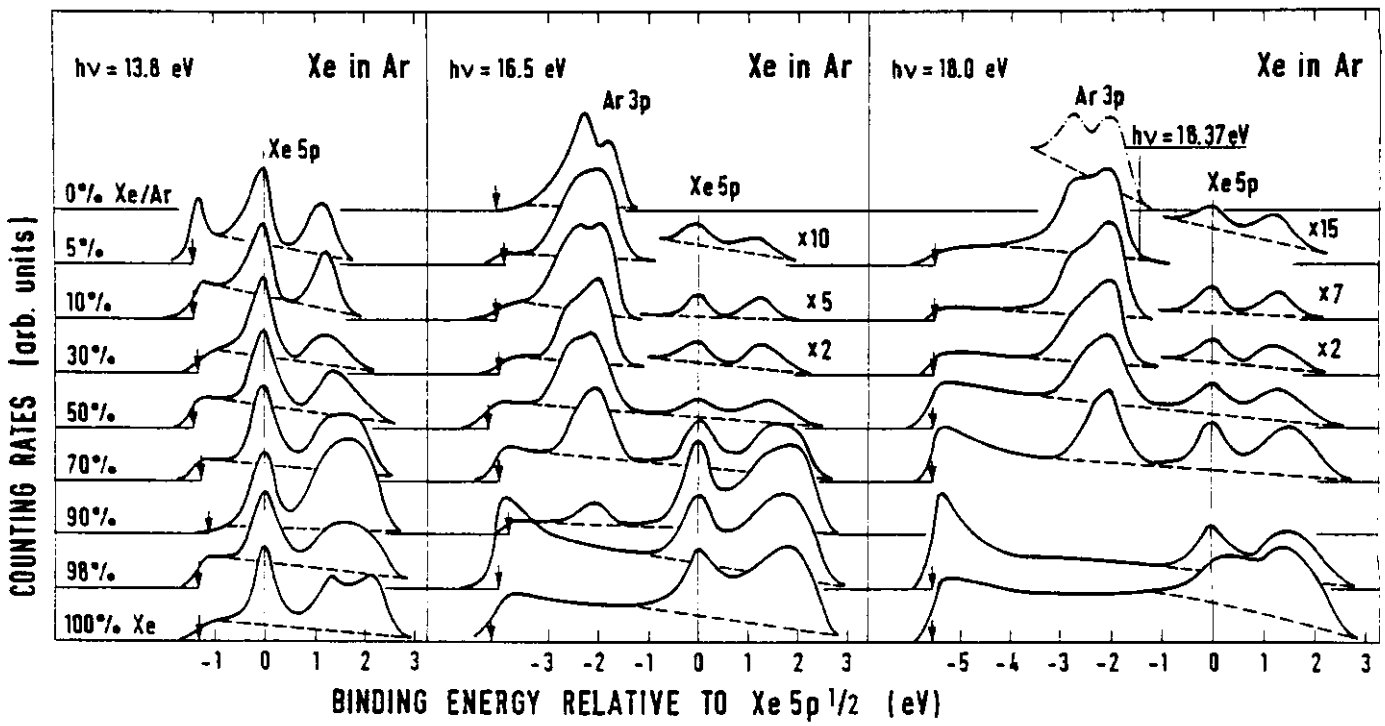
hν = 13.8 eV
Xe in Ar
hν = 16.5 eV
Xe in Ar
hν = 18.0 eV
Xe in Ar
Xe 5p
Ar 3p
hν = 18.37 eV
0% Xe/Ar
5%
10%
30%
50%
70%
90%
98%
100% Xe
x10
x5
x2
x15
x7
x2
COUNTING RATES (arb. units)
BINDING ENERGY RELATIVE TO Xe 5p 1/2 (eV)

Fig. 28

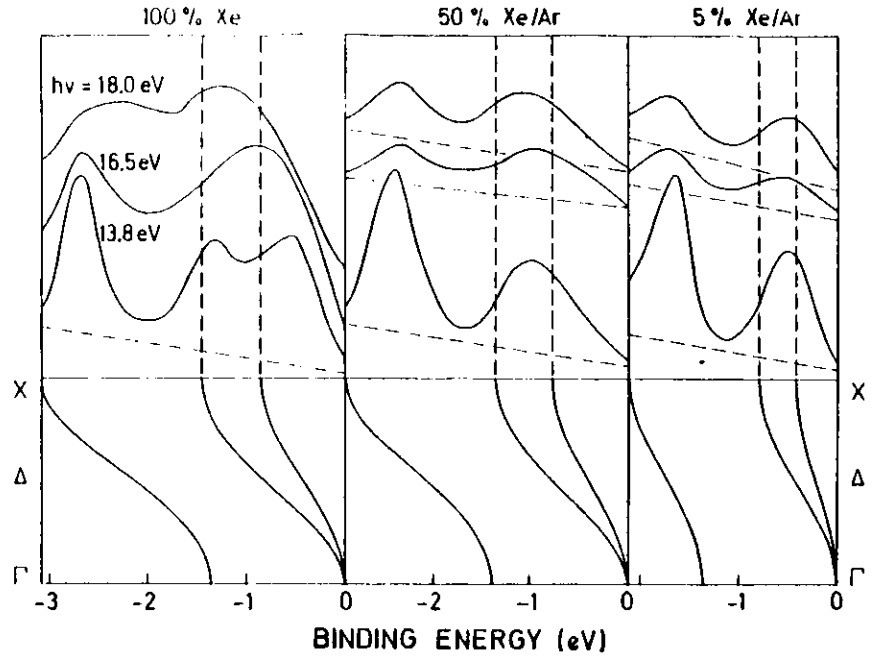
100 % Xe
50 % Xe/Ar
5 % Xe/Ar
hv = 18.0 eV
16.5eV
13.8eV
X
Δ
Γ
-3
-2
-1
0
BINDING ENERGY (eV)

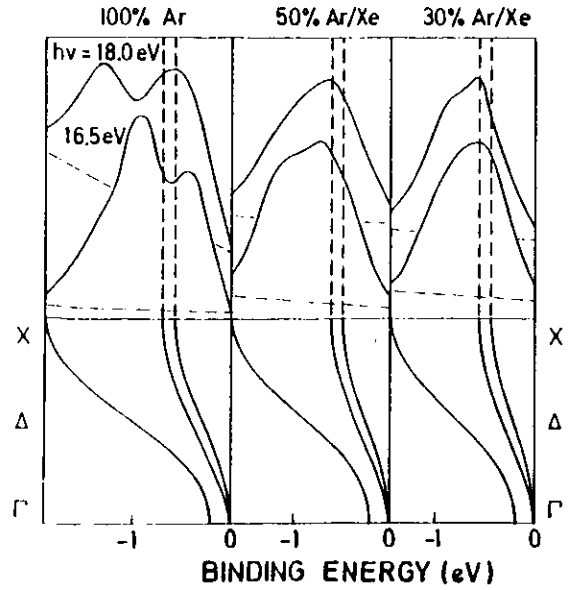
100% Ar
50% Ar/Xe
30% Ar/Xe
hv = 18.0 eV
16.5eV
X
Δ
Γ
-1
0
BINDING ENERGY (eV)

Fig. 30

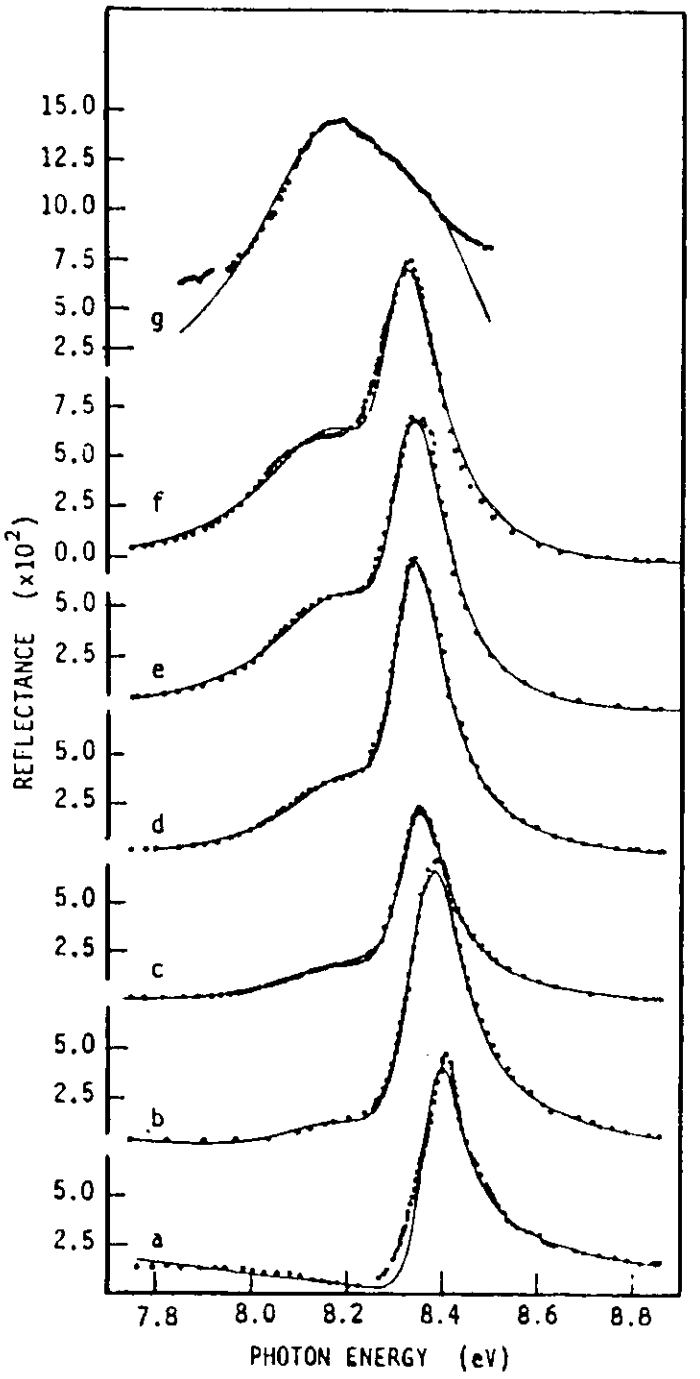
REFLECTANCE (x10²)
15.0
12.5
10.0
7.5
5.0
2.5
0.0
g
f
e
d
c
b
a
7.8
8.0
8.2
8.4
8.6
8.8
PHOTON ENERGY (eV)

Fig. 31

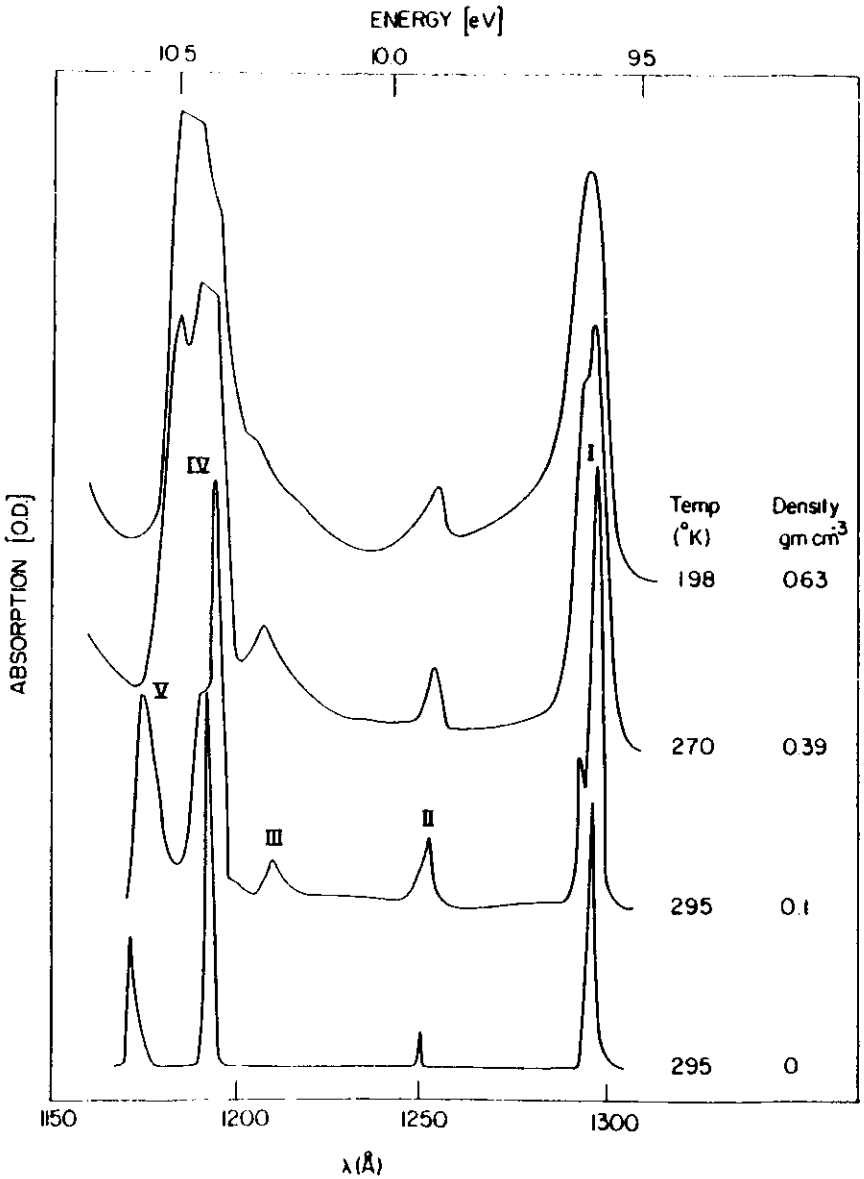
ENERGY [eV]
10.5
10.0
9.5
ABSORPTION [O.D.]
IV
V
III
II
I
Temp (°K)
Density gm cm⁻³
198
0.63
270
0.39
295
0.1
295
0
1150
1200
1250
1300
λ (Å)

Fig. 32

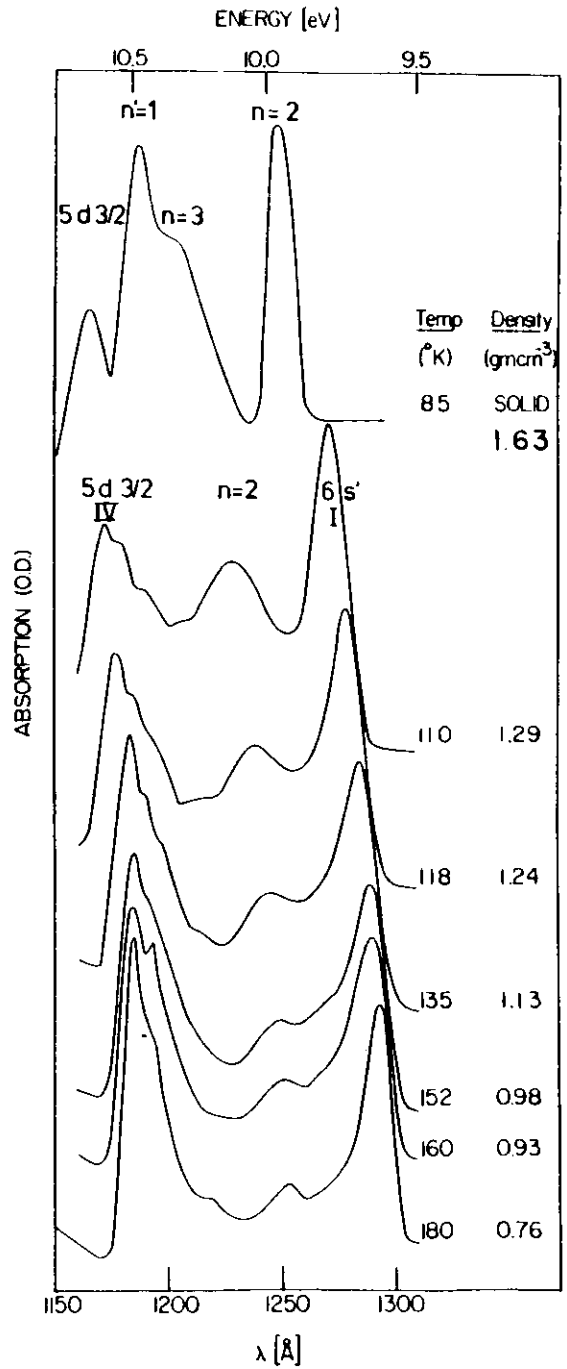
ENERGY [eV]
10.5
10.0
9.5
n=1
n=2
5d 3/2
n=3
Temp (°K)
Density (gmcm⁻³)
85
SOLID
1.63
5d 3/2
IV
n=2
6s'
I
ABSORPTION (O.D.)
110
1.29
118
1.24
135
1.13
152
0.98
160
0.93
180
0.76
1150
1200
1250
1300
λ [Å]

Fig. 33

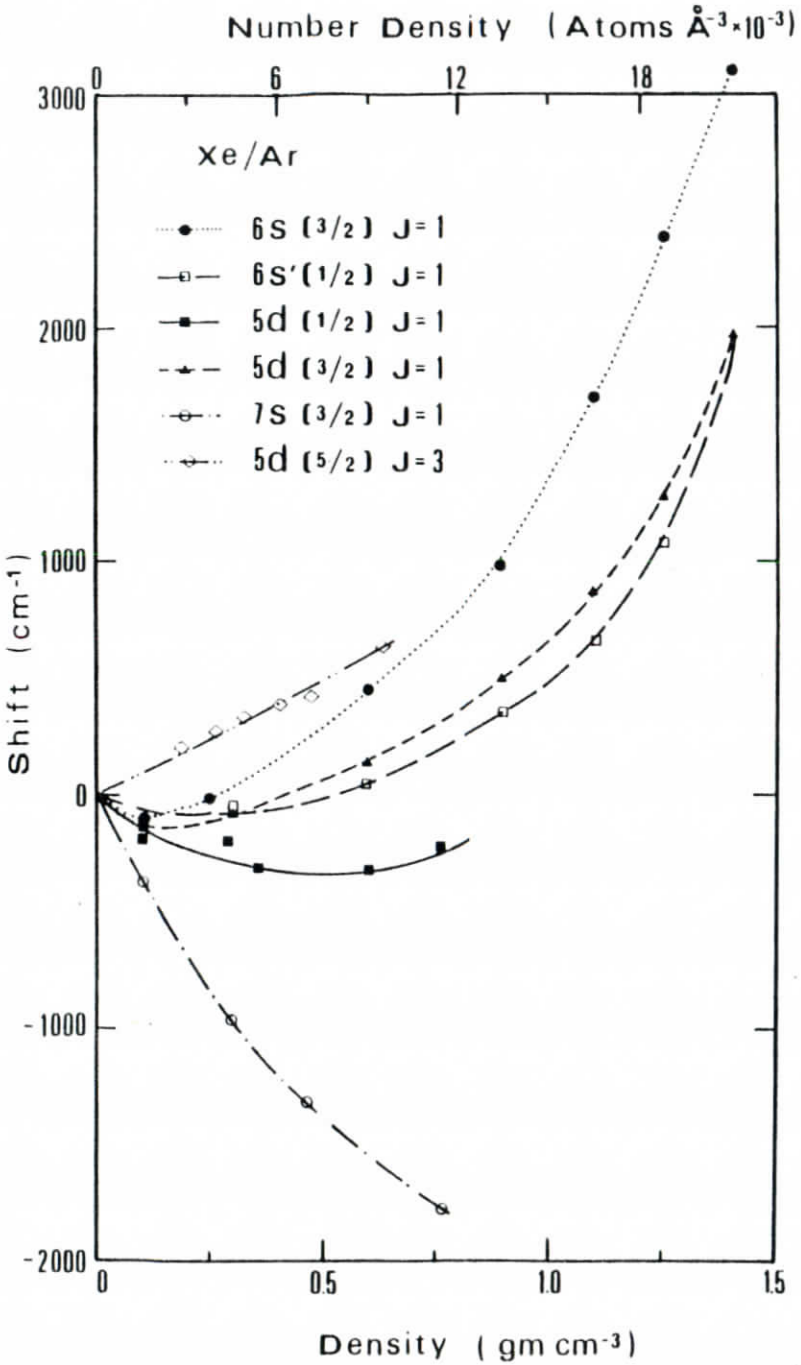

30056

Fig. 34

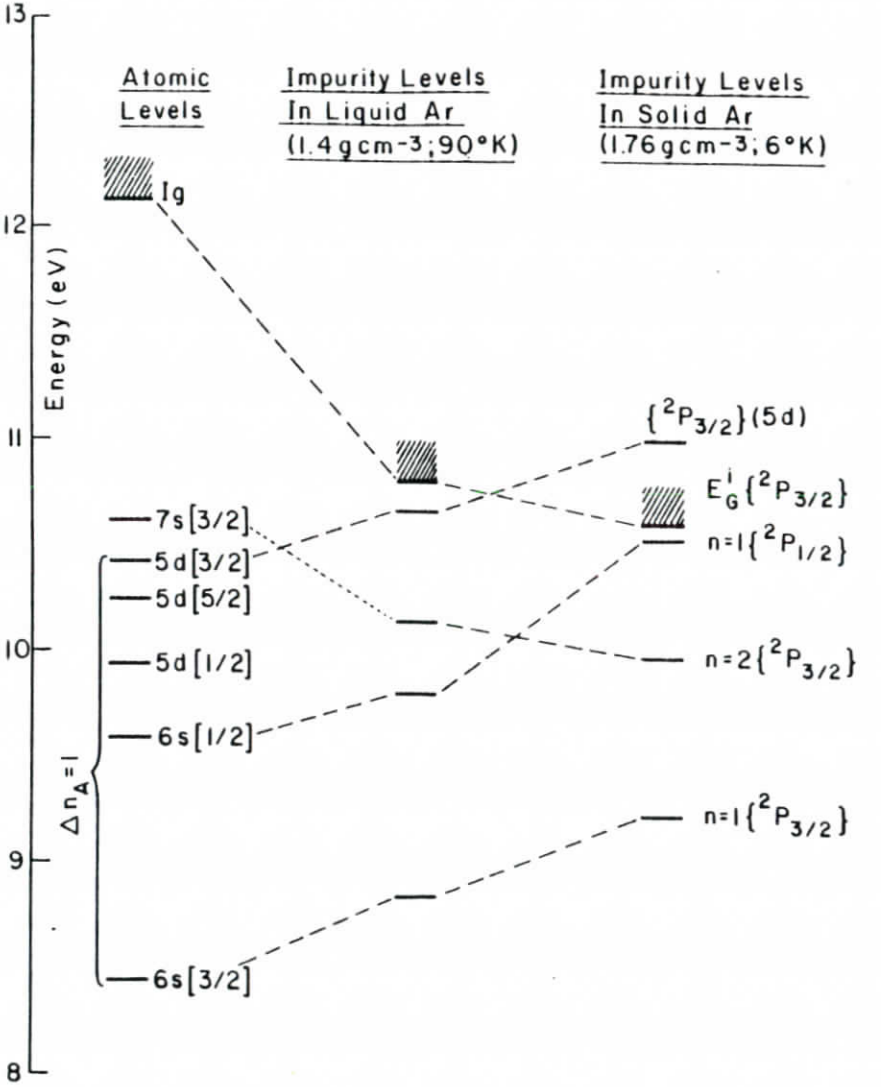

Fig. 35

30055

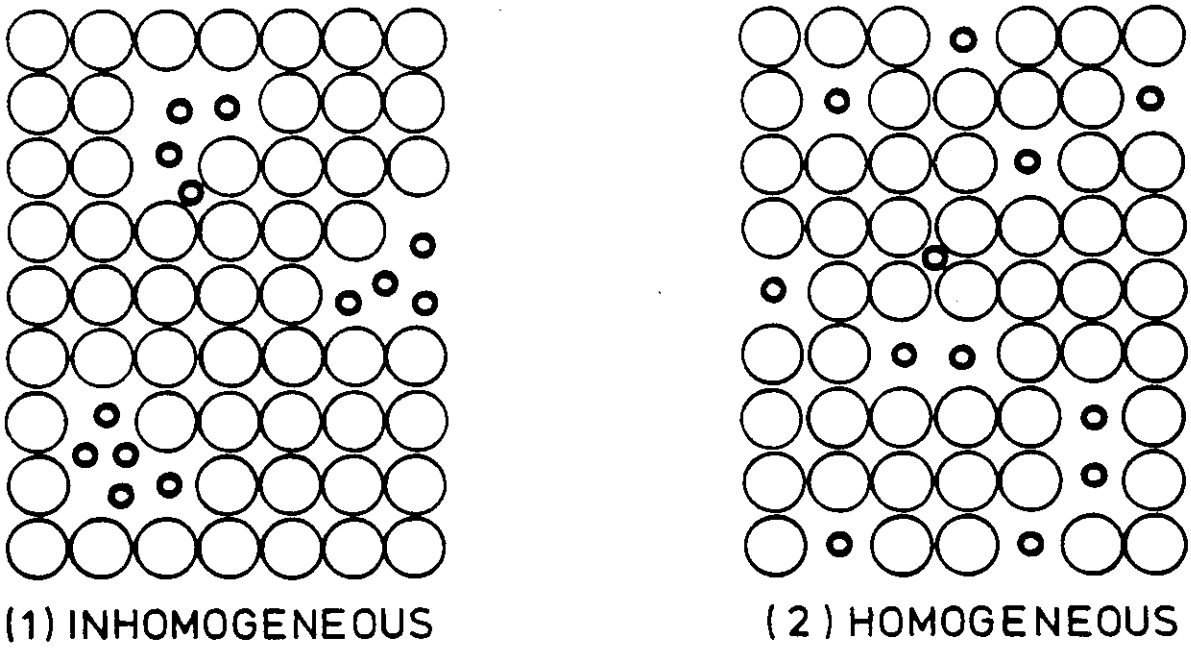
(1) INHOMOGENEOUS
(2) HOMOGENEOUS

Fig. 37

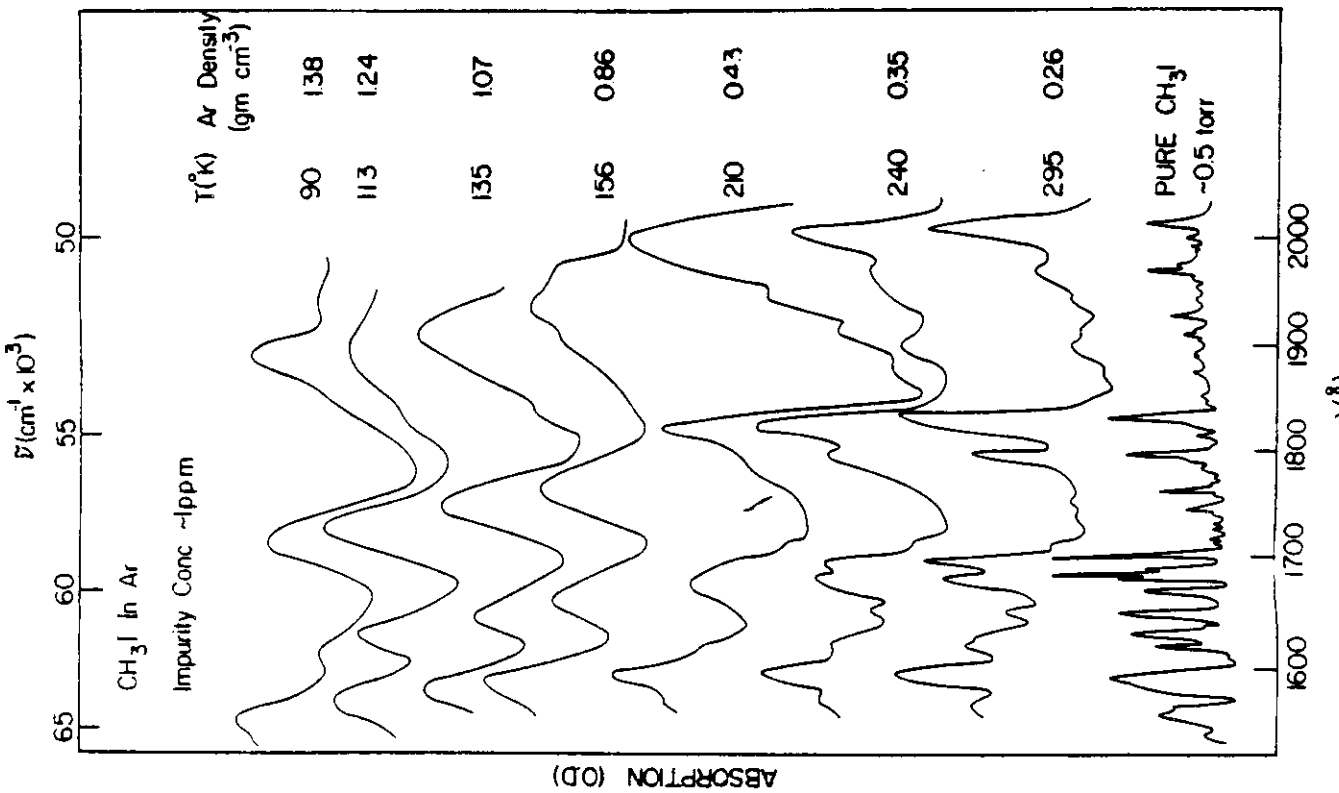
$\bar{\nu}(cm^{-1} \times 10^3)$
65
60
55
50
CH_3I in Ar
Impurity Conc ~1ppm
T(°K) Ar Density (gm cm^{-3})
90 138
113 124
135 107
156 086
210 043
240 035
295 026
PURE CH_3I ~0.5 torr
ABSORPTION (OD)
1600
1700
1800
1900
2000
λ(Å)

Fig. 36

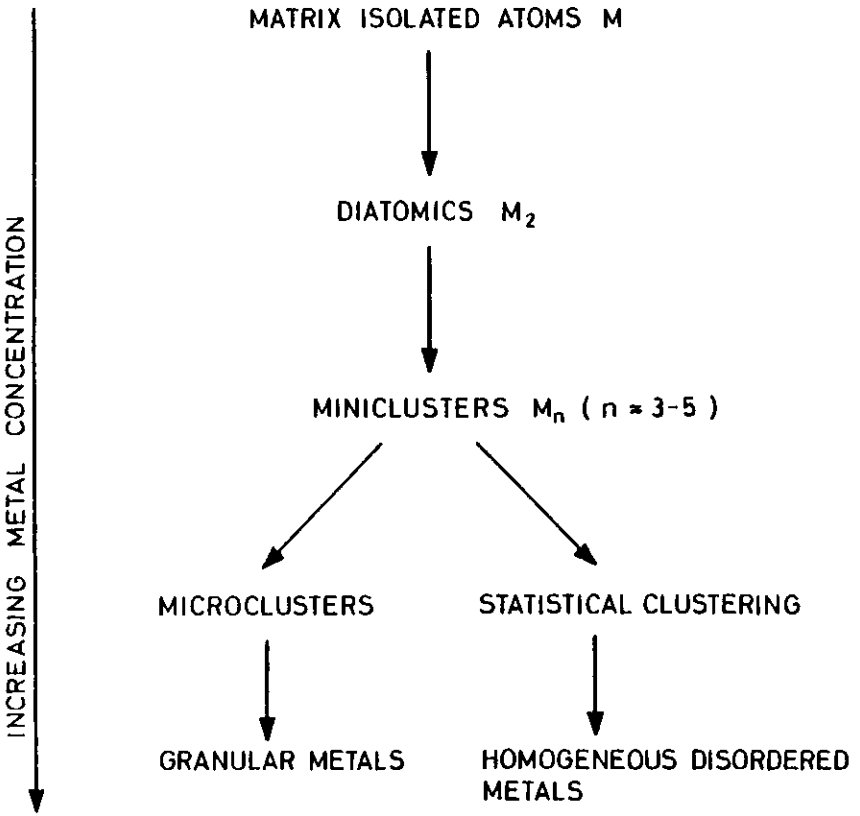
INCREASING METAL CONCENTRATION
MATRIX ISOLATED ATOMS M
DIATOMICS M_2
MINICLUSTERS M_n (n ≈ 3-5)
MICROCLUSTERS
STATISTICAL CLUSTERING
GRANULAR METALS
HOMOGENEOUS DISORDERED METALS
29905

Fig. 38

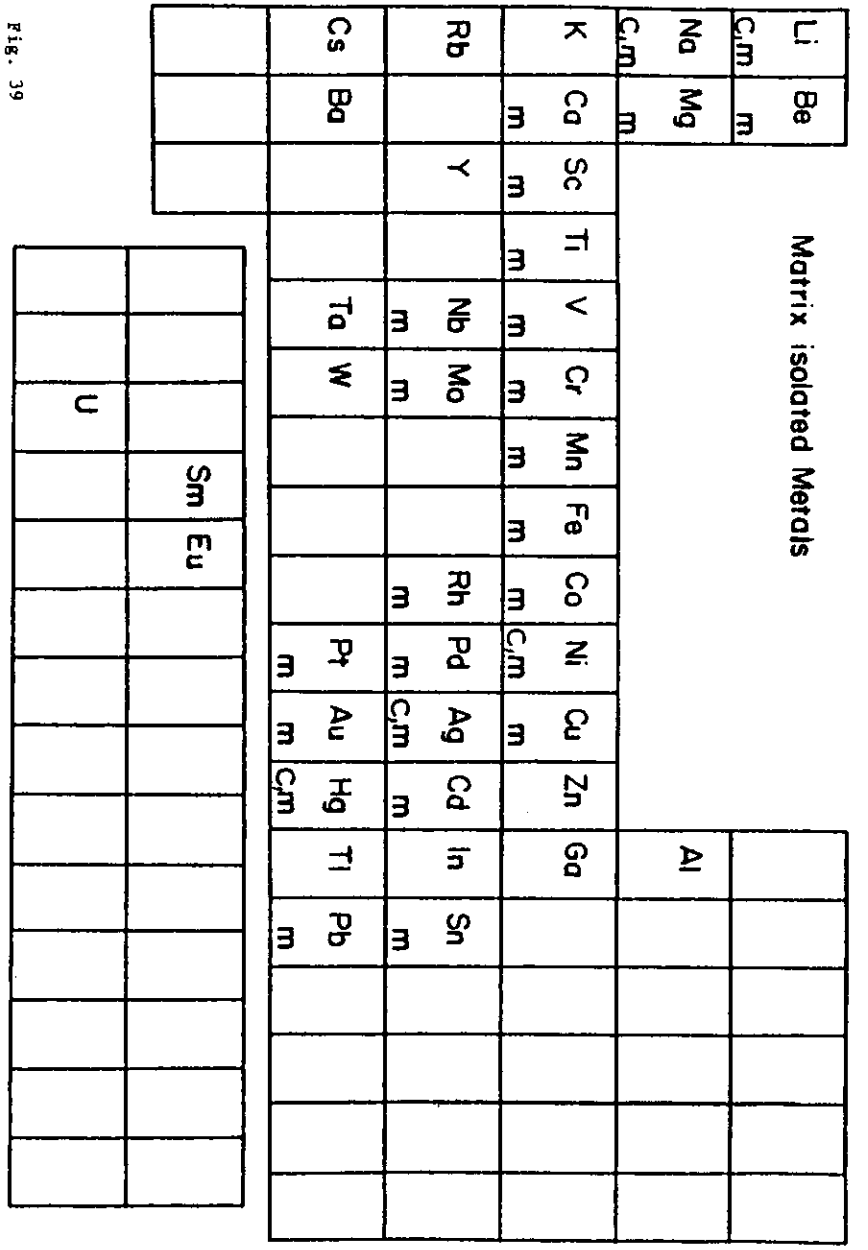
Matrix isolated Metals
Li Be
Na Mg
K Ca Sc Ti V Cr Mn Fe Co Ni Cu Zn Ga Al
Rb Y Nb Mo Rh Pd Ag Cd In Sn
Cs Ba Ta W Pt Au Hg Tl Pb
U Sm Eu
C,m m

Fig. 39

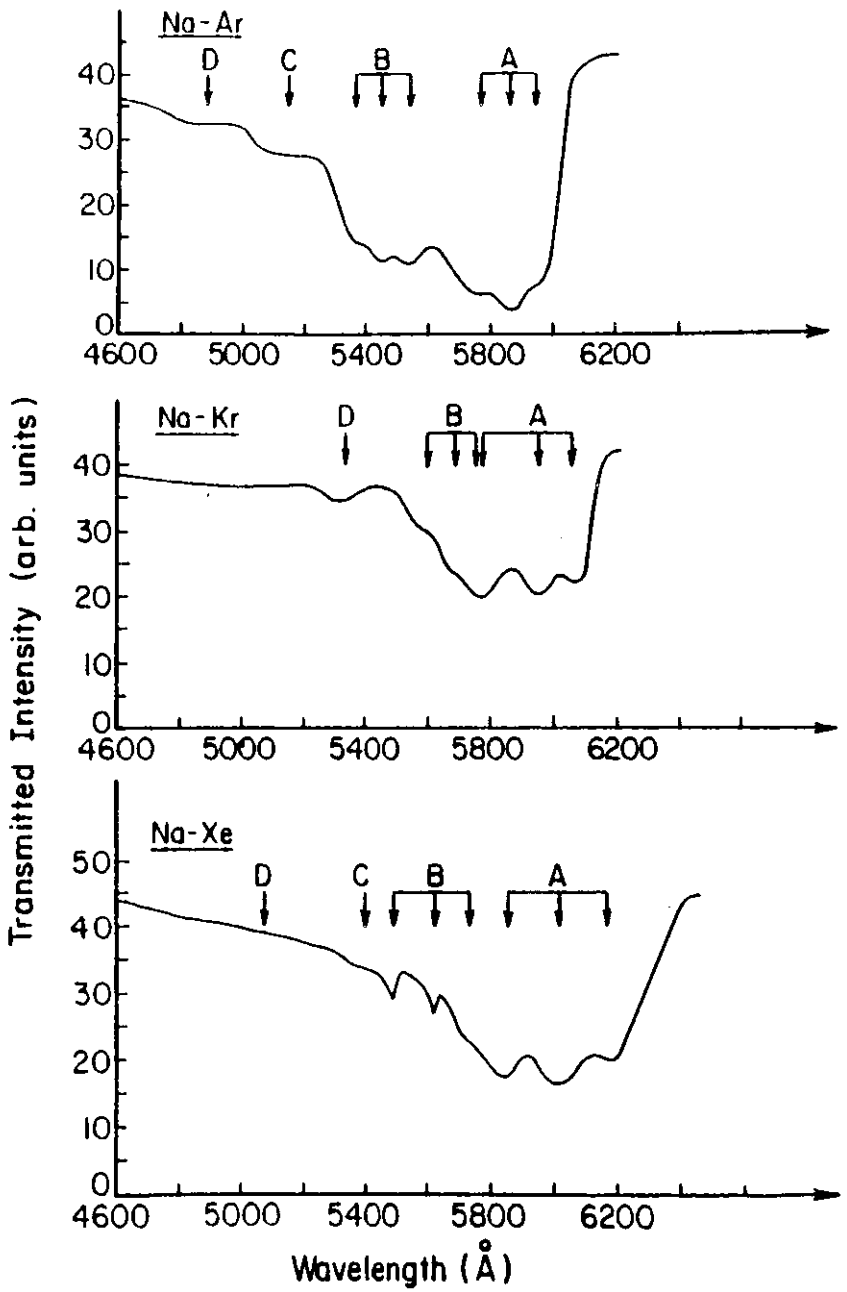
Na-Ar
D
C
B
A
Na-Kr
Na-Xe
Transmitted Intensity (arb. units)
Wavelength (Å)
4600
5000
5400
5800
6200

Fig. 40

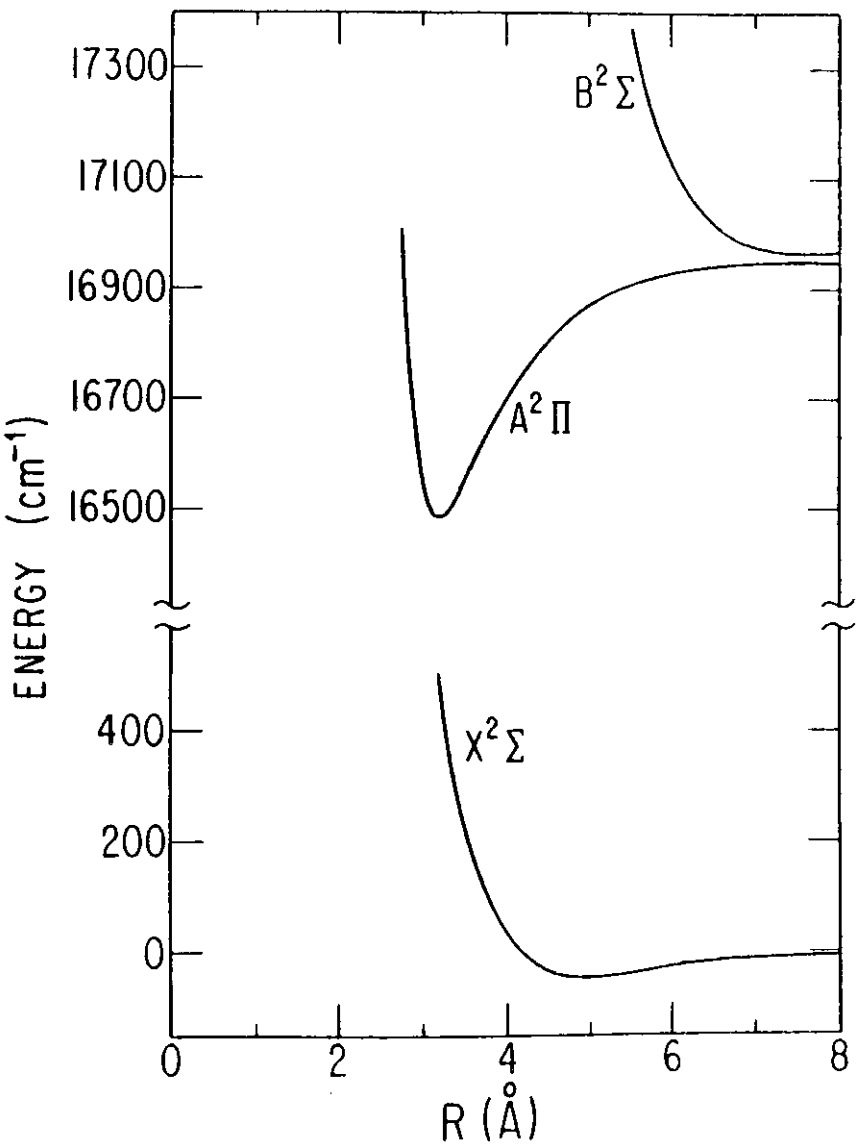
ENERGY (cm⁻¹)
R (Å)
B² Σ
A² Π
X² Σ
17300
17100
16900
16700
16500
400
200
0
2
4
6
8

Fig. 41

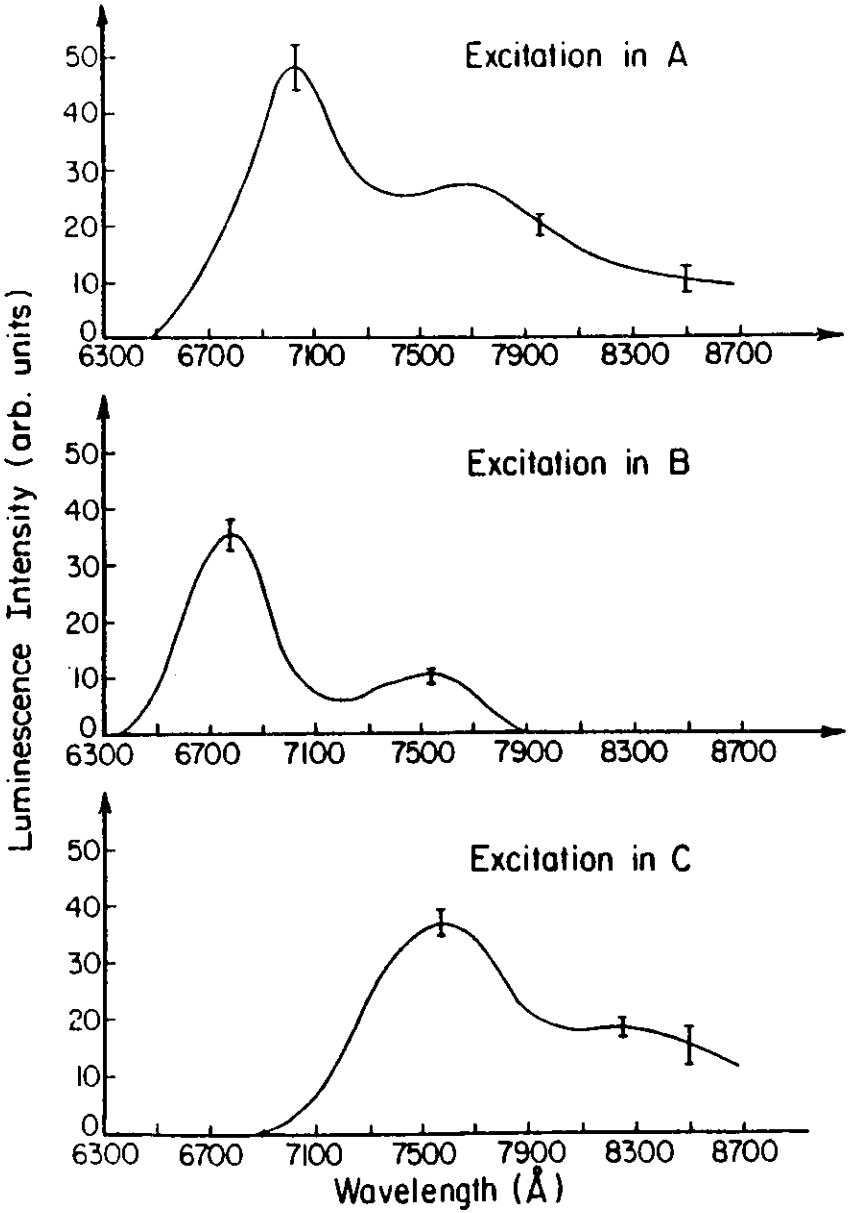
Excitation in A
Excitation in B
Excitation in C
Luminescence Intensity (arb. units)
Wavelength (Å)
6300 6700 7100 7500 7900 8300 8700
0 10 20 30 40 50

Fig. 42

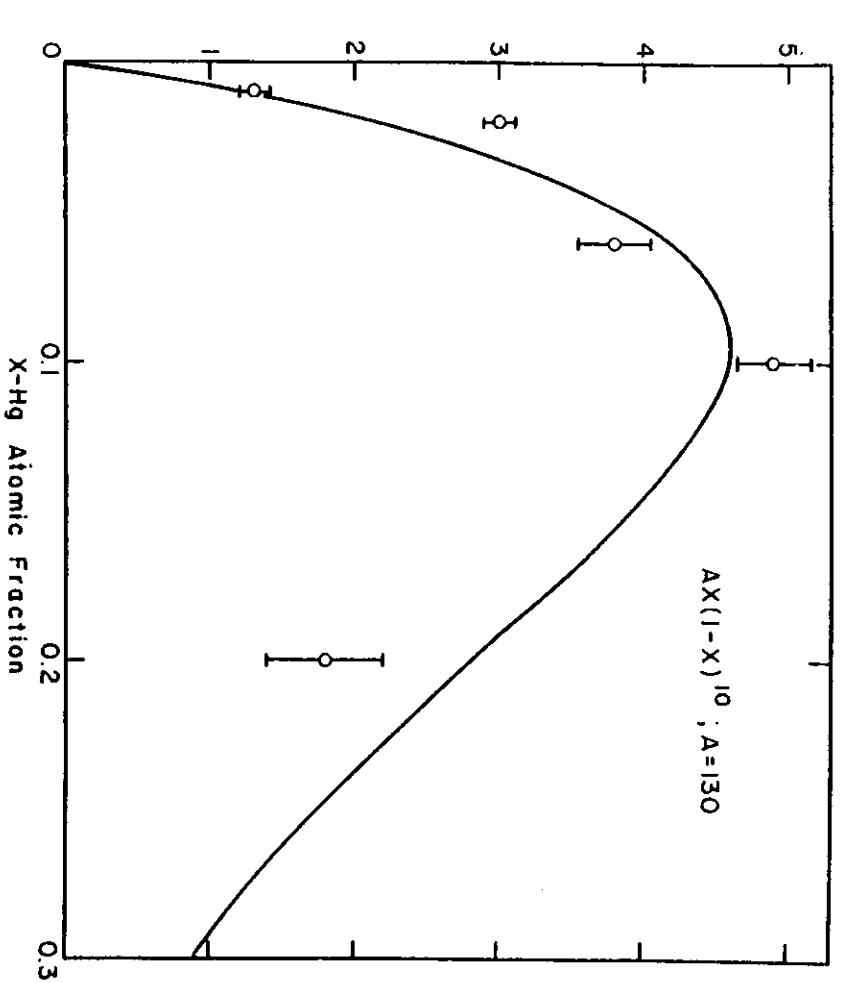
X-Hg Atomic Fraction
0 0.1 0.2 0.3
0 1 2 3 4 5
AX(1-X)^10 ; A=130

Fig. 43

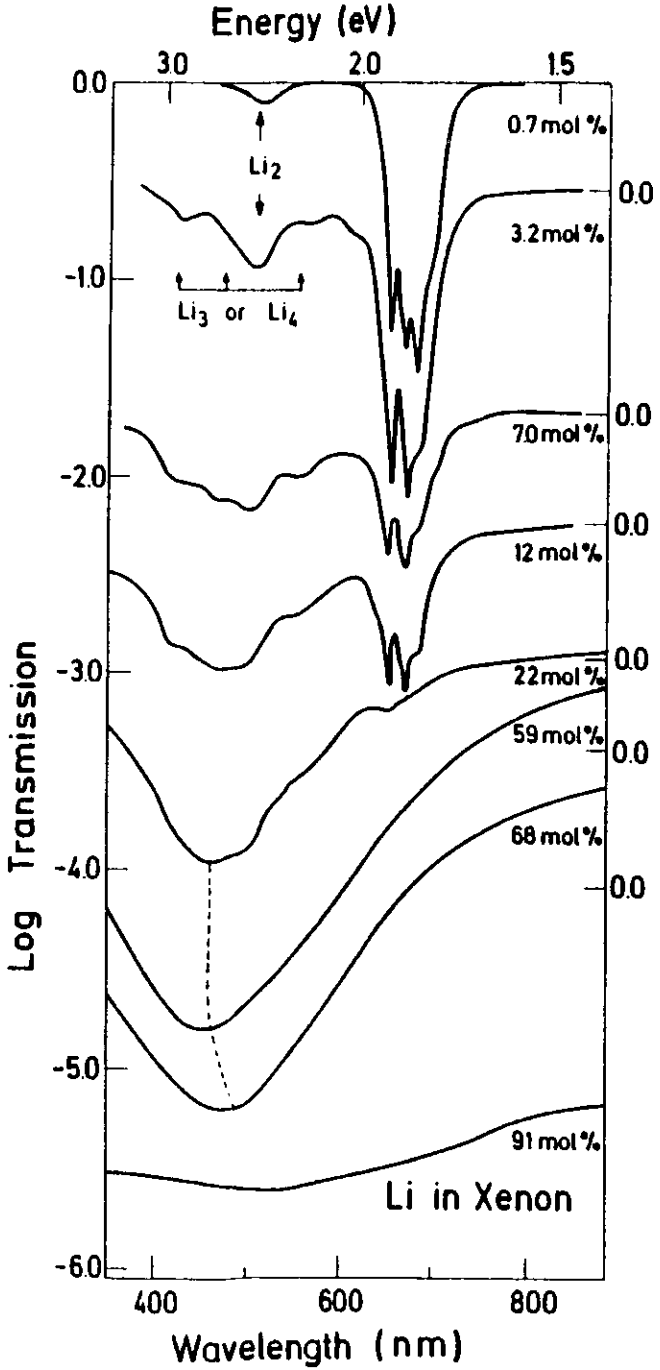
Energy (eV)
3.0
2.0
1.5
0.0
-1.0
-2.0
-3.0
-4.0
-5.0
-6.0
Li2
Li3 or Li4
0.7 mol %
3.2 mol %
7.0 mol %
12 mol %
22 mol %
59 mol %
68 mol %
91 mol %
0.0
Li in Xenon
Log Transmission
400
600
800
Wavelength (nm)

Fig. 44

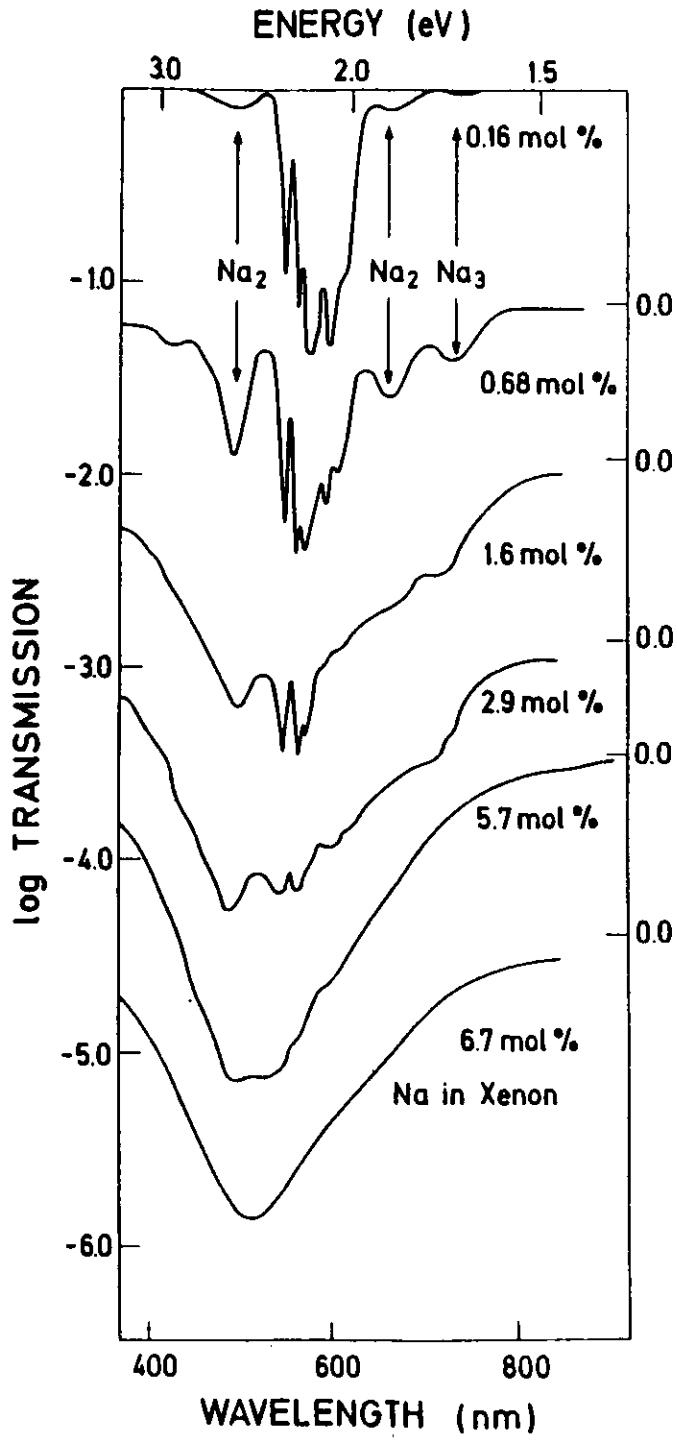
ENERGY (eV)
3.0
2.0
1.5
-1.0
-2.0
-3.0
-4.0
-5.0
-6.0
Na2
Na2
Na3
0.16 mol %
0.68 mol %
1.6 mol %
2.9 mol %
5.7 mol %
6.7 mol %
0.0
Na in Xenon
log TRANSMISSION
400
600
800
WAVELENGTH (nm)

Fig. 45

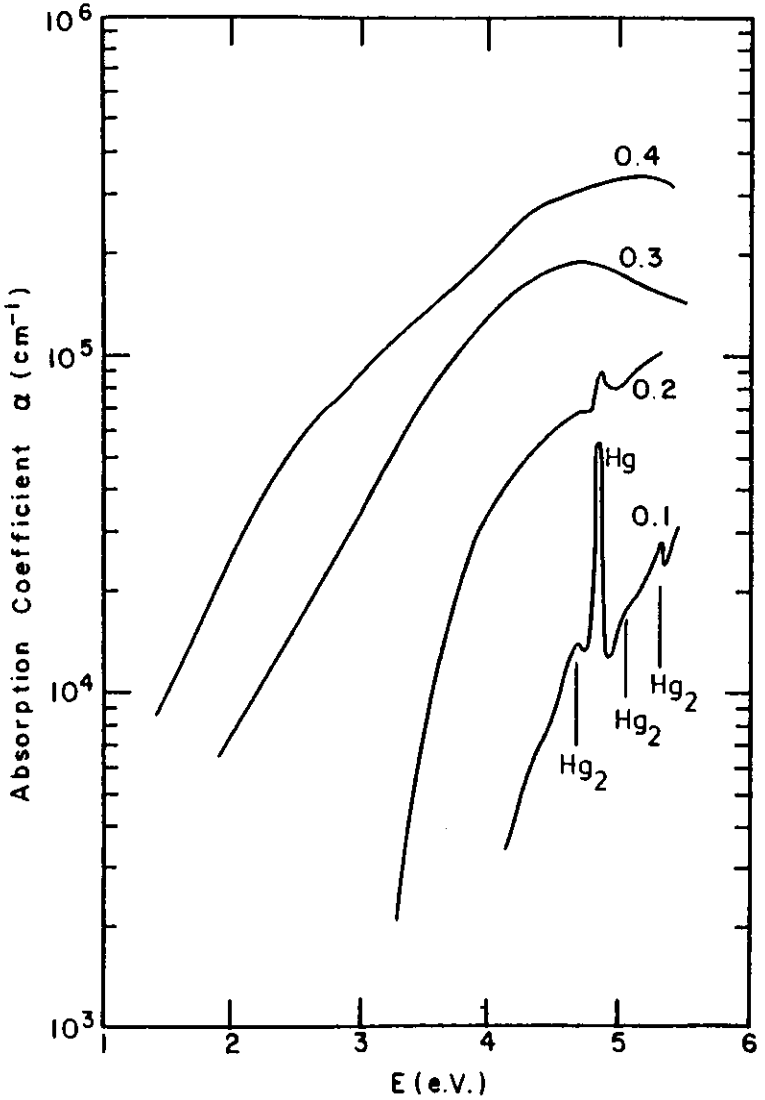
Absorption Coefficient α (cm⁻¹)
E (e.V.)
0.4
0.3
0.2
0.1
Hg
Hg2
Hg2
Hg2

Fig. 46

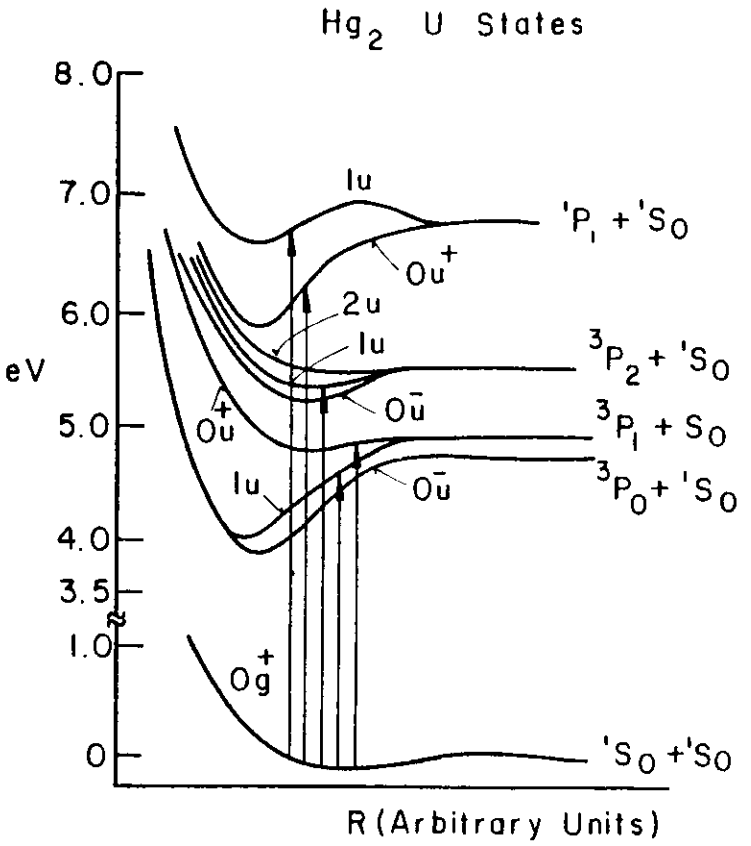
Hg2 U States
eV
R (Arbitrary Units)
1u
0u+
2u
1u
0u-
0u+
1u
0u-
0g+
1P1 + 1S0
3P2 + 1S0
3P1 + S0
3P0 + 1S0
1S0 + 1S0

Fig. 47

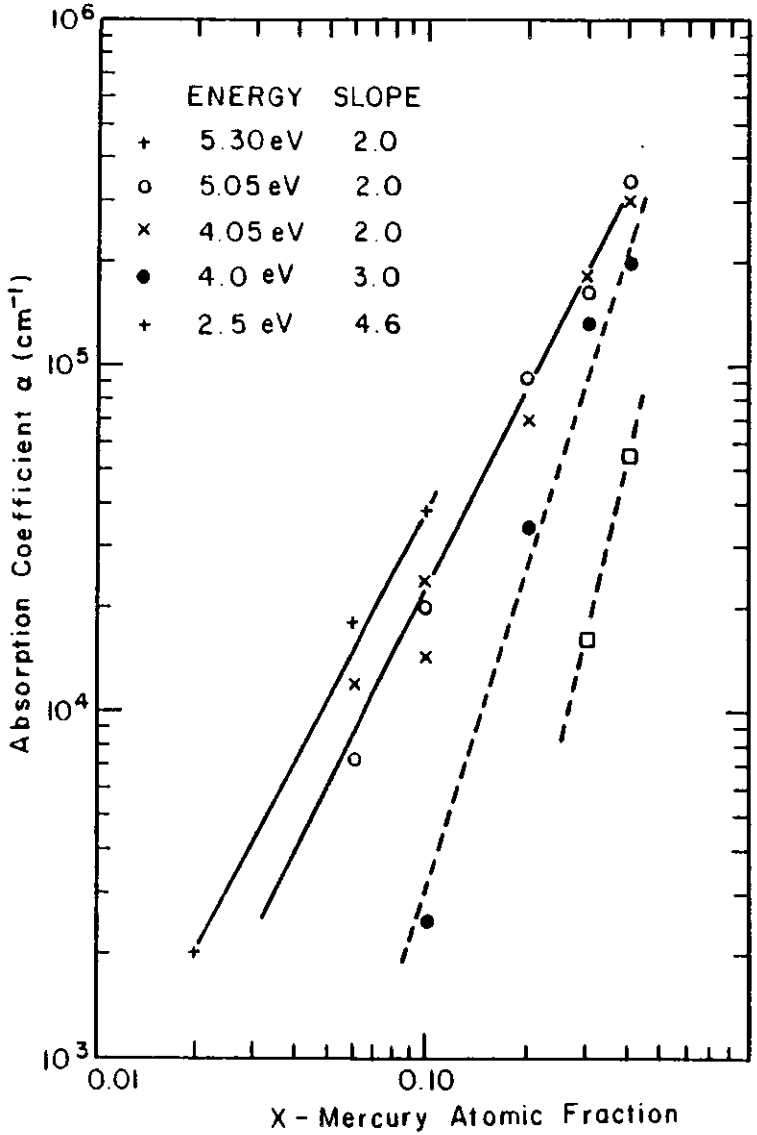
ENERGY SLOPE
5.30 eV 2.0
5.05 eV 2.0
4.05 eV 2.0
4.0 eV 3.0
2.5 eV 4.6
Absorption Coefficient α (cm⁻¹)
X - Mercury Atomic Fraction
0.01
0.10

Fig. 48

Fig. 49

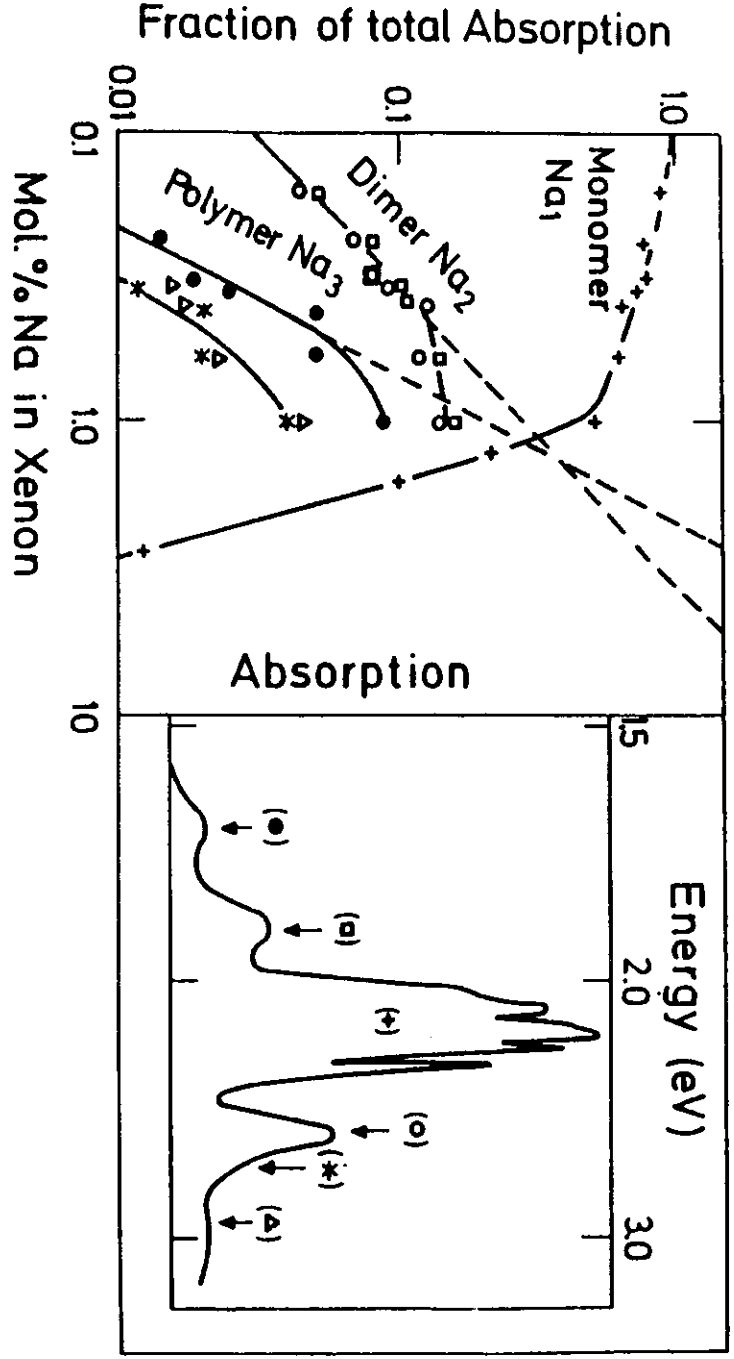
Fraction of total Absorption
Mol.% Na in Xenon
Monomer Na1
Dimer Na2
Polymer Na3
Absorption
Energy (eV)

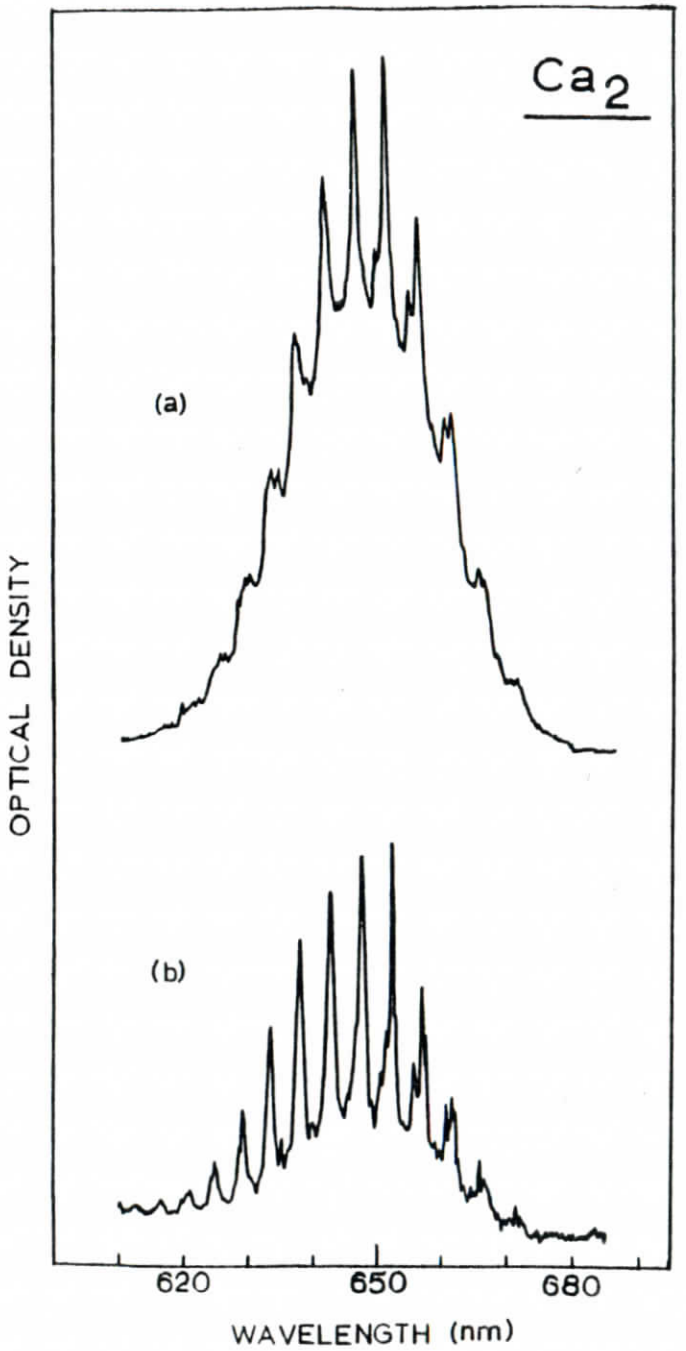
Ca2
(a)
(b)
OPTICAL DENSITY
620
650
680
WAVELENGTH (nm)

Fig. 50

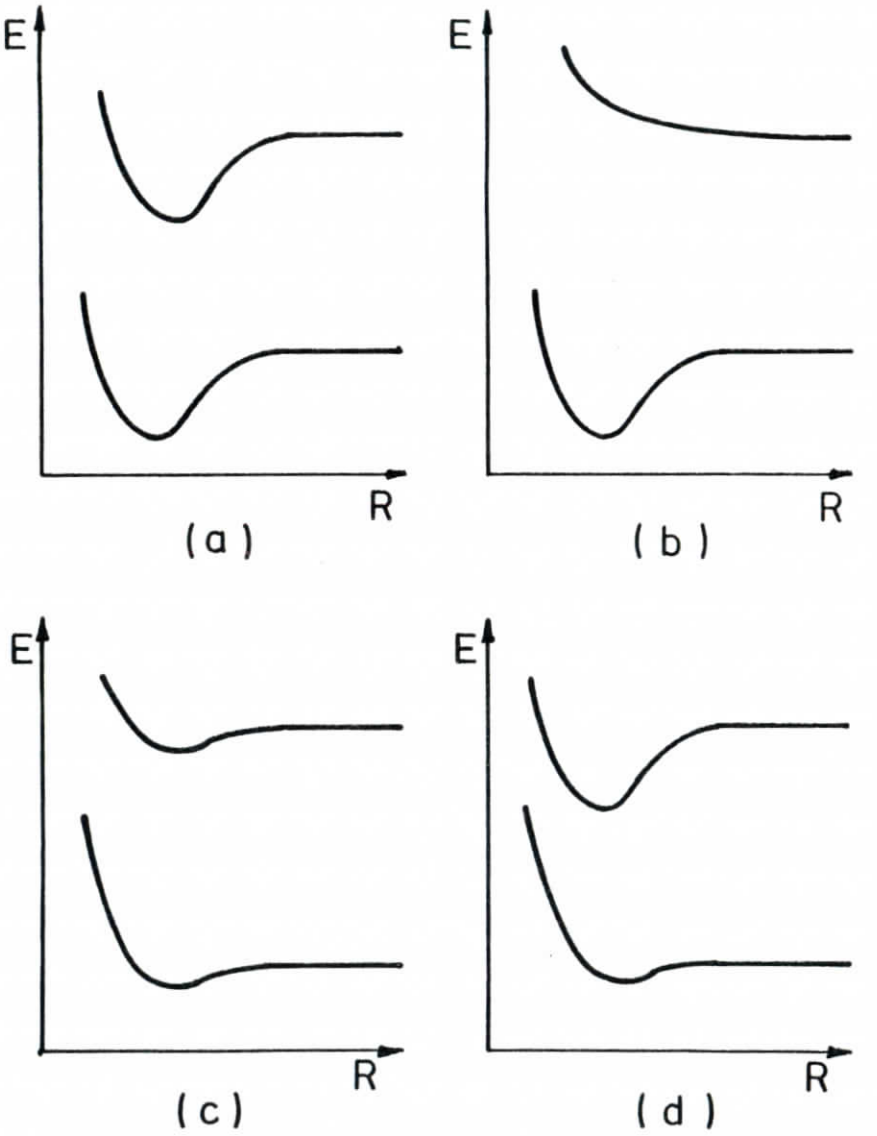
E
R
(a)
E
R
(b)
E
R
(c)
E
R
(d)

Fig. 51

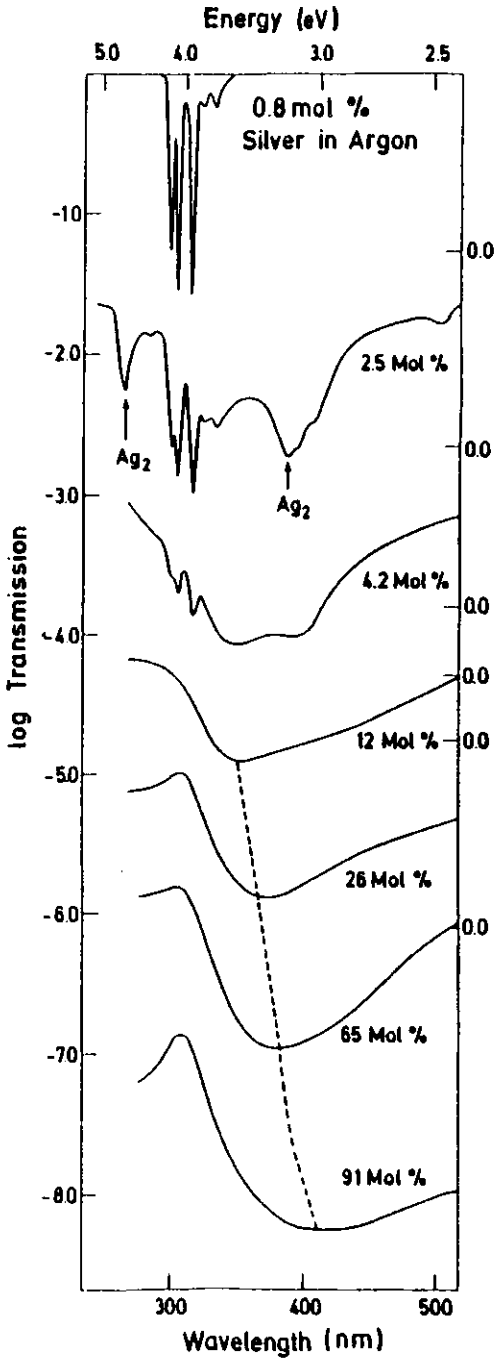
Energy (eV)
5.0
4.0
3.0
2.5
0.8 mol %
Silver in Argon
2.5 Mol %
4.2 Mol %
12 Mol %
26 Mol %
65 Mol %
91 Mol %
Ag2
Ag2
log Transmission
-1.0
-2.0
-3.0
-4.0
-5.0
-6.0
-7.0
-8.0
0.0
300
400
500
Wavelength (nm)

Fig. 52

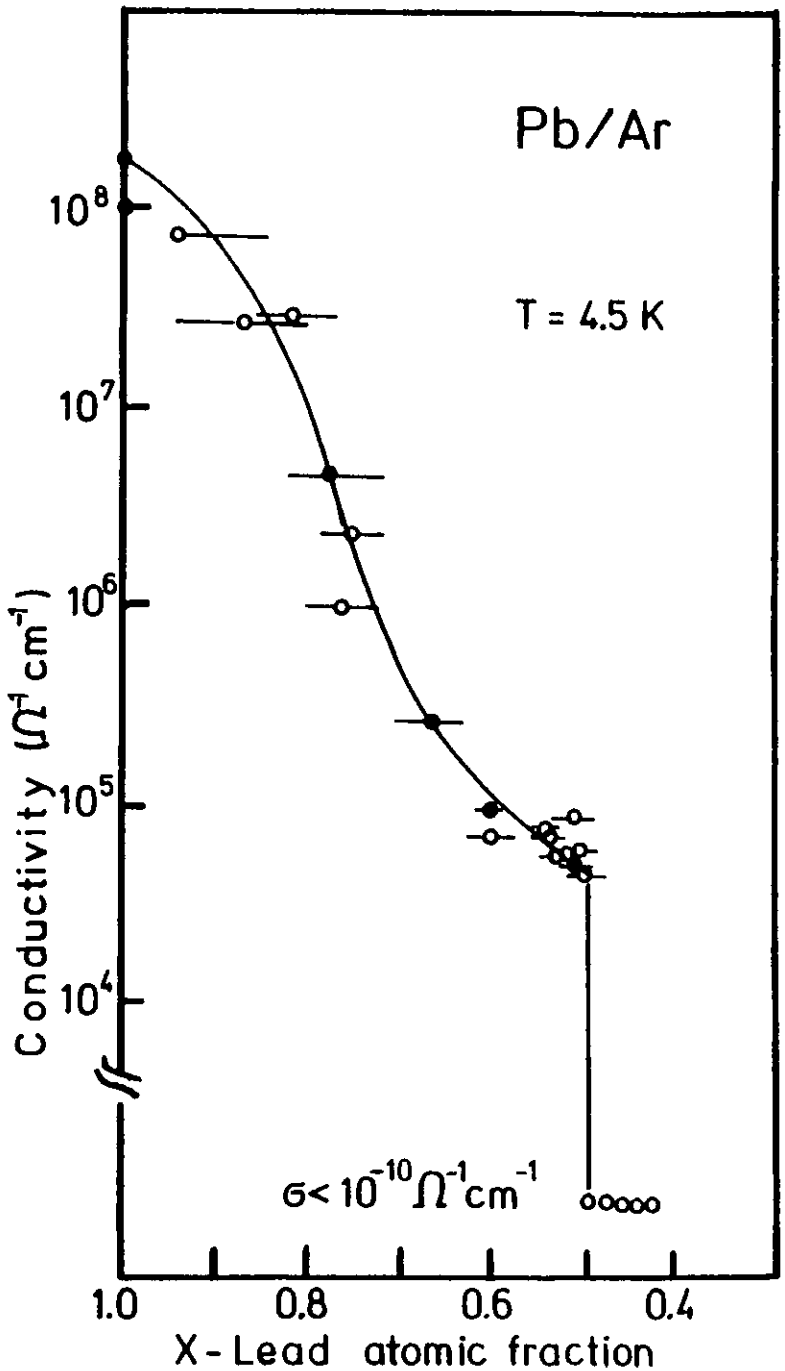
Pb/Ar
T = 4.5 K
Conductivity (Ω⁻¹cm⁻¹)
10⁸
10⁷
10⁶
10⁵
10⁴
σ< 10⁻¹⁰Ω⁻¹cm⁻¹
1.0
0.8
0.6
0.4
X - Lead atomic fraction

Fig. 53

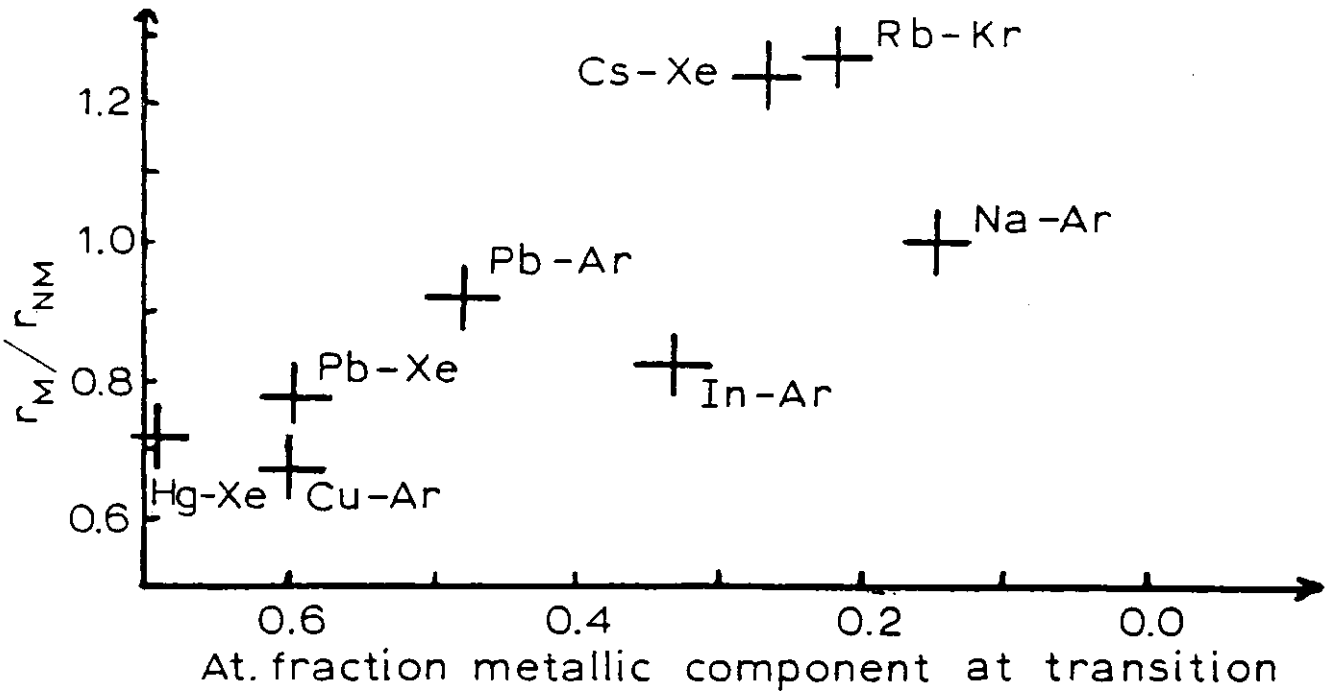
Cs-Xe
Rb-Kr
Na-Ar
Pb-Ar
Pb-Xe
In-Ar
Hg-Xe
Cu-Ar
1.2
1.0
0.8
0.6
r_M / r_{NM}
0.6
0.4
0.2
0.0
At. fraction metallic component at transition

Fig. 55

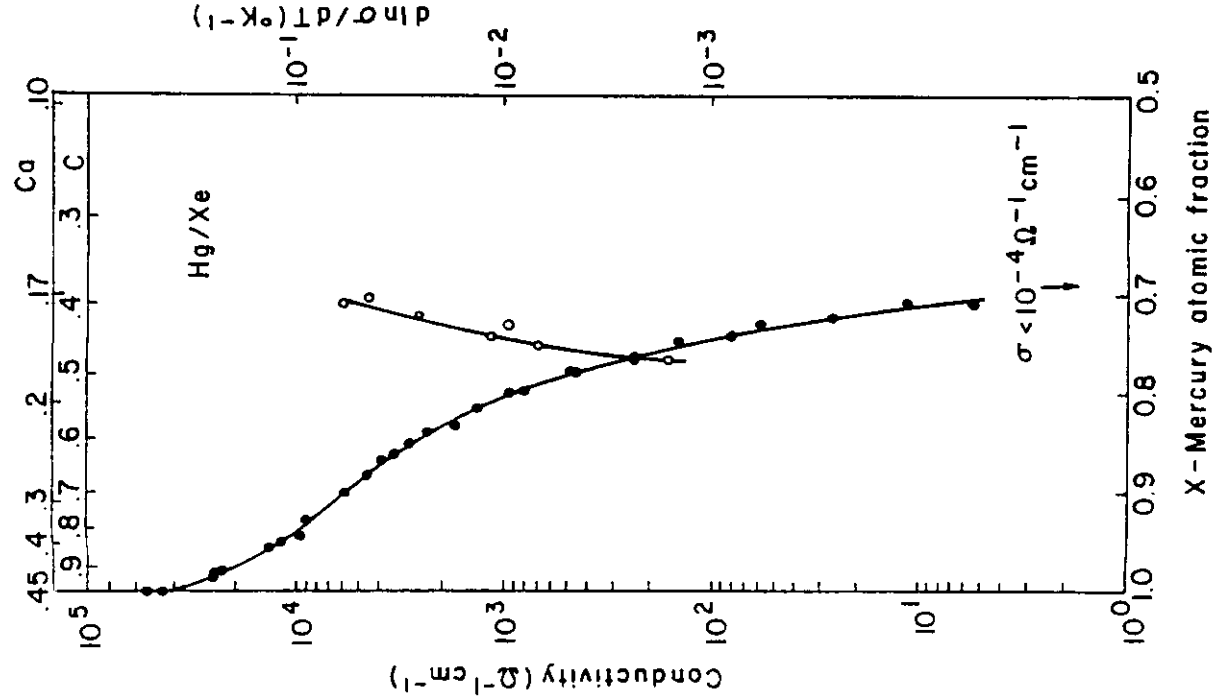
$d\ln\sigma/dT\,(°K^{-1})$
10^{-1}
10^{-2}
10^{-3}
Ca
Hg/Xe
$\sigma < 10^{-4}\,\Omega^{-1}cm^{-1}$
X-Mercury atomic fraction
Conductivity $(\Omega^{-1}cm^{-1})$
10^5
10^4
10^3
10^2
10^1
10^0

Fig. 54

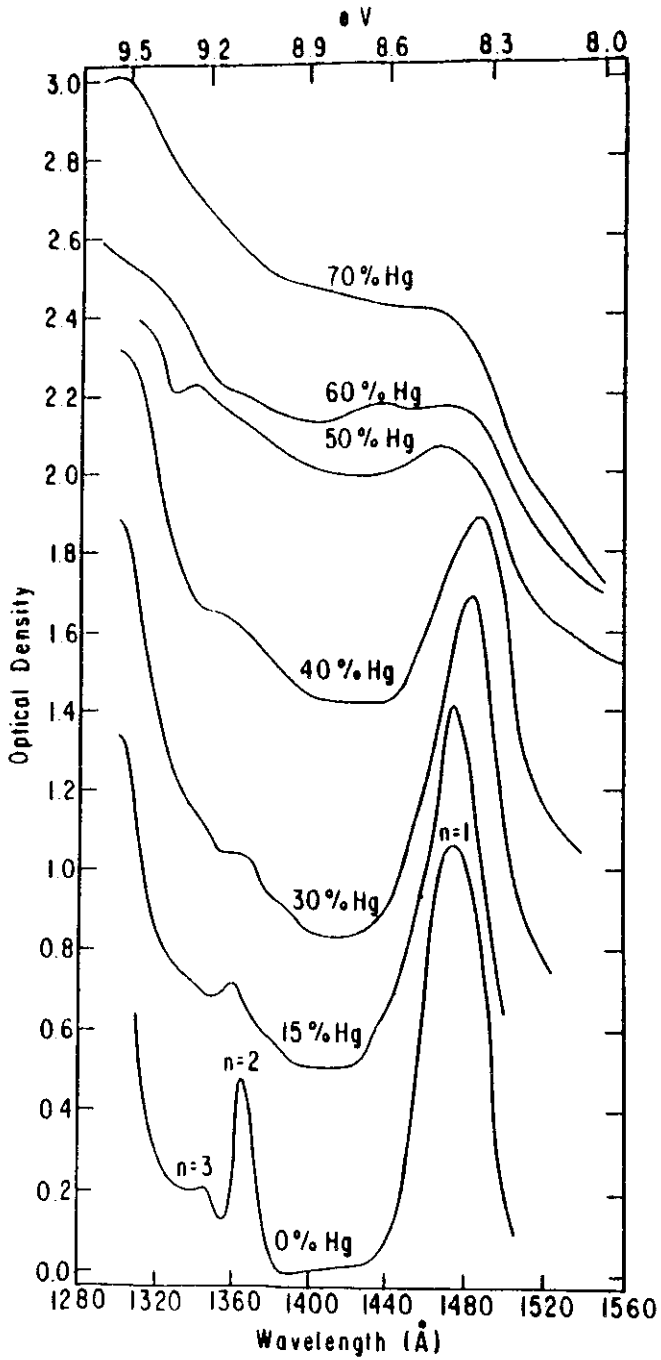
eV
9.5
9.2
8.9
8.6
8.3
8.0
3.0
2.8
2.6
2.4
2.2
2.0
1.8
1.6
1.4
1.2
1.0
0.8
0.6
0.4
0.2
0.0
Optical Density
70% Hg
60% Hg
50% Hg
40% Hg
30% Hg
15% Hg
0% Hg
n=1
n=2
n=3
1280
1320
1360
1400
1440
1480
1520
1560
Wavelength (Å)

Fig. 56

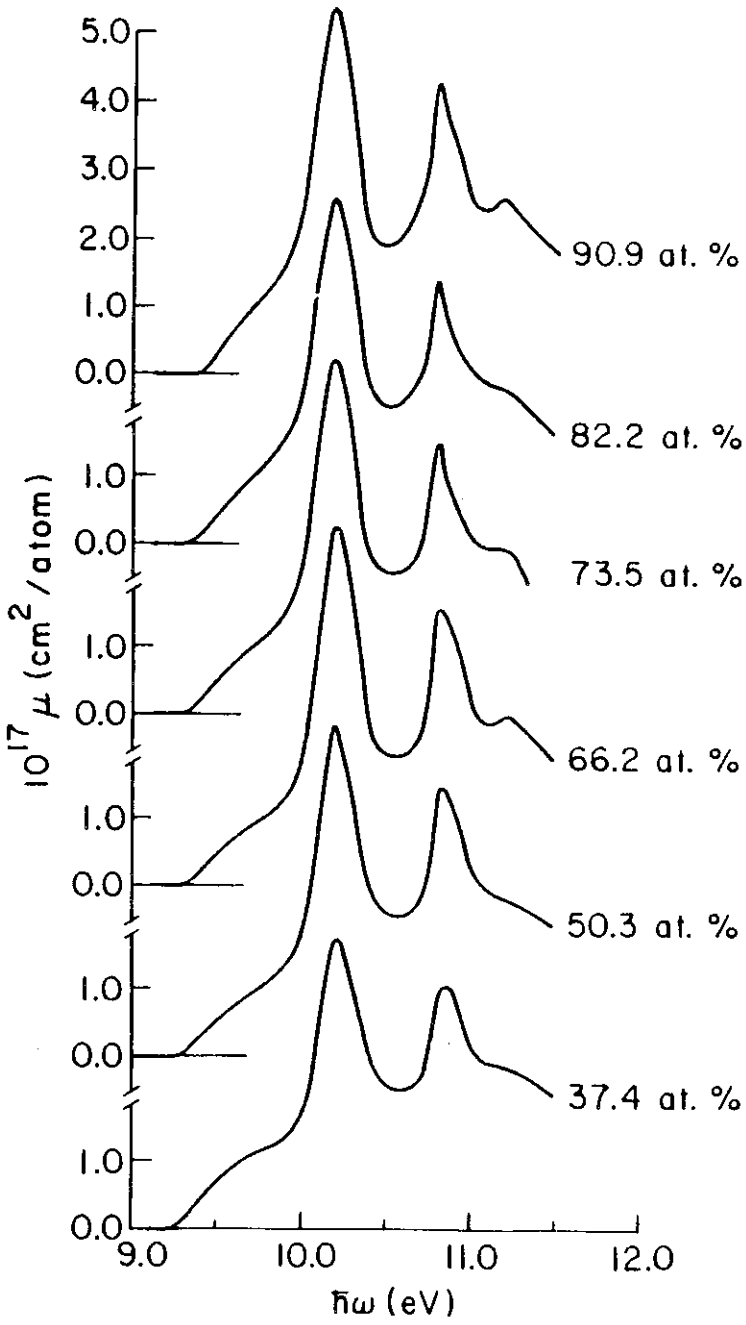
5.0
4.0
3.0
2.0
1.0
0.0
$10^{17}\mu$ (cm^2/atom)
90.9 at. %
82.2 at. %
73.5 at. %
66.2 at. %
50.3 at. %
37.4 at. %
9.0
10.0
11.0
12.0
$\hbar\omega$ (eV)

Fig. 57

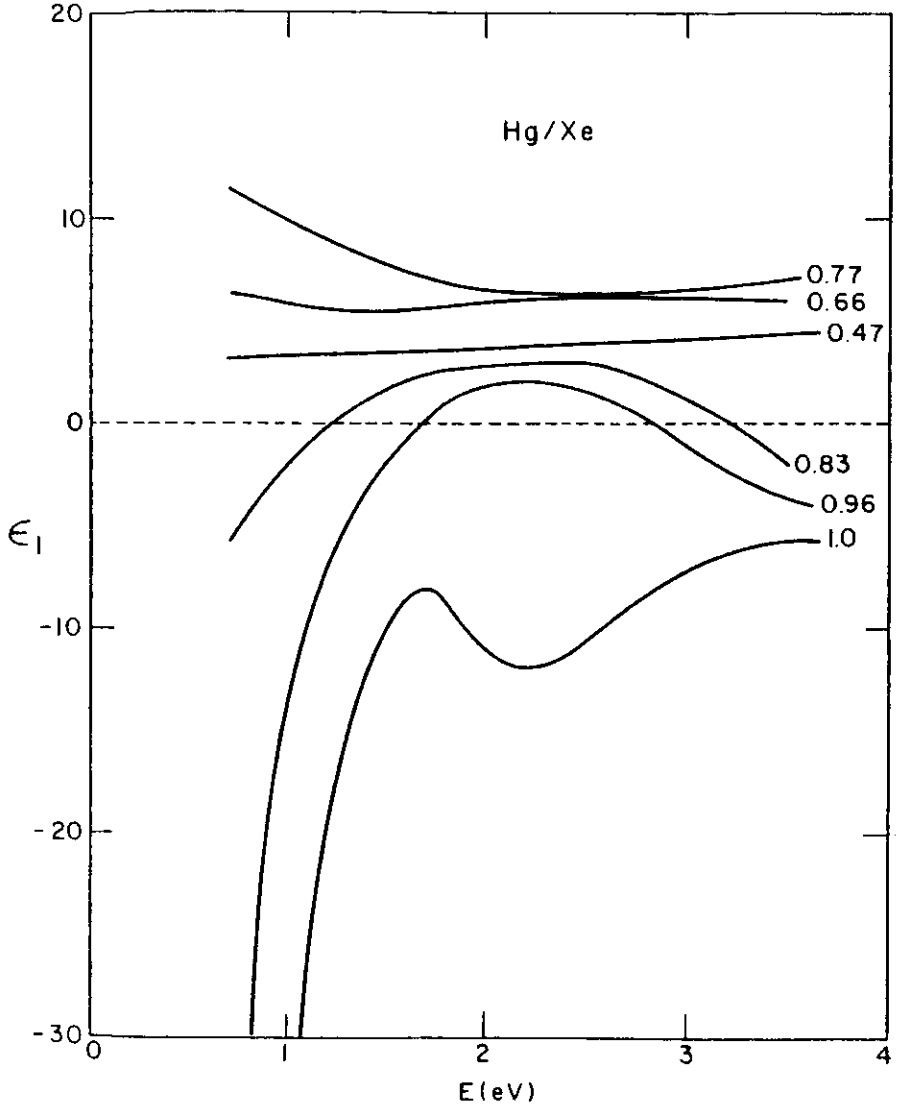
Hg/Xe
0.77
0.66
0.47
0.83
0.96
1.0
ϵ_1
E(eV)

Fig. 58

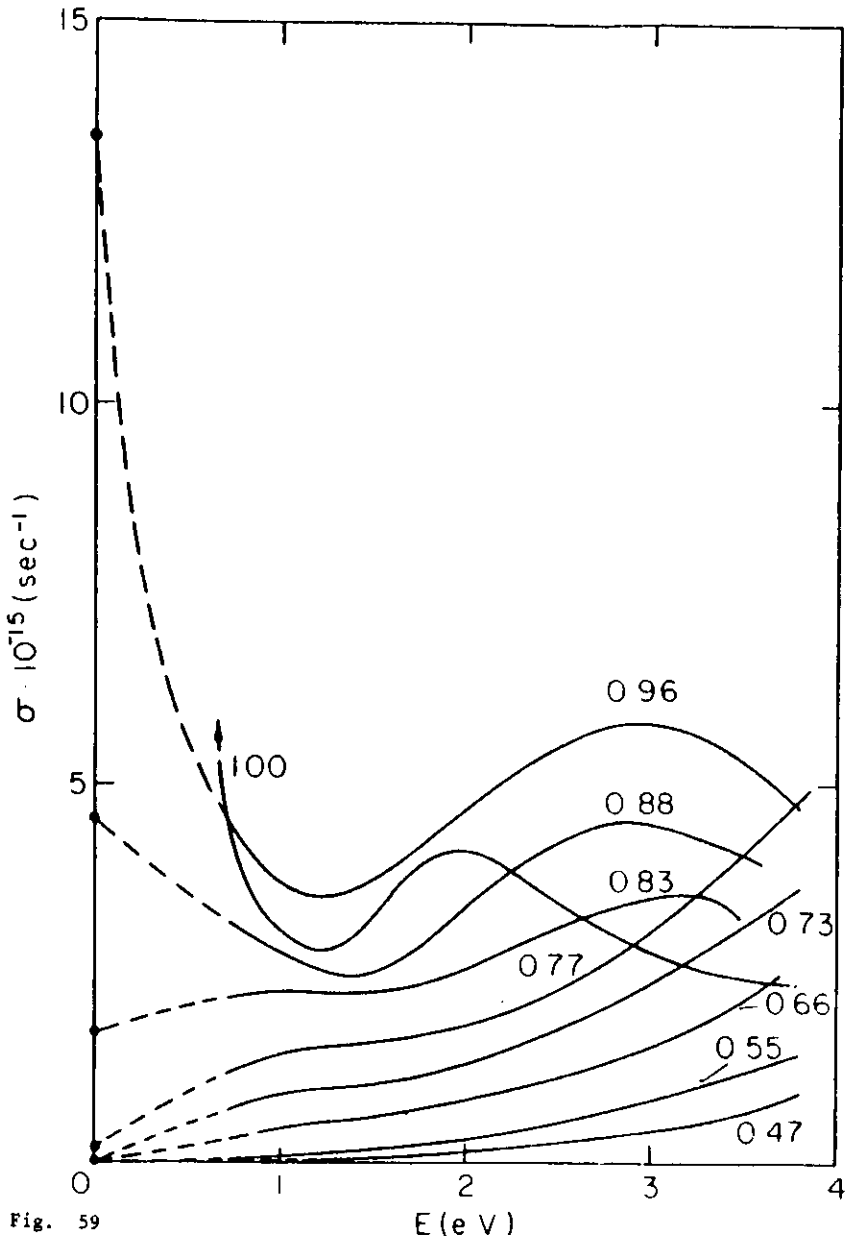
$\sigma \cdot 10^{-15}$ (sec^{-1})
1.00
0.96
0.88
0.83
0.77
0.73
0.66
0.55
0.47
E(eV)

Fig. 59

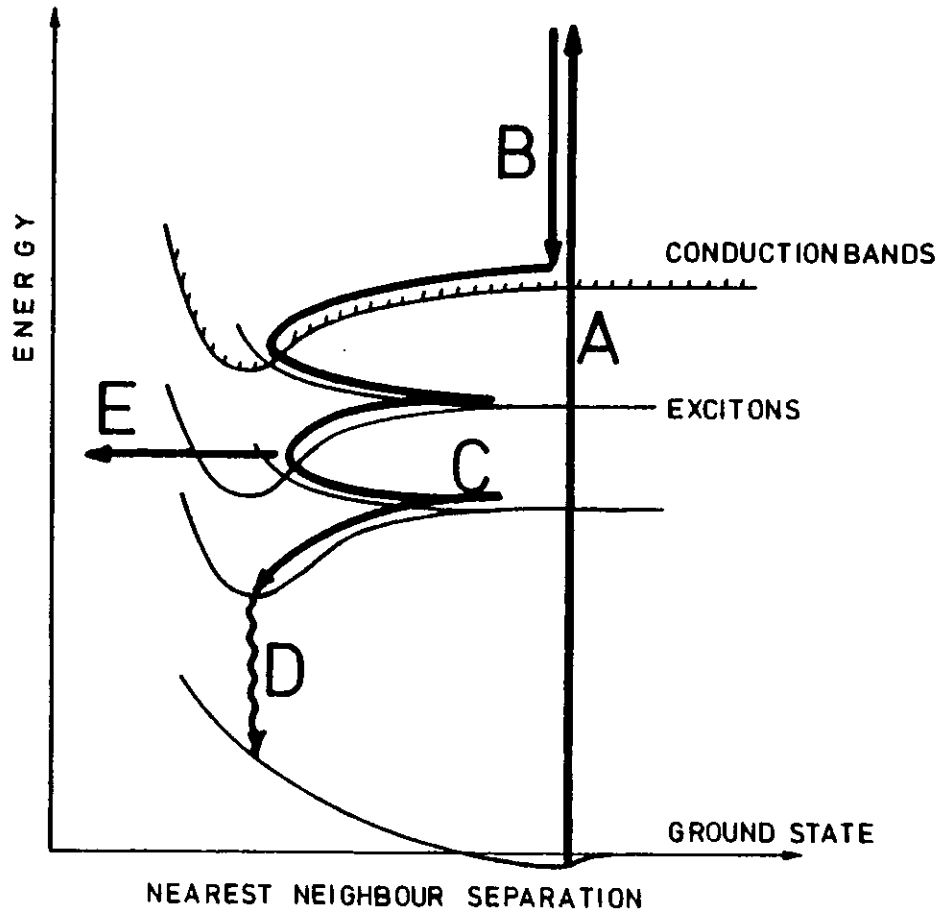
ENERGY
B
A
CONDUCTION BANDS
E
EXCITONS
C
D
GROUND STATE
NEAREST NEIGHBOUR SEPARATION

Fig. 60

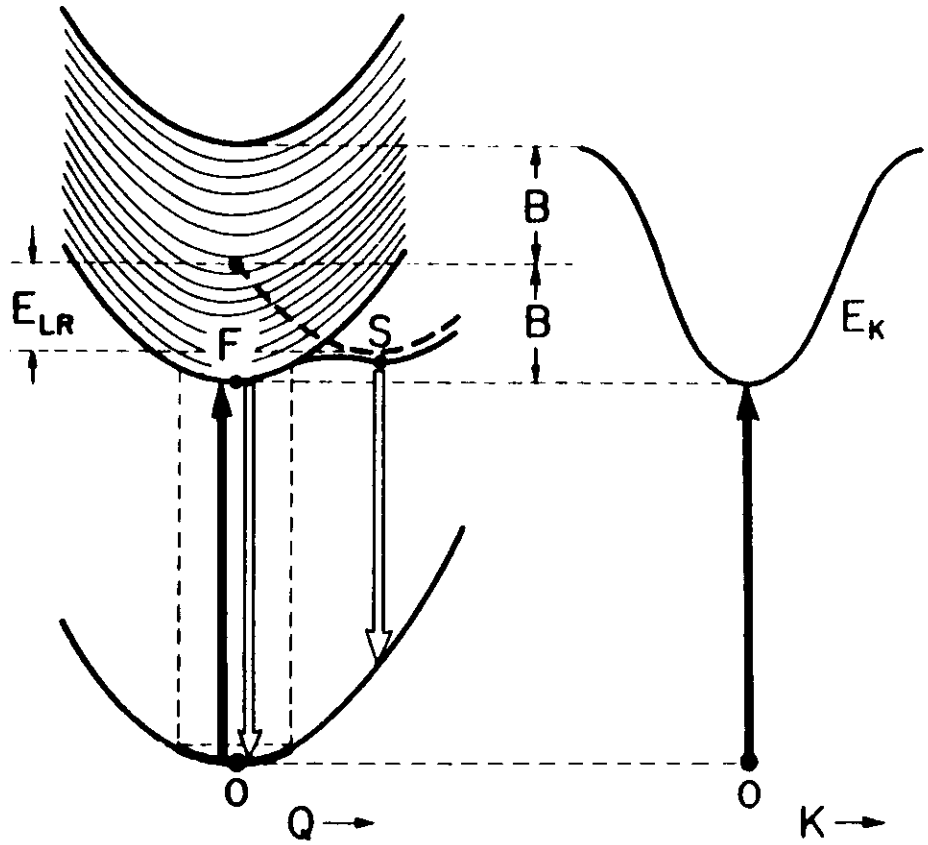
B
B
E_{LR}
F
S
E_K
0
Q
0
K

Fig. 61

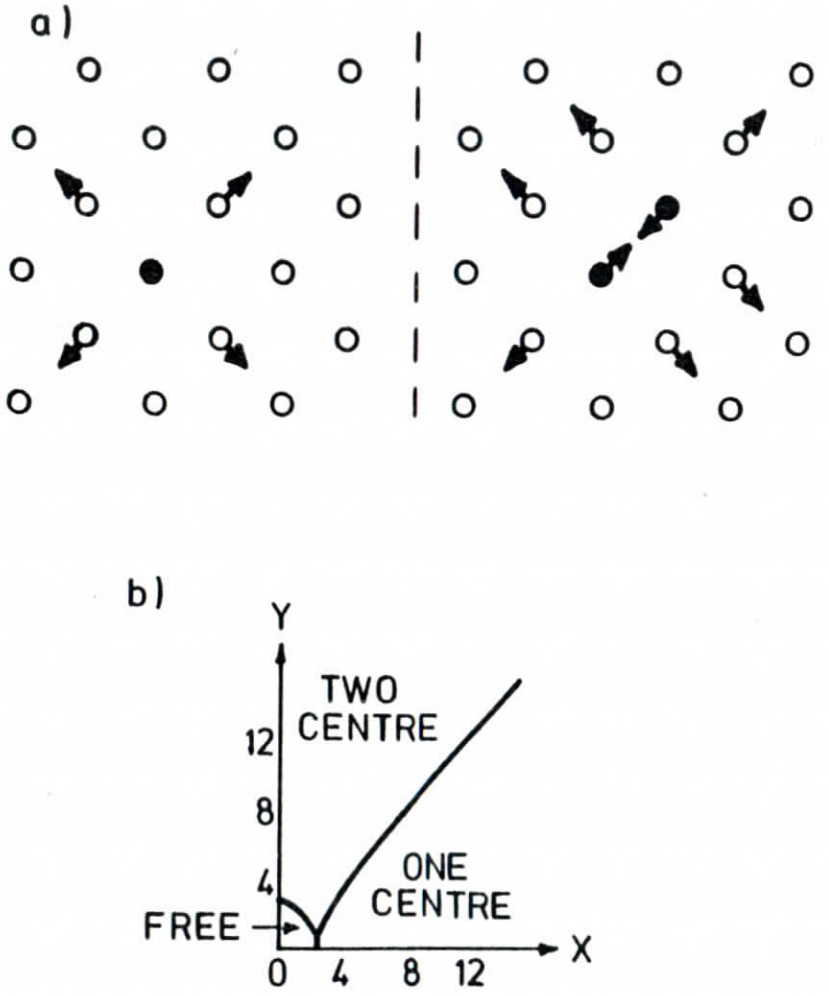
a)
b)
Y
TWO
CENTRE
12
8
4
ONE
CENTRE
FREE
X
0
4
8
12

Fig. 62

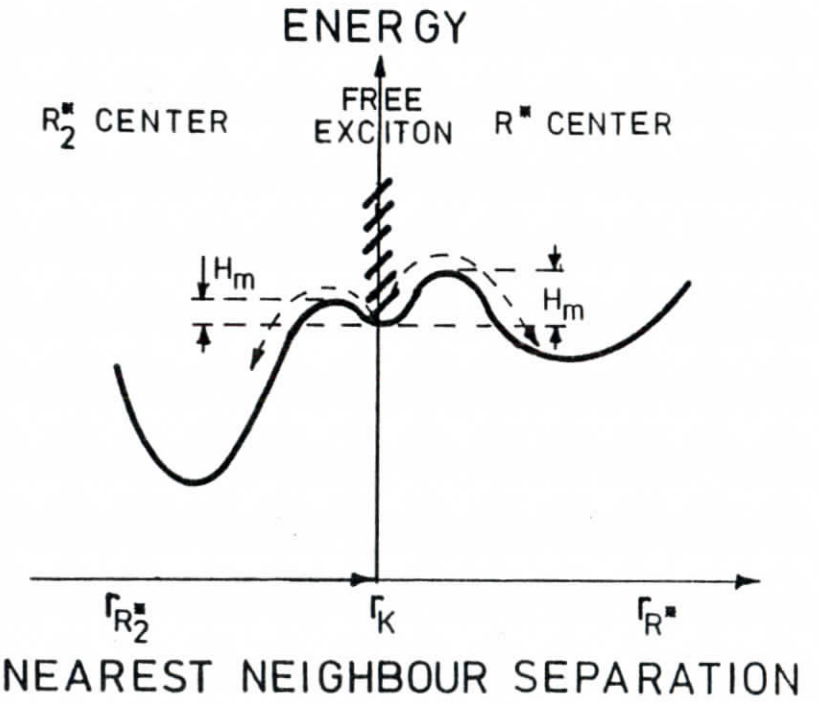
ENERGY
R_2^* CENTER
FREE
EXCITON
R^* CENTER
H_m
H_m
$r_{R_2^*}$
r_K
r_{R^*}
NEAREST NEIGHBOUR SEPARATION

Fig. 63

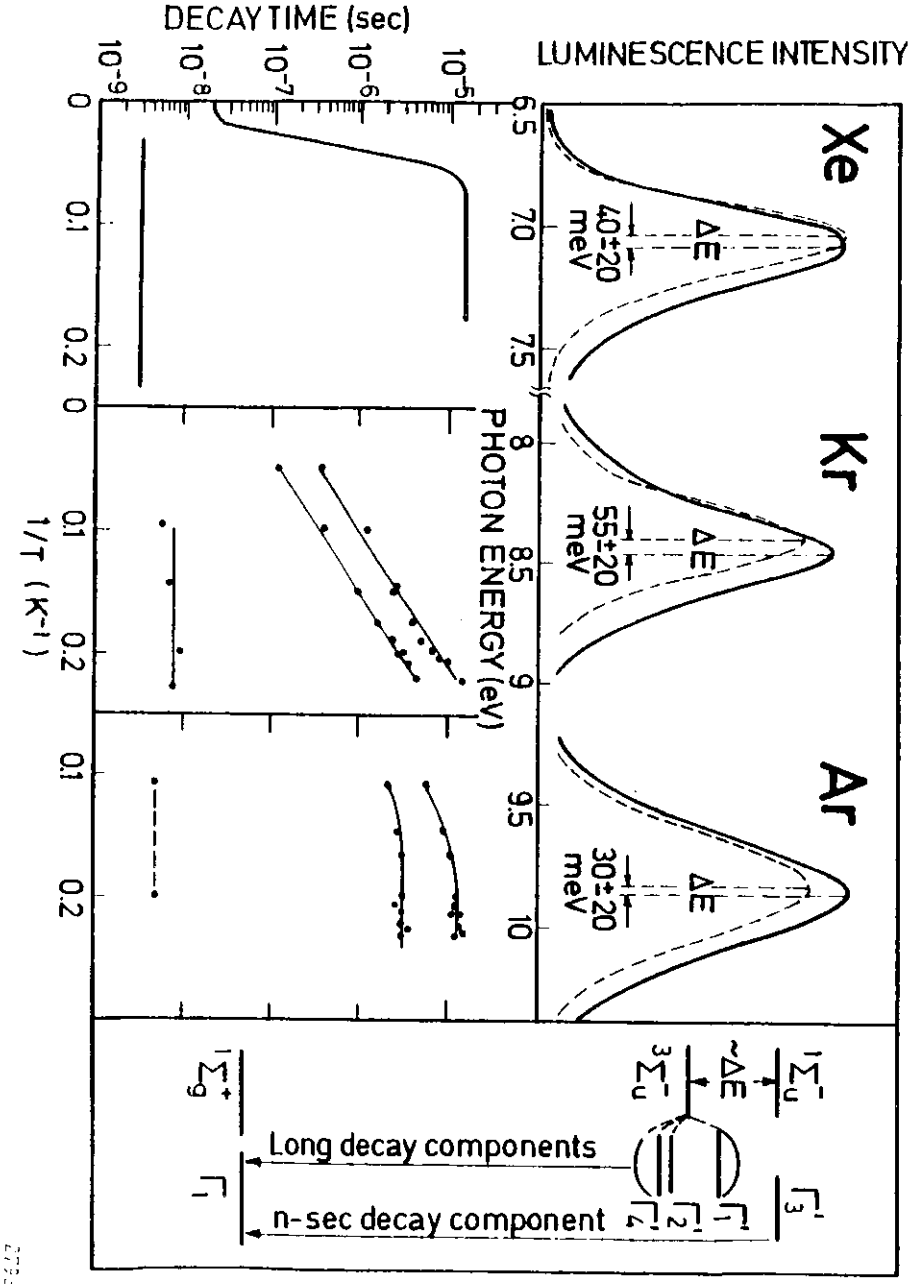
DECAY TIME (sec)
LUMINESCENCE INTENSITY
Xe
Kr
Ar
ΔE
40±20 meV
55±20 meV
30±20 meV
PHOTON ENERGY (eV)
1/T (K⁻¹)
Long decay components
n-sec decay component

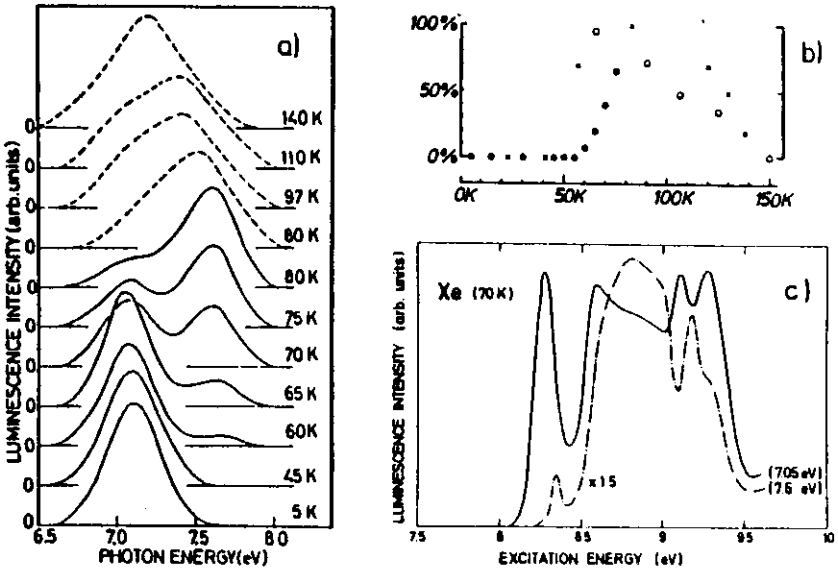
a)
b)
c)
LUMINESCENCE INTENSITY (arb.units)
PHOTON ENERGY(eV)
140 K
110 K
97 K
80 K
80 K
75 K
70 K
65 K
60K
45 K
5 K
100%
50%
0%
0K
50K
100K
150K
Xe (70 K)
x15
(7.05 eV)
(7.6 eV)
EXCITATION ENERGY (eV)

Fig. 65

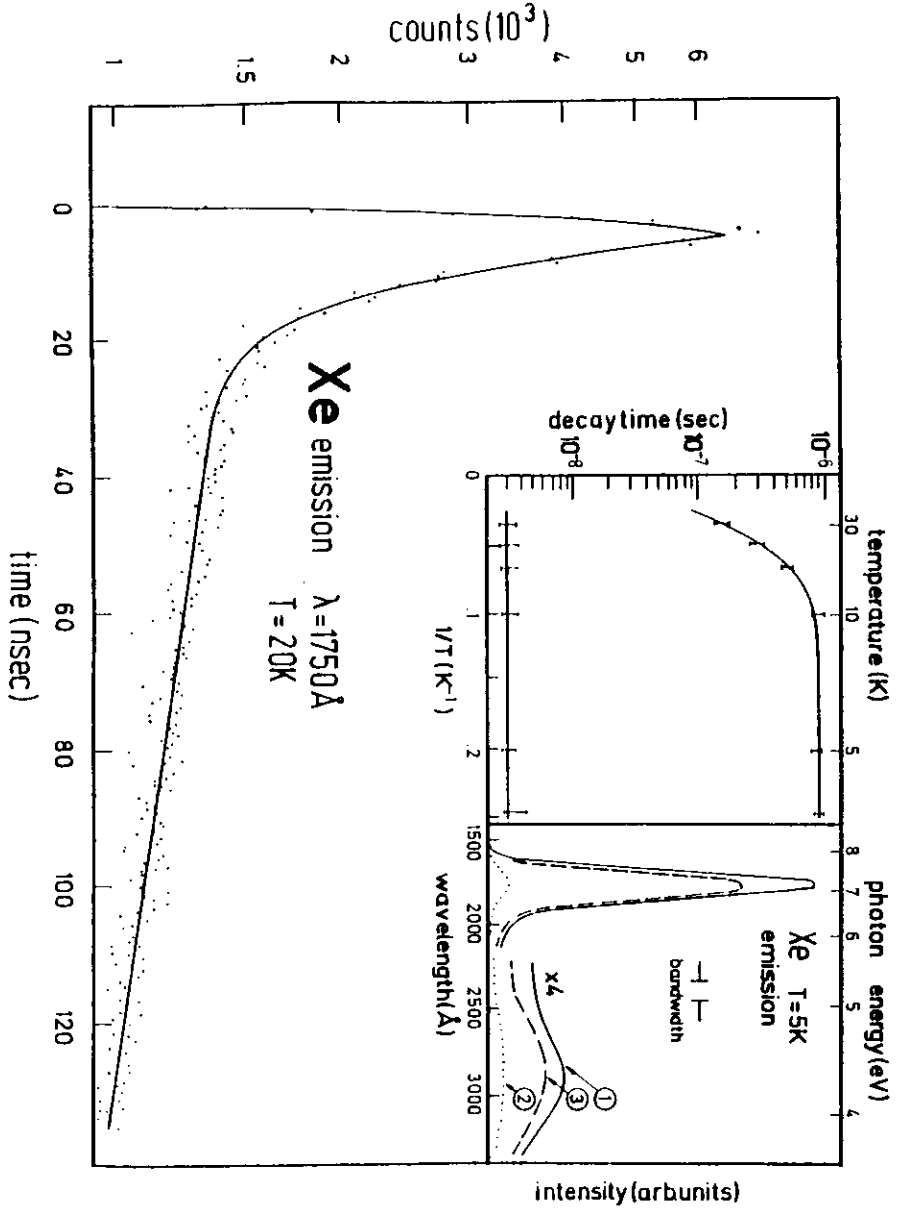
counts(10^3)
Xe emission λ=1750Å
T = 20K
time (nsec)
decay time (sec)
1/T (K^-1)
temperature (K)
Xe T=5K emission
bandwidth
x4
wavelength(Å)
photon energy(eV)
intensity(arbunits)

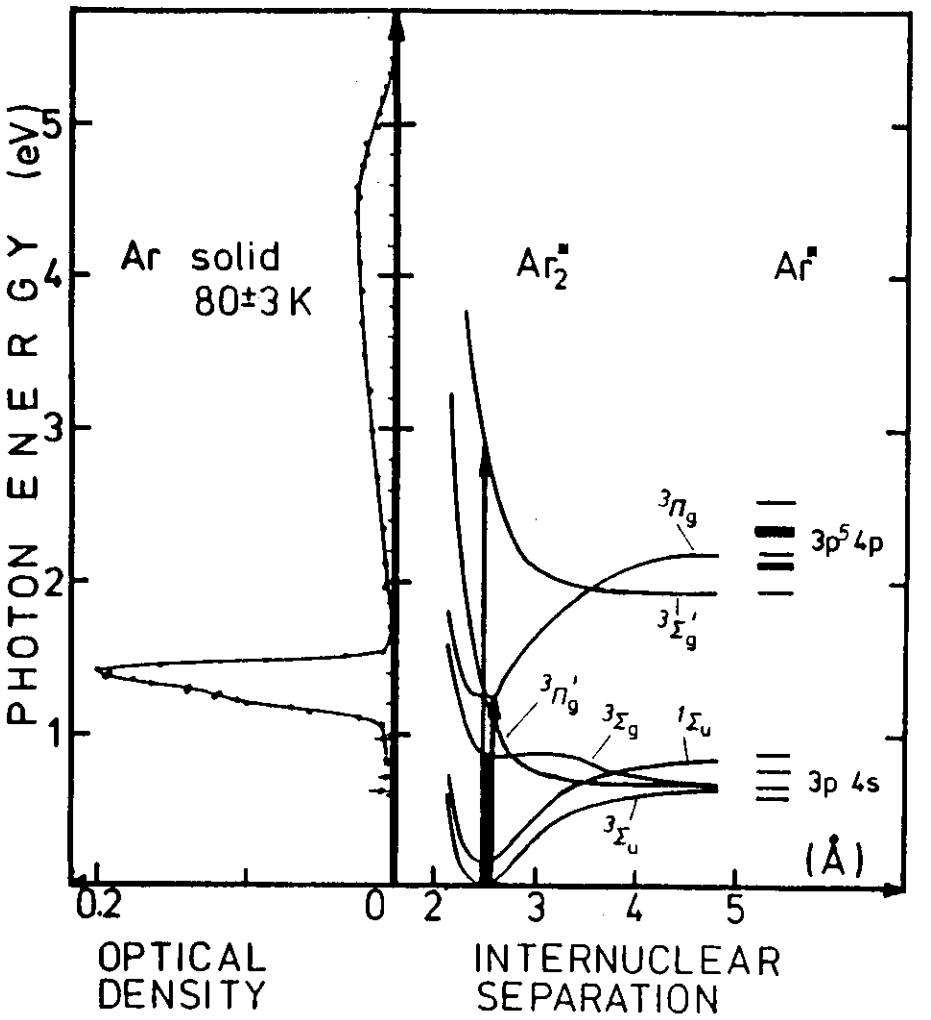
PHOTON ENERGY (eV)
Ar solid
80±3 K
Ar2*
Ar*
3Πg
3p5 4p
3Σg'
3Πg'
3Σg
1Σu
3p 4s
3Σu
(Å)
OPTICAL DENSITY
INTERNUCLEAR SEPARATION

Fig. 67

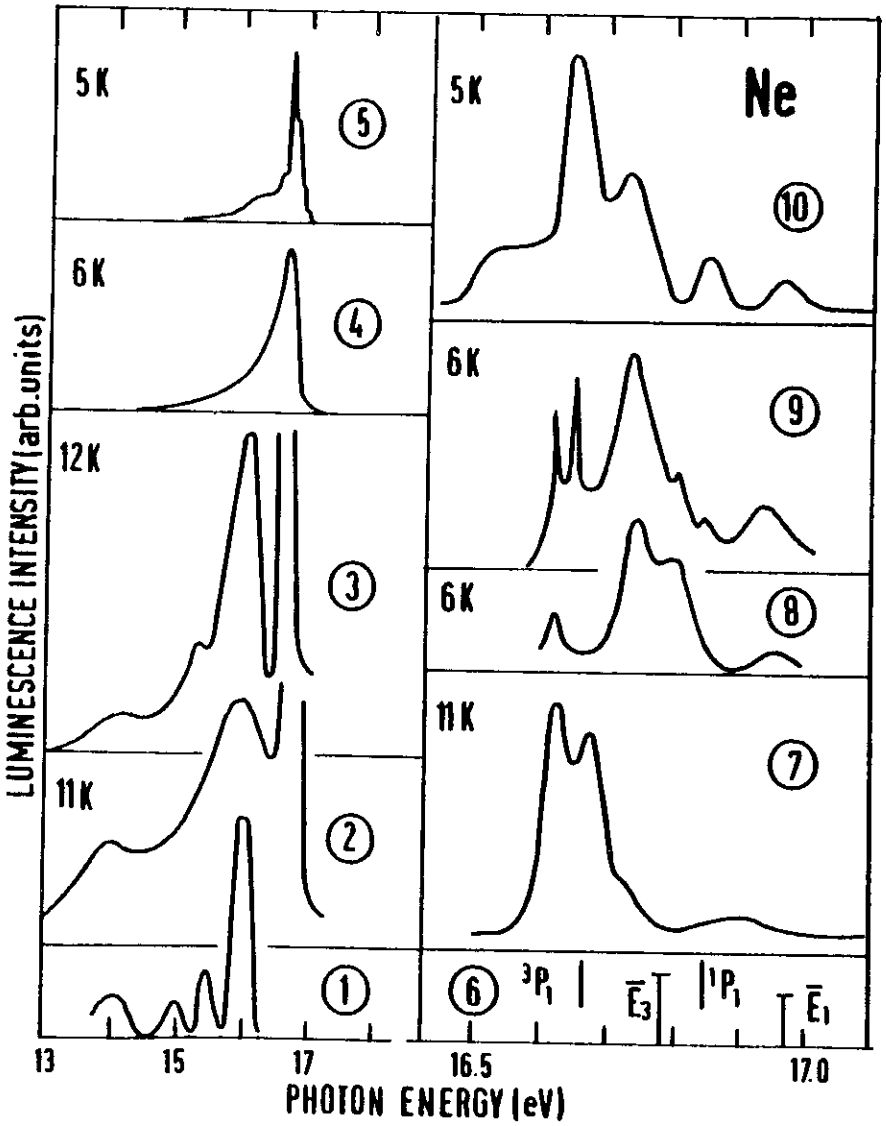
LUMINESCENCE INTENSITY (arb.units)
5K
6K
12K
11K
5K
Ne
6K
6K
11K
⑤
④
③
②
①
⑩
⑨
⑧
⑦
⑥
$^3P_1$
$\bar{E}_3$
$^1P_1$
$\bar{E}_1$
13
15
17
16.5
17.0
PHOTON ENERGY (eV)

Fig. 68

Fig. 69

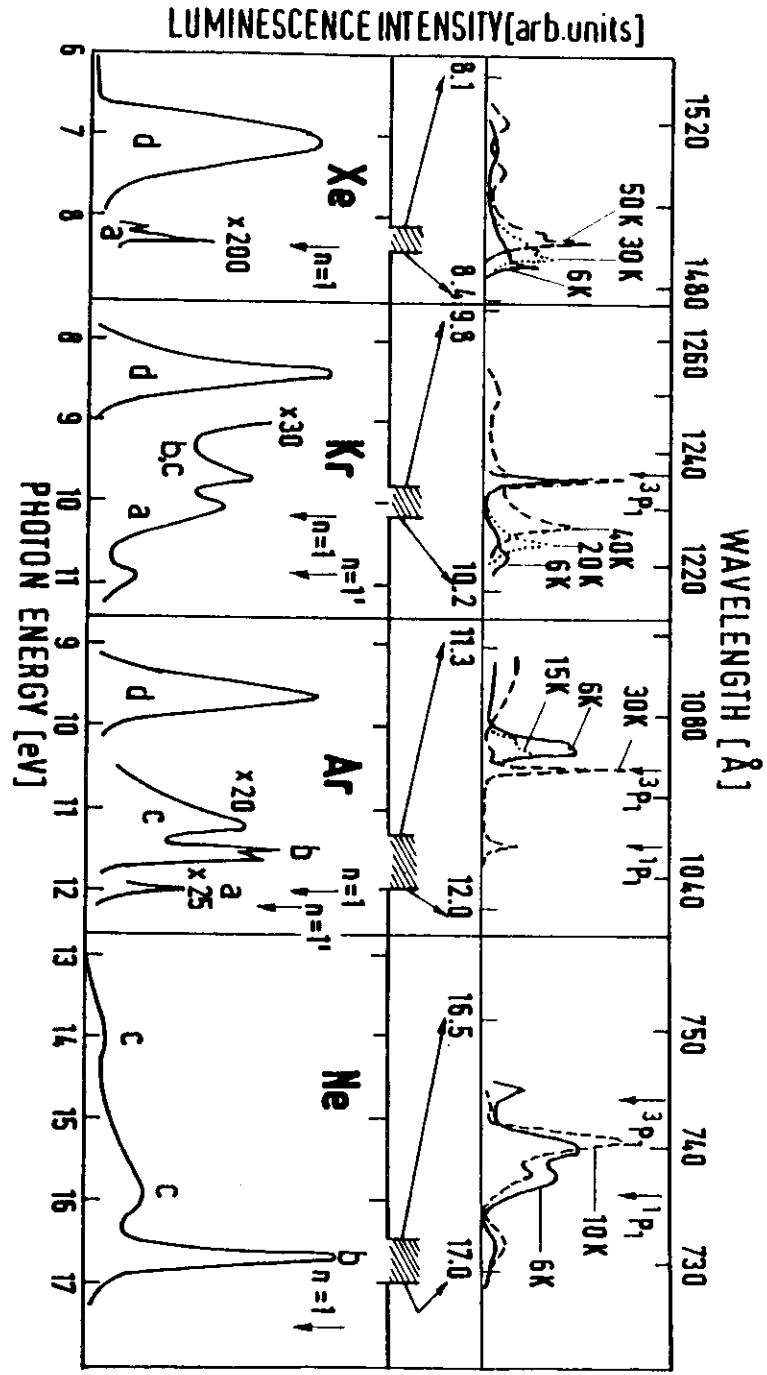
LUMINESCENCE INTENSITY (arb.units)
WAVELENGTH (Å)
PHOTON ENERGY (eV)
Xe
Kr
Ar
Ne
n=1
n=1'
n=1''
x200
x30
x20
x25
a
b
c
d
8.1
8.4
9.8
10.2
11.3
12.0
16.5
17.0
50K 30K 6K
40K 20K 6K
30K 15K 6K
10K 6K
$^3P_1$
$^1P_1$

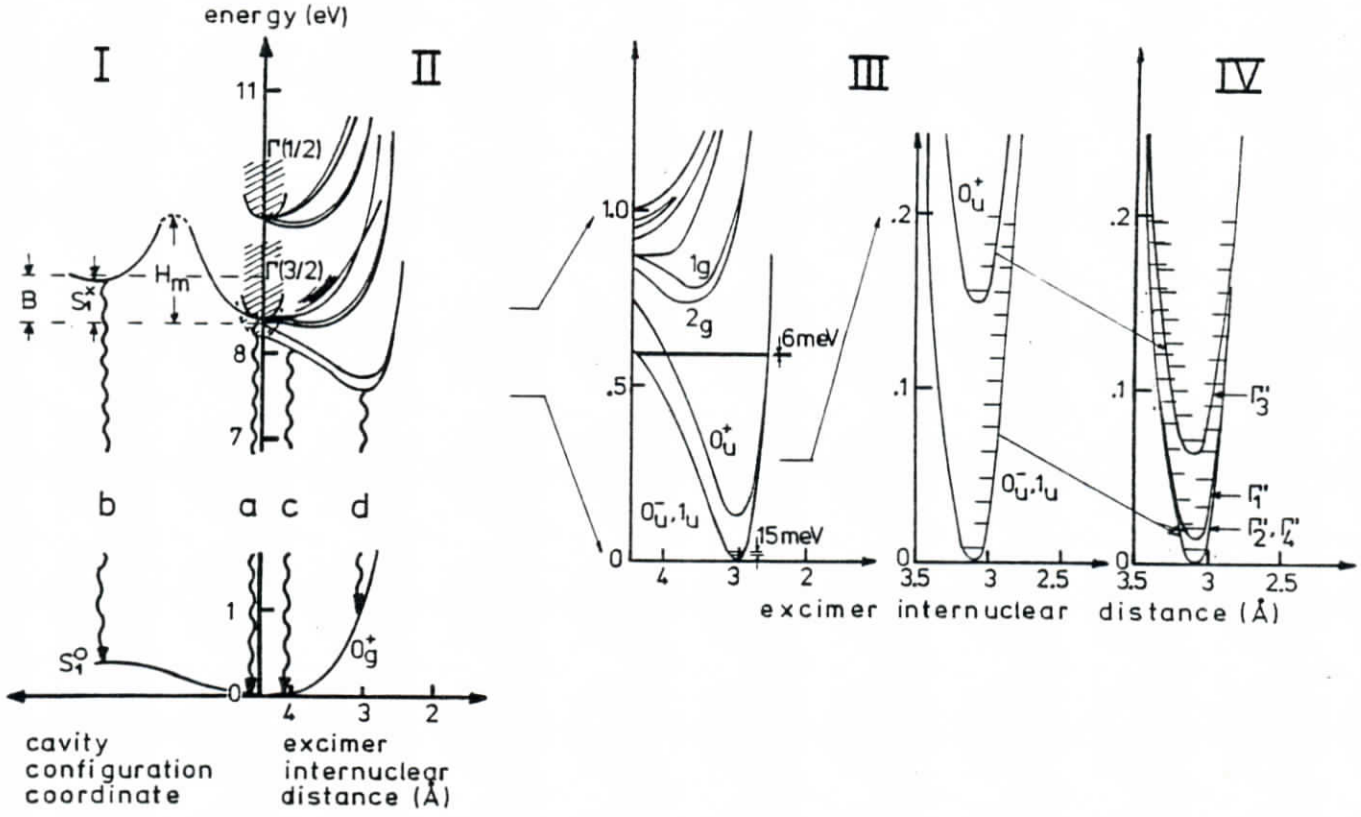
energy (eV)
I
II
III
IV
11
8
7
Γ(1/2)
Γ(3/2)
B
S_x
H_m
b
a
c
d
S_1^0
0_g^+
1
0
4
3
2
cavity configuration coordinate
excimer internuclear distance (Å)
1.0
.5
0
1g
2_g
6meV
0_u^+
$0_u^-,1_u$
15meV
.2
.1
3.5
2.5
excimer internuclear distance (Å)
Π_3
Π_1
Π_2,Π_4

Fig. 71

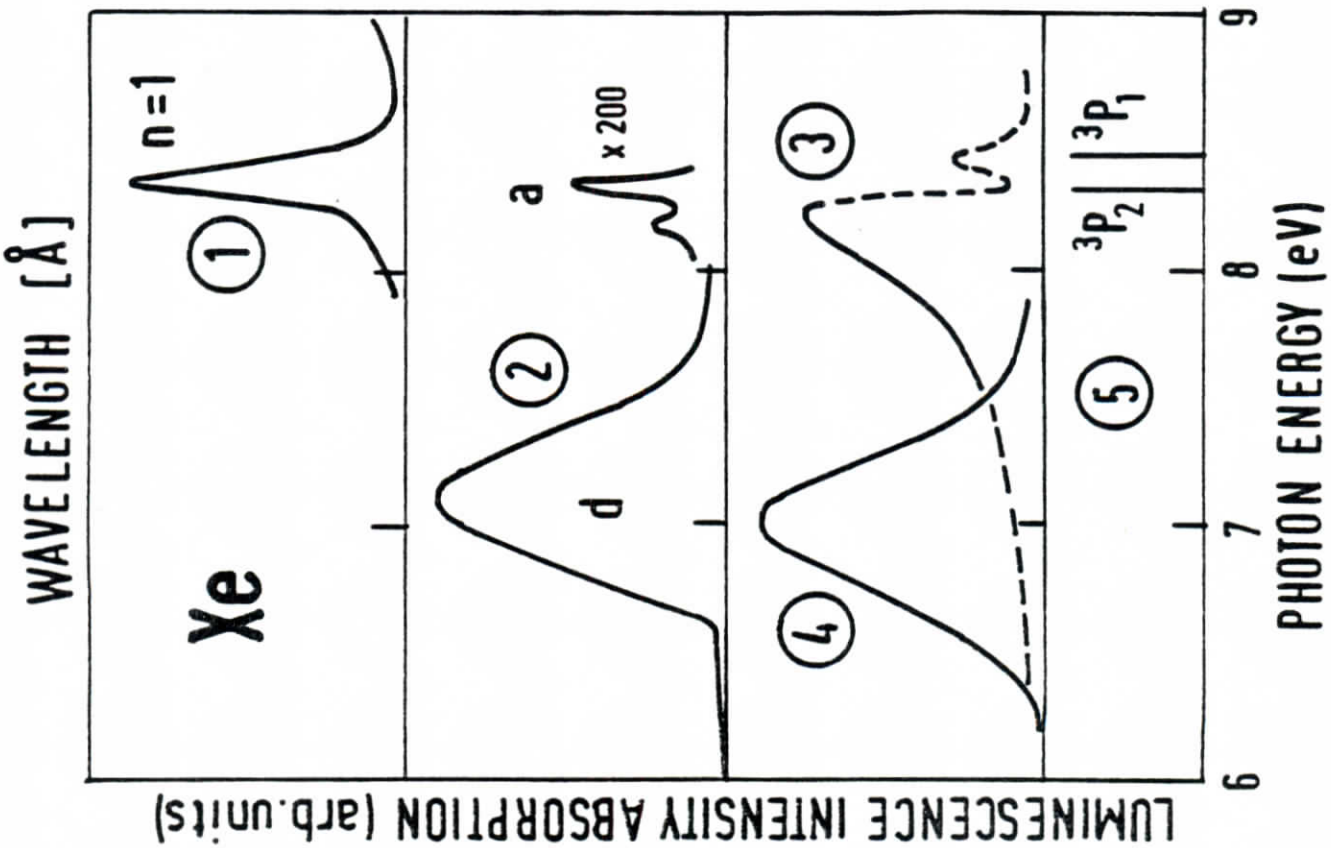
WAVELENGTH [Å]
Xe
n=1
x 200
a
d
$^3P_2$
$^3P_1$
1
2
3
4
5
6
7
8
9
PHOTON ENERGY (eV)
LUMINESCENCE INTENSITY ABSORPTION (arb.units)

Fig. 70

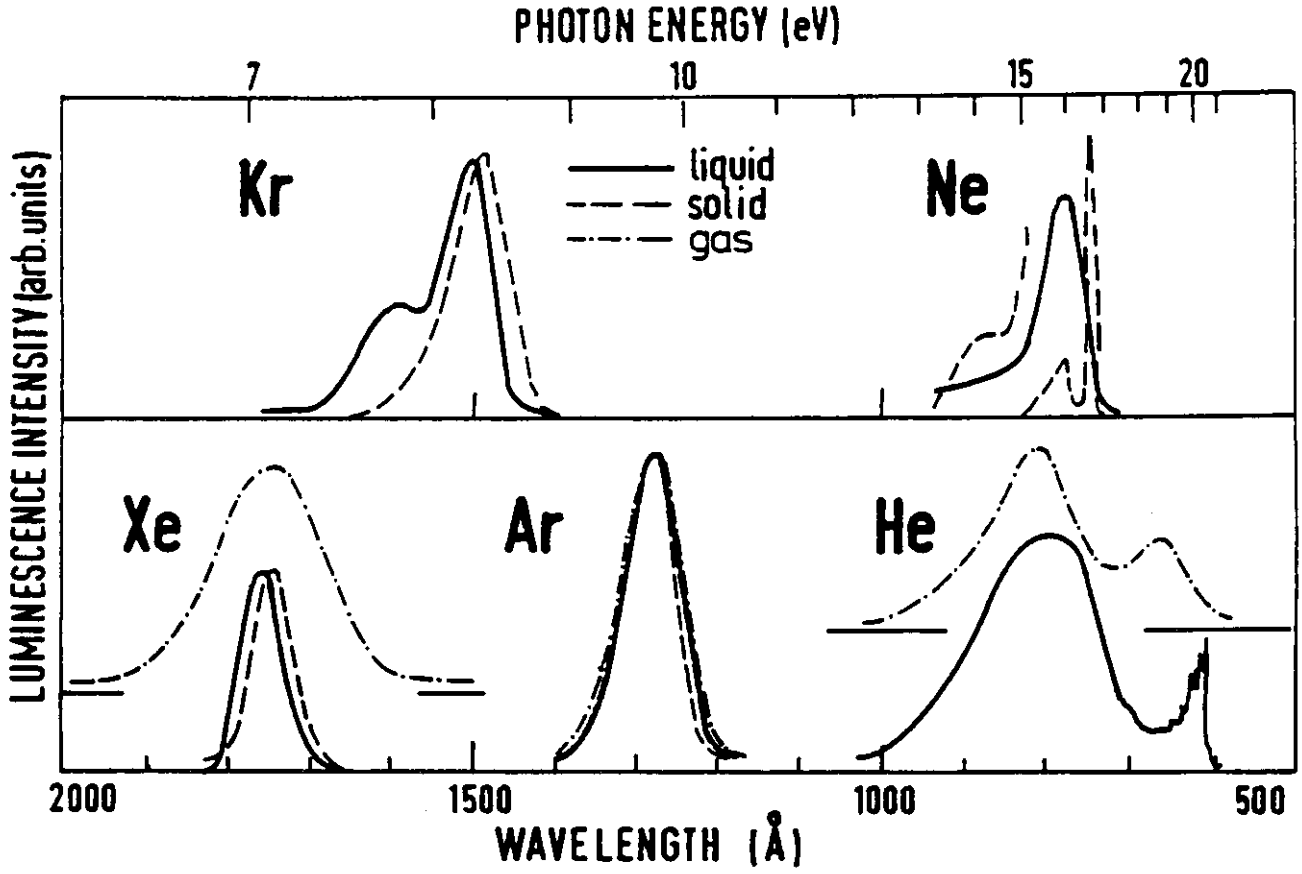
PHOTON ENERGY (eV)
7
10
15
20
Kr
liquid
solid
gas
Ne
Xe
Ar
He
LUMINESCENCE INTENSITY (arb.units)
2000
1500
1000
500
WAVELENGTH (Å)

Fig. 73

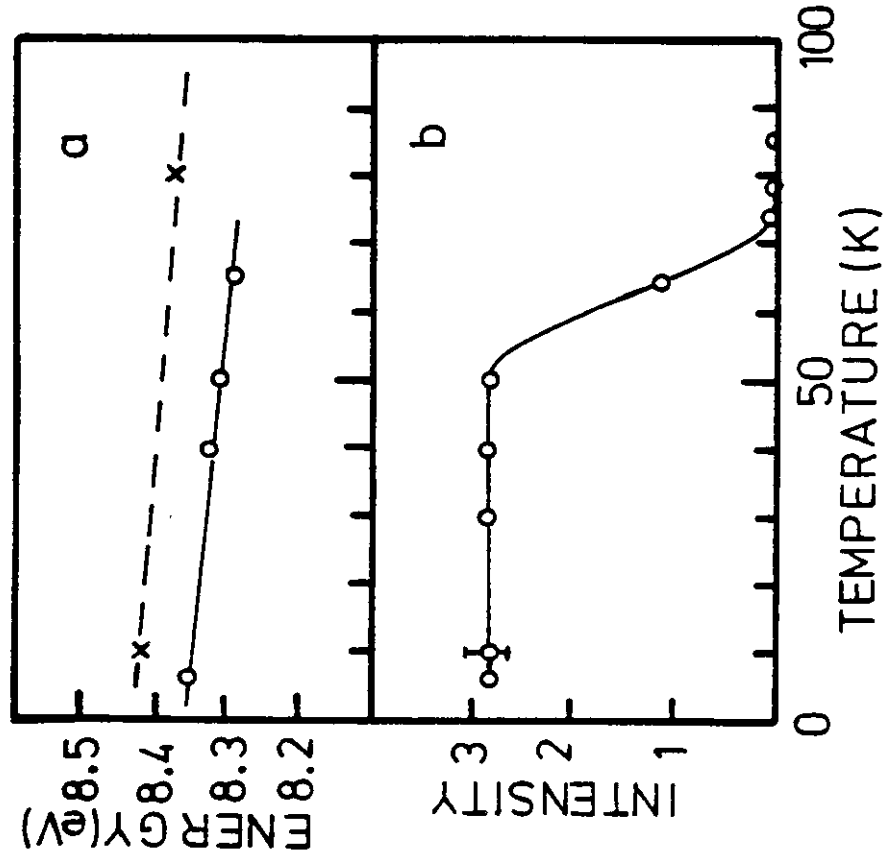
a
b
ENERGY (eV)
8.5
8.4
8.3
8.2
INTENSITY
3
2
1
0
50
100
TEMPERATURE (K)

Fig. 72

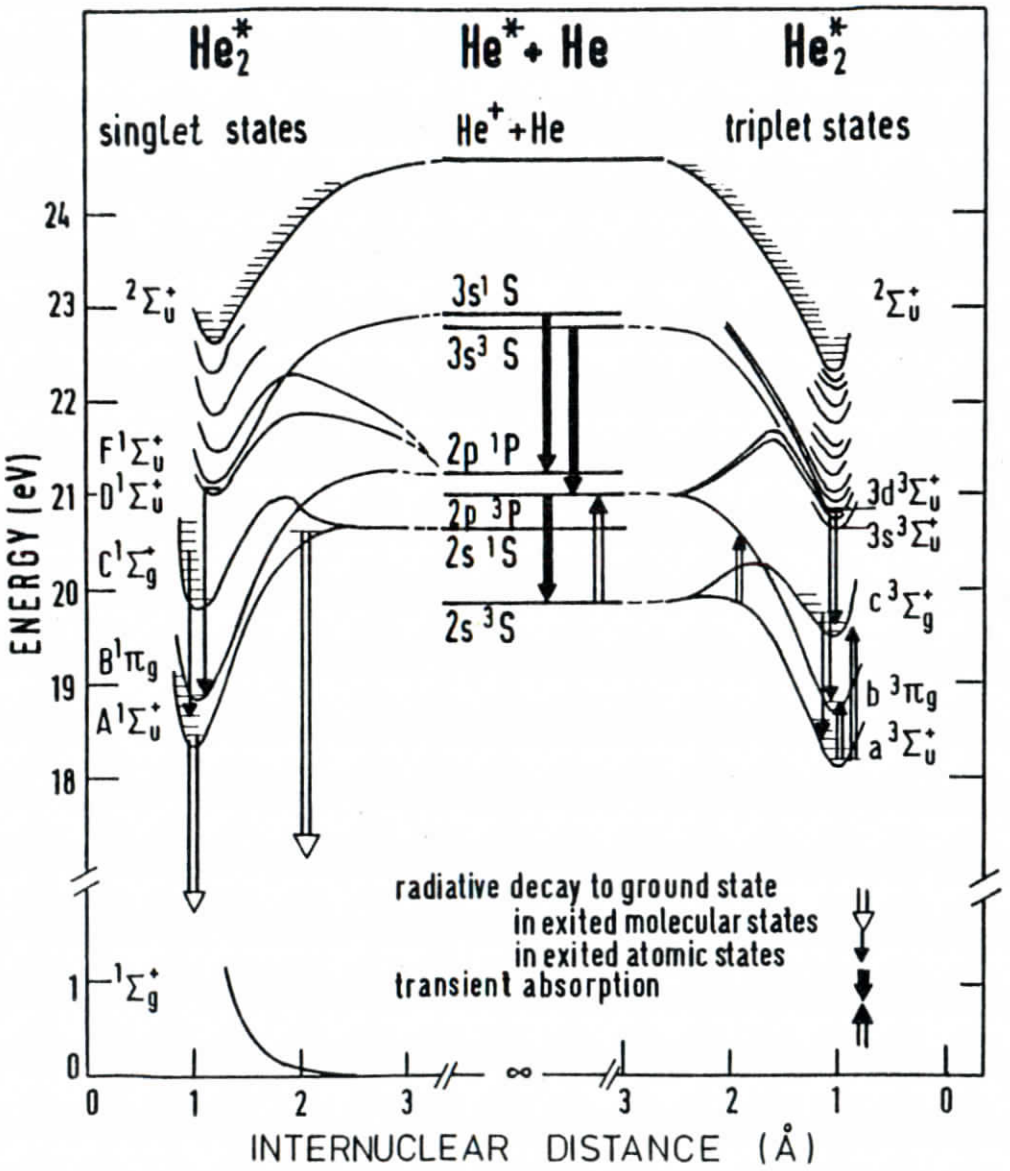
He*2
He* + He
He*2
singlet states
He+ + He
triplet states
ENERGY (eV)
24
23
22
21
20
19
18
1
0
2Σ+u
F1Σ+u
D1Σ+u
C1Σ+g
B1πg
A1Σ+u
1Σ+g
3s1 S
3s3 S
2p 1P
2p 3P
2s 1S
2s 3S
2Σ+u
3d3Σ+u
3s3Σ+u
c3Σ+g
b3πg
a3Σ+u
radiative decay to ground state
in exited molecular states
in exited atomic states
transient absorption
0 1 2 3 ∞ 3 2 1 0
INTERNUCLEAR DISTANCE (Å)

Fig. 74

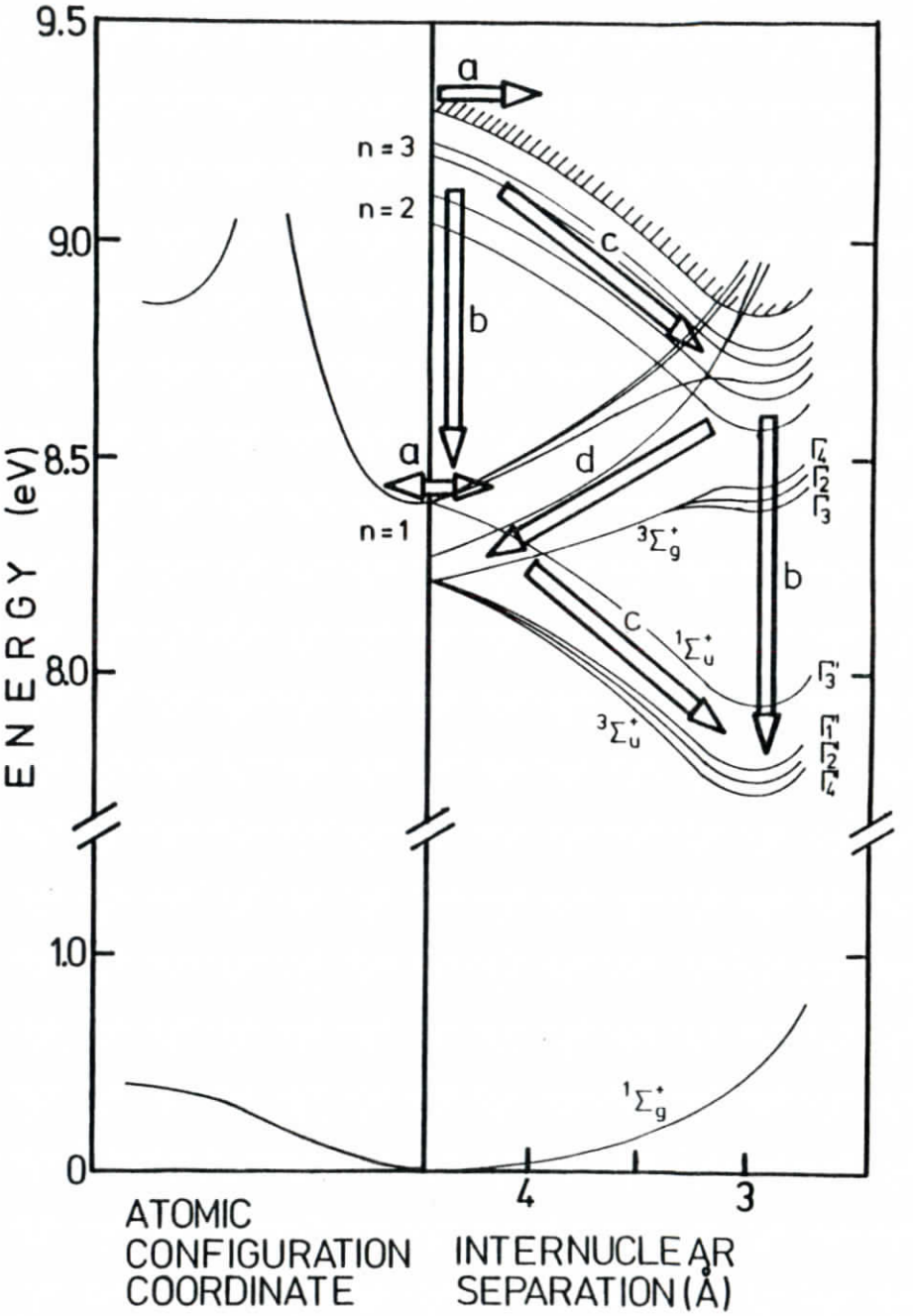
9.5
9.0
8.5
8.0
1.0
0
ENERGY (eV)
n = 3
n = 2
n = 1
a
b
c
d
a
b
c
3Σ+g
1Σ+u
3Σ+u
1Σ+g
4 3
ATOMIC CONFIGURATION COORDINATE
INTERNUCLEAR SEPARATION (Å)

Fig. 75

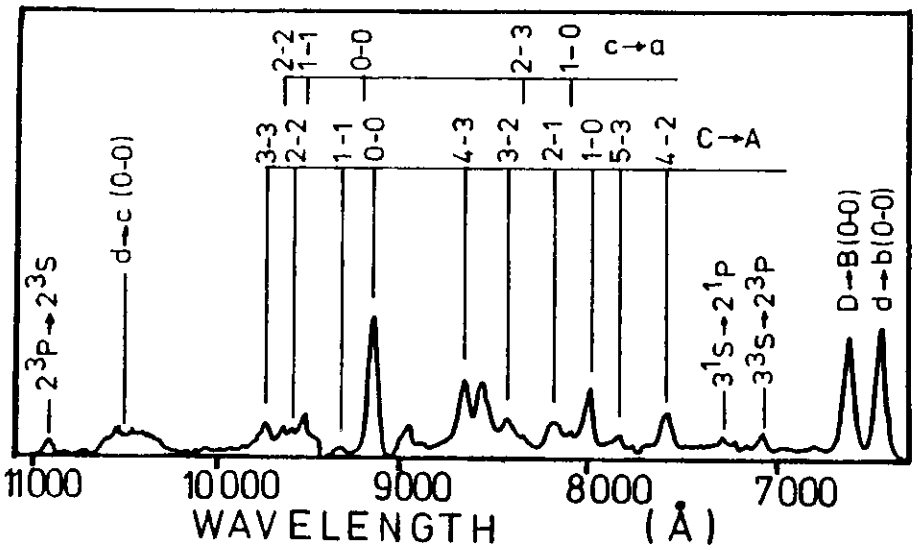
2-2
1-1
0-0
2-3
1-0
c→a
3-3
2-2
1-1
0-0
4-3
3-2
2-1
1-0
5-3
4-2
C→A
$2^3P \rightarrow 2^3S$
d→c (0-0)
$3^1S \rightarrow 2^1P$
$3^3S \rightarrow 2^3P$
D→B(0-0)
d→b(0-0)
11000
10000
9000
8000
7000
WAVELENGTH (Å)

Fig. 76

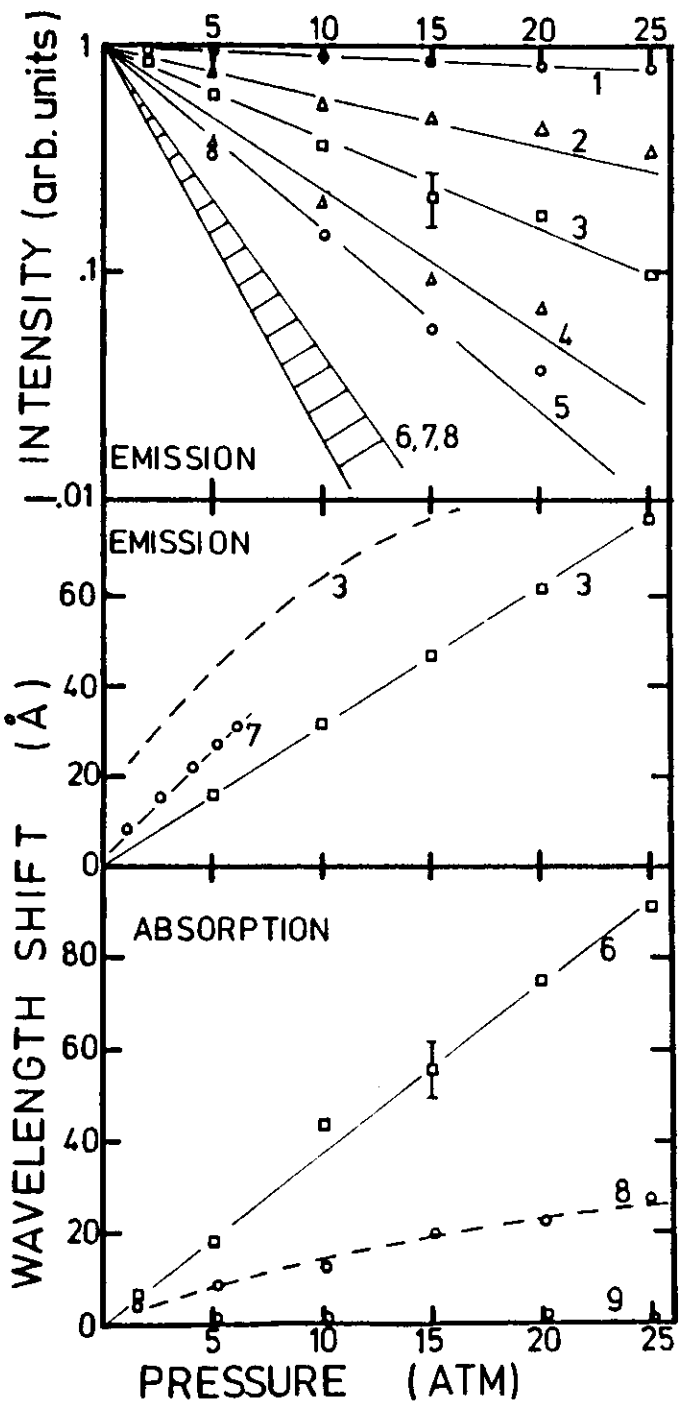
INTENSITY (arb.units)
1
.1
.01
5
10
15
20
25
EMISSION
1
2
3
4
5
6,7,8
EMISSION
3
3
7
WAVELENGTH SHIFT (Å)
60
40
20
0
ABSORPTION
6
8
9
80
60
40
20
0
PRESSURE (ATM)

Fig. 77

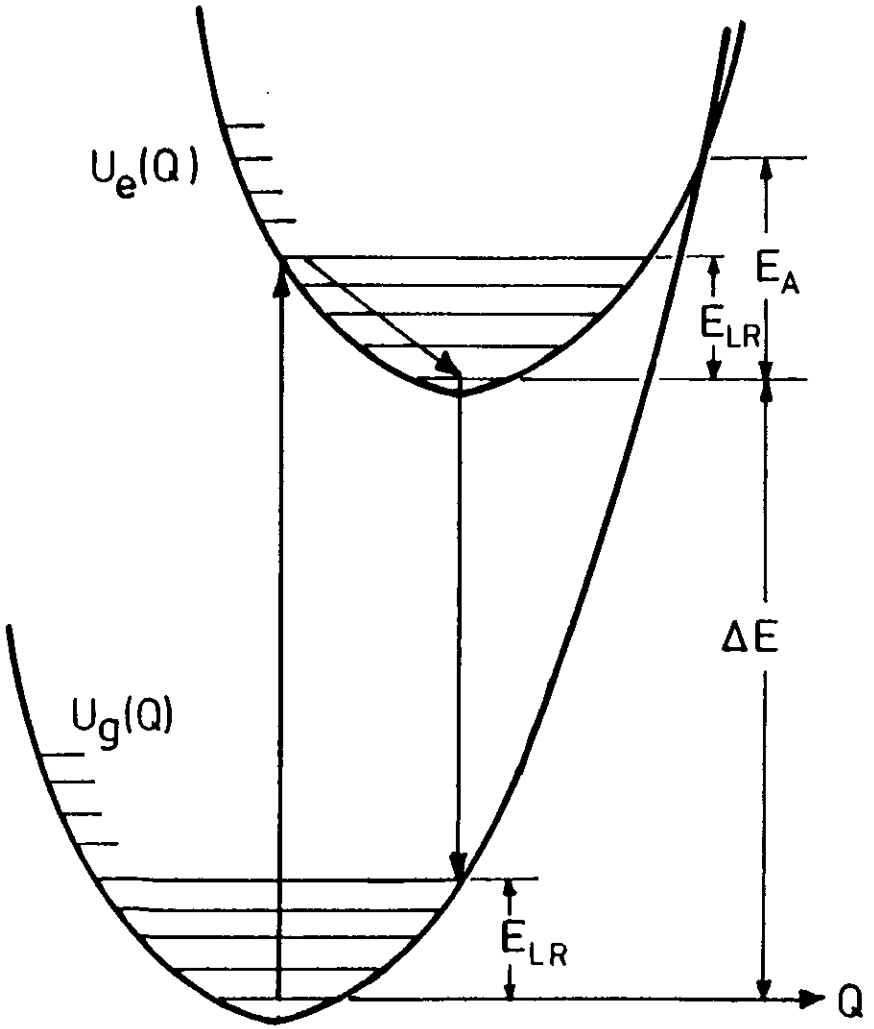
$U_e(Q)$
E_A
E_{LR}
ΔE
$U_g(Q)$
E_{LR}
Q

Fig. 78

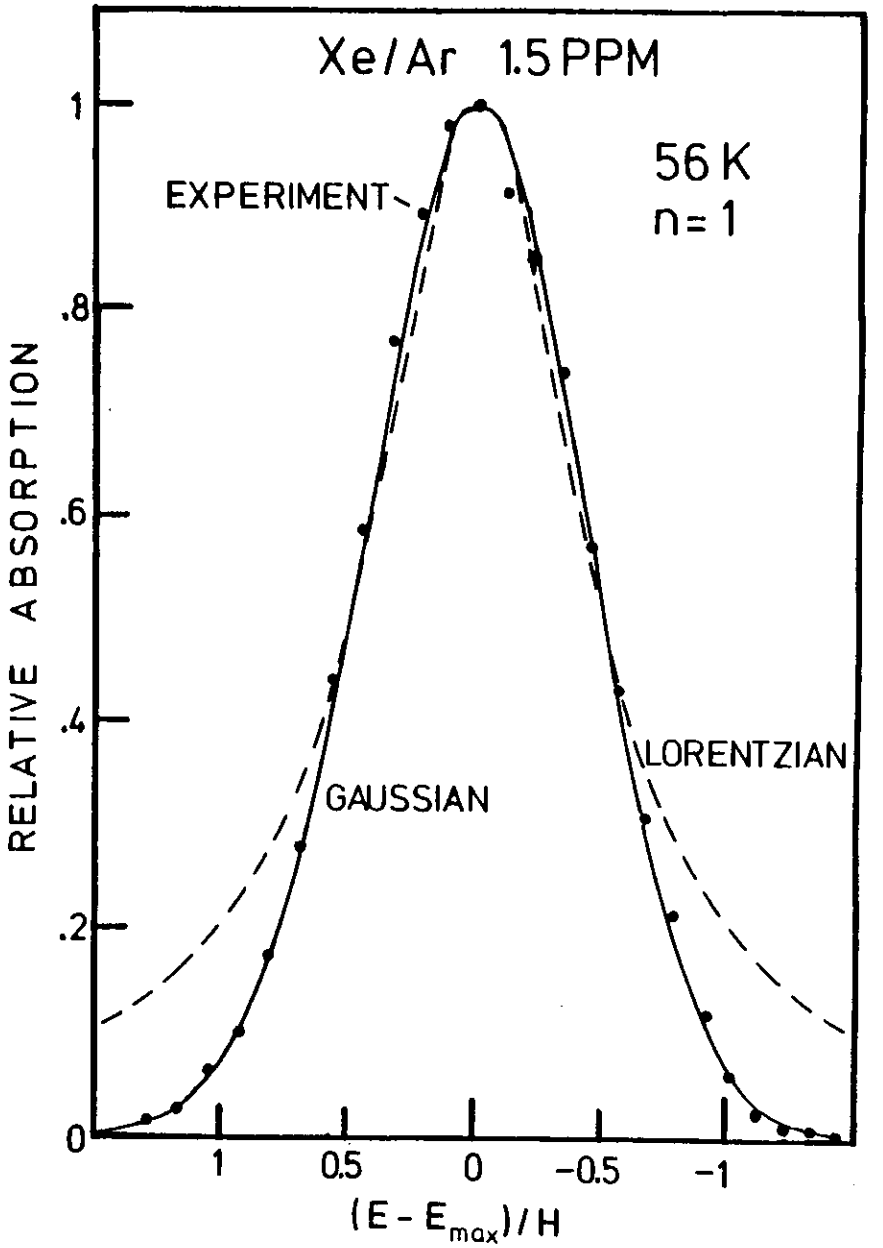
Xe/Ar 1.5 PPM
56 K
n = 1
EXPERIMENT
GAUSSIAN
LORENTZIAN
RELATIVE ABSORPTION
1
.8
.6
.4
.2
0
1
0.5
0
-0.5
-1
$(E - E_{max})/H$

Fig. 79

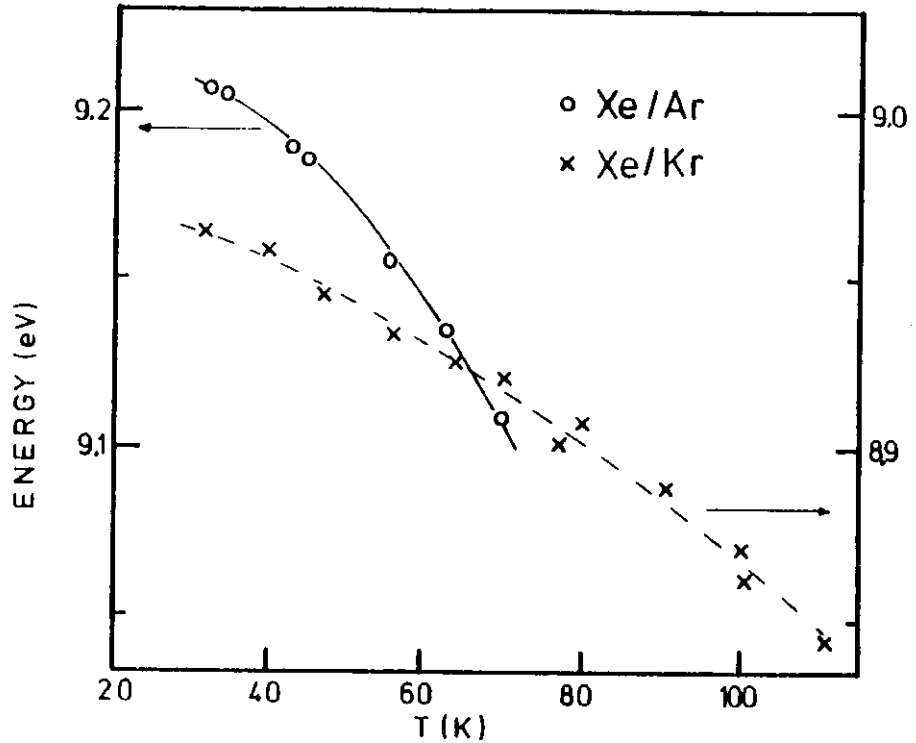
o Xe / Ar
× Xe / Kr
9.2
9.1
9.0
8.9
ENERGY (eV)
20
40
60
80
100
T (K)

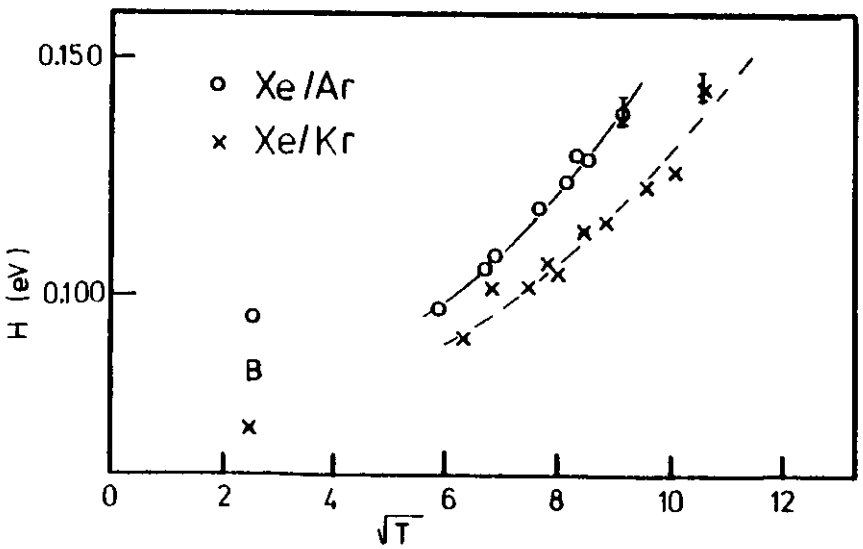
o Xe / Ar
× Xe / Kr
0.150
0.100
H (eV)
B
0
2
4
6
8
10
12
√T

Fig. 80

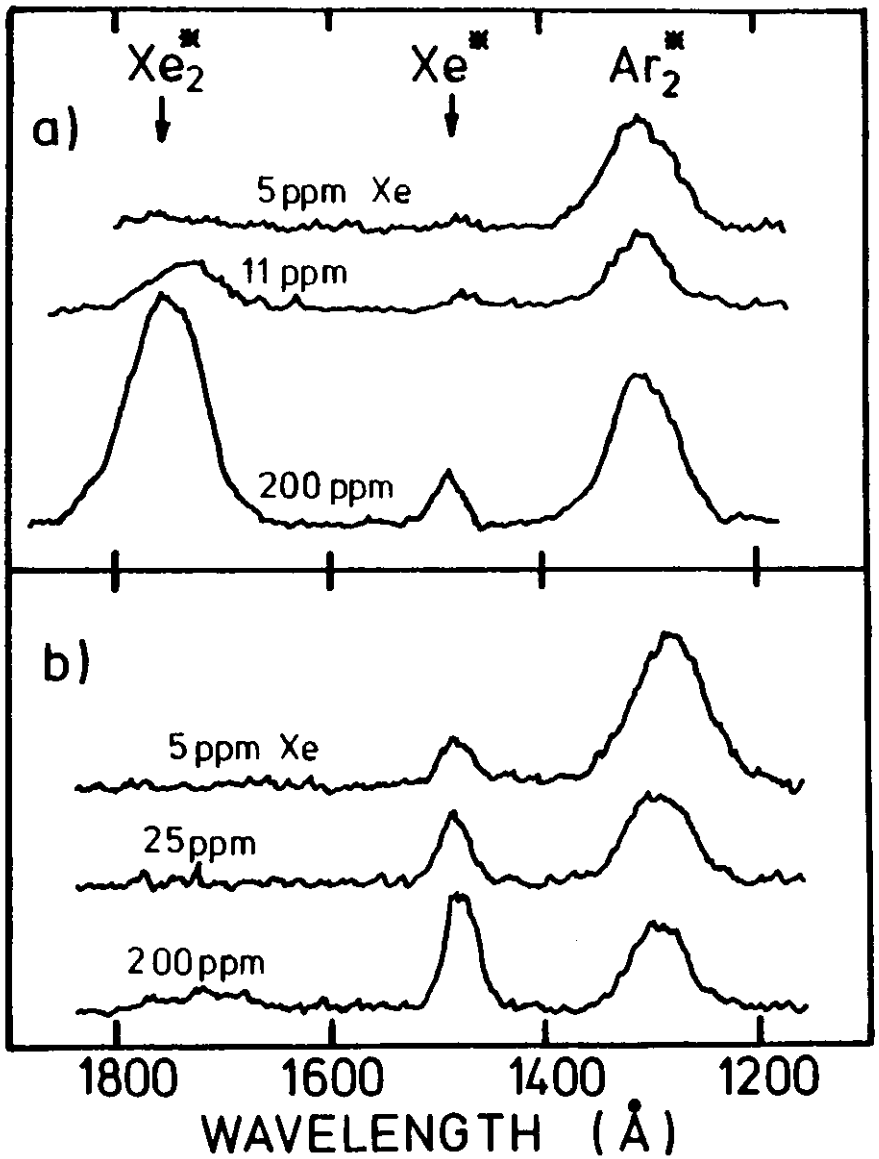
Xe₂*
Xe*
Ar₂*
a)
5 ppm Xe
11 ppm
200 ppm
b)
5 ppm Xe
25 ppm
200 ppm
1800
1600
1400
1200
WAVELENGTH (Å)

Fig. 81

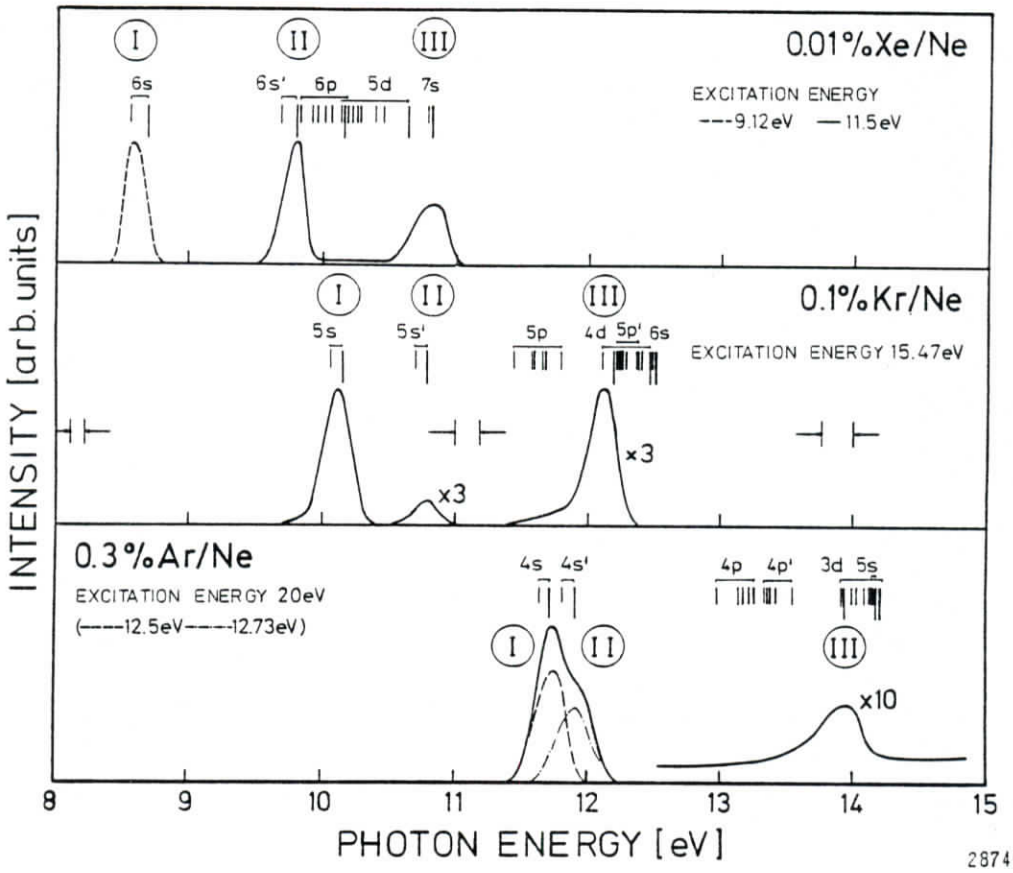
INTENSITY [arb. units]
PHOTON ENERGY [eV]
0.01%Xe/Ne
EXCITATION ENERGY
---9.12eV —11.5eV
6s
6s' 6p 5d 7s
0.1%Kr/Ne
EXCITATION ENERGY 15.47eV
5s
5s'
5p
4d 5p' 6s
×3
0.3%Ar/Ne
EXCITATION ENERGY 20eV
(----12.5eV----12.73eV)
4s 4s'
4p 4p'
3d 5s
×10
28748

Fig. 83

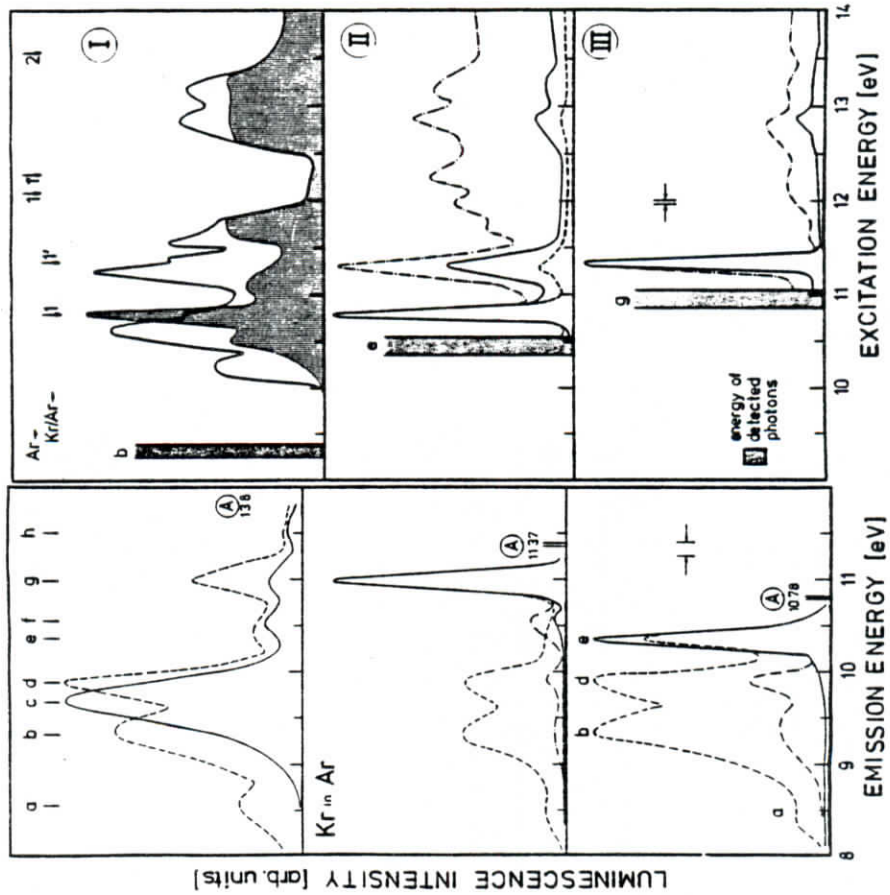
EXCITATION ENERGY [eV]
EMISSION ENERGY [eV]
LUMINESCENCE INTENSITY [arb. units]
Ar–Kr/Ar–
Kr in Ar
energy of detected photons

Fig. 82

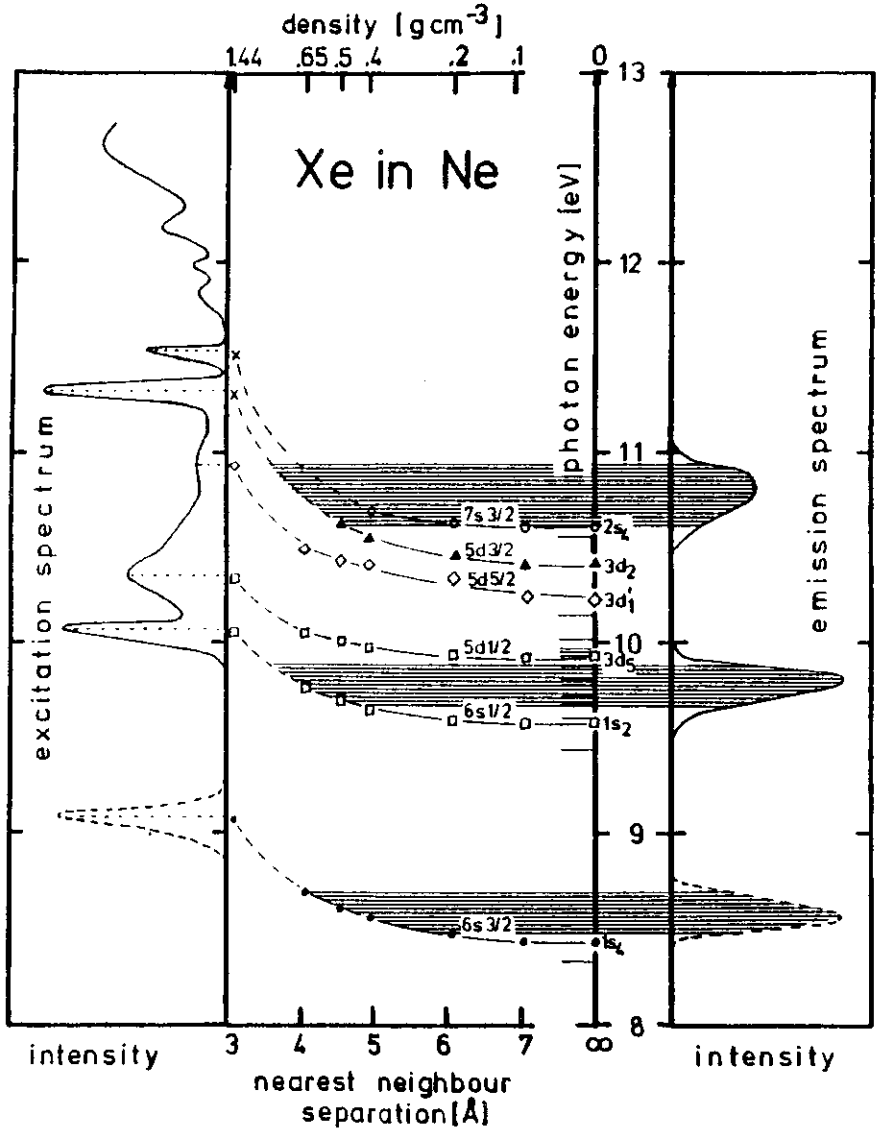
density [g cm^{-3}]
1.44 .65 .5 .4 .2 .1 0
Xe in Ne
photon energy [eV]
13
12
11
10
9
8
excitation spectrum
emission spectrum
7s 3/2
5d 3/2
5d 5/2
5d 1/2
6s 1/2
6s 3/2
2s$_4$
3d$_2$
3d$_1$
3d$_5$
1s$_2$
1s$_4$
intensity
3 4 5 6 7 ∞
nearest neighbour separation [Å]
intensity

Fig. 84

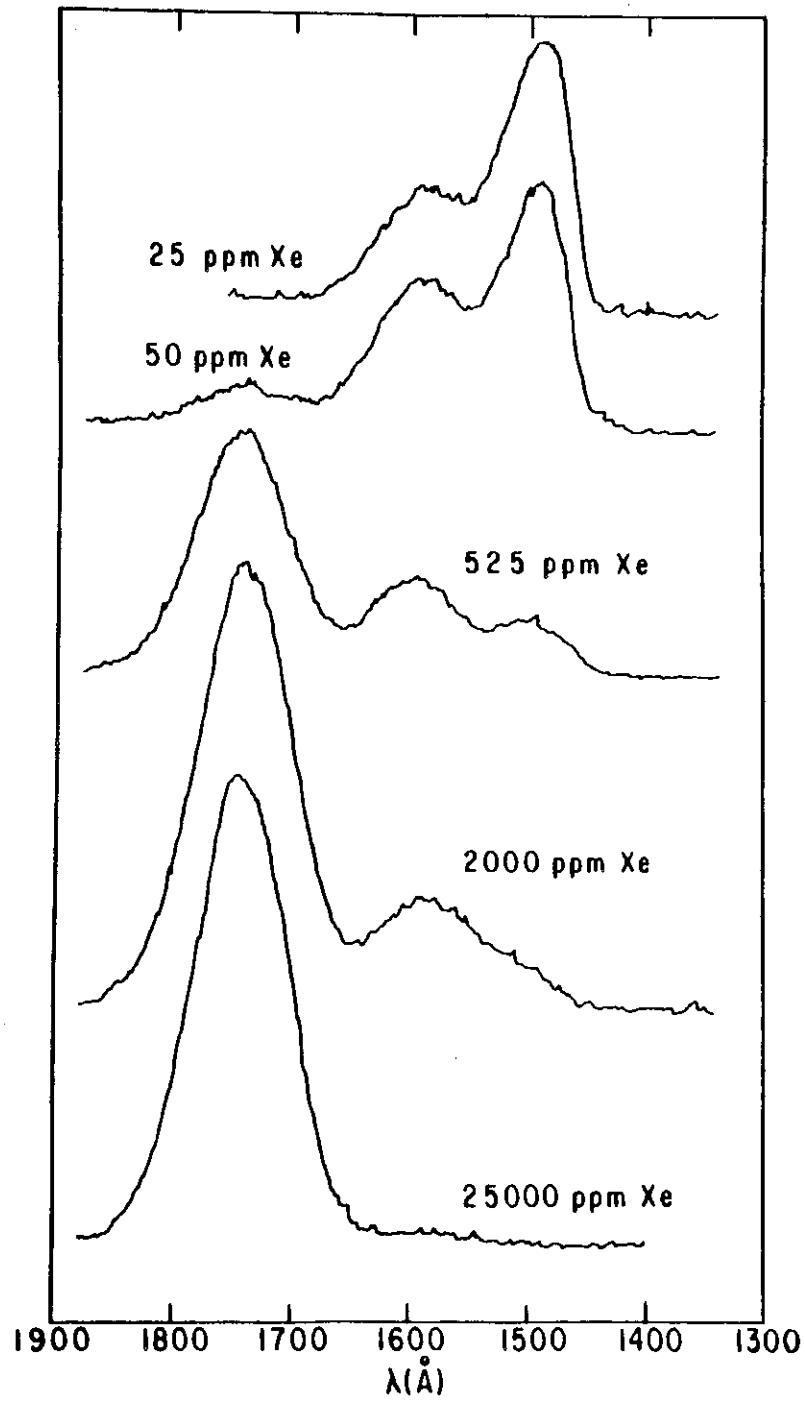
25 ppm Xe
50 ppm Xe
525 ppm Xe
2000 ppm Xe
25000 ppm Xe
1900 1800 1700 1600 1500 1400 1300
λ(Å)

Fig. 85

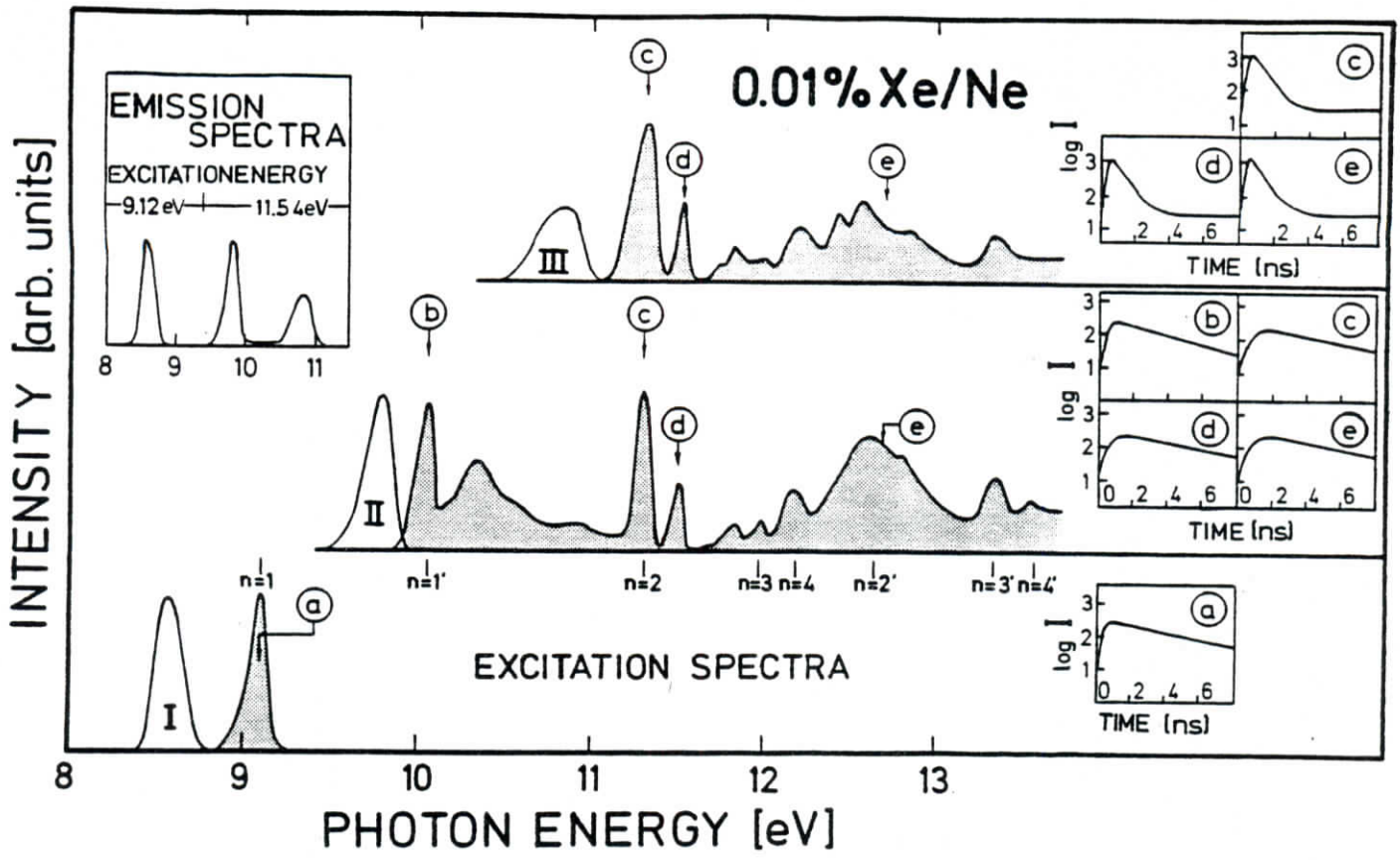
0.01% Xe/Ne
EMISSION SPECTRA
EXCITATION ENERGY
9.12 eV
11.54 eV
INTENSITY [arb. units]
EXCITATION SPECTRA
PHOTON ENERGY [eV]
TIME (ns)
log I
n=1
n=1'
n=2
n=3
n=4
n=2'
n=3'
n=4'

Fig. 87

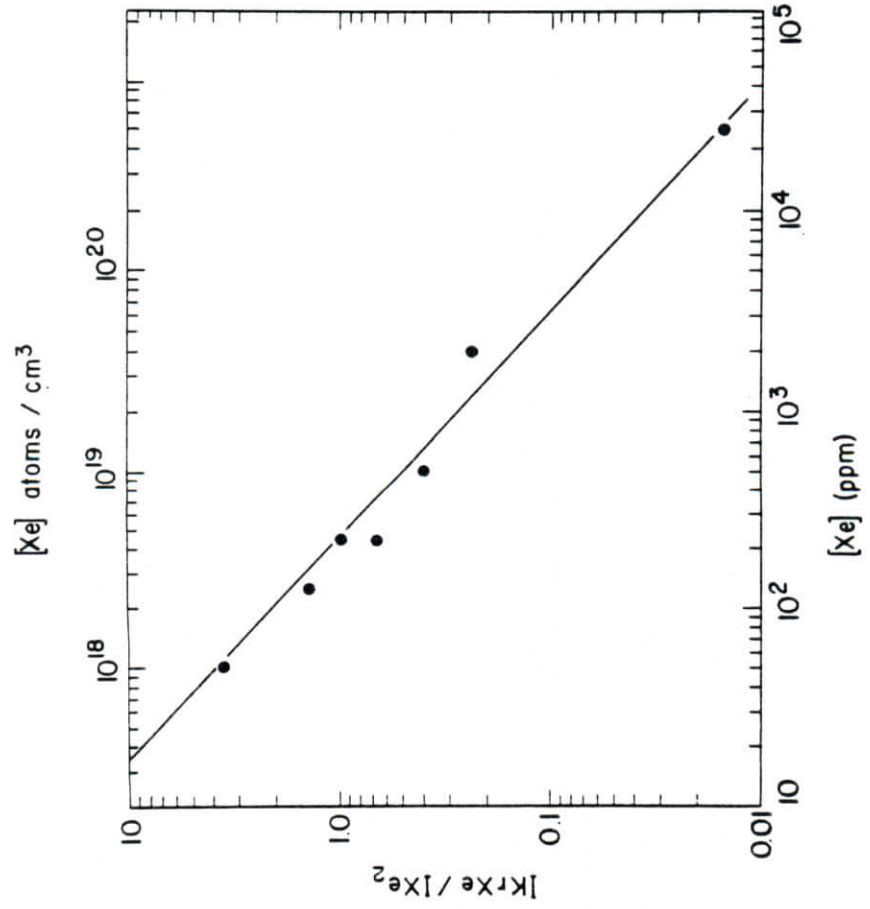
[Xe] atoms / cm3
[Xe] (ppm)
IKrXe / IXe2

Fig. 86

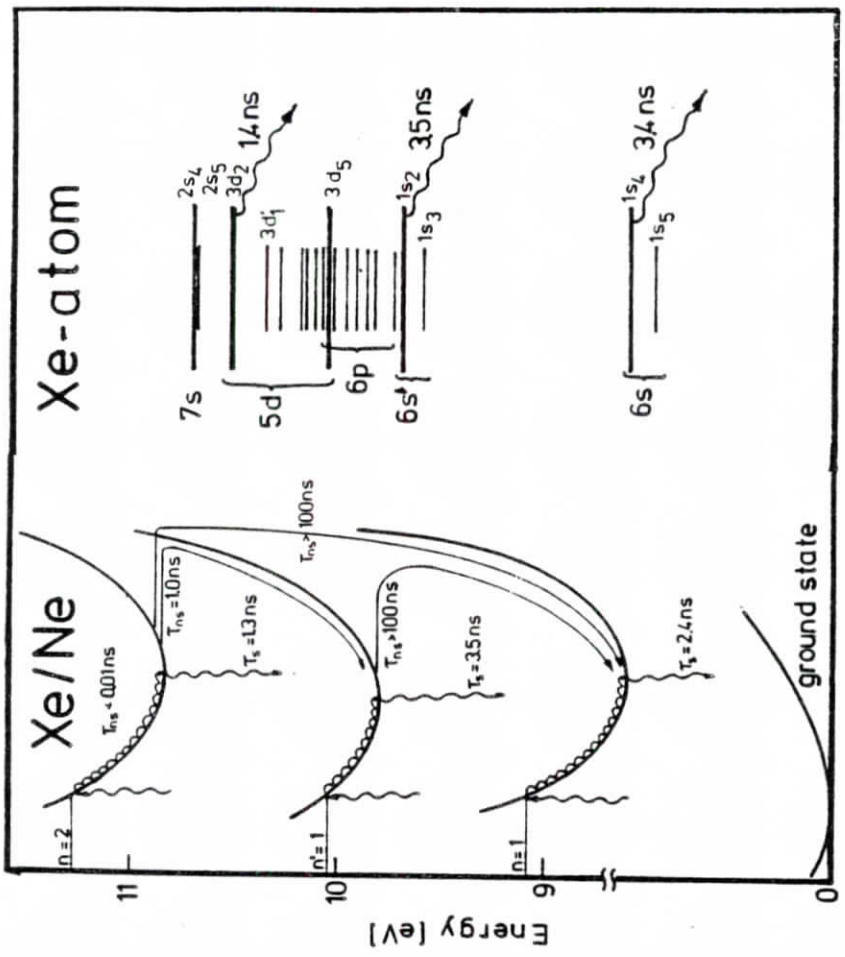
Xe-atom
7s
5d
6p
6s'
6s
Xe/Ne
ground state
Configuration Coordinate
Energy [eV]
n=2
n'=1
n=1
11
10
9
0

Fig. 89

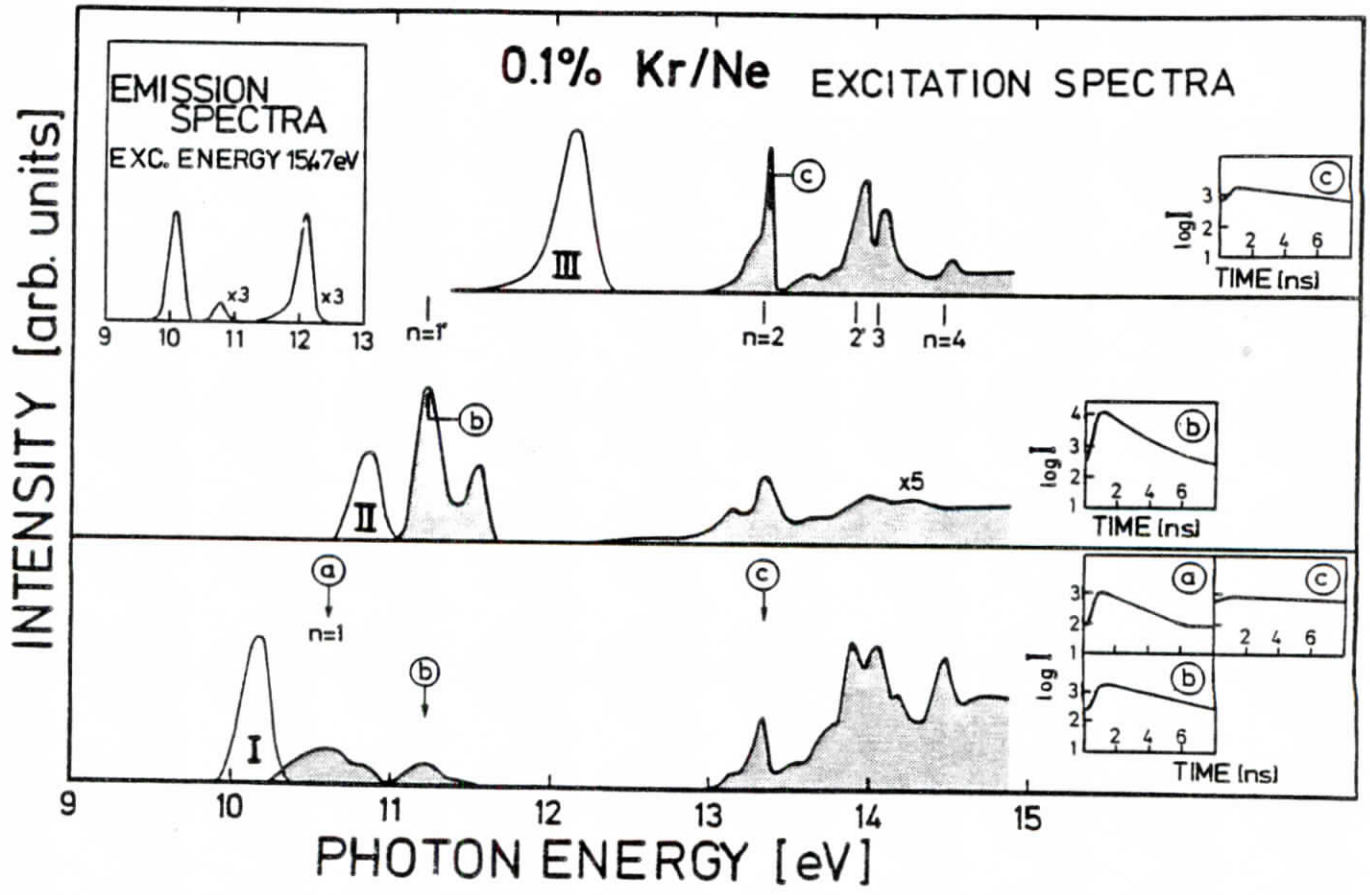
0.1% Kr/Ne EXCITATION SPECTRA
EMISSION SPECTRA
EXC. ENERGY 15.7eV
INTENSITY [arb. units]
PHOTON ENERGY [eV]
TIME (ns)
n=1
n=2
n=4
x5
x3

Fig. 88

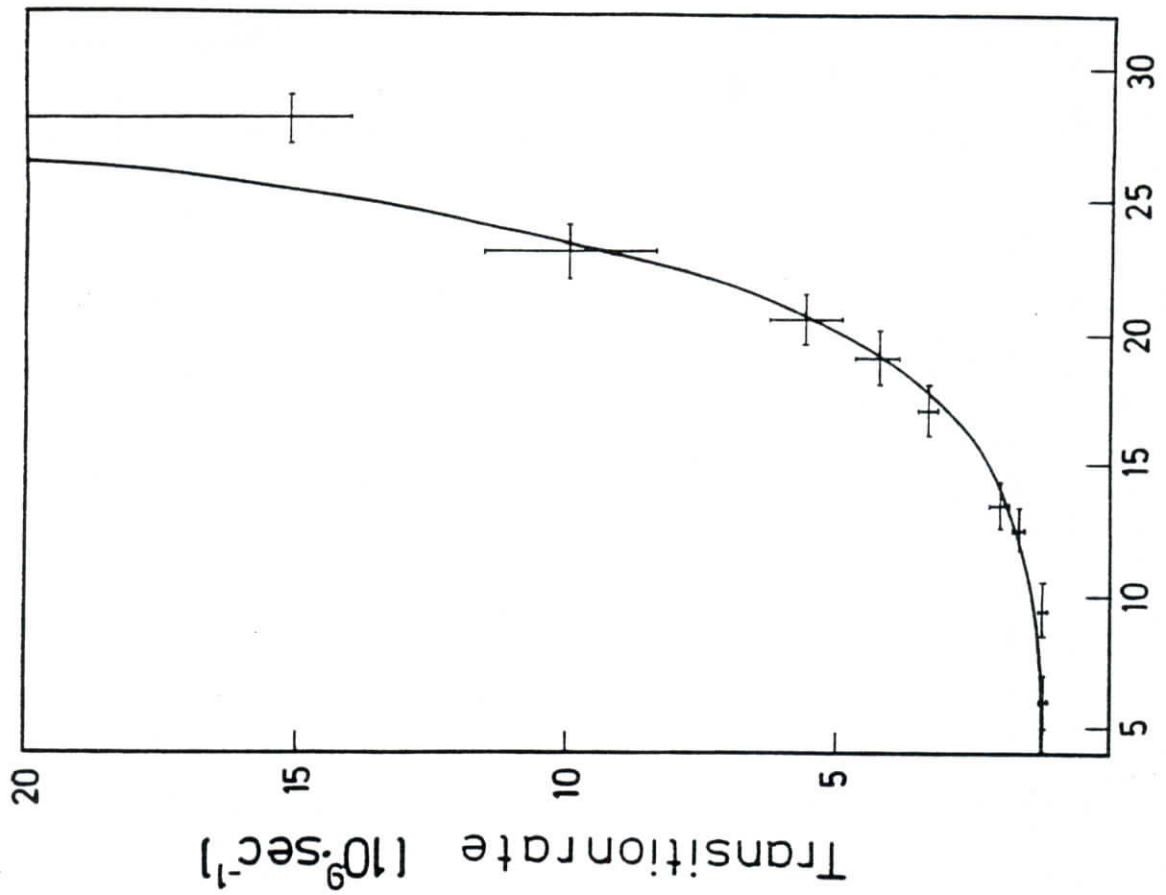
Transitionrate (10⁹·sec⁻¹)
20
15
10
5
Temperature(°K)
30
25
20
15
10
5

Fig.91

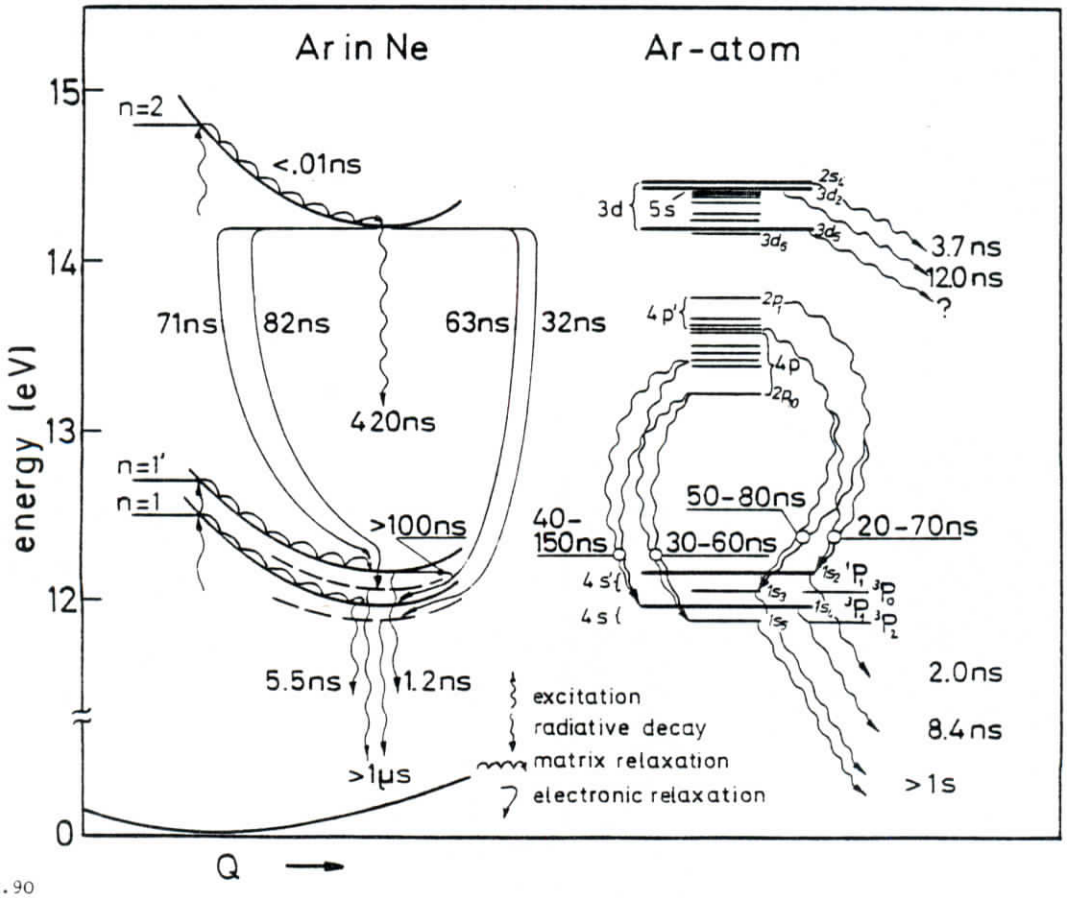
Ar in Ne
Ar-atom
energy (eV)
15
14
13
12
0
n=2
<.01ns
71ns
82ns
63ns
32ns
420ns
n=1'
n=1
>100ns
5.5ns
1.2ns
>1µs
3d
5s
3.7ns
12.0ns
?
4p'
4p
50-80ns
40-
150ns
30-60ns
20-70ns
4s'
4s
2.0ns
8.4ns
>1s
excitation
radiative decay
matrix relaxation
electronic relaxation
Q

Fig.90

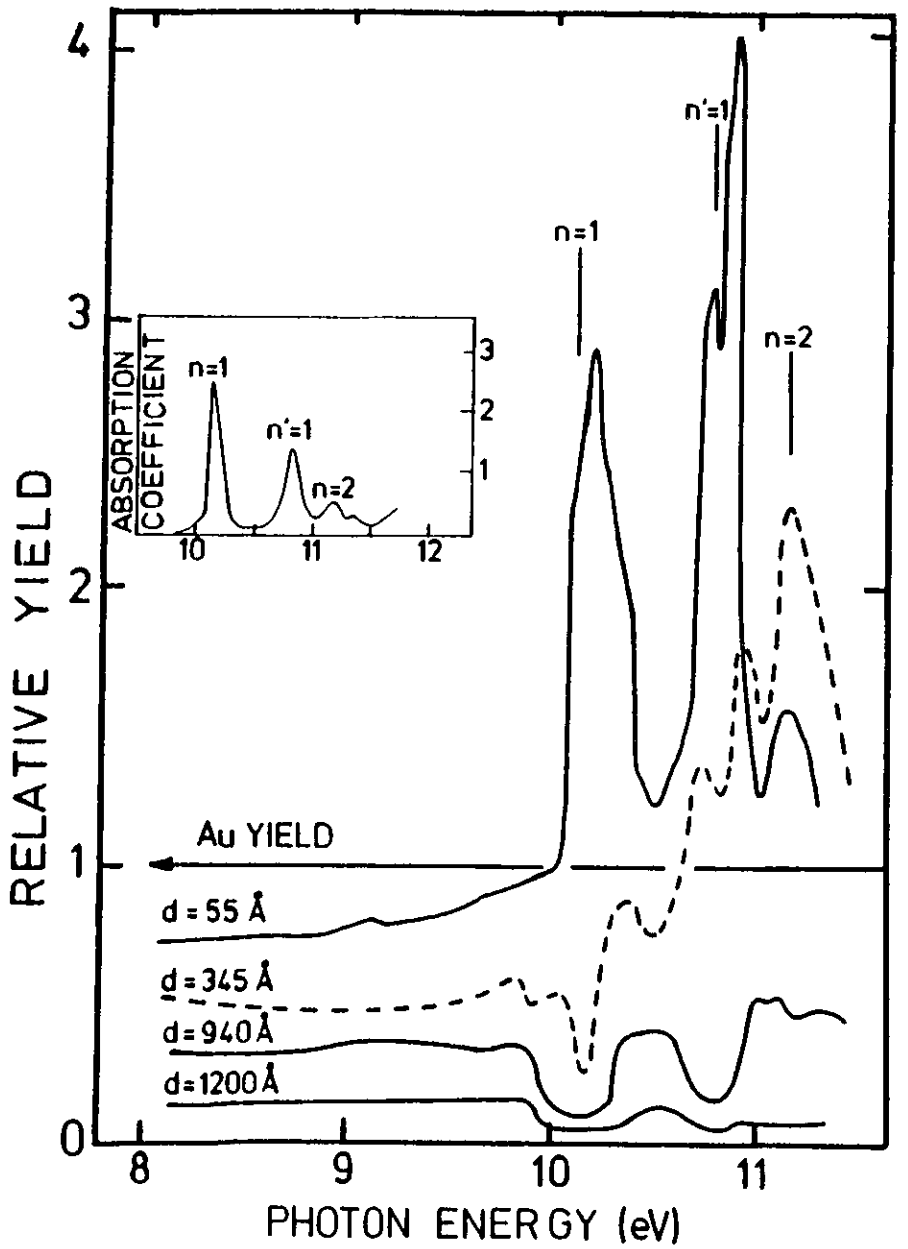
RELATIVE YIELD
PHOTON ENERGY (eV)
n=1
n'=1
n=2
Au YIELD
d = 55 Å
d = 345 Å
d = 940 Å
d = 1200 Å
ABSORPTION COEFFICIENT

Fig.92

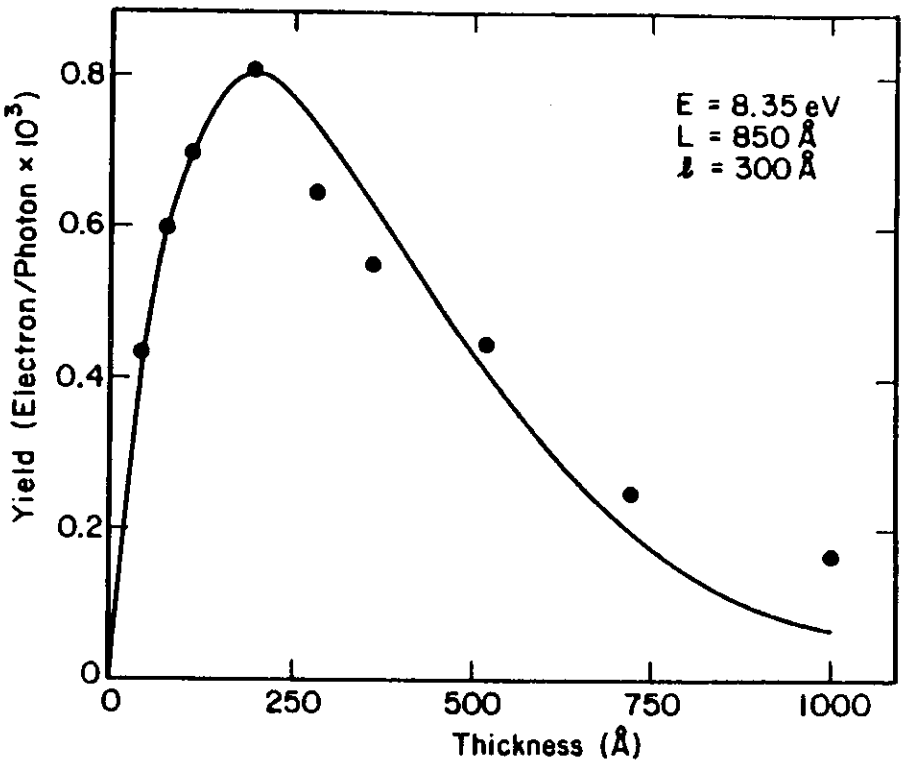
Yield (Electron/Photon × 10³)
Thickness (Å)
E = 8.35 eV
L = 850 Å
ℓ = 300 Å

Fig.93

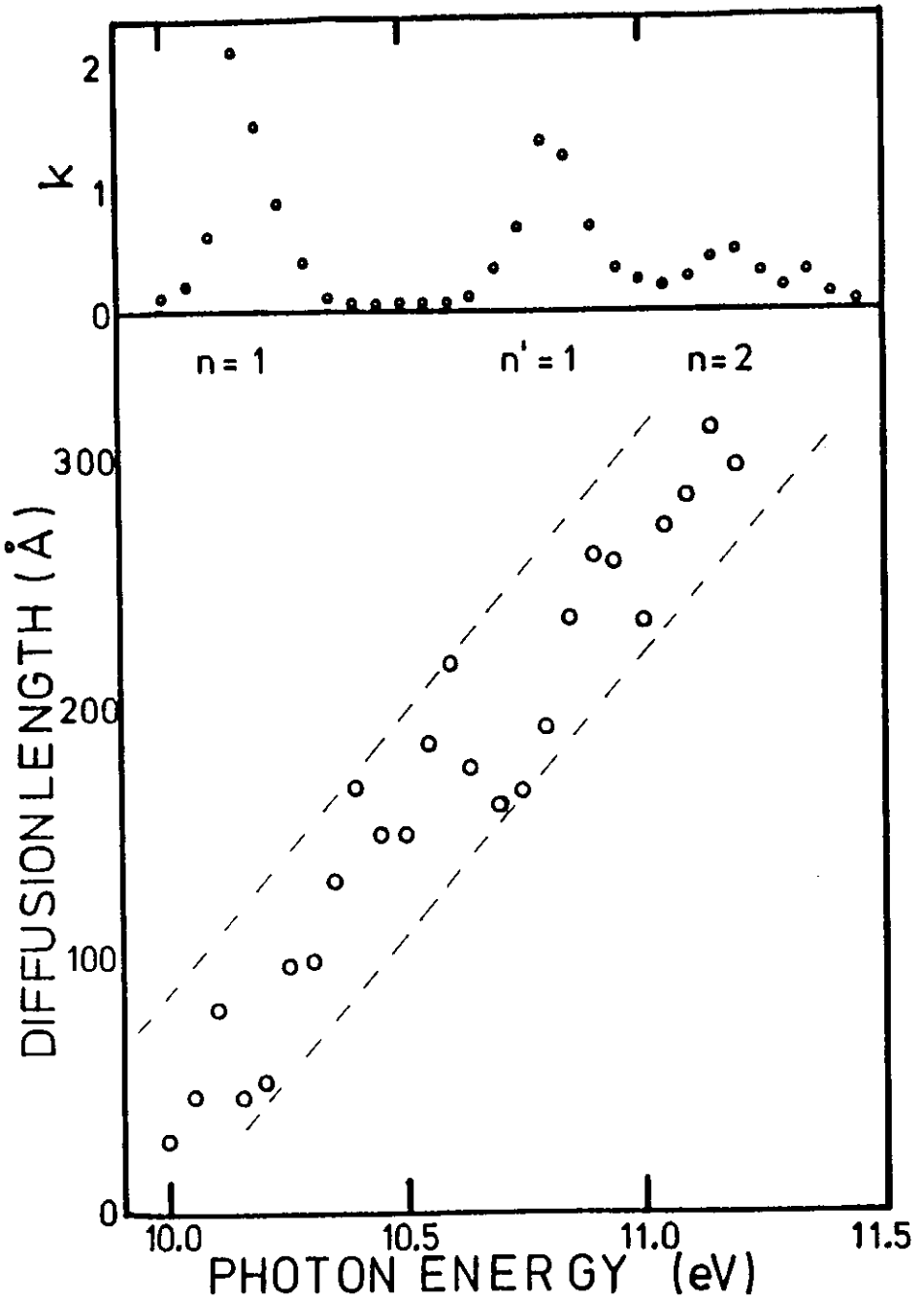
k
2
1
0
n = 1
n' = 1
n = 2
300
200
100
0
DIFFUSION LENGTH (Å)
10.0
10.5
11.0
11.5
PHOTON ENERGY (eV)

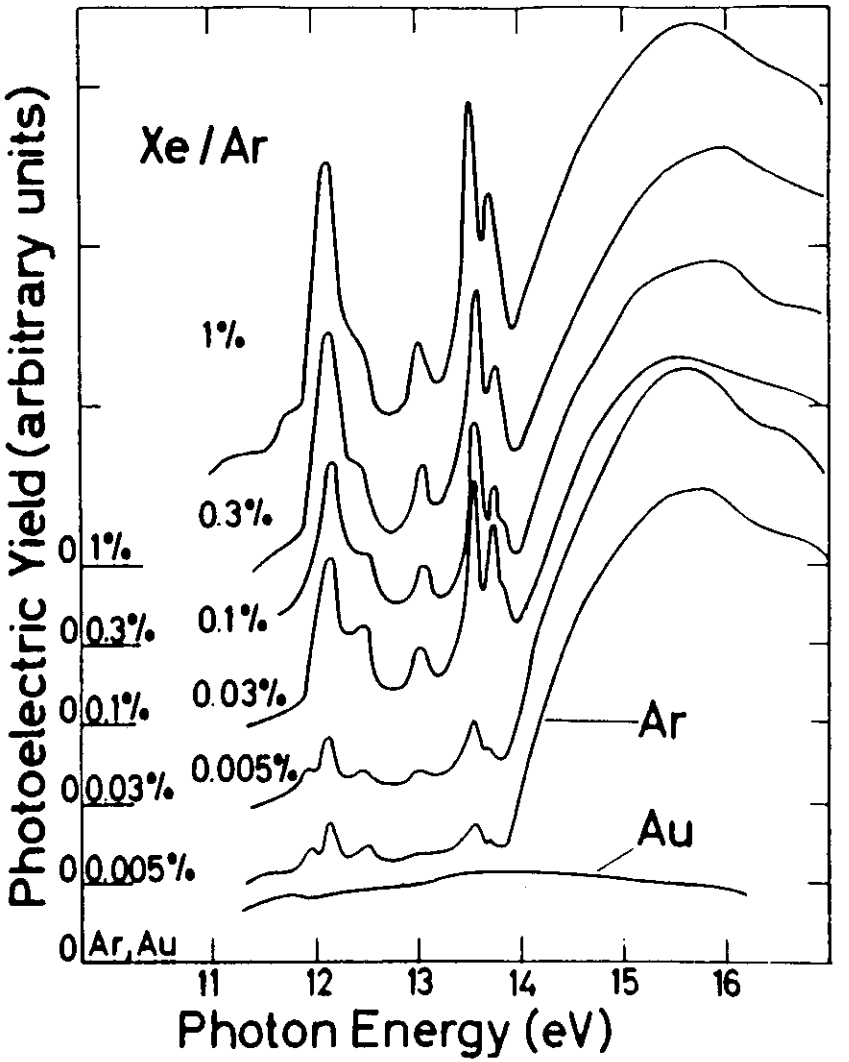
Xe / Ar
1%
0.3%
0.1%
0.03%
0.005%
Ar
Au
Photoelectric Yield (arbitrary units)
0 1%
0 0.3%
0 0.1%
0 0.03%
0 0.005%
0 Ar, Au
11
12
13
14
15
16
Photon Energy (eV)

Fig.95

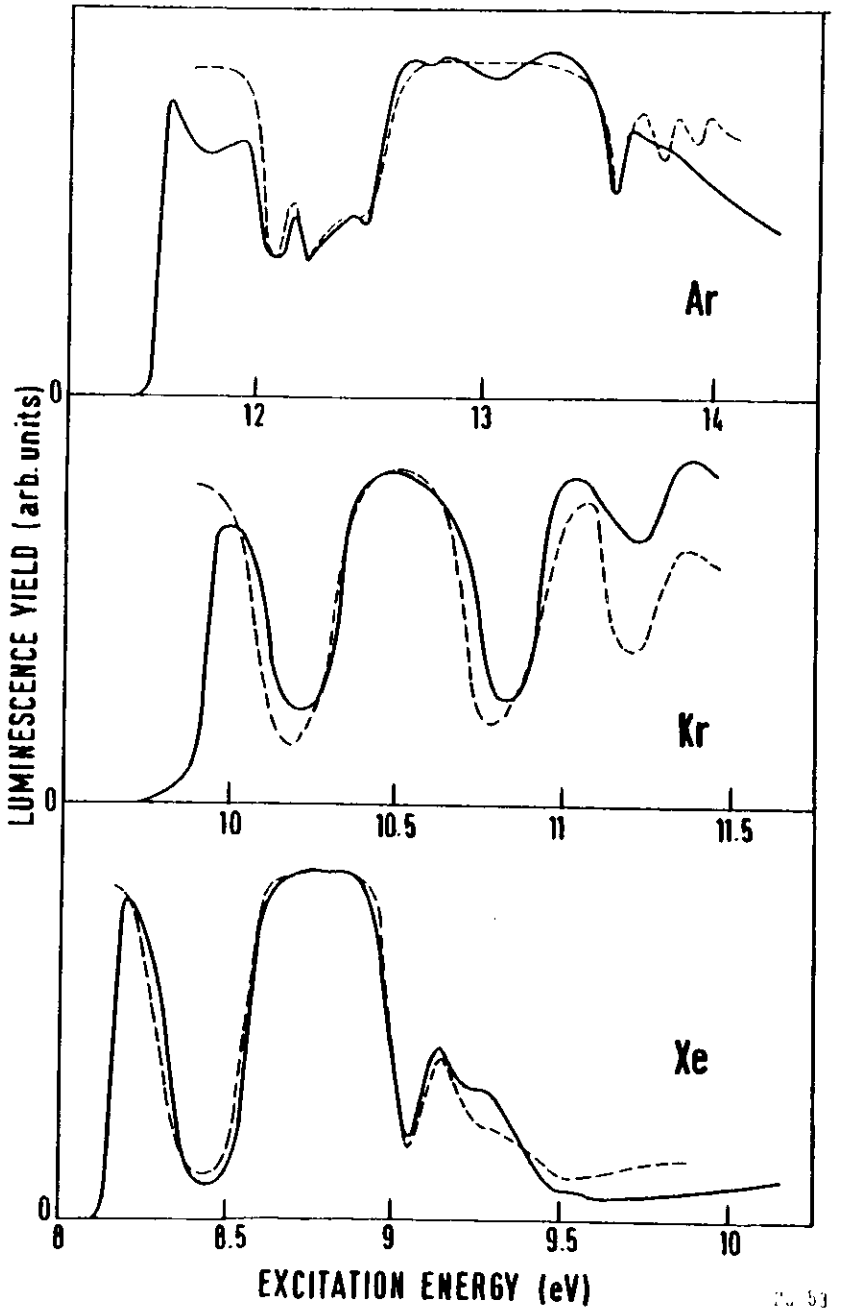
LUMINESCENCE YIELD (arb. units)
Ar
Kr
Xe
0
12
13
14
10
10.5
11
11.5
8
8.5
9
9.5
10
EXCITATION ENERGY (eV)

Fig.96

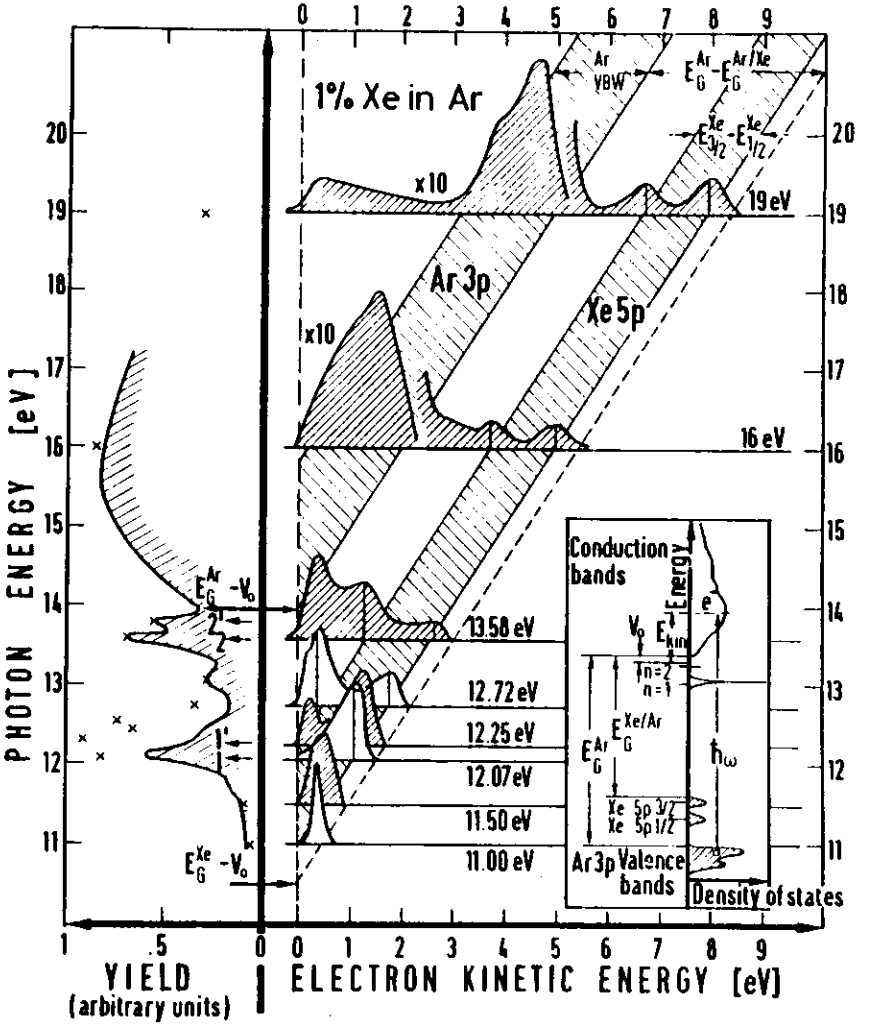
1% Xe in Ar
Ar VBW
$E_G^{Ar} - E_G^{Ar/Xe}$
$E_{3/2}^{Xe} - E_{1/2}^{Xe}$
x10
19eV
Ar 3p
Xe 5p
16 eV
13.58 eV
12.72 eV
12.25 eV
12.07 eV
11.50 eV
11.00 eV
$E_G^{Ar} - V_o$
$E_G^{Xe} - V_o$
Conduction bands
Energy
V_o
E_{kin}
e⁻
n=2
n=1
E_G^{Ar}
$E_G^{Xe/Ar}$
$h\omega$
Xe 5p 3/2
Xe 5p 1/2
Ar 3p Valence bands
Density of states
PHOTON ENERGY [eV]
YIELD (arbitrary units)
ELECTRON KINETIC ENERGY [eV]

Fig.97

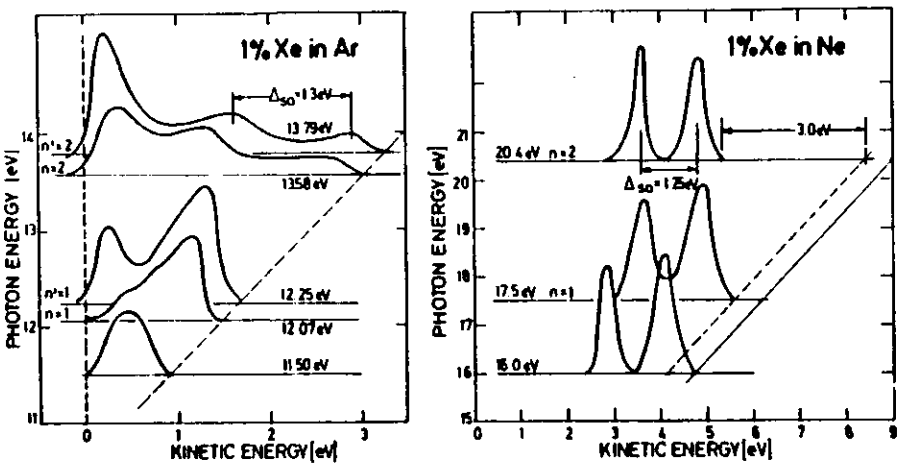
1% Xe in Ar
Δso=1.3eV
13.79eV
n'=2
n=2
13.58 eV
n'=1
n=1
12.25 eV
12.07 eV
11.50 eV
PHOTON ENERGY (eV)
KINETIC ENERGY (eV)
1% Xe in Ne
3.0eV
20.4 eV n=2
Δso=1.25eV
17.5 eV n=1
16.0 eV
PHOTON ENERGY (eV)
KINETIC ENERGY (eV)

Fig.98

Fig.99

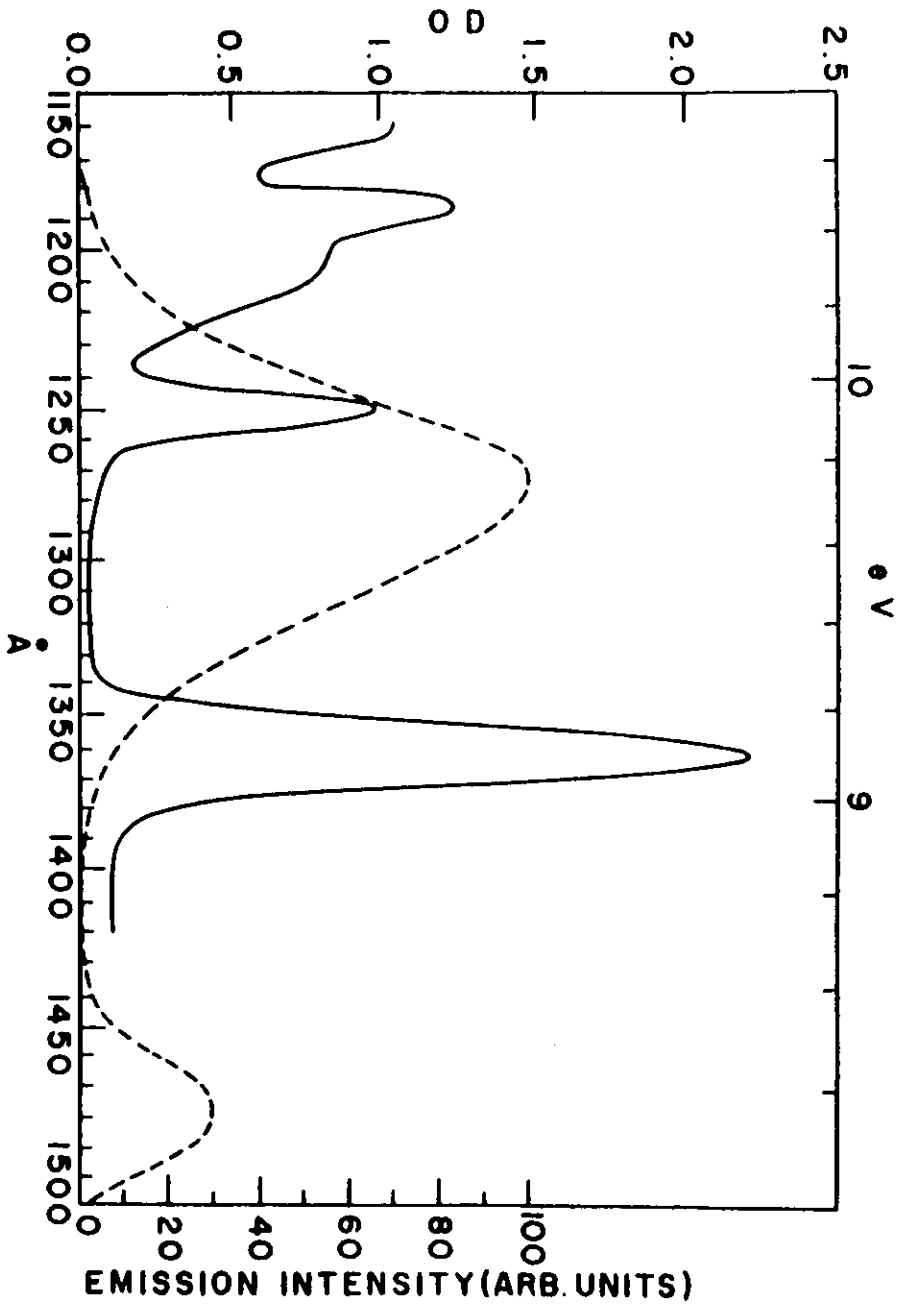
O D
0.0
0.5
1.0
1.5
2.0
2.5
1150
1200
1250
1300
1350
1400
1450
1500
Å
10
9
eV
0
20
40
60
80
100
EMISSION INTENSITY (ARB. UNITS)

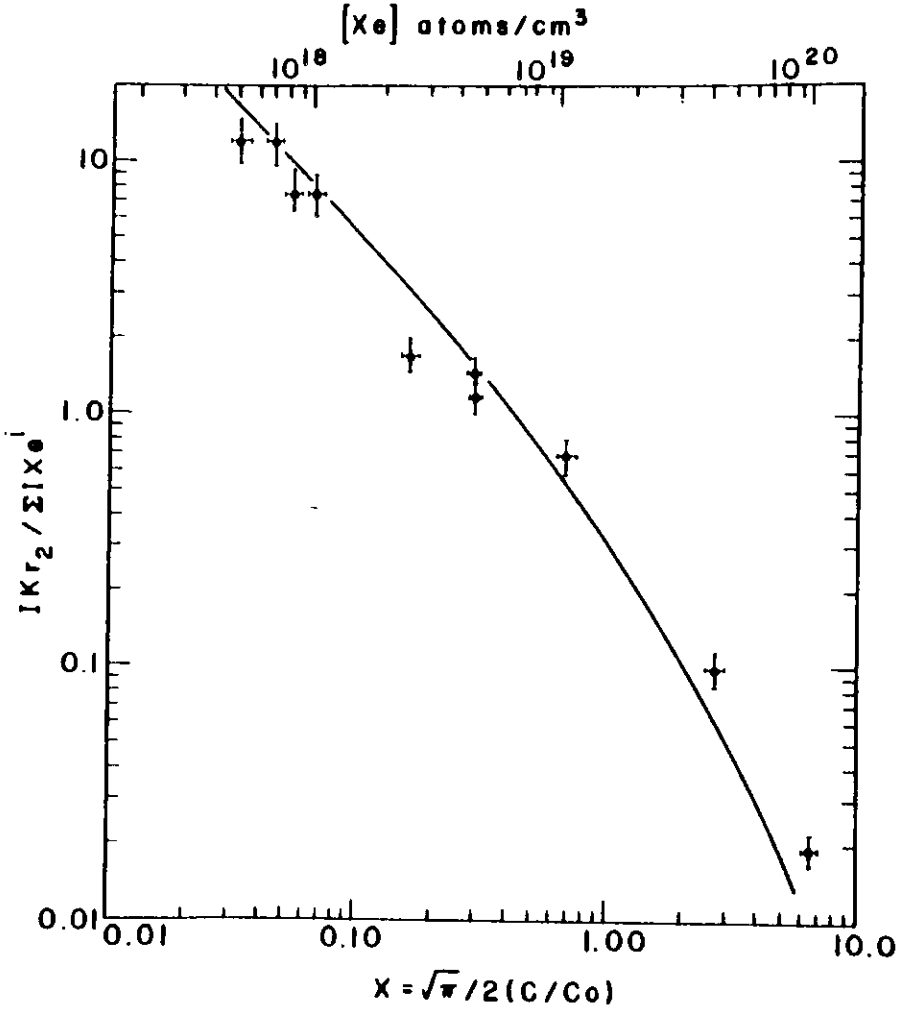

Fig. 100

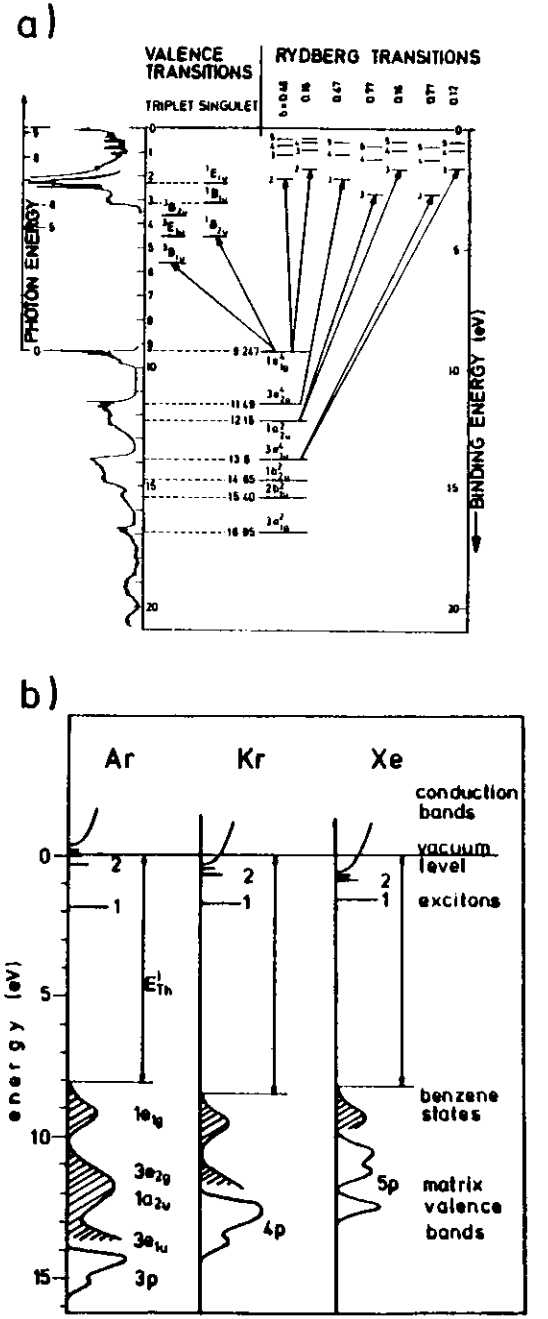

Fig. 101

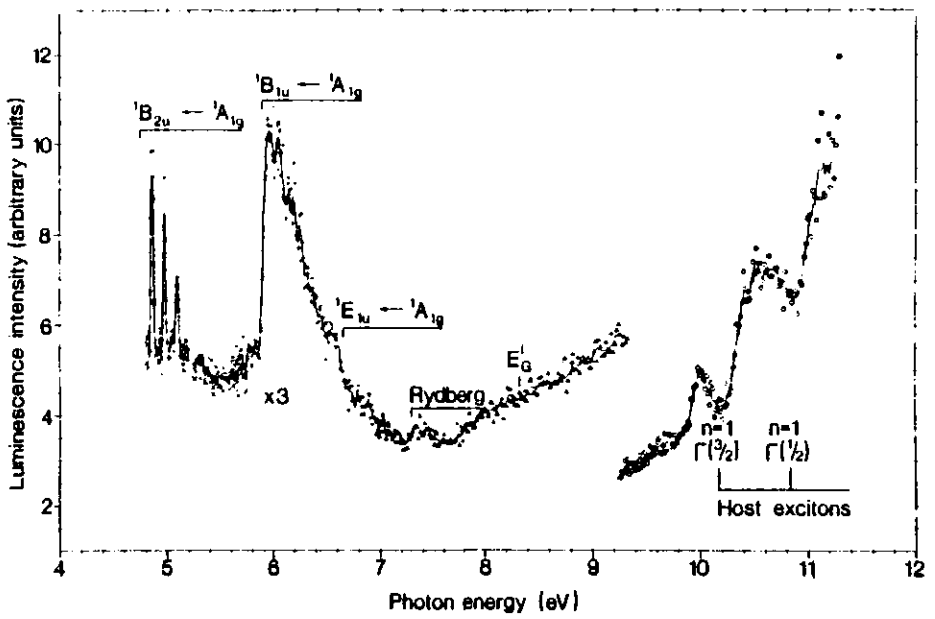

Fig. 102

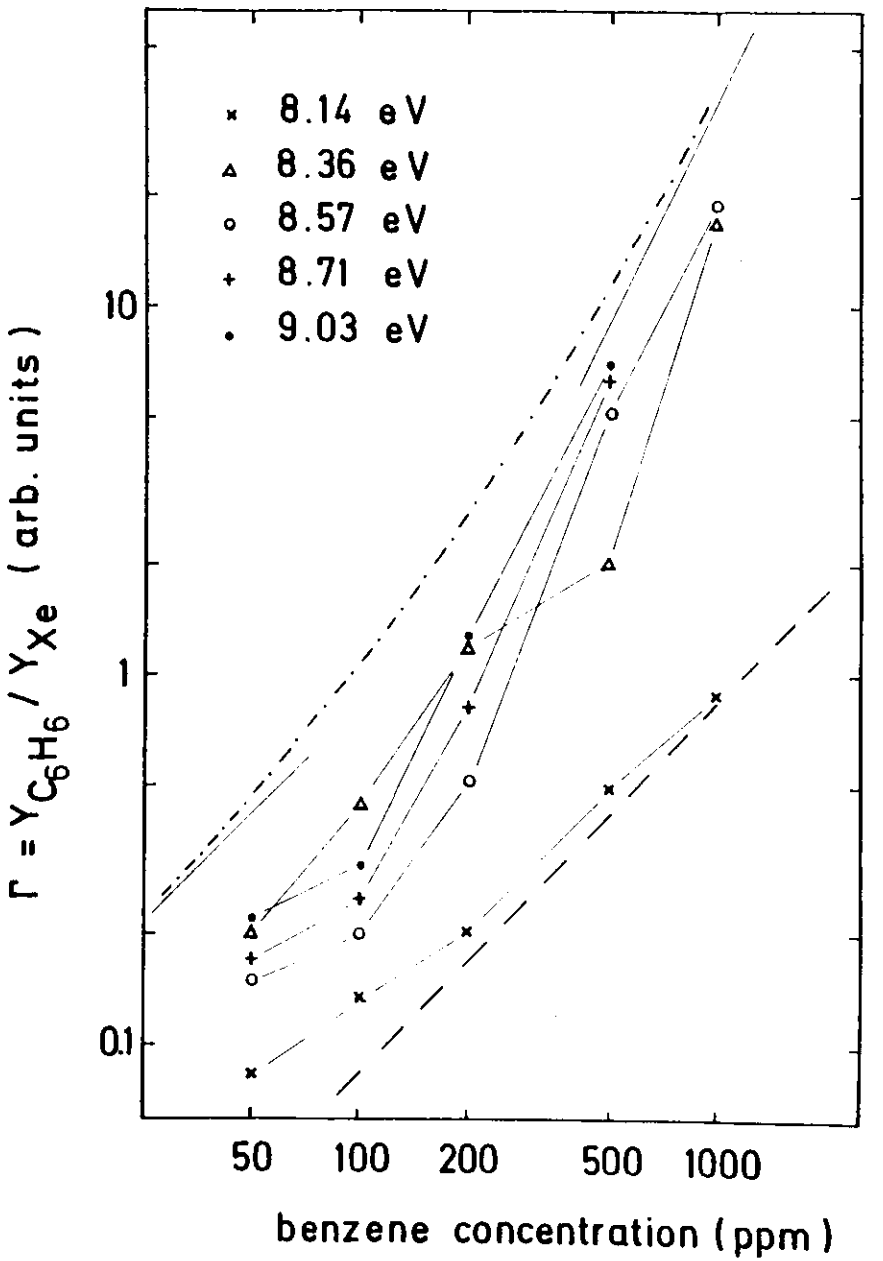

Fig. 103

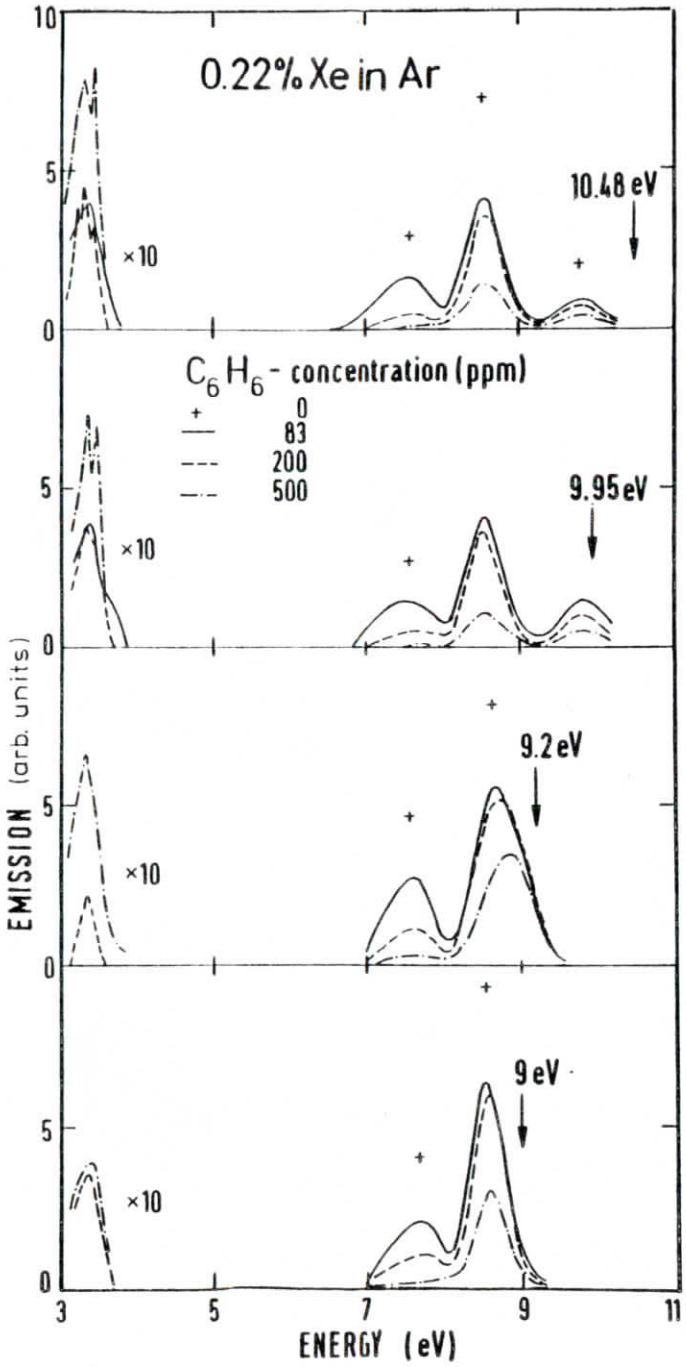

Fig. 104

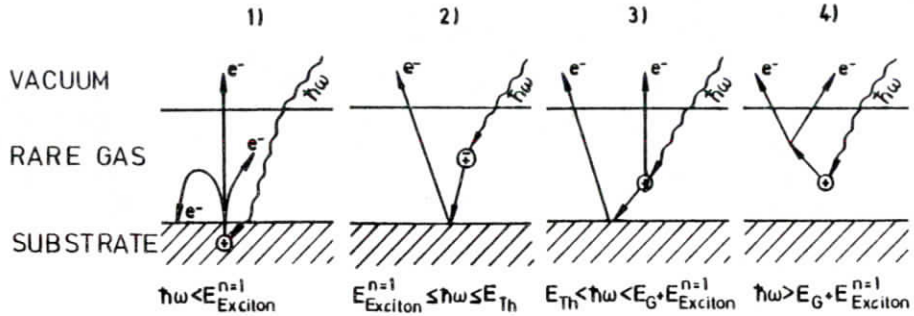

Fig. 105

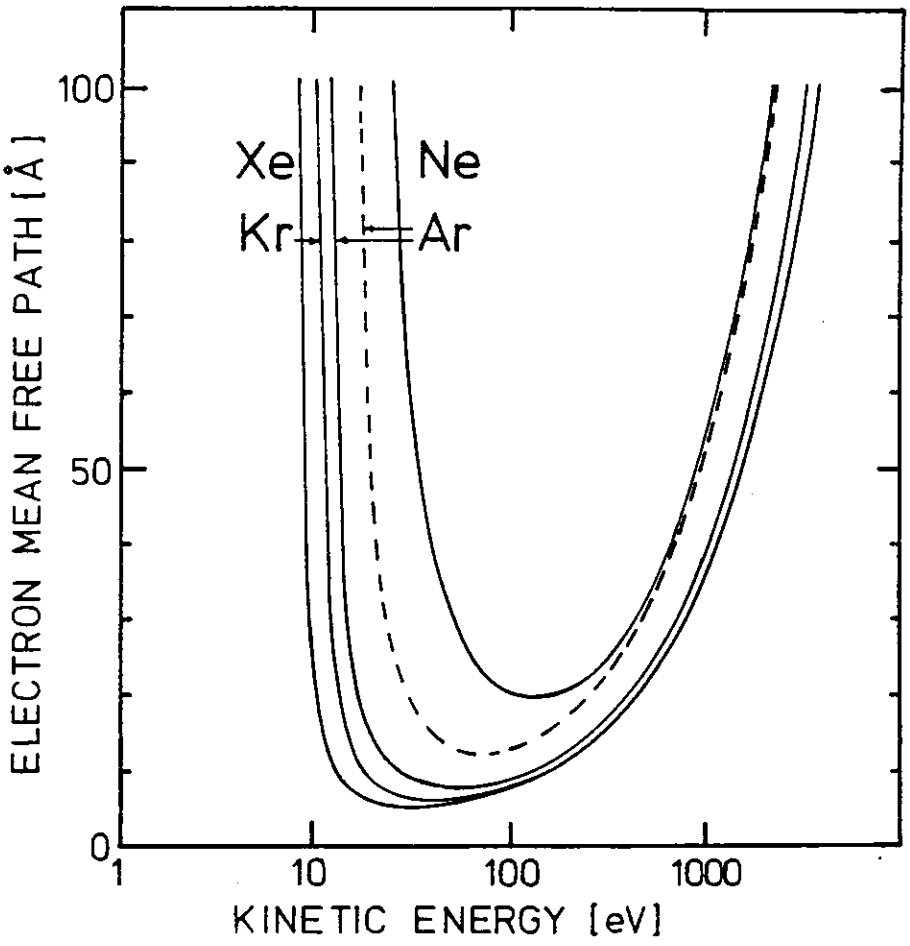

Fig.106

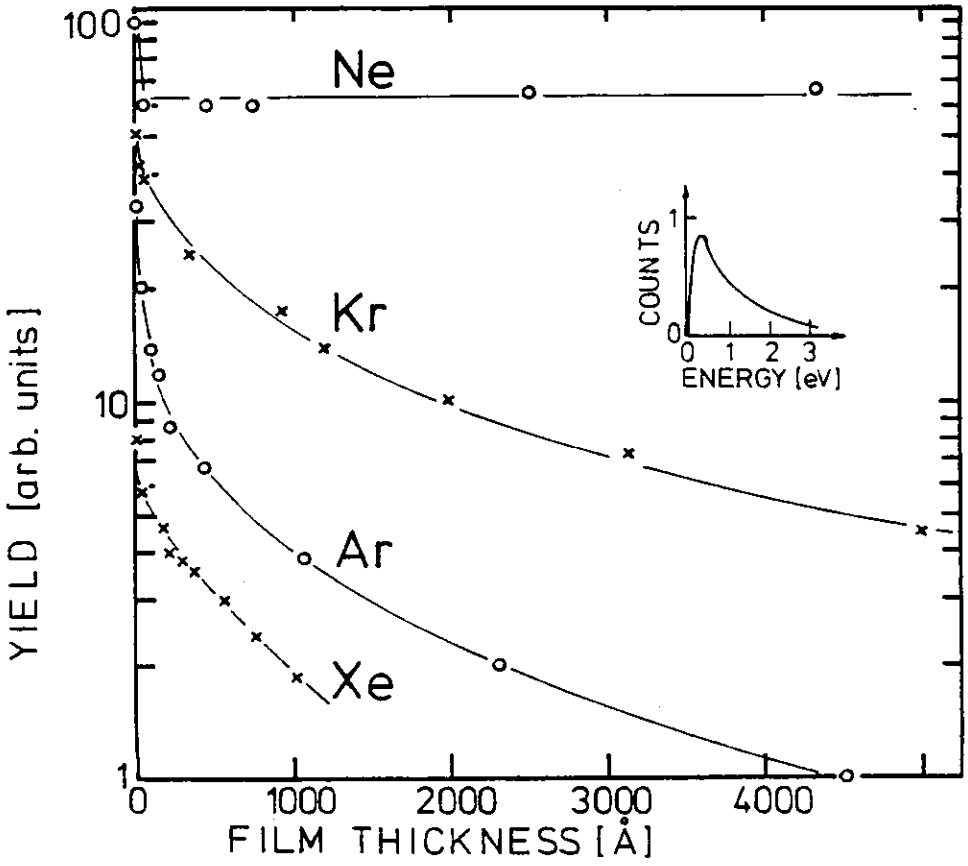

Fig.107

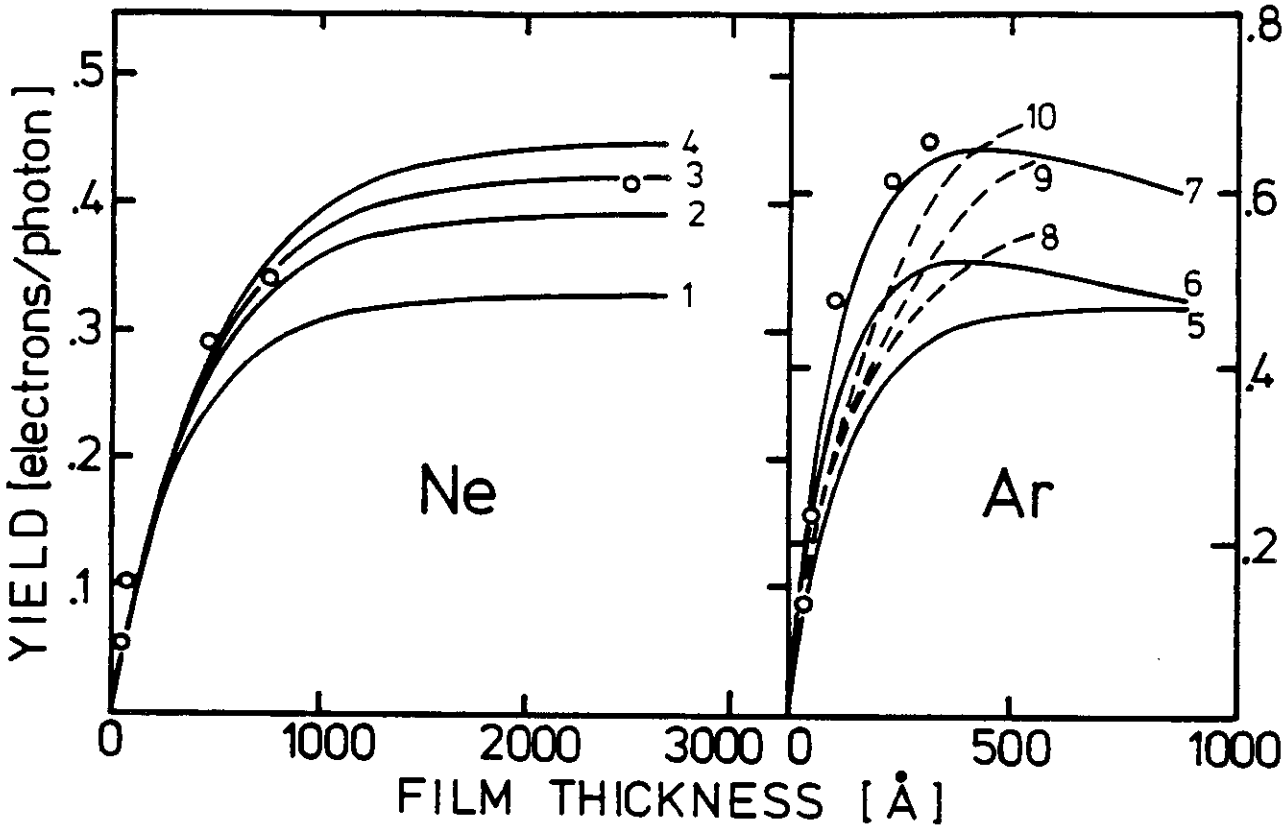

Fig.108

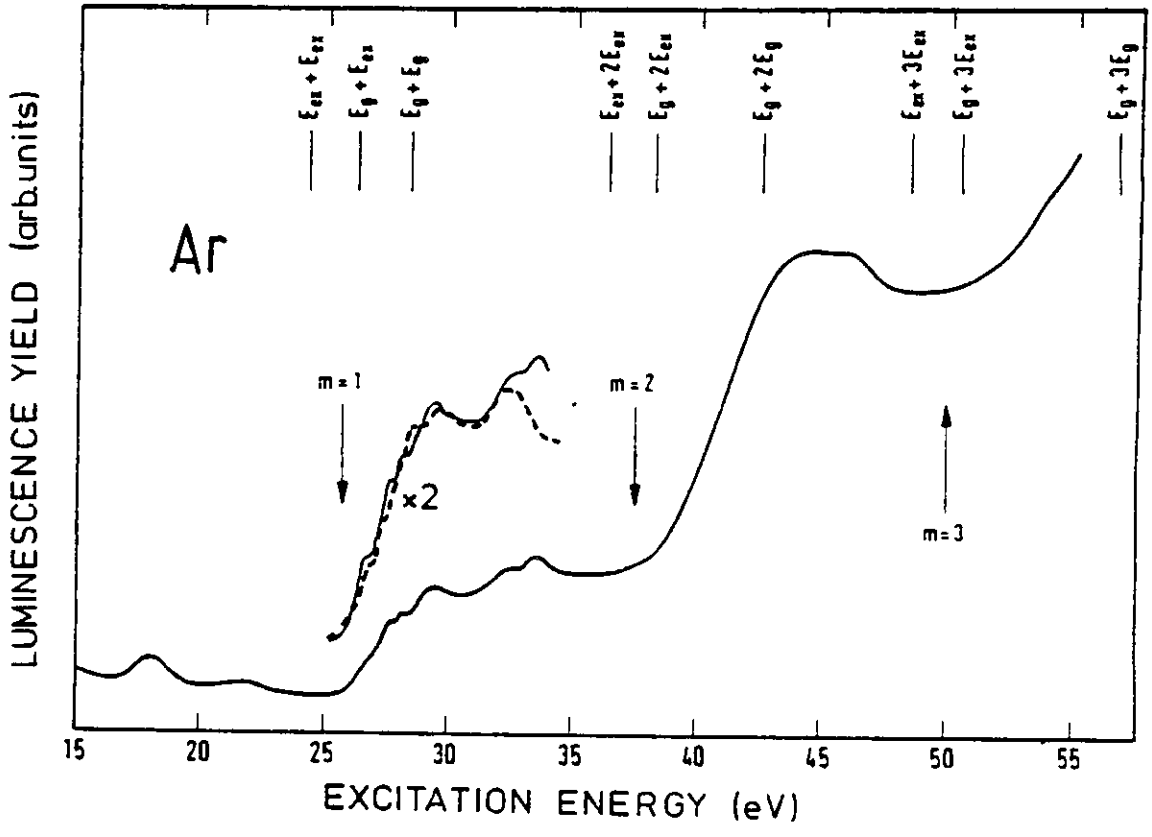

Fig.109

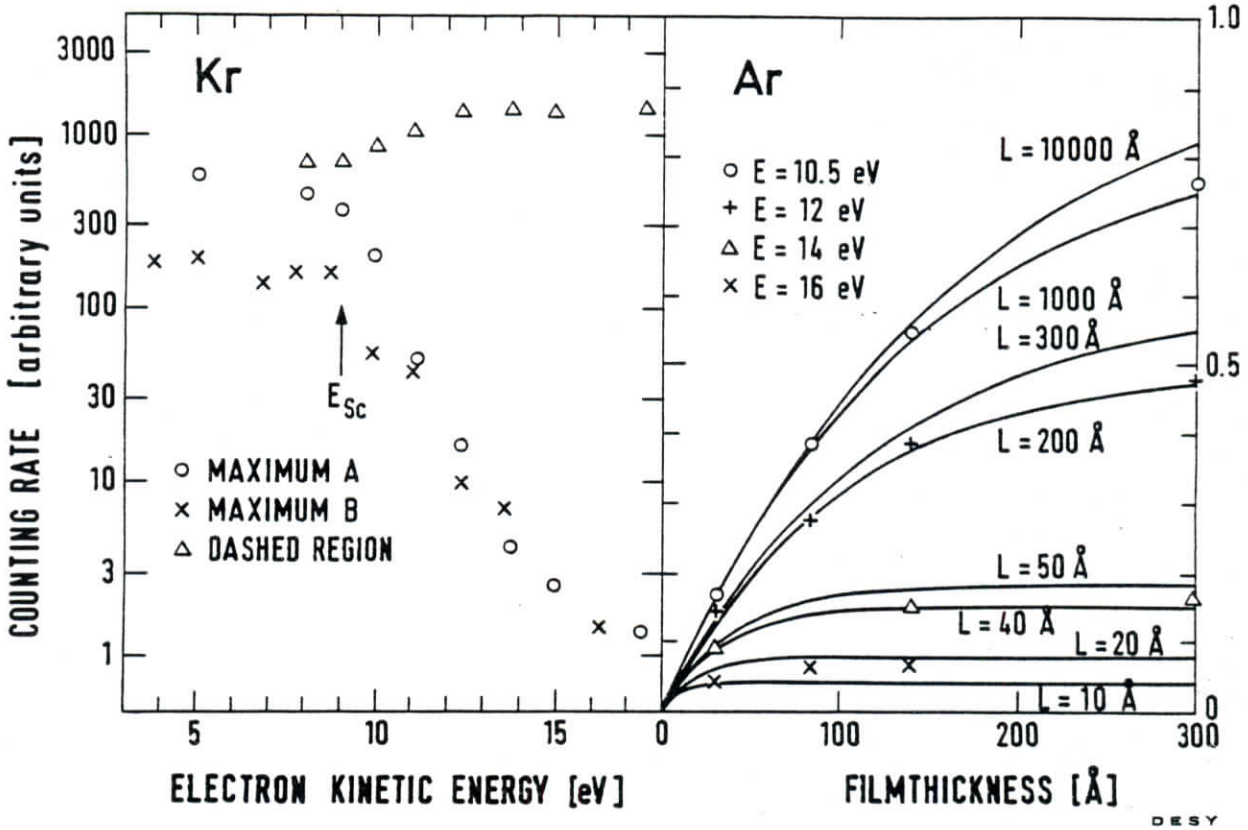

Fig.111

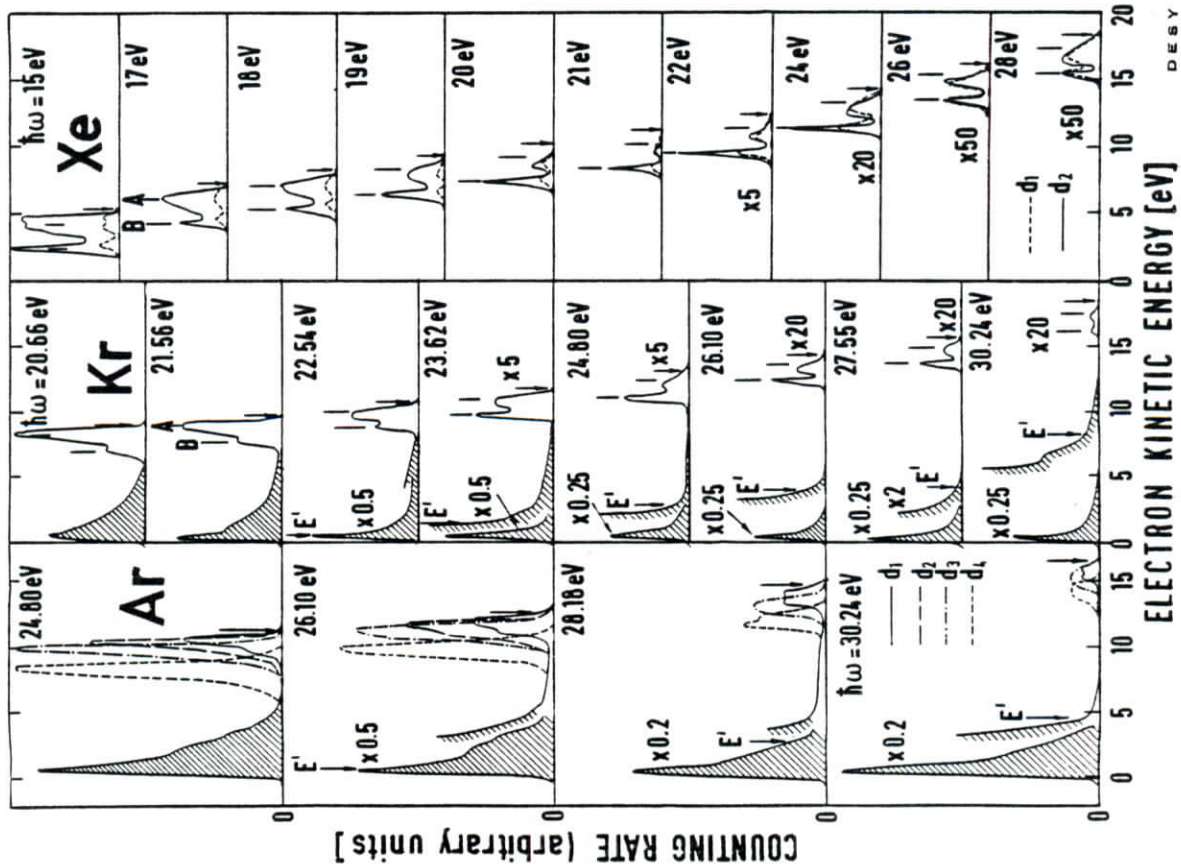

Fig.110

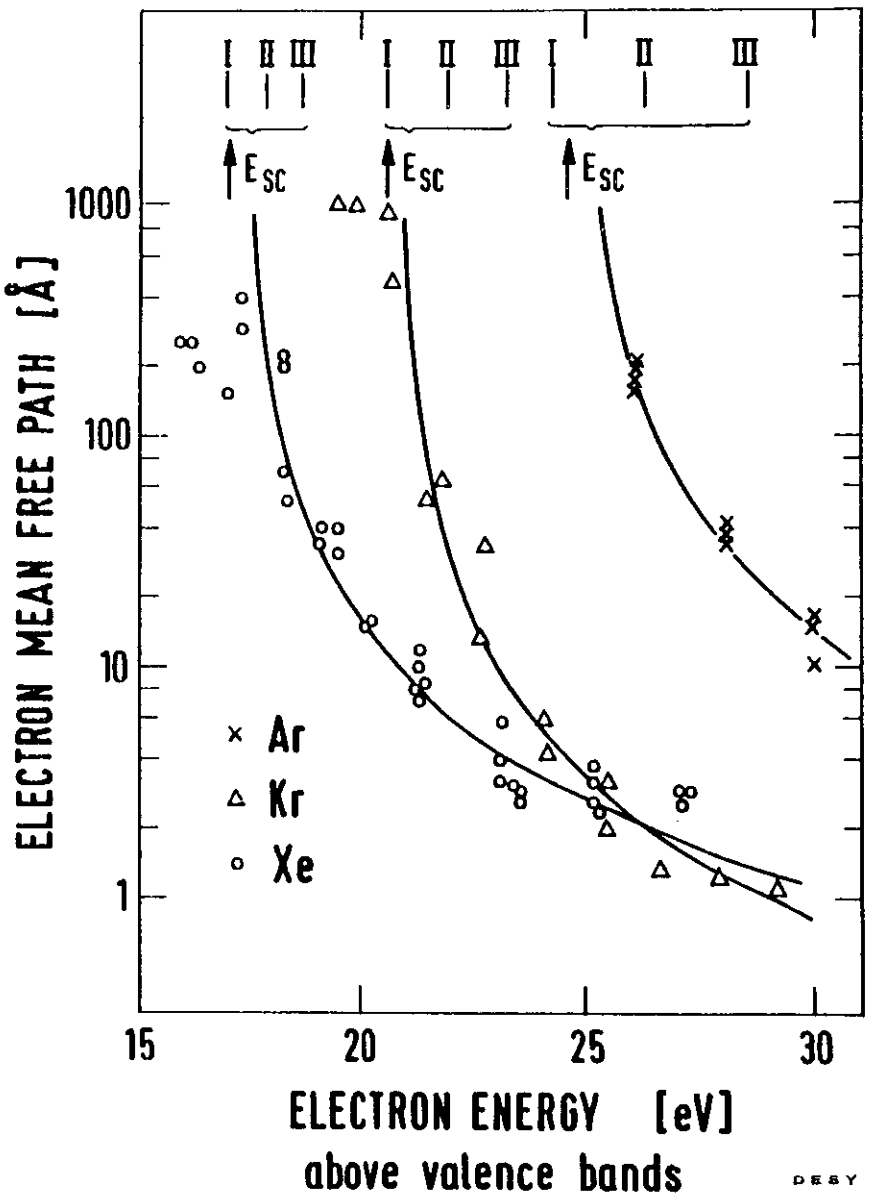

Fig.112

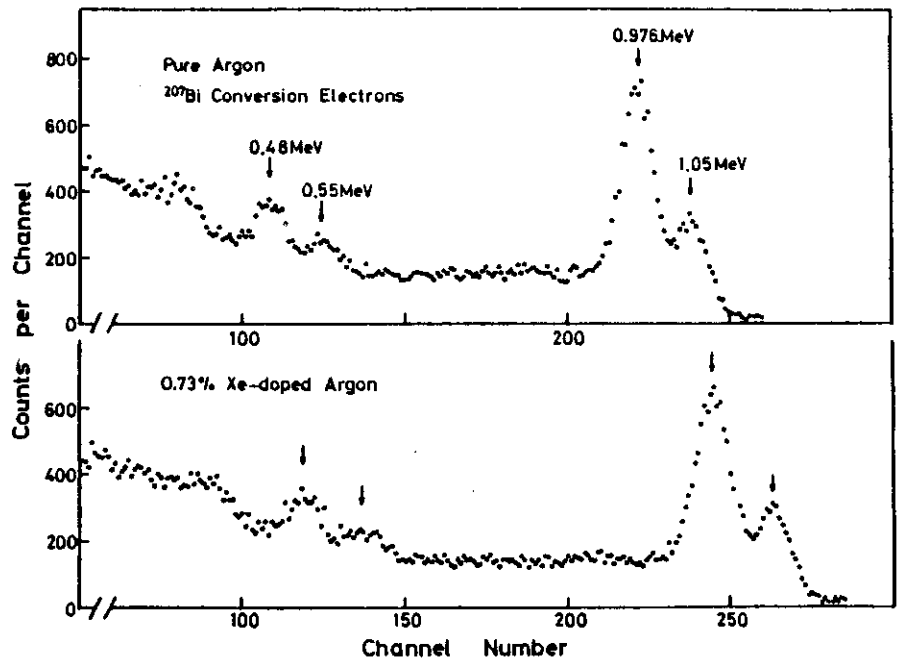

Fig.113